東京大学学位論文

Flux Synthesizing Linear Induction Motor

(磁束合成形リニア誘導モータに関する研究)

KOSEKI, Takafumi
古関　隆章
(東京都)

Department of Electrical Engineering,
The University of Tokyo
東京大学大学院工学系研究科電気工学専攻

Research supervisor: Professor MASADA, Eisuke
指導教官:　正田　英介　教授
Submitted: 20. December 1991
提出日:　平成３年１２月２０日 (金)

Acknowledgement

My first acknowledgement of indebtedness goes to Prof. Eisuke Masada, my research supervisor at the University of Tokyo, and *Prof. Dr. -Ing.* Herbert Weh at the *Technischen Universität Braunschweig,* who so generously provided assistance in the execusion of this research.

I am also grateful to Dr. H. Ohsaki, Mr. M. Tamura, Dr. T. Nakajima, Mr. S. Torii, Mr. L. Matakas Jr., Mr. T. Morizane, Mr. T. Imazu, Mr. H. Okada, Mr. T. Shibuya, and Ms. K. Miyagawa at the Department of Electrical Engineering of the University of Tokyo, and Dr. H. Mosebach, Mr. H. May, Mr. W. Schmid, Mr. A. Taleirus, Mr. B. Degele, Mr. A. Steingröver, and Mr. G. Groβkopf, and all my colleagues at the *Institut für Elektrische Maschinen, Antriebe und Bahnen der Technischen Universität Braunschweig,* for their kind assistance and cooperation.

My grateful appreciation is also due to the DAAD *(dem Deutschen Akademischen Austauschdienst)* and to the JSPS (Japan Society for the Promotion of Science) for the financial supports in the Federal Republic of Germany and in Japan respectively.

Ms. M. Zingel at the *Goethe Institut Göttingen* and Mr. V. Langeheine at the *Sprachkurs der TU Braunschweig* were very helpful in my learning German language necessary for my research work at Braunschweig. For this I am thankful.

I also wish to acknowledge my gratitude to Prof. T. Kohno at the University of Tokyo, Mr. M. Karita at the Shinko Electric Co., Mr. A. Seki at the Central Japanese Railway Co., Prof. D. Ebihara at the Musashi Institute of Technology, and Prof. Y. Ohira at the Nihon University for their kind assistance, both direct and indirect, in the execution of this research work.

Last but not least, I would like to record my sincere thanks to my family, Dr. T. Kubota, Mr. B. Martin, Dr. G. Watanabe, Dr. Y. Kodama, Mr. F. Araujo, Mr. K. Tsoukalas, Mr. F. Fouladi, Dr. J. Landrath, Ms. K. Tagashira, Ms. J. Gasperoni and all my friends for their inspiration and encouragement.

論文の内容の要旨

論文題目 Flux Synthesizing Linear Induction Motor
（磁束合成形リニア誘導モータに関する研究）

氏名　古関 隆章

リニアモータは新しい交通機関（リニア・モータ・カー）や自動化工場の搬送装置の推進装置などに応用され、今後の輸送・生産プロセスの鍵となる先端技術として各分野で研究開発が進められている。しかし、電気機械としての性能を見た場合、特にリニア誘導モータに関しては、端効果による効率・力率の低下や、電気的過渡現象の遅さに起因する発生力の整定時間の長さが制御の特性を損ない、このような高度な応用の可能性を阻む原因となっている。従って効率・力率の低さを認めてもなおリニアドライブの長所を十分に生かせるような応用を考えるとともに、推進力制御時の応答の速さを実現するような駆動法の検討が重要である。また、端効果を抑制できるような方法が見いだせればさらによい。しかし、従来の 3 相巻線に基づいたハード構成では、劇的な改善策は望むべくもなく、リニアモータの特性が常に回転機よりも劣ってしまうのは避けられない。一方、近年のパワーエレクトロニクス技術の発展は著しく、多数のスイッチング素子をモータの一部分として用いることが可能となっている。その成果を生かし、従来の回転機を単に切り開いた物というリニアモータとは全く発想の異なるハード構成及び駆動法を生み出すことが、ダイレクトドライブによるアクチュエータの高性能化が要求される 21世紀に向けて求められている。

そこで、本論文では、このリニア誘導モータの性能の向上をめざし、図 1 に示すような複数の半導体電力変換素子をモータ構成要素として用いる「磁束合成形リニア誘導モータ」という概念が提唱された。そして、その基本特性を調べ、駆動の大きな自由度を生かした制御法について検討している。

まず、磁界解析に基づくシミュレーションにより新概念の有効性を検討するため、二次元時間依存電磁場の数値計算手法を、コントロール・ボリューム法に基づき導出した。本方法によれば、べき乗法と呼ばれる離散化係数間の重み付の関係を場の風上性に応じて自動調整するアルゴリズムにより、導体の速度項に起因する数値計算への悪影響を効果的に抑制することができる。また、広く電気機械の解析に用いられている、一次三角形要素を用いた有限要素法との関係が、論文中で数学的に検討されている。さらに、回転形試験機を用いた測定との対照、および古典的な回転機理論から得られる特性との比較検討が詳細に行われ、解析手法の妥当性が検証された。

上述の基本的な検討結果により、図 1 のようなシングル・ターンの形で磁束合成形リニア誘導モータの実機を構成することは、特に電源側から見たインピーダンスの問題を考慮して、実際問題として困難であることがわかった。そこで、具体的な検討対象機として、図 2 に示すような 12 のスロットをもつ円筒形リニア誘導モータが選ばれた。

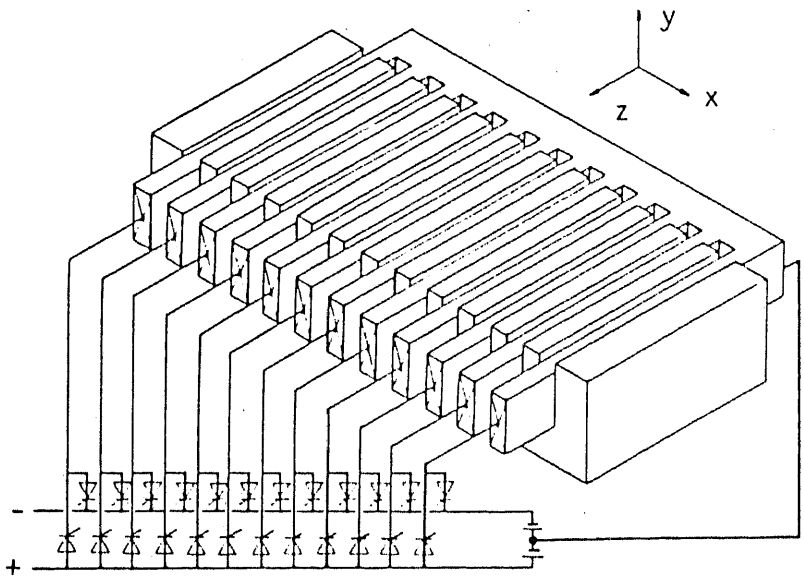

図 1　磁束合成形リニア誘導モータの基本構成

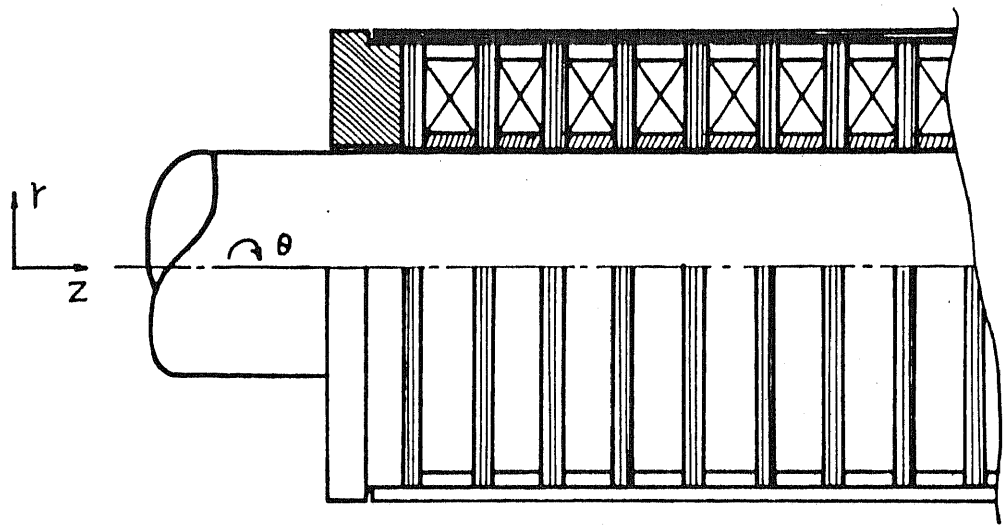

図2　磁束合成形リニア誘導モータの有効性を実証する為の円筒形リニア誘導試験機（全長で12スロット）

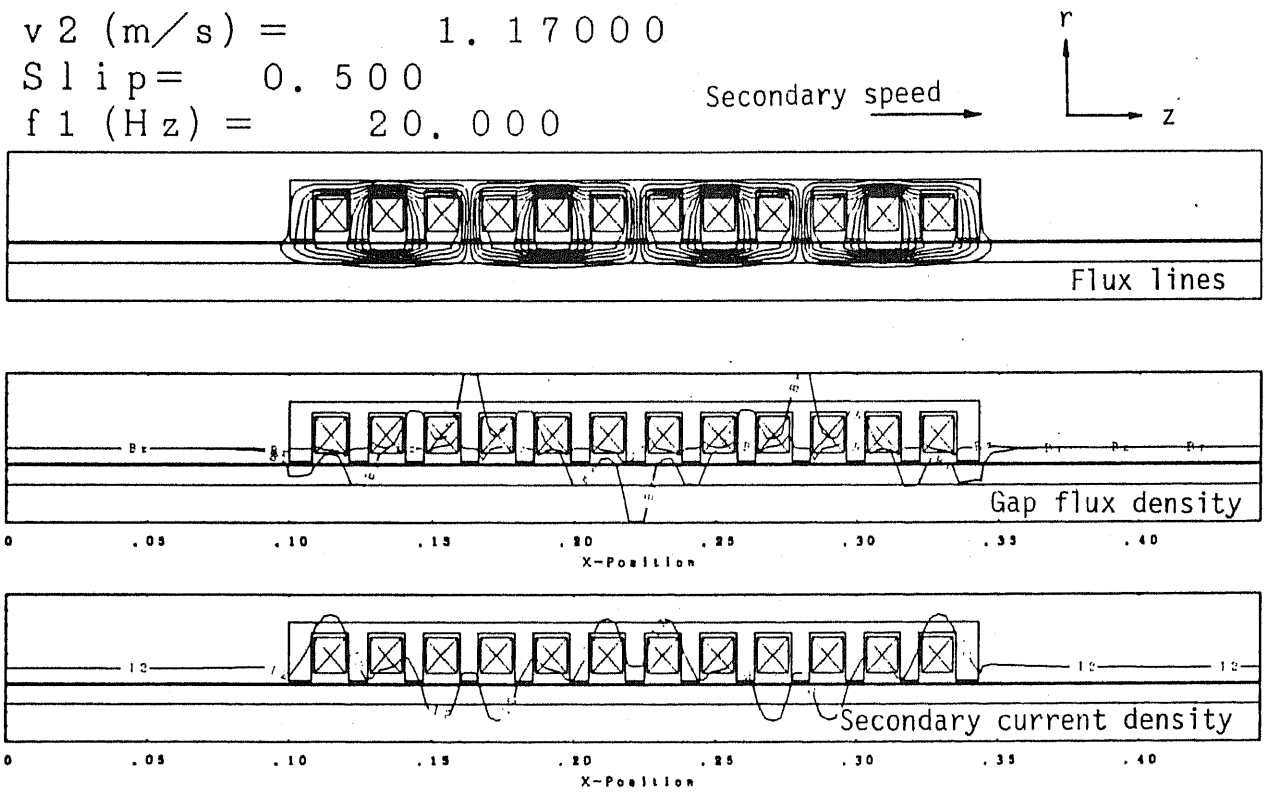

図3　円筒形試験機の軸対称三次元渦電流磁場解析法に基づく計算結果の一例

前述の解析法の一部を修正して、軸対称三次元場解析プログラムを開発し、数値シミュレーションによる詳細検討がおこなわれた。具体的には、図3のような解析を行い、電流源駆動、電圧源駆動、そして一様なギャップ磁束密度を発生するような磁束合成法の比較を行った。さらに、多入力線形システムの理論に基づいて計算上それらが具体的にどのように実現され、各々どのような特徴があるのか

ということを詳細に論じた。その結果の一例を図 4 に示す。ここでは、特に複雑な制御法を用いず、単純に平衡した多相電圧源を図 1 に描かれているように印加するだけでも、出入口の磁束不均一の影響を局所的にとどめ、三相直列結線方法に比較して特性が改善される可能性が示されている。また、そのうちで電圧源駆動に関しては、数値解析プログラムを用いた検討結果の正当性を証明するための円筒形試験機を用いた測定と、その結果についても言及した。

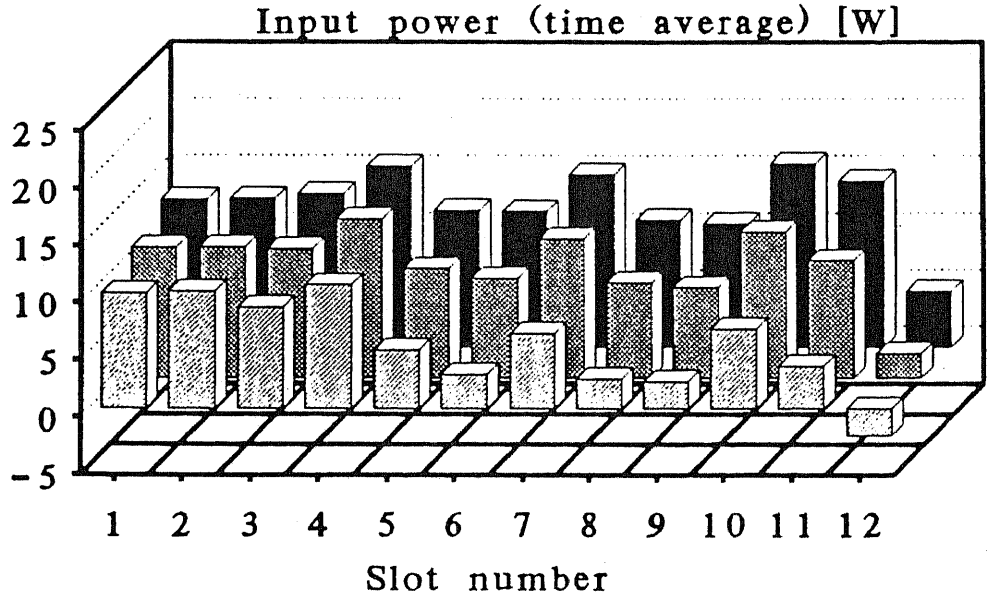

(a) 三相四極直列結線の場合

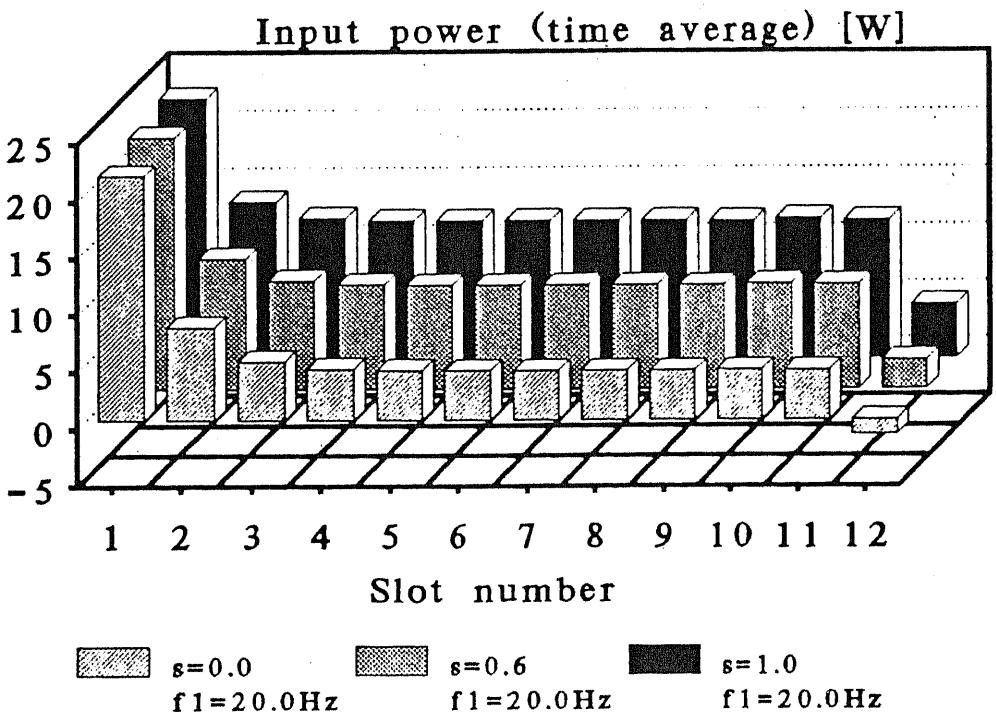

(b) 各スロットの巻線が１２本各電圧源に直接結線されている場合

図4　各スロットへの入力電力（電圧源駆動時の直・並列結線の比較）

さらに、図 5 に示されるフィールド座標系に基づく推進力制御の実現を目的として、 Leonhardに準拠し、等価面電流を用いた解析モデルに基づくリニア誘導モータの数学的定式化を行った。これによって、回転機のベクトル制御の物理的意味を明確にするとともに、同制御法をリニアモータに応用するために必要な条件、および、等価回路を用いずに制御に必要な定数を決定するための具体的方法を整理した。さらに、ギャップ磁束密度を一定とした場合のすべり周波数 — 推進力特性を計算し、推進力制御に必要とされる特性の直線性が図 6 のように得られることを確認した。検討例としたモータは、ギャップ磁束分布の空間高調波が多く、それによるエネルギー損失のために、速度に伴う推進力の低下が見られる。この点は、等価面電流に基づく理想的な解析モデルから予想される特性とは異なる。しかし、これは、スロット高調波などの空間高調波成分を低減する、モータそのものの設計の工夫によって克服されるべきであり、磁束合成の有効性が基本的には示されたと考えてよい。

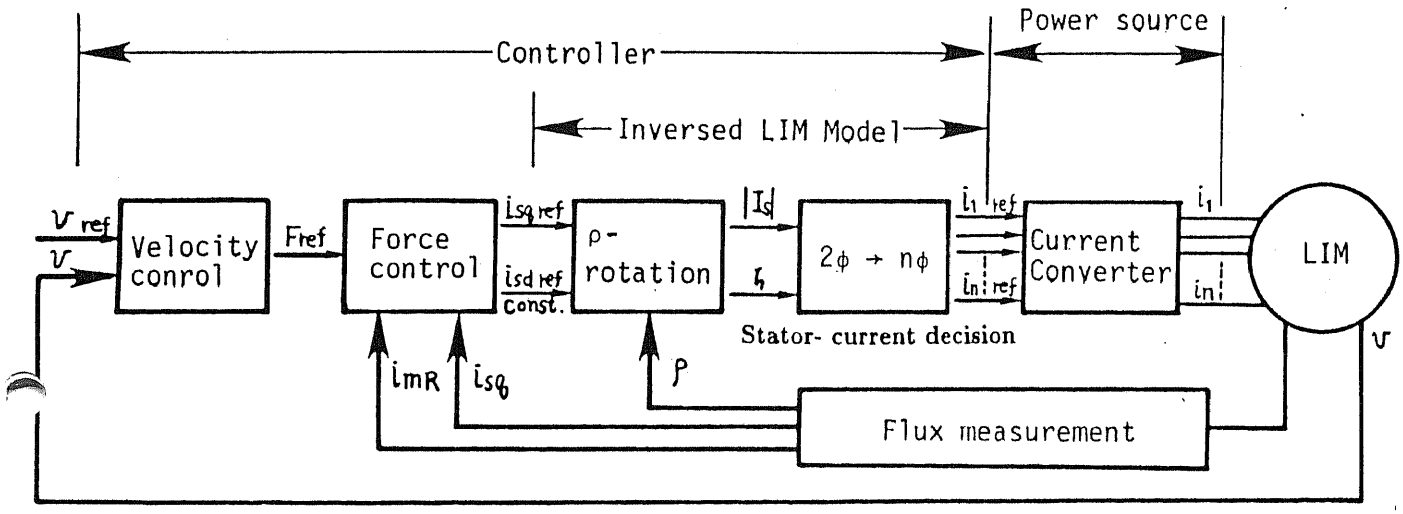

図5 フィールド座標系に基づくリニア誘導モータ推進力制御系の基本構成

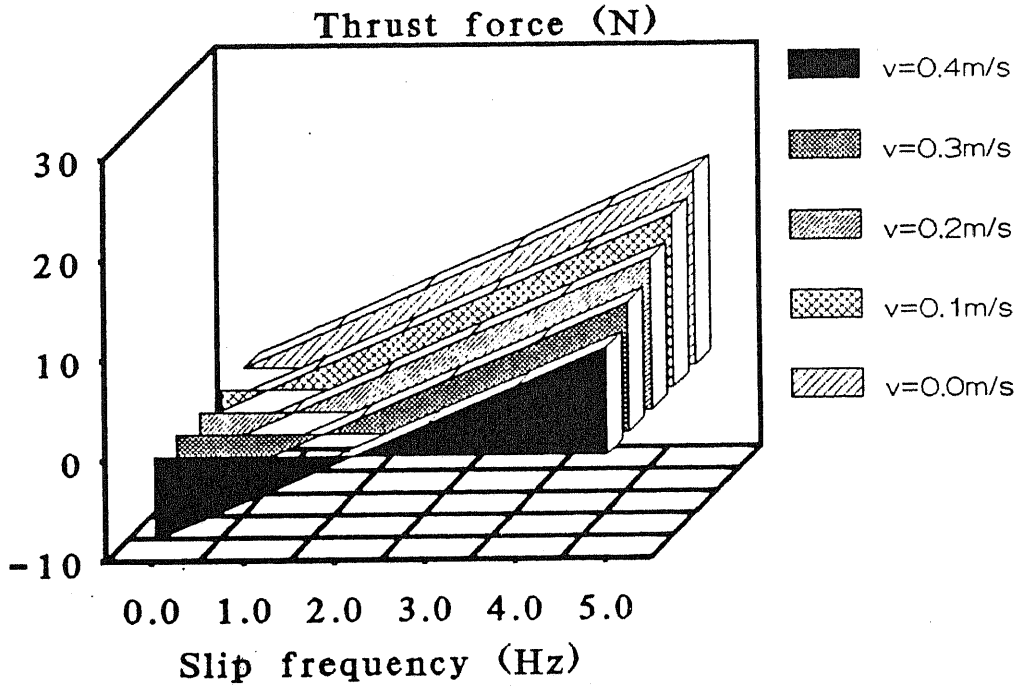

図6　磁束合成をして、ギャップ磁束密度を一定に保った場合の推進力 — すべり周波数特性

以上のようにして、本論文中では、ダイレクトドライブのための制御用アクチュエータとしての磁束合成形リニア誘導モータ適用の可能性と、それに対するフィールド座標系に基づく推進力制御の応用のための具体的な手法、および問題点が示され、結論の章において考察が加えられている。

ABSTRACT

Linear induction motor (LIM) has the merits of direct drive, simple structure, low noise, and low cost for maintenance. It is, therefore, being used in public transport systems and automated factory lines. A conventional LIM has, however, a large air gap and an open magnetic circuit; the power factor and the energy efficiency are, consequently, low in comparison with rotary induction motors. Motors therefore tend to be relatively large and heavy, and it takes long time to produce intended forces. Furthermore, the LIM has the end effect, which worsens electric characteristics of the motor, especially in the high speed region. Strategies against the effect are unfortunately limited because of the conventional three- phase construction.

On the other hand, the technical progress of power switching devices and power electronics is remarkable nowadays. High speed power switching devices are available at reasonable cost presently; it is possible to use many switching devices as part of electric machines.

According to the present technical situation mentioned above, the author proposes a novel control concept of the linear motors, where switching devices are integrated into the motor's structure and magnetic flux in the gaps can be arbitrarily synthesized. The motor has been named:

"Flux Synthesizing Linear Induction Motor (FSLIM)"

In this thesis, the concept of the FSLIM is introduced. The time-dependent electromagnetic field analysis theory is mathematically formulated for investigations and simulations of the FSLIM. Some calculated results are compared with measurements in order to verify the analysis method. Further theoretical investigations of the control scheme and the flux synthesis are described with a field-coordinates oriented control scheme.

Key Words

Linear Induction Motor (LIM), Flux Synthesizing LIM (FSLIM), PWM Chopper, Current-control-unit, Arbitrary magnetic flux distribution, Control Volume Method, Impedance matrix, Field coordinates control scheme

Table of Contents

NOMENCLATURE

Chapters are subdivided into sections, which are numbered 1.1, 1.2, 1.3, and so on. Sections may be divided into subsections, which are numbered 1.1.1, 1.1.2, and so on. Figures, tables, references, and similar features are numbered consecutively within each chapter, prefixed by the chapter number; only in the chapter 2, equations are prefixed by the section number. Vectors are denoted by boldface letters, matrices by capital italic letters, and complex variables by characters below dots. It has, however, not been possible to adhere to these rules completely consistently.

Commonly used symbols

$\mathbf{A}$	magnetic vector potential
A	vector potential, system matrix
a	coefficients of discretized equations
B	magnetic flux density
b	energy term of discretized equations
E	electric field
$\mathbf{f}$	input vector of system matrix
$f(t)$	primary frequency
$\mathbf{I}$	input current vector
$\mathbf{i}_S$	stator current vector
i_{Sd}, i_{Sq}	two axes components of stator current
$\mathbf{I}_{mR}$	field current vector
i_{mR}	amplitude of field current
$\mathbf{J}_0$	forced current
k	coefficients between currents and force
L	inductance
M	mutual inductance
N_i	weighting function
N_R, N_S	winding number
P	Peclet number, coefficients matrix
Q	coefficients matrix (P^{-1})
r	radius on cylindrical coordinates
$s(t)$	slip
t	time
T	potential, connection matrix
T_R	time constant of rotor
U	modified magnetic potential: $A \cdot r$
u, U	terminal voltage
$\mathbf{V}$	terminal voltage, absolute value of velocity

$\mathbf{v}$	velocity of conductor
x, y	position on initial coordinates
X, Y	position on transformed coordinates
z	position on initial coordinates
Z	impedance matrix
α, β, γ	coefficients in a triangular element, angle in a motor
δ	phase difference between stator- and field- current
μ	permeability
ν	magnetic reluctivity
ω	angular velocity of secondary part
$\omega_2(t)$	slip angular frequency
$\omega_s(t)$	synchronous angular frequency
ϕ	magnetic scalar potential
Φ	transition matrix
ψ	magnetic flux
$\rho(t)$	phase angle of gap flux
σ	conductivity
θ	angle on cylindrical coordinates
Θ	magnetomotive force
τ	time
τ_p	pole pitch
ζ	phase angle of stator- current vector, area coordinates

SI units

A	ampere
deg, $^\circ$	degree
Hz	hertz
kg	kilogram
m	meter
N	newton
rad	radian
s	second
T	tesla
V	volt
Ω	ohm

Chapter 1: Introduction

1.1 Purpose of the research

It is essential for civilized societies to transport people and materials. In particular, a railway transport system of high quality is important. With this in mind, the MAGLEV (magnetic levitation transport system)[1-1] is being developed in Germany[1-2], Japan[1-3], Canada and the United Kingdom.

A maglev transport system, with short stator linear induction motor drives and an electromagnetic suspension system, has the advantage of simple and cheap facilities on the ground. It is being developed in Japan as an advanced ground transportation system of medium capacity and over medium distances. It was demonstrated and evaluated by the HSST vehicles at EXPO'85 (Tsukuba), at EXPO'86 (Vancouver) and at EXPO'89 (Yokohama)[1-4]; the evaluation of the system for a practical application is being carried out in Nagoya with the support of the Japanese Ministry of International Trade and Industry. Furthermore, the development of new vehicles is being continued for future utilities.

In addition, linear motors can also be applied to drives of automated factory lines, because of the merits of direct drive, simple structure, low noise, no pollution and low cost for maintenance.

A conventional linear induction motor (LIM) has, however, a large air gap and an opened magnetic circuit; the power factor and the energy efficiency are consequently low. Therefore, the machine is compelled to be relatively large and heavy, and it takes a larger time to realize intended forces than rotary motors. Furthermore, the LIM has the end effect (see the subsection 4.2.1.), which worsens the electric characteristics of the motors, especially in high speed drives. Strategies against these undesirable effects are inherently limited by the structure of the conventional three- phase windings.

Nowadays, the technical progress of power switching devices and power electronics is remarkable. High speed power switching devices are, therefore, available with reasonable cost at present; it is possible to use many switching devices as parts of electric machines.

Considering the present technical aspects above, I have proposed a novel structure- and control- concept of linear motors, where magnetic flux in the gaps can be arbitrarily synthesized. If the flux distribution in the gap can be produced and controlled with reference values, the advantage of the new concept is

remarkable.

The purpose of this research is:

(1) Suppression of the end effect of a LIM.

(2) Improvement of the force response

The following points are described in detail:

(1) The proposal of the new concept of the flux synthesizing linear induction motor (FSLIM) of multi-phase drives with power switching devices.

(2) The possibility to apply the field-coordinates oriented drive control theory to the linear induction motor.

(3) Verification of a novel control scheme for the FSLIM.

1.2 Scope of the research

Theoretical study and numerical evaluation are necessary for the investigation about novel control concepts. With this in mind, the following topics are investigated:

(1) Derivation of simultaneous equations for numerical calculations of eddy-current problems with a velocity term: time dependent electromagnetic field including a moving conductor.

(2) Numerical simulation for a LIM with the $e^{j\omega t}$- method based on (1).

(3) Numerical simulation for a LIM with time differential method based on (1).

(4) Formulation of an analysis method for the induced voltage and the impedances in the primary windings.

(5) Verification of the simulation described above with some experiments.

(6) Investigation about a concrete decision scheme of switching patterns for flux-synthesis.

(7) Investigation about possibility to applicate the field coordinates oriented control theory to the FSLIM.

References

[1-1] H. Weh: "Magnetic Levitation Technology and its Development Potential", Maglev '89, pp. 1-10, 1989, Yokohama

[1-2] H. G. Raschbichler and M. Wackers: "Application of the Magnetic Levitation Train in the Federal Republic of Germany", Maglev '89, pp. 37-46, 1989, Yokohama

[1-3] J. Fujie: "Current Status of EDS System in Japan", Maglev '89, pp. 81-84, 1989, Yokohama

[1-4] A. Ohishi: "HSST-05 System General and Operational Outline at YES'89", Maglev '89, pp. 93-100, 1989, Yokohama

Chapter 2: Numerical analysis of linear induction motors

Introduction

This chapter deals with numerical analyses of induction motors. The main purpose of this chapter is to establish a fundamental framework of solving eddy current problems from Maxwell's equations to prepare a useful tool for calculations in the following chapters. We proceed the discussion on solving the equations based on the control volume method on the Cartesian coordinates for analyzing ordinary LIMs, and on the cylindrical coordinates for analyzing tubular LIMs. Further discussion on irregular triangular elements is of a more advanced nature; it concerns mathematical compatibility of the discretizing method with the finite element method. The topics next dealt with is a method to calculate asymmetrical LIMs with finite length driven by voltage sources by applying a theory of multi-terminal linear systems.

2.1. Difficulties of analyzing linear induction motors

It is inherently difficult to calculate electromagnetic characteristics of induction motors numerically, because the basic equations for it are complicated as described in the next section. In particular, the following problems make the calculation difficult:

(1) Mathematical and physical treatment of the electric scalar potential ϕ.

(2) Theoretical and numerical treatment of the time dependence.

(3) Numerical treatment of the velocity term with the up-wind scheme.

These difficulties and mathematical strategies against them are discussed in the following sections: the sections 2.2 for (1), 2.3 for (2), and 2.4 for (3).

2.2. Mathematical formulation and treatment of the electric scalar potential ϕ

2.2.1. Basic equations and assumptions

From the Maxwell's equations, one can derive the following basic equation with the $\mathbf{A}-\phi$ method:

$$\nabla \times \left\{ \nu \left[\nabla \times \mathbf{A} \right] \right\} = \mathbf{J}_0 + \sigma \left\{ -\frac{\partial \mathbf{A}}{\partial t} - \nabla\phi + \mathbf{v} \times \left[\nabla \times \mathbf{A} \right] \right\} \tag{2.2.1}$$

where ν is magnetic reluctivity, $\mathbf{J}_0$ is a force-current density, and $\mathbf{v}$ is a velocity of a secondary conductor. Furthermore one needs an appropriate constraint condition with the electric scalar potential ϕ.

On the Cartesian-Descartes coordinates, each factor of the magnetic vector potential in the equation (2.2.1) is written as follows.

$$\begin{aligned} &\frac{\partial}{\partial y}\left[\nu_z \frac{\partial A_y}{\partial x}\right] + \frac{\partial}{\partial z}\left[\nu_y \frac{\partial A_z}{\partial x}\right] - \frac{\partial}{\partial y}\left[\nu_z \frac{\partial A_x}{\partial y}\right] - \frac{\partial}{\partial z}\left[\nu_y \frac{\partial A_x}{\partial z}\right] \\ &= J_{0x} - \sigma \frac{\partial A_x}{\partial t} - \sigma \frac{\partial \phi}{\partial x} + \sigma \left[v_y \left[\frac{\partial A_y}{\partial x} - \frac{\partial A_x}{\partial y} \right] - v_z \left[\frac{\partial A_x}{\partial z} - \frac{\partial A_z}{\partial x} \right] \right] \end{aligned} \tag{2.2.2.a}$$

$$\begin{aligned} &\frac{\partial}{\partial z}\left[\nu_x \frac{\partial A_z}{\partial y}\right] + \frac{\partial}{\partial x}\left[\nu_z \frac{\partial A_x}{\partial y}\right] - \frac{\partial}{\partial z}\left[\nu_x \frac{\partial A_y}{\partial z}\right] - \frac{\partial}{\partial x}\left[\nu_z \frac{\partial A_y}{\partial x}\right] \\ &= J_{0y} - \sigma \frac{\partial A_y}{\partial t} - \sigma \frac{\partial \phi}{\partial y} + \sigma \left[v_z \left[\frac{\partial A_z}{\partial y} - \frac{\partial A_y}{\partial z} \right] - v_x \left[\frac{\partial A_y}{\partial x} - \frac{\partial A_x}{\partial y} \right] \right] \end{aligned} \tag{2.2.2.b}$$

$$\begin{aligned} &\frac{\partial}{\partial x}\left[\nu_y \frac{\partial A_s}{\partial z}\right] + \frac{\partial}{\partial y}\left[\nu_x \frac{\partial A_y}{\partial z}\right] - \frac{\partial}{\partial x}\left[\nu_y \frac{\partial A_z}{\partial x}\right] - \frac{\partial}{\partial y}\left[\nu_x \frac{\partial A_z}{\partial y}\right] \\ &= J_{0z} - \sigma \frac{\partial A_z}{\partial t} - \sigma \frac{\partial \phi}{\partial z} + \sigma \left[v_x \left[\frac{\partial A_x}{\partial z} - \frac{\partial A_z}{\partial x} \right] - v_y \left[\frac{\partial A_z}{\partial y} - \frac{\partial A_y}{\partial z} \right] \right] \end{aligned} \tag{2.2.2.c}$$

In addition to the equations (2.2.2), a condition of the scalar potential ϕ must be solved simultaneously, *i.e.*, one must solve the four time-dependent second-order partial differential equations with the four dependent- and the four independent-variables in a pure three-dimensional analysis of induction motors. Obviously, this is mathematically very complicated.

Although "a pure two-dimensional" analysis is inherently impossible in eddy current problems for the reasons described later, the following assumptions of quasi- two- dimensional analysis are made for simplicity.

(1) In the analyzed region, currents flow only in the z-direction. (J_{0z} will be written as J_0 for simplicity in the following expressions.)

(2) Hence, $A_x = A_y = 0$. (A_z will be written as A.)

(3) The conductive part moves only in the x-direction. (v_x will be written as v.)

According to the assumptions above, the following simple equation is derived from the equation (2.2.2.c).

$$\frac{\partial}{\partial x}\left[\nu_y \frac{\partial A}{\partial x}\right] + \frac{\partial}{\partial y}\left[\nu_x \frac{\partial A}{\partial y}\right] = -J_0 + \sigma\left\{\frac{\partial A}{\partial t} + v_2 \frac{\partial A}{\partial x} + \frac{\partial \phi}{\partial z}\right\} \qquad (2.2.3)$$

The last term $\frac{\partial \phi}{\partial z}$ seems a little funny in the two-dimensional calculation, where all the quantities are homogeneous along the z-axis; in the "pure two-dimensional" field, the basic equation should be:

$$\frac{\partial}{\partial x}\left[\nu_y \frac{\partial A}{\partial x}\right] + \frac{\partial}{\partial y}\left[\nu_x \frac{\partial A}{\partial y}\right] = -J_0 + \sigma\left\{\frac{\partial A}{\partial t} + v_2 \frac{\partial A}{\partial x}\right\}. \qquad (2.2.3')$$

This is the first theoretical difficulty of the eddy-current problem, which will be discussed in the following subsection in detail.

2.2.2. The electric scalar potential ϕ in the two- dimensional eddy current problem [2-1]

I will discuss here the simple example, in which conductive parts have no motion, and eddy currents are induced by a forced AC magnetic field due to a forced AC current, as shown in the figure 2.1 (a). Both of the three- dimensional structures (b) and (c) are possible corresponding to the cross-section drawn in (a). The physical phenomena in the structures are, however, completely different. In the case of (b), the gap flux density is formed homogeneous caused by the shield effect of the eddy-currents in the two side conductors, where the gap flux in the case of (c) is almost compensated by the eddy current in the surrounding conductor. That means, one must consider *return paths of induced eddy currents* even in a case of *two dimensional calculations;* the *"pure two-dimensional"* analysis has no sense in the time-dependent field calculation with eddy currents. The term $\frac{\partial \phi}{\partial z}$ seems funny as mentioned in the previous subsection, however, one can view this term as a correction of a "quasi- three- dimensional effect," to take the return path of the eddy currents into account in the two- dimensional analysis. In the following

discussion, we write $\frac{\partial \phi}{\partial z}$ as ϕ' for simplicity.

It is already known, that the condition of the divergence of currents, $\nabla \cdot \mathbf{J} = 0$, in the whole analysis region is implicitly satisfied in the two- dimensional calculation with the equation (2.2.3'), in which the scalar potential is assumed to be always zero. The scalar potential ϕ, hence also ϕ' , is constant in a cross-section of a conductor. Because eddy currents in the x- or y- direction would exist according to the equations (2.2.2.a) and (2.2.2.b), if it were not constant in a cross-section; it would be contradictory to the assumption (3). Therefore, we should add the unknown variables $\phi'_1, \phi'_2, \ldots, \phi'_n$ (n: number of independent conductors) to the simultaneous equations for formulating the current constraints $\int_S J_{ez}\, dxdy = 0$ explicitly, corresponding to the number of the independent conductors; one ϕ' can be decided arbitrarily. If there is only one conductor in the analyzed region by chance, one can calculate the field based on the (2.2.3'), since one can give zero value to the single scalar potential. In the analysis of a linear induction motor, whose eddy current exists only in a secondary reaction plate, the equation (2.2.3') can be used as a basic equation.

2.3. Mathematical formulation of the time dependence

2.3.1. Complex variable method (" $e^{j\omega t}$ -method") for a quasi- stationary field analysis

This method is applied to A.C. stationary fields, whose physical variables, *e.g.* magnetic vector potential and current *etc.*, vary sinusoidally; one can replace the operator $\frac{\partial}{\partial t}$ with $j\omega t$ and all the independent variables are written as complex numbers. One can obtain a proper results in a linear field, where both the applied voltages and the resultant currents vary sinusoidally. It cannot be applied if an analyzed system has some nonlinearity, *e.g.* saturation and hysteresis, or if the phenomena are transient.

The vector potential A and the forced current J_0 are written with complex variables as $\dot{A} \cdot e^{j\omega t}$ and $\dot{J}_0 \cdot e^{j\omega t}$, where the dot ($\cdot$) expresses complex variables.

$$\frac{\partial}{\partial x}\left[\nu_y \frac{\partial \dot{A}}{\partial x}\right] + \frac{\partial}{\partial y}\left[\nu_x \frac{\partial \dot{A}}{\partial y}\right] = -\dot{J}_0 + \sigma\left\{j\omega \dot{A} + v_2 \frac{\partial \dot{A}}{\partial x}\right\}. \qquad (2.3.1)$$

The results are given as complex numbers. The standard vector is chosen based on a phase angle of a forced current; an phase angle of a resultant complex number means the phase difference from the standard vector.

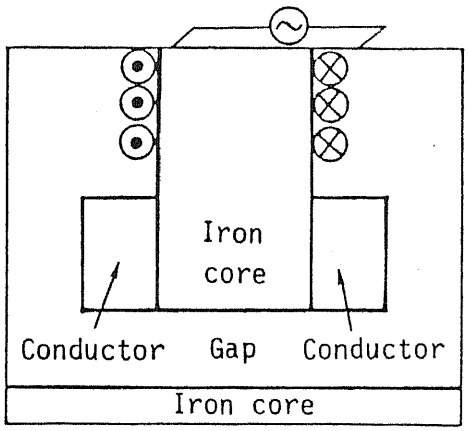

(a) An exsample of 2-dimensional eddy-current problems

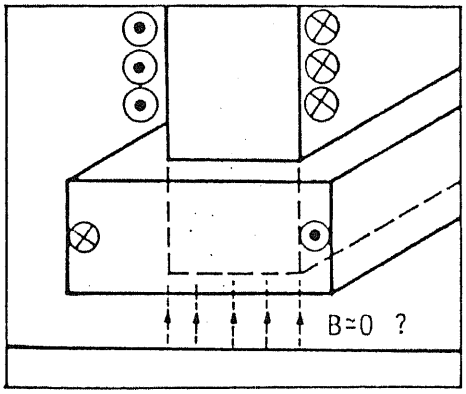

(b) A possible structure with one conductor

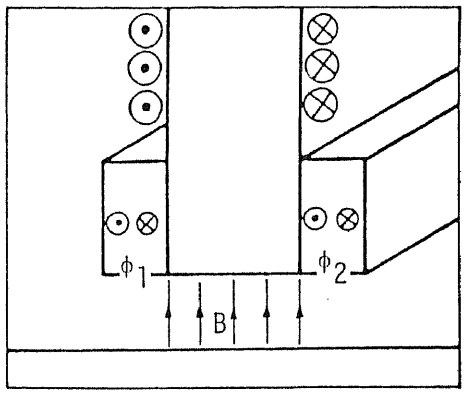

(c) A possible structure with two conductors

Figure 2.1. Physical model and scalar potential.

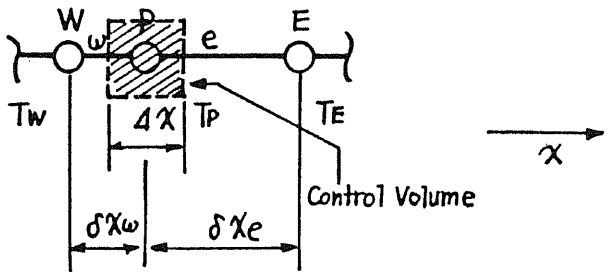

Figure 2.2. Simple one- dimensional model.

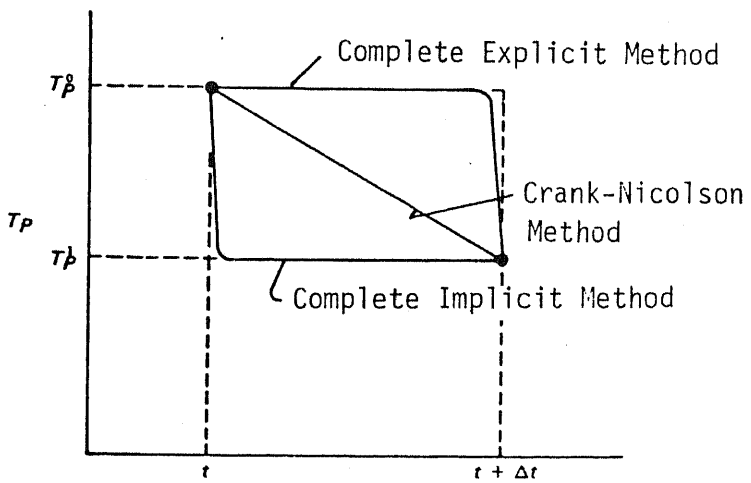

Figure 2.3. Comparison of time discretizing methods.

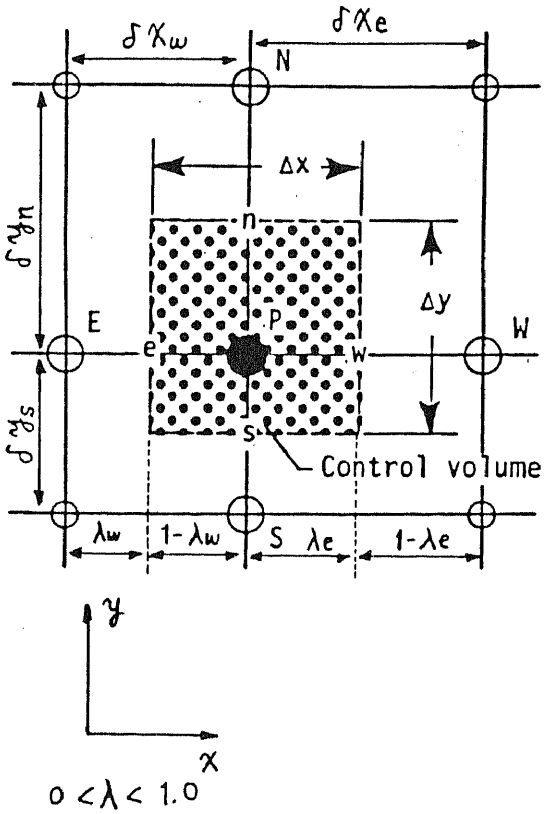

Figure 2.4. Two- dimensional C. V. model.

One can calculate A.C. complex impedances directly by calculating electromotive forces induced in primary windings in this calculation; it is important for comparing calculated results with classic A.C.-motor investigations based on linear algebra, linear circuit theory, and function theory of complex variables, *e.g.* the equivalent circuit, current vector loci, and multi-terminal linear system theory. Since the agreement with the classic methods supports the propriety of the numerical investigation, it is one of the most important points in this field of research.

2.3.2. Time discrete differential method

For analyzing transient phenomena of the LIM, we investigate the time finite differential method, in which the time is discretized with a short time step Δt. We will discuss on a following example of a one-dimensional diffusion problem for simplicity in this subsection. (See the figure 2.2.)

$$k_1 \frac{\partial T}{\partial t} = \frac{\partial}{\partial x}\left[k_2 \frac{\partial T}{\partial x}\right] \tag{2.3.2}$$

The time is a "one-directional" variable, *i.e.*, one can solve the differential equation by executing iterative procedures with a given initial condition; a new T at $t=t_{old}+\Delta t$, using the old T^0 at $t=t_{old}$ on a grid point has to be calculated. Let us assume new unknown values at $t_{new} = t_{old}+\Delta t$ as T_P, T_E, T_W, and old known values at t_{old} as T_P^0, T_E^0, T_W^0, on grid points P, E, and W. The equation (2.3.2) is integrated along the x- and t- axis based on the *Weighted Residual Method* [2-2] as described later. I assume the time-variant form of the T between t_{old} and $t_{new} \equiv t_{old}+\Delta t$ as follows:

$$\int_{t_{old}}^{t_{old}+\Delta t} T_P dt = \left[f \cdot T_P + \left(1-f\right) \cdot T_P^0\right] \Delta t \tag{2.3.3}$$

where f: $0.0 \leq f \leq 1.0$ is a weighting factor. Finally, the following discrete equations are derived:

$$\begin{aligned} a_P T_P = {} & a_E\left[fT_E + \left(1-f\right) T_E^0\right] + a_W\left[fT_W + \left(1-f\right) T_W^0\right] \\ & + \left[a_{P0} - \left(1-f\right) a_E - \left(1-f\right) a_W\right] T_P^0 \end{aligned} \tag{2.3.4}$$

where $a_E = \dfrac{k_{2e}}{\delta x_e}$, $a_W = \dfrac{k_{2w}}{\delta x_w}$, $a_{P0} = k_1 \dfrac{\Delta x}{\Delta t}$, and $a_P = fa_E + fa_W + a_{P0}$.

(1) Complete explicit method (f = 0.0)

It is assumed in this method, that the old value T_P^0 at $t=t_{old}$ is dominant at $t_{old} < t \leq t_{old}+\Delta t$. The new value T_P can be derived with the known values T_P^0, T_E^0, T_W^0 without solving simultaneous equations. However, there is a strict

constraint for the Δt, concerning the numerical stability. The following equation is derived from the equation (2.6) by giving zero to the f.

$$a_P T_P = a_E T_E^0 + a_W T_W^0 + \left[a_{P0} - a_E - a_W\right] T_P^0 \qquad (2.3.5)$$

In the equation above, the coefficient of the T_P^0 can be negative. If it is negative, T_P decrease when the T_P^0 would increase; it is physically irrational. Hence, "$a_P^0 > a_E + a_W$" is the condition for the numerical stability: in a particular case of regular grids, *i.e.*, $\Delta x \equiv \delta x_e = \delta x_w$, the condition is written as "$\Delta t < \dfrac{k_1(\Delta x)^2}{2k_2}$". This equation means that you must take the small Δt's when you make Δx's small for accurate calculations; it could cause an enormous computing time.

(2) Crank-Nicolson method (f = 0.5)

It is assumed that the T_P varies linearly during the time step Δt, it is physically correct in the case of sufficiently short time steps.

(3) Complete implicit method (f = 1.0)

It is assumed that T_P varies immediately from the old value T_P^0 to a new one T_P, and the new value is kept all the rest during the time step Δt. In this complete implicit scheme, the coefficients in the equation (2.3.5) are always non-negative, *i.e.*, one can choose the time steps Δt arbitrarily without considering any conditions for the numerical stability, *i.e.*, time-consuming very small time steps are not necessary. I will formulate, therefore, transient models of LIMs in this dissertation on the basis of this complete implicit method.

Characteristics of the models are compared visually in the figure 2.3.

2.4. Control volume method (1): Cartesian coordinates [2-3]

In this section, I describe mathematical formulations of discretization based on the Control Volume method (C. V. method) on the Cartesian Descartes coordinates. The C. V. method is one of the weighted residual methods: the basic equation is multiplied with the weighting function, which is 1.0 in the control volume, and 0.0 out of it. The basic equation is discretized by putting the residual function integrated in the whole region to zero. This method has been originally developed for a heat flow analysis and implemented in the general heat flow analysis code "PHOENICS" [2-4] (© Prof. Spalding, Imperial College, British Kingdom & CHAM co.), on the basis of the "SIMPLE" (Semi-Implicit Method for Pressure Linked Equations).

It is known that numerical oscillations occur in a calculation of an eddy current field with a velocity term, when the *Peclet number* [2-5], which will be explained in detail later, is large; the Up-wind scheme [2-6] is often applied to FEM- (finite element method) formulations as a mathematical strategy against it after experiences in the fluid dynamic computation. The physical meaning of the scheme is, however, not obvious. In this research, the *Peclet number* is investigated based on the principle, that **coefficients in the discretized equations are "conductances" between the physical variables on grids; for numerically stable computation, they must always be non-negative.** It has been resulted that linear interpolating functions cause the numerical oscillation, since the coefficients in the discretized basic equations can be negative in the following cases:

(1) if the magnetic permeability is large,

(2) if the electric conductivity is large,

(3) if the velocity of the conductor is large, and

(4) if the grids for the discretization are rough.

Furthermore, the two- dimensional eddy current analysis with a velocity term has been numerically stabilized by introducing the *modified exponential interpolating function,* with which the up-wind effect is automatically adjusted corresponding to the *"strength of a wind in the field"* on each grid.

2.4.1. Two conditions for physical propriety of a discretized equation [2-3]

(1) All the coefficients in discretized equations must be non-negative.

(2) The summation of the coefficients of all the adjacent coefficients must be equal to the coefficient of the central point.

2.4.2. Discrete formulation with a linear interpolating function — corresponding to a normal FEM with linear triangular elements

First of all, I describe a formulation with a linear interpolating function in this subsection, assuming that the electromagnetic potential A varies linearly between two grid points. The two- dimensional grids, the control volumes and symbols used in the formulations are shown in the figure 2.4.

From the equation (2.2.3'):

$$\sigma\frac{\partial A}{\partial t} + \frac{\partial}{\partial x}\left[\sigma v_2 A - \nu_y\frac{\partial A}{\partial x}\right] + \frac{\partial}{\partial y}\left[-\nu_x\frac{\partial A}{\partial y}\right] = J_0(t). \qquad (2.4.1)$$

If you write $\psi_x = \sigma v_2 A - \nu_y\frac{\partial A}{\partial x}$, $\psi_y = -\nu_x\frac{\partial A}{\partial y}$, the equation (2.4.1) can be written:

$$\sigma\frac{\partial A}{\partial t} + \frac{\partial \psi_x}{\partial x} + \frac{\partial \psi_y}{\partial y} = J_0(t) \tag{2.4.2}$$

By applying the complete implicit method, the both hand sides of the equation (2.4.2) are integrated along x- and y- axes:

$$\sigma_P\frac{\left(A_P - A_P^0\right)\Delta x\Delta y}{\Delta t} + \Psi_{xe} - \Psi_{xw} + \Psi_{yn} - \Psi_{ys} = J_P\Delta x\Delta y \tag{2.4.3}$$

where the A_P^0 is the value at the $t = t_{old}$, A_P is the value at the $t = t_{new} \equiv t_{old} + \Delta t$, $\Psi_{xe} \equiv \int_e \psi_x dy$ (2.4.4 a), $\Psi_{xw} \equiv \int_w \psi_x dy$ (2.4.4 b), $\Psi_{yn} \equiv \int_n \psi_y dx$ (2.4.4 c), and $\Psi_{ys} \equiv \int_s \psi_y dx$ (2.4.4.d).

According to the assumption of linear interpolation,

$$A_e = \left(1-\lambda_e\right)A_P + \lambda_e A_E \tag{2.4.5}$$

$$A_w = \left(1-\lambda_w\right)A_W + \lambda_w A_P \tag{2.4.6}$$

$$A_n = \left(1-\lambda_n\right)A_P + \lambda_n A_N \tag{2.4.7}$$

$$A_s = \left(1-\lambda_s\right)A_S + \lambda_s A_P \tag{2.4.8}$$

$$\left(1-\lambda_w\right)\delta x_w + \lambda_e \delta x_e = \Delta x \tag{2.4.9}$$

$$\left(1-\lambda_s\right)\delta y_s + \lambda_n \delta y_n = \Delta y. \tag{2.4.10}$$

Putting them into the equations (2.4.4),

$$\begin{aligned}\Psi_{xe} &= \left[\sigma_e v_{2e}A_e - \nu_{ye}\frac{A_E - A_P}{\delta x_e}\right]\Delta y \\ &= \left[\sigma_e v_{2e}\left\{\left(1-\lambda_e\right)A_P + \lambda_e A_E\right\} - \nu_{ye}\frac{A_E - A_P}{\delta x_e}\right]\Delta y\end{aligned} \tag{2.4.11}$$

$$\begin{aligned}\Psi_{xw} &= \left[\sigma_w v_{2w}A_w - \nu_{yw}\frac{A_P - A_W}{\delta x_w}\right]\Delta y \\ &= \left[\sigma_w v_{2w}\left\{\left(1-\lambda_w\right)A_W + \lambda_w A_W\right\} - \nu_{yw}\frac{A_P - A_W}{\delta x_w}\right]\Delta y\end{aligned} \tag{2.4.12}$$

$$\Psi_{yn} = \left[-\nu_{xn}\frac{A_N - A_P}{\delta y_n}\right]\Delta x \tag{2.4.13}$$

$$\Psi_{ys} = \left[-\nu_{xs}\frac{A_P - A_S}{\delta y_s}\right]\Delta x. \tag{2.4.14}$$

These Ψ's are substituted into the equation (2.4.3); the following equation is derived in the same way as (2.3.5):

$$a_P A_P = a_E A_E + a_W A_W + a_N A_N + a_S A_S + b \tag{2.4.15}$$

where

$$a_{P0} = \frac{\sigma_P \Delta x \Delta y}{\Delta t} \tag{2.4.16}$$

$$a_E = \left[-\sigma_e v_{2e} \lambda_{ye} + \frac{\nu_{ye}}{\delta x_e} \right] \Delta y \tag{2.4.17}$$

$$a_W = \left[+\sigma_w v_{2w} \left[1 - \lambda_w \right] + \frac{\nu_{yw}}{\delta x_w} \right] \Delta y \tag{2.4.18}$$

$$a_N = \frac{\nu_{xn}}{\delta y_n} \Delta x \tag{2.4.19}$$

$$a_S = \frac{\nu_{xs}}{\delta y_s} \Delta x \tag{2.4.20}$$

$$a_P = a_E + a_W + a_N + a_S + a_{P0} + \left[\sigma_e v_{2e} - \sigma_w v_{2w} \right] \tag{2.4.21}$$

and

$$b = J_P \Delta x \Delta y + a_{P0} A_P^0. \tag{2.4.23}$$

There is no problem practically if $\sigma_e v_{2e} = \sigma_w v_{2w} \equiv \sigma v_2$ is assumed.

In these equations, there is no problem in the case of:

$$-\frac{\nu_{yw}}{\left[1 - \lambda_w \right] \delta x_w} \leq \sigma v_2 \leq \frac{\nu_{ye}}{\lambda_e \delta x_e} \tag{2.31}$$

however, if the conditions in the subsection 2.4.1 are not satisfied, the validity of the numerical calculation is not guaranteed. That is to say, numerically oscillating solutions can be obtained in the case of high speed or rough discretization; this is a defect of this discretizing scheme.

2.4.3. Exponential method

An improved formulation is described in this subsection in order to avoid the numerical oscillation by applying *the up-wind scheme* to the interpolation with an exponential function.

First of all, I discuss an example of a passive one-dimensional model, in which the time dependence and the input term are neglected from the equation (2.4.1) for

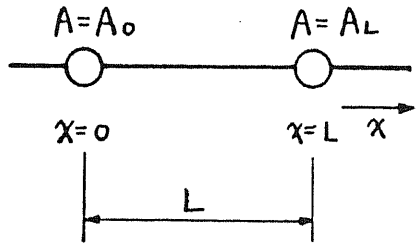

Figure 2.5. Passive one- dimensional model.

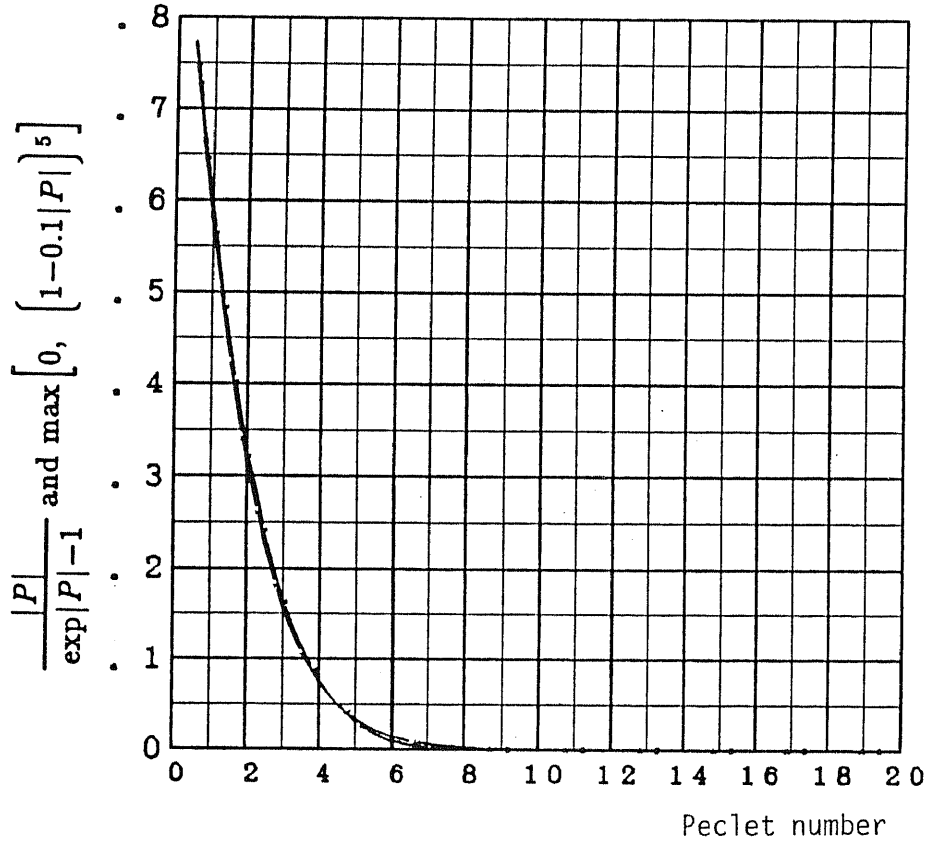

Figure 2.6. Comparison between $\frac{|P|}{\exp|P|-1}$ and $\max\left[0,\ \left(1-0.1|P|\right)^5\right]$.

A: Exponential interpolating function
B: Modified exponential interpolating function

simplicity, illustrated in the figure 2.5.

$$\Psi_x = \sigma v_2 A - \nu_y \frac{\partial A}{\partial x} = 0 \tag{2.4.24}$$

The equation (2.4.24) is an ordinary differential equation of the separation of variable:

$$\nu_y \frac{dA}{dt} = \sigma v_2 A. \tag{2.4.25}$$

$A=A_0$ at $x=0$ is an initial condition, and $A=A_L$ at $x=L$ is given as a supplemental condition.

$$\int_{A_0}^{A(x)} \frac{dA}{A} = \int_0^L \frac{\sigma v_2}{\nu_y}\, dx \tag{2.4.26}$$

where v_2 and ν_y should be constant in the considered region.

$$A(x) = A_0\, e^{\frac{v_2}{\nu_y}x} \tag{2.4.27}$$

Hence,

$$\frac{A-A_0}{A_L-A_0} = \frac{A_0 e^{\frac{\sigma v_2}{\nu_y}x} - A_0}{A_0 e^{\frac{\sigma v_2}{\nu_y}L} - A_0} = \frac{\exp\left[\frac{\sigma v_2}{\nu_y}x\right]-1}{\exp\left[\frac{\sigma v_2}{\nu_y}L\right]-1}.$$

I define the distance l_e between the central point P and the boundary of the control volume e, and introduce the *local magnetic Peclet number* $P_e = \frac{\sigma v_{2e}\delta x_e}{\nu_{ye}}$. By substituting $x=l_e$ and $L=\delta x_e$ into the equation (2.27),

$$\frac{A_e-A_P}{A_E-A_P} = \frac{\exp\left[\frac{P_e l_e}{\delta x_e}\right]-1}{\exp\left[P_e\right]-1}$$

Hence,

$$A_e = \frac{\left[\exp\left[P_e\right]-\exp\left[\frac{P_e l_e}{\delta x_e}\right]\right]}{\exp\left[P_e\right]-1}A_P + \frac{\left[\exp\left[\frac{P_e l_e}{\delta x_e}\right]-1\right]}{\exp\left[P_e\right]-1}A_E \tag{2.4.28}$$

$$\psi_{xe} = \sigma_e v_{2e} A_e - \nu_{ye}\frac{\partial A_e}{\partial x}$$

$$= \sigma_e v_{2e} \left[\frac{\exp\left(P_e\right)}{\exp\left(P_e\right)-1} A_P - \frac{1}{\exp\left(P_e\right)-1} A_E \right]$$

$$= \sigma_e v_{2e} \left[A_P + \frac{A_P - A_E}{\exp\left(P_e\right)-1} \right] \tag{2.4.29}$$

For the left side of the central point P, the following equation is derived in the same way by introducing the *local Peclet number* $P_w = \dfrac{\sigma_w v_{2w} \delta x_w}{\nu_{yw}}$.

$$\psi_{xw} = \sigma_w v_{2w} \left[A_W + \frac{A_W - A_P}{\exp\left(P_w\right)-1} \right] \tag{2.4.30}$$

The equations (2.4.19), (2.4.20), (2.4.28) and (2.4.29) are substituted into (2.4.1), and (2.4.15) is derived with the following coefficients.

$$a_P A_P = a_E A_E + a_W A_W + a_N A_N + a_S A_S + b \tag{2.4.31}$$

$$a_{P0} = \frac{\sigma_P \Delta x \Delta y}{\Delta t} \tag{2.4.32}$$

$$a_E = \frac{\sigma_e v_{2e} \Delta y}{\exp\left(P_e\right)-1}$$

$$= \frac{\nu_{ye} \Delta y}{\delta x_e} \cdot \frac{|P_e|}{\exp|P_e|-1} + Max\left[-\sigma_e v_{2e} \Delta y,\, 0\right] \tag{2.4.33}$$

$$a_W = \frac{\sigma_w v_{2w} \exp\left(P_w\right) \Delta y}{\exp\left(P_w\right)-1}$$

$$= \frac{\nu_{yw} \Delta y}{\delta x_w} \cdot \frac{|P_w|}{\exp|P_w|-1} + Max\left[+\sigma_w v_{2w} \Delta y,\, 0\right] \tag{2.4.34}$$

where $P_{(e \text{ or } w)} = \dfrac{\sigma_{(e \text{ or } w)} v_2 \, \delta x}{\nu_{(e \text{ or } w)\, y}}$ is the *Peclet number.*

$$a_N = \frac{\nu_{xn}}{\delta y_n} \Delta x \tag{2.4.35}$$

$$a_S = \frac{\nu_{xs}}{\delta y_s}\Delta x \tag{2.4.36}$$

$$a_P = a_E + a_W + a_N + a_S + a_{P0} + \left[\sigma_e v_{2e} - \sigma_w v_{2w}\right] \tag{2.4.37}$$

and

$$b = J_P \Delta x \Delta y + a_{P0} A_P^0 \tag{2.4.38}$$

In this formulation, all the coefficients are non-negative.

2.4.4 Modified exponential method

The exponential method described in the previous subsection is a good method, in which the numerical stability is always guaranteed by modifying automatically the form of the interpolating function corresponding to the *Peclet number.* However, the time consuming exponential calculation must be carried out on every grid points, in addition, $\frac{0}{0}$ and $\frac{\infty}{\infty}$ can occur numerically; such weak points should be removed for a numerical computation. The exponential interpolating function $\frac{|P|}{\exp|P|-1}$, therefore, is substituted with the multinominal approximation $Max\left[0, \left[1-0.1|P|\right]^5\right]$; the two functions are compared in the figure 2.6. As results, the coefficients in the equation (2.4.15) are written as follows:

$$a_P A_P = a_E A_E + a_W A_W + a_N A_N + a_S A_S + b \tag{2.4.39}$$

$$a_{P0} = \frac{\sigma_P \Delta x \Delta y}{\Delta t} \tag{2.4.40}$$

$$a_E = \frac{\nu_{ye}\Delta y}{\delta x_e} Max\left[0, (1-0.1|P_e|)^5\right] + Max\left[-\sigma_e v_{2e}\Delta y, 0\right] \tag{2.4.41}$$

$$a_W = \frac{\nu_{yw}\Delta y}{\delta x_w} Max\left[0, (1-0.1|P_w|)^5\right] + Max\left[\sigma_w v_{2w}\Delta y, 0\right] \tag{2.4.42}$$

where $P_{(e\ or\ w)} = \frac{\sigma_{(e\ or\ w)} v_2\ \delta x}{\nu_{(e\ or\ w)\ y}}$ is the *Peclet number.*

$$a_N = \frac{\nu_{xn}}{\delta y_n}\Delta x \tag{2.4.43}$$

$$a_S = \frac{\nu_{xs}}{\delta y_s}\Delta x \tag{2.4.44}$$

$$a_P = a_E + a_W + a_N + a_S + a_{P0} + \left[\sigma_e v_{2e} - \sigma_w v_{2w}\right] \tag{2.4.45}$$

$$b = J_P \Delta x \Delta y + a_{P0} A_P^0. \tag{2.4.46}$$

All the following calculated results in this dissertation are based on the modified exponential method.

2.4.5. Stationary analysis — $e^{j\omega t}$-method

The discretized equation with complex variables is as follows:

$$\dot{a}_P \dot{A}_P = a_E \dot{A}_E + a_W \dot{A}_W + a_N \dot{A}_N + a_S \dot{A}_S + \dot{b} \tag{2.4.47}$$

where the dot $(\cdot)$ means a complex variable, and a_E, a_W, a_N and a_S are the same real coefficients as in the previous subsection, and:

$$\dot{a}_P = a_E + a_W + a_N + a_S + j\omega\sigma_P \Delta x \Delta y + \left[\sigma_{2e} v_{2e} - \sigma_{2w} v_{2e}\right] \Delta y \tag{2.4.48}$$

$$\dot{b} = \dot{J}_0 \Delta x \Delta y. \tag{2.4.49}$$

2.4.6. Calculation of magnetic flux density, secondary current, primary voltage and forces

Since the analysis described in the previous subsection is two- dimensional, contour lines of the vector potential A_z mean magnetic flux lines as shown in the figure 3.8 (b). The magnetic flux density is calculated as follows.

$$\mathbf{B} = \nabla \times \mathbf{A} \tag{2.4.50}$$

The secondary current density is derived considering that the scalar potential ϕ is assumed to be zero.

$$i_{2z} = -\sigma \left[\frac{\partial A_z}{\partial t} + v_2 \frac{\partial A_z}{\partial x} \right] \tag{2.4.51}$$

The forces are calculated by integrating the Maxwell's stress tensor in the gap.

The terminal voltage is calculated by integrating the induced electromotive force **E** along windings. Particularly, in the two- dimensional analysis in this research, one needs only to multiply an effective core width by the electromotive force E_z, since the end portions of a winding are neglected. From the Maxwell's equations and the equation (2.4.50), the following one is derived.

$$\mathbf{E} = -\left[\frac{\partial \mathbf{A}}{\partial t} + \nabla \phi \right] \tag{2.4.52}$$

Particularly, in the two- dimensional analysis with $\phi = 0$,

$$E_z = -\frac{\partial A_z}{\partial t}. \tag{2.4.53}$$

Since the voltage is calculated using the magnetic vector potential, which is the solution of the field analysis, the calculation is possible *only after* the field analysis with a current source. Therefore, the voltage-source simulation should be carried out in the case of linear fields †) as follows:

(1) the preliminary current-source field is analyzed for calculating induced primary terminal voltages,

(2) the impedances are calculated,

(3) the primary currents are calculated corresponding to the given terminal voltages using the impedances calculated above, and

(4) the field is analyzed with the modified primary currents again.

The procedures above are simple in the stationary calculation. On the other hand, transient voltage-source problems should be solved iteratively with a transition matrix; the mathematical procedure will be described in the subsection 2.8.

The terminal voltage and the impedance are written in the stationary analysis as follows:

$$\dot{E}_z \equiv \hat{E}_z \cdot e^{j\omega t} \tag{2.4.54}$$

$$\dot{A}_z \equiv \hat{A}_z \cdot e^{j\omega t}. \tag{2.4.55}$$

According to the equation (2.4.53),

$$\hat{E}_z = -j\omega \hat{A}_z \tag{2.4.56}$$

For instance in the case shown in the figure 2.7,

$$\hat{V}_{UN} = N_s \cdot \left[-\hat{A}_1 + \hat{A}_2\right] \cdot L \cdot \left[-j\omega\right] \tag{2.4.57}$$

$$\hat{Z}_{UN} = \frac{\hat{V}_{UN}}{\hat{I}_U}. \tag{2.4.58}$$

(In the case of a three- phase drive for instance, $\hat{I}_U = I_U$, $\hat{I}_V = I_V \cdot e^{-j\frac{2}{3}\pi}$, and $\hat{I}_W = I_W \cdot e^{-j\frac{4}{3}\pi}$.)

†) If you would treat all the primary currents as unknown variables, you could analyze a LIM with a voltage source directly. In this case, however, the band width of the coefficients matrix, which is substantially sparse, in the field analysis is much larger than with a current source; it consumes naturally much more computing time.

There may be no considerable difference, either if one would calculate the induced voltage only on a central point of the cross-section of a primary conductor, or if one would take an average value on the cross-section.

A primary resistance R_S and a leakage inductance at the coil-end portion of the primary winding, which is a considerable part of a primary leakage inductance $L_{S\sigma}$, are neglected in the impedance calculations; the neglected impedances should be added to the main impedance after the preliminary field analysis in the simulation procedures.

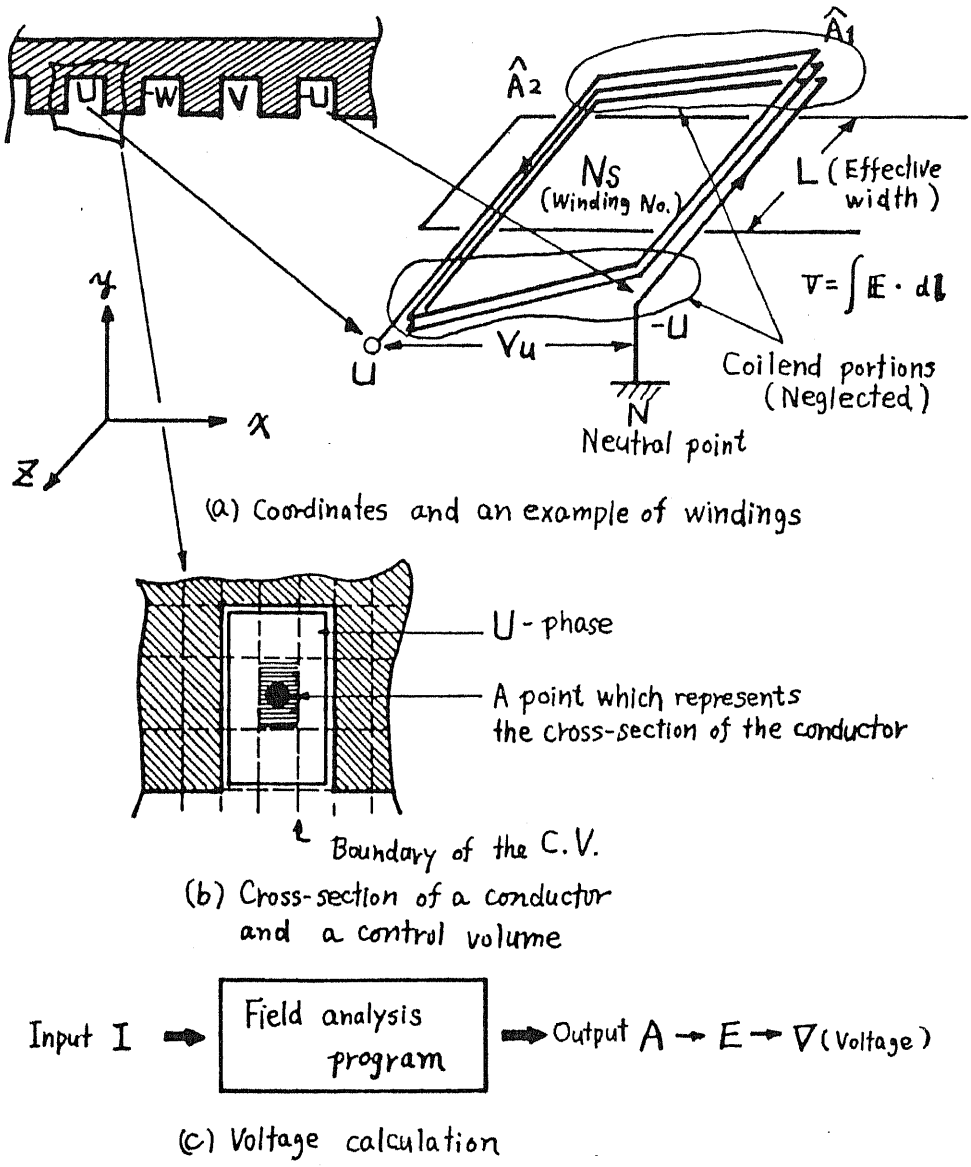

Figure 2.7. An example of a concrete model and principle of voltage calculation.

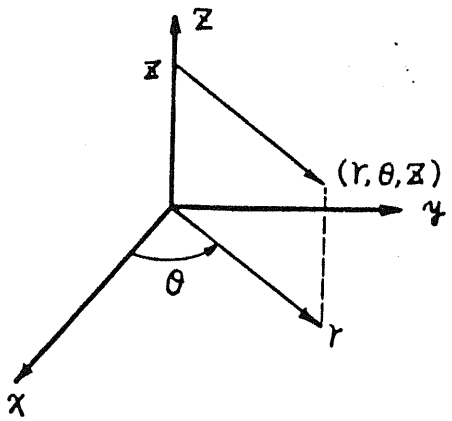

Figure 2.8. Three- dimensional cylindrical coordinates.

2.5. Control volume method (2): cylindrical coordinates

2.5.1. Application of the analysis

The discrete formulation on the cylindrical coordinates will be described in this section also using the control volume method. One can analyze a tubular LIM, which has substantially a coaxial structure; calculated results will be shown in the chapter 6. The formulation on the cylindrical coordinates can be applied also to two- dimensional analyses of rotary motors in the $r-\theta$ cross-section; the concrete formulation will be described in the appendix I.

2.5.2. Basic equations

The following equation, which has already been written in the subsection 2.2.1.,is derived with the $A-\phi$ method from the Maxwell's equations:

$$\nabla \times \left\{\nu\left[\nabla \times \mathbf{A}\right]\right\} = \mathbf{J}_0 + \sigma\left\{-\frac{\partial \mathbf{A}}{\partial t} - \nabla\phi + \mathbf{v} \times \left[\nabla \times \mathbf{A}\right]\right\} \tag{2.2.1}$$

where ν is magnetic reluctivity, $\mathbf{J}_0$ is a force-current density, and $\mathbf{v}$ is a velocity of a secondary conductor. One needs an appropriate constraint of the electric scalar potential ϕ in addition, as mentioned in the subsection 2.2.1.

On the three- dimensional cylindrical coordinates in the figure 2.8, each factor of the magnetic vector potential is written as follows.

$$\frac{1}{r}\frac{\partial}{\partial\theta}\left[\frac{\nu_z}{r}\left[\frac{\partial(rA_\theta)}{\partial r} - \frac{\partial A_r}{\partial\theta}\right]\right] - \frac{\partial}{\partial z}\left[\nu_\theta\left[\frac{\partial A_r}{\partial z} - \frac{\partial A_z}{\partial r}\right]\right]$$

$$= J_{0r} + \sigma\left[-\frac{\partial A_r}{\partial t} - \frac{\partial\phi}{\partial r} + \frac{v_\theta}{r}\left[\frac{\partial(rA_\theta)}{\partial r} - \frac{\partial A_r}{\partial\theta}\right] - v_z\left[\frac{\partial A_r}{\partial z} - \frac{\partial A_z}{\partial r}\right]\right] \tag{2.5.1.a}$$

$$\frac{\partial}{\partial z}\left[\nu_r\left[\frac{1}{r}\frac{\partial A_z}{\partial\theta} - \frac{\partial A_\theta}{\partial z}\right]\right] - \frac{\partial}{\partial r}\left[\frac{\nu_z}{r}\left[\frac{\partial(rA_\theta)}{\partial r} - \frac{\partial A_r}{\partial\theta}\right]\right]$$

$$= J_{0\theta} + \sigma\left[-\frac{\partial A_\theta}{\partial t} - \frac{1}{r}\frac{\partial\phi}{\partial\theta} + v_z\left[\frac{1}{r}\frac{\partial A_z}{\partial\theta} - \frac{\partial A_\theta}{\partial z}\right] - v_r\frac{1}{r}\left[\frac{\partial(rA_\theta)}{\partial r} - \frac{\partial A_r}{\partial\theta}\right]\right] \tag{2.5.1.b}$$

$$\frac{1}{r}\frac{\partial}{\partial r}\left[\nu_\theta r\left[\frac{\partial A_r}{\partial z} - \frac{\partial A_z}{\partial\theta}\right]\right] - \frac{1}{r}\frac{\partial}{\partial\theta}\left[\nu_r\left[\frac{1}{r}\frac{\partial A_z}{\partial\theta} - \frac{\partial A_\theta}{\partial z}\right]\right]$$

$$= J_{0z} + \sigma\left[-\frac{\partial A_z}{\partial t} - \frac{\partial\phi}{\partial z} + v_r\left[\frac{\partial A_r}{\partial z} - \frac{\partial A_z}{\partial r}\right] - v_\theta\left[\frac{1}{r}\frac{\partial A_z}{\partial\theta} - \frac{\partial A_\theta}{\partial z}\right]\right] \tag{2.5.1.c}$$

$+$*Gauge condition*

2.5.3. Maxwell stress tensor

A basic mathematical formulation is described in this subsection for calculating forces with the Maxwell-stress method on the cylindrical coordinates.

The Lorenz force **f** in a volume illustrated in the figure 2.9 is calculated with the magnetic flux density **B** and the total current **i** including magnetization current as follows:

$$\mathbf{f} = \mathbf{j} \times \mathbf{B} \tag{2.5.2}$$

The total magnetic force applied to the volume is calculated by integrating the **f** as follows.

$$\mathbf{F} = \iiint_v \mathbf{f}\, dr \cdot r d\theta \cdot dz \tag{2.5.3}$$

From the Maxwell's equations:

$$\mathbf{j} = \nabla \times \mathbf{H} = \frac{1}{\mu_0} \nabla \times \mathbf{B} \tag{2.5.4}$$

the force consequently is written as follows.

$$\mathbf{f} = \frac{1}{\mu_0} \Big[\nabla \times \mathbf{B} \Big] \times \mathbf{B} \tag{2.5.5}$$

With the following formula of the vector algebra,

$$\nabla(\mathbf{u} \cdot \mathbf{v}) = (\mathbf{u} \cdot \nabla)\mathbf{v} + (\mathbf{v} \cdot \nabla)\mathbf{u} + \mathbf{u} \times (\nabla \times \mathbf{v}) + \mathbf{v} \times (\nabla \times \mathbf{u}) \tag{2.5.6}$$

hence,

$$\nabla(\mathbf{B} \cdot \mathbf{B}) = 2\,(\mathbf{B} \cdot \nabla)\mathbf{B} + 2\mathbf{B} \times (\nabla \times \mathbf{B}) \tag{2.5.7}$$

the force is separated into two terms as follows.

$$\mathbf{f} = \frac{1}{\mu_0} (\nabla \times \mathbf{B}) \times \mathbf{B} = \frac{1}{\mu_0} \left\{ (\mathbf{B} \cdot \nabla)\mathbf{B} - \frac{1}{2} \nabla(\mathbf{B} \cdot \mathbf{B}) \right\} \tag{2.5.8}$$

The first factor of the vector equation (2.5.8) is:

$$f_r = \frac{1}{\mu_0} \left\{ B_r \frac{\partial B_r}{\partial r} + B_\theta \frac{1}{r} \frac{\partial B_r}{\partial \theta} + B_z \frac{\partial B_r}{\partial z} - \frac{1}{2} \frac{\partial}{\partial r} (B_r^2 + B_\theta^2 + B_z^2) \right\} \tag{2.5.9}$$

When the following formulas are applied to the equation (2.5.9),

$$\frac{\partial (B_r^2)}{\partial r} = 2 B_r \frac{\partial B_r}{\partial r}$$

$$\frac{1}{r} \frac{\partial (B_r B_\theta)}{\partial \theta} = \frac{1}{r} B_r \frac{\partial B_\theta}{\partial \theta} + \frac{1}{r} B_\theta \frac{\partial B_r}{\partial \theta}$$

$$\frac{\partial (B_r B_z)}{\partial z} = B_r \frac{\partial B_z}{\partial z} + B_z \frac{\partial B_r}{\partial z}$$

then

$$B_r\frac{\partial B_r}{\partial r}+B_\theta\frac{1}{r}\frac{\partial B_r}{\partial \theta}+B_z\frac{\partial B_r}{\partial z}$$

$$=\frac{\partial(B_r^2)}{\partial r}+\frac{1}{r}\frac{\partial(B_rB_\theta)}{\partial\theta}+\frac{\partial(B_rB_z)}{\partial z}-B_r\left[\frac{\partial B_r}{\partial r}+\frac{1}{r}\frac{\partial B_\theta}{\partial\theta}+\frac{\partial B_z}{\partial z}\right]$$

$$=\frac{\partial(B_r^2)}{\partial r}+\frac{1}{r}\frac{\partial(B_rB_\theta)}{\partial\theta}+\frac{\partial(B_rB_z)}{\partial z}-B_r\left[\nabla\cdot\mathbf{B}\right]_{=0!}$$

$$=\frac{\partial(B_r^2)}{\partial r}+\frac{1}{r}\frac{\partial(B_rB_\theta)}{\partial\theta}+\frac{\partial(B_rB_z)}{\partial z} \qquad (2.5.11)$$

the following expression is derived as a result.

$$f_r=\frac{1}{\mu_0}\left\{\frac{1}{2}\frac{\partial}{\partial r}\left[B_r^2-B_\theta^2-B_z^2\right]+\frac{1}{r}\frac{\partial}{\partial\theta}\left[B_rB_\theta\right]+\frac{\partial}{\partial z}\left[B_rB_z\right]\right\} \qquad (2.5.12)$$

The second- and the third- factors are derived in the same way as follows:

$$f_\theta=\frac{1}{\mu_0}\left\{\frac{\partial}{\partial r}\left[B_\theta B_r\right]+\frac{1}{2}\frac{1}{r}\frac{\partial}{\partial\theta}\left[B_\theta^2-B_z^2-B_r^2\right]+\frac{\partial}{\partial z}\left[B_\theta B_z\right]\right\} \qquad (2.5.13)$$

$$f_z=\frac{1}{\mu_0}\left\{\frac{\partial}{\partial r}\left[B_zB_r\right]+\frac{1}{r}\frac{\partial}{\partial\theta}\left[B_zB_\theta\right]+\frac{1}{2}\frac{\partial}{\partial z}\left[B_z^2-B_r^2-B_\theta^2\right]\right\} \qquad (2.5.14)$$

The force element f_r is integrated here. If one defines the vector $\mathbf{F}_r\equiv\left[\frac{1}{2}\frac{1}{\mu_0}\left[B_r^2-B_\theta^2-B_z^2\right],\ \frac{1}{\mu_0}B_rB_\theta,\ \frac{1}{\mu_0}B_rB_z\right]^t$, the following form is derived from the Gauss' divergence theorem:

$$F_r=\iiint_v f_r\,dr\,rd\theta\,dz=\iiint_v\nabla\cdot\mathbf{F}_r\,dr\,rd\theta\,dz=\iint_S\mathbf{F}_r\cdot\mathbf{n}dS$$

$$=\iint_{S_r}\frac{1}{2\mu_0}\left[B_r^2-B_\theta^2-B_z^2\right]\mathbf{e}_r\cdot\mathbf{n}\,rd\theta\,dz+\iint_{S_\theta}\frac{1}{\mu_0}\left[B_rB_\theta\right]\mathbf{e}_\theta\cdot\mathbf{n}\,dr\,dz$$

$$+\iint_{S_z}\frac{1}{\mu_0}\left[B_rB_z\right]\mathbf{e}_z\cdot\mathbf{n}\,dr\,rd\theta \qquad (2.5.15)$$

where the S_r, S_θ and S_z mean the surfaces whose normal vectors are in the directions of r, θ, and z respectively. The other two factors are integrated in the same way.

Finally, the volume integral of the Lorenz force has been substituted by the surface integral of the following Maxwell's stress tensors.

$$\frac{1}{\mu_0}\begin{bmatrix}\frac{1}{2}\left[B_r^2-B_\theta^2-B_z^2\right] & B_rB_\theta & B_rB_z\\ B_\theta B_r & \frac{1}{2}\left[B_\theta^2-B_z^2-B_r^2\right] & B_\theta B_z\\ B_zB_r & B_zB_\theta & \frac{1}{2}\left[B_z^2-B_r^2-B_\theta^2\right]\end{bmatrix} \qquad (2.5.16)$$

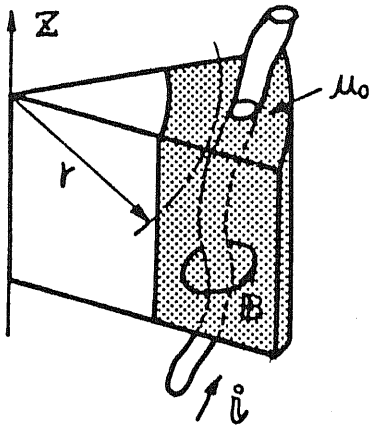

Figure 2.9. Lorenz force in a volume.

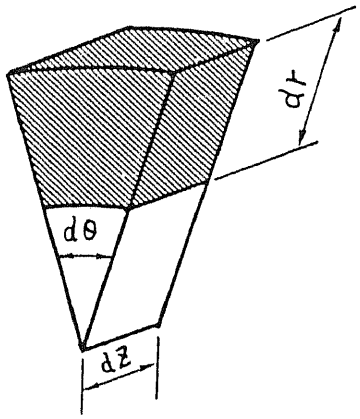

Figure 2.10. Control volume in the three-dimensional cylindrical coordinates.

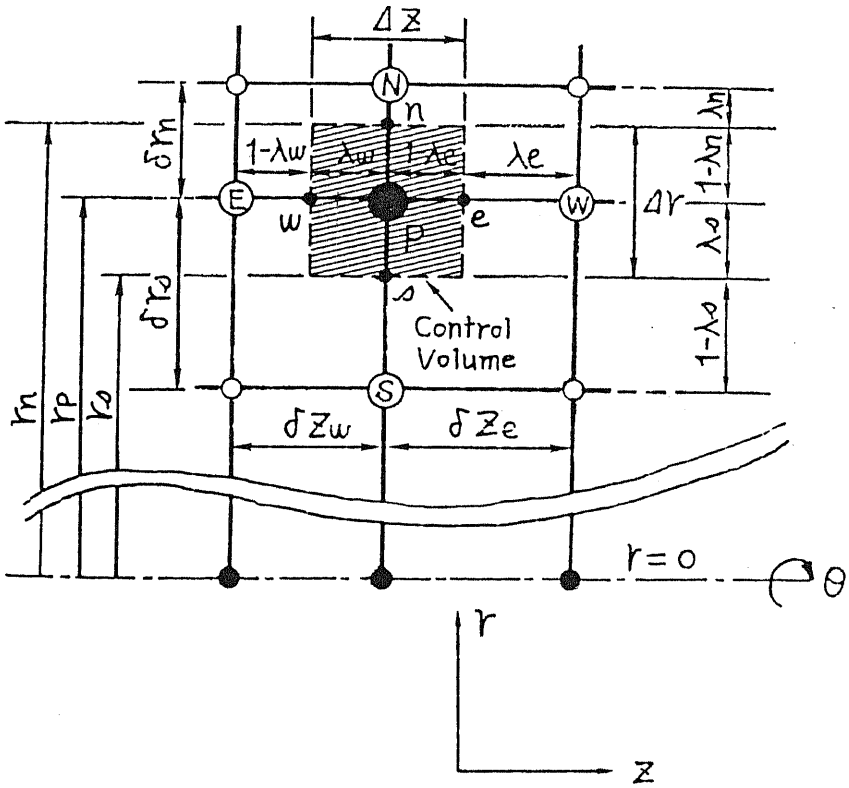

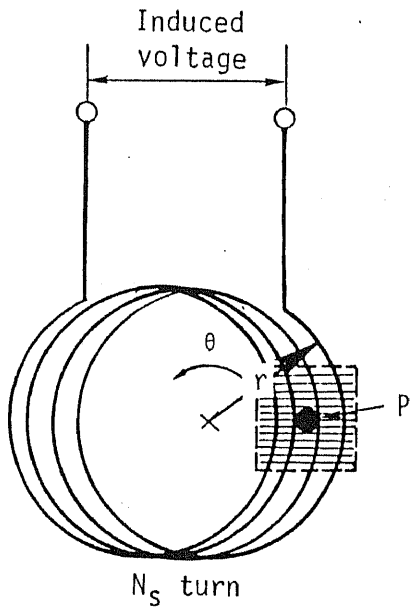

Figure 2.11. Control volume and grid points in a coaxial cross-section.

2.5.4. Formulation for a tubular LIM — integral of a control volume

For simplicity of analyzing a coaxial symmetrical tubular LIM with a single continuous secondary conductor, one should accept the following assumptions:

(1) In the analyzed region, currents flow only in the θ-direction. ($J_{0\theta}$ will be simply written as J_0 in the following formulations.)

(2) Hence, $A_r = A_z = 0$. (A_θ will be simply written as A.)

(3) The conductor moves only in the z- direction. (v_z will be written as v.)

(4) Eddy current flows only in a continuous secondary part.

According to the assumptions, the following simple basic equation is derived where a new dependent unknown variable $U \equiv A \cdot r$ is defined; thanks to the assumption (4), one can choose the simplest gauge-condition $\phi = 0$.

$$\sigma \frac{1}{r}\frac{\partial U}{\partial t} = \frac{\partial}{\partial z}\left[\frac{\nu_r}{r}\frac{\partial U}{\partial z}\right] + \frac{\partial}{\partial r}\left[\frac{\nu_z}{r}\frac{\partial U}{\partial r}\right] - \sigma v \frac{1}{r}\frac{\partial U}{\partial z} + J_0 \qquad (2.5.17)$$

The equation (2.5.17) is multiplied by the step-weighting function, which is unity in the control volume and zero out of it, to discretize the basic equation based on the control volume method, where the control volume is illustrated in the figure 2.10.

$$\frac{1}{\Delta t}\int_t^{t+\Delta t}\int_w^e\int_s^n \left[\frac{\sigma}{r}\frac{\partial U}{\partial t} - \frac{\partial}{\partial z}\left[\frac{\nu_r}{r}\frac{\partial U}{\partial z}\right] - \frac{\partial}{\partial r}\left[\frac{\nu_z}{r}\frac{\partial U}{\partial r}\right] + \frac{\sigma v}{r}\frac{\partial U}{\partial z} - J_0\right] r\, dr\, dz\, dt = 0 \qquad (2.5.18)$$

2.5.5. Discrete formulation with a linear interpolation function — the "A_R-" method

First of all, a formulation with a linear interpolating function is described in this subsection, assuming the potential variable U varies linearly between two grid points. The quasi-three- dimensional grids in a coaxial cross-section are illustrated in the figure (2.11). According to the assumptions, the potentials on boundaries of a control volume are written as follows:

$$U_e = (1-\lambda_e)U_E + \lambda_e U_P \qquad (2.5.19)$$

$$U_w = (1-\lambda_w)U_P + \lambda_w U_W \qquad (2.5.20)$$

$$U_n = (1-\lambda_n)U_N + \lambda_n U_P \qquad (2.5.21)$$

$$U_s = (1-\lambda_s)U_P + \lambda_s U_S \qquad (2.5.22)$$

The first term of the equation (2.5.18):

$$= \sigma_P \frac{U_P U_P^0}{\Delta t}\,\Delta r\,\Delta z$$

$$[2nd\ term] = -\left[\nu_r \frac{\partial U}{\partial z}\right]_w^e \Delta r$$

$$= -\nu_{re}\frac{U_E - U_P}{\delta Z_e}\Delta r + \nu_{rw}\frac{U_P - U_W}{\delta z_w}\Delta r$$

$$= \left(\frac{\nu_{re}}{\delta z_e} + \frac{\nu_{rw}}{\delta z_w}\right)\Delta r U_P - \frac{\nu_{re}\Delta r}{\delta z_e}U_E - \frac{\nu_{rw}\Delta r}{\delta z_w}U_W$$

$$[3rd\ term] = -\Delta z \int_s^n r \frac{\partial}{\partial r}\left\{\frac{\nu_z}{r}\frac{\partial U}{\partial r}\right\} dr$$

$$= -\Delta z\left[r\frac{\nu_z}{r}\frac{\partial U}{\partial r}\right]_s^n + \Delta z\int_s^n \left(\frac{\nu_z}{r}\frac{\partial U}{\partial r}\right) dr$$

$$= \left[-\frac{\nu_{zn}(U_N - U_P)}{\delta r_n} + \frac{\nu_{zs}(U_P - U_S)}{\delta r_s} + \int_s^P \left\{\frac{\nu_{zs}(U_P - U_S)}{\delta r_s}\right\}\frac{dr}{r} + \int_P^n \left\{\frac{\nu_{zn}(U_N - U_P)}{\delta r_n}\right\}\frac{dr}{r}\right]\Delta z$$

$$= \left[-\frac{\nu_{zn}(U_N - U_P)}{\delta r_n} + \frac{\nu_{zs}(U_P - U_S)}{\delta r_s} + \frac{\nu_{zs}(U_P - U_S)}{\delta r_s}\ln\frac{r_P}{r_s} + \frac{\nu_{zn}(U_N - U_P)}{\delta r_n}\ln\frac{r_n}{r_P}\right]\Delta z$$

$$= \left\{\frac{\nu_{zn}}{\delta r_n}\left[1 + \ln\frac{r_n}{r_P}\right] + \frac{\nu_{zs}}{\delta r_s}\left[1 + \ln\frac{r_P}{r_s}\right]\right\}\Delta z U_P - \frac{\nu_{zn}}{\delta r_n}\left[1 + \ln\frac{r_n}{r_P}\right]\Delta z U_N - \frac{\nu_{zs}}{\delta r_s}\left[1 + \ln\frac{r_P}{r_s}\right]\Delta z U_S$$

$$[4th\ term] = \left\{\sigma_e v_e \lambda_e - \sigma_w v_w (1 - \lambda_w)\right\}\Delta Z U_P + \sigma_e v_e (1 - \lambda_e)\Delta r U_E - \sigma_w v_w \lambda_w U \Delta r U_W$$

$$[5th\ term] = -J_0 \Delta z \int_s^n r\, dr = -J_{0P}\Delta z \frac{(r_n + r_s)}{2}(r_n - r_s) = -J_{0P} r_P \Delta r \Delta z$$

These results are substituted into the equation (2.5.18); the following discretized equation is derived:

$$a_P U_P - a_E U_E - a_W U_W - a_N U_N - a_S U_S = b \tag{2.5.23}$$

where

$$a_E = \left\{\frac{\nu_{re}}{\delta z_e} - \sigma_e v_e (1 - \lambda_e)\right\}\Delta r \tag{2.5.24}$$

$$a_W = \left\{\frac{\nu_{rw}}{\delta z_w} - \sigma_w v_w \lambda_w\right\}\Delta r \tag{2.5.25}$$

$$a_N = \frac{\nu_{zn}}{\delta r_n}\left[1 + \ln\frac{r_n}{r_P}\right]\Delta z \tag{2.5.26}$$

$$a_S = \frac{\nu_{zs}}{\delta r_s}\left[1+\ln\frac{r_P}{r_s}\right]\Delta z \tag{2.5.27}$$

$$a_P^0 = \frac{\sigma_P \Delta z \Delta r}{\Delta t} \tag{2.5.28}$$

$$b = J_{0P} r_P \Delta r \Delta z + a_P^0 U_P^0 \tag{2.5.29}$$

and

$$a_P = a_E+a_W+a_N+a_S+a_P^0+\left[\sigma_e v_e-\sigma_w v_w\right]\Delta r \tag{2.5.30}$$

2.5.6. Modified exponential method

With complete implicit discrete time method and consideration of the up-wind effect [2-3] in the same way as the subsection 2.4.4., the resultant discrete equation for general transient phenomena is derived as follows:

$$a_P U_P - a_E U_E - a_W U_W - a_N U_N - a_S U_S = b \tag{2.5.31}$$

$$a_E = \frac{\nu_{re}\Delta r}{\delta z_e}\cdot Max\left[0,\ \left[1-0.1|P_e|\right]^5\right] + Max\left[-\sigma_e v_e \Delta r,\ 0\right] \tag{2.5.32}$$

$$a_W = \frac{\nu_{rw}\Delta r}{\delta z_w}\cdot Max\left[0,\ \left[1-0.1|P_w|\right]^5\right] + Max\left[\sigma_w v_w \Delta r,\ 0\right] \tag{2.5.33}$$

where the Peclet numbers P_e and P_w are defined as follows:

$$P_e = \frac{\sigma_e v_e \delta z_e}{\nu_{re}} \tag{2.5.34}$$

$$P_w = \frac{\sigma_w v_w \delta z_w}{\nu_{rw}} \tag{2.5.35}$$

$$a_N = \frac{\nu_{zn}}{\delta r_n}\left[1+\ln\frac{r_n}{r_P}\right]\Delta z \tag{2.5.36}$$

$$a_S = \frac{\nu_{zs}}{\delta r_s}\left[1+\ln\frac{r_P}{r_s}\right]\Delta z \tag{2.5.37}$$

$$a_P^0 = \frac{\sigma_P \Delta z \Delta r}{\Delta t} \tag{2.5.38}$$

$$b = J_{0P} r_P \Delta r \Delta z + a_P^0 U_P^0 \tag{2.5.39}$$

and

$$a_P = a_E+a_W+a_N+a_S+a_P^0+\left[\sigma_e v_e-\sigma_w v_w\right]\Delta r \tag{2.5.40}$$

It is said that accuracy of the calculation is relatively bad near the central axis r=0 in an ordinary finite element method with linear triangular elements due to the following approximation of the integral in an element:

$$\iint_{S^{(e)}} \frac{1}{r} N_{ie} N_{je}\, dr\, dz \approx \frac{1}{9 r_0^{(e)}}\, \Delta^{(e)} \tag{2.5.41}$$

where the (e) means a region in an element; $\Delta^{(e)}$: area of the element; N_{ie}: shape function; and $r_0^{(e)}$ r-value of the weight point of the triangular element. This approximation corresponds to substituting the $\ln\frac{r_P}{r_s}$ with $\Delta^{(e)}\frac{r_P}{r_s}$, and $\ln\frac{r_n}{r_P}$ with $\Delta^{(e)}\frac{r_n}{r_P}$; the formulation described here is, therefore, more accurate than the ordinary FEM with linear triangular elements.

2.5.7. Stationary analysis — $e^{j\omega t}$- method

For a stationary analysis using $e^{j\omega t}$:

$$\dot{a}_P \dot{U}_P - a_E \dot{U}_E - a_W \dot{U}_W - a_N \dot{U}_N - a_S \dot{U}_S = \dot{b} \tag{2.5.31'}$$

$$\dot{a}_P = a_E + a_W + a_N + a_S + j\omega\sigma_P \Delta z \Delta r \tag{2.5.40'}$$

$$\dot{b} = \dot{J}_{0P} r_P \Delta r \Delta z \tag{2.5.39'}$$

2.5.8. Calculation of magnetic flux density, secondary current, primary voltage and forces

Magnetic flux densities are written as:

$$B_r = -\frac{1}{r}\frac{\partial U}{\partial z} \tag{2.5.42}$$

$$B_z = \frac{1}{r}\frac{\partial U}{\partial r} \tag{2.5.43}$$

$$i_{2\theta} = -\frac{\sigma}{r}\left[\frac{\partial U}{\partial t} + v\frac{\partial U}{\partial z}\right] \tag{2.5.44}$$

Normal force density in the r- direction and thrust force are calculated from the equation (2.5.16) as follows:

$$F'_r = \frac{1}{2\mu_0}\int_{z_1}^{z_2}\left[B_r^2 - B_z^2\right]_{r=r_{gap}} dz \qquad [\mathrm{N/m}] \tag{2.5.45}$$

$$F_z = \frac{2\pi r_{gap}}{\mu_0}\int_{z_1}^{z_2}\left[B_r \cdot B_z\right]_{r=r_{gap}} dz \qquad [\mathrm{N}] \tag{2.5.46}$$

The primary voltage is calculated from the figure 2.11. (b):

$$E_\theta = -\frac{\partial A_\theta}{\partial t} \quad [\mathrm{V/m}] \tag{2.5.47}$$

$$V = N_s \cdot E_\theta \cdot 2\pi r_P = -2\pi N_s \frac{\partial U_P}{\partial t} \quad [\mathrm{V}] \tag{2.5.48}$$

2.6. Control volume method (3): two- dimensional general irregular triangular elements

The mathematical formulations on rectangular coordinates based on the *Control Volume Method* were described in the previous sections: it is also applicable to irregular triangular elements like the finite element methods with a sophisticated mathematical technique [2-8], although the procedure is a little more complicated.

In this section, a conventional FEM formulation will be introduced in the first place for a comparison, which is followed by the description of the direct application of the Ampere's law and the control volume methods with the linear- and the exponential- interpolating functions.

2.6.1. Conventional method: finite element method

2.6.1.1. Formulation based on the Galerkin method with linear shape- and weighting- functions

The basic equation is named $R^*(A)$ for applying the Galerkin method as follows.

$$R^*(A) = \frac{\partial}{\partial x}\left[\nu_y \frac{\partial A}{\partial x}\right] + \frac{\partial}{\partial y}\left[\nu_x \frac{\partial A}{\partial y}\right] - \sigma\left[v_x \frac{\partial A}{\partial x} + v_y \frac{\partial A}{\partial y}\right] - \sigma \frac{\partial A}{\partial t} + J_0 \tag{2.6.1}$$

The linear interpolating function in the triangular element illustrated in the figure 2.12 is defined as follows.

$$A_{inner} = \alpha + \beta x + \gamma y \tag{2.6.2}$$

The coefficients are determined by the following simultaneous equations:

$$\begin{bmatrix} A_1 \\ A_2 \\ A_3 \end{bmatrix} = \begin{bmatrix} 1 & x_1 & y_1 \\ 1 & x_2 & y_2 \\ 1 & x_3 & y_3 \end{bmatrix} \begin{bmatrix} \alpha \\ \beta \\ \gamma \end{bmatrix} \tag{2.6.3}$$

where A_1, A_2 and A_3 are the vector potentials on the three corner nodes of the element. Although it can be easily solved as follows:

$$\begin{bmatrix} \alpha \\ \beta \\ \gamma \end{bmatrix} = \begin{bmatrix} 1 & x_1 & y_1 \\ 1 & x_2 & y_2 \\ 1 & x_3 & y_3 \end{bmatrix}^{-1} \begin{bmatrix} A_1 \\ A_2 \\ A_3 \end{bmatrix} \tag{2.6.4}$$

the following relation is also well known by using the local *area coordinates* as follows.

$$A_{inner} = \sum_{s=1}^{3} \zeta_s A_s \tag{2.6.5}$$

$$S_{s=1,\ldots,3} \equiv (\alpha_s + \beta_s x + \gamma_s y) \tag{2.6.6.a}$$

$$S \equiv \frac{1}{2} \det \begin{bmatrix} 1 & x_1 & y_1 \\ 1 & x_2 & y_2 \\ 1 & x_3 & y_3 \end{bmatrix} \tag{2.6.6.b.}$$

$$\zeta_{s=1,\ldots,3} \equiv \frac{S_s}{S} \tag{2.6.6.c}$$

$$2S = \alpha_1 + \alpha_2 + \alpha_3 \tag{2.6.7}$$

$$\alpha_1 = x_2y_3 - x_3y_2 \qquad \alpha_2 = x_3y_1 - x_1y_3 \qquad \alpha_3 = x_1y_2 - x_2y_1$$
$$\beta_1 = y_2 - y_3 \qquad \beta_2 = y_3 - y_1 \qquad \beta_3 = y_1 - y_2$$
$$\gamma_1 = x_3 - x_2 \qquad \gamma_2 = x_1 - x_3 \qquad \gamma_3 = x_2 - x_1$$

(2.6.8)

$$\alpha = \frac{\alpha_1 A_1 + \alpha_2 A_2 + \alpha_3 A_3}{2S} \tag{2.6.9}$$

$$\beta = \frac{\beta_1 A_1 + \beta_2 A_2 + \beta_3 A_3}{2S} \tag{2.6.10}$$

$$\gamma = \frac{\gamma_1 A_1 + \gamma_2 A_2 + \gamma_3 A_3}{2S} \tag{2.6.11}$$

The original x- and y- coordinates are expressed by using the local area coordinates as follows.

$$x = \zeta_1 x_1 + \zeta_2 x_2 + \zeta_3 x_3 \tag{2.6.12}$$

$$y = \zeta_1 y_1 + \zeta_2 y_2 + \zeta_3 y_3 \tag{2.6.13}$$

The shape- and weighting- functions in the FEM with linear triangular elements based on the Galerkin method are written using the local area coordinates as follows.

$$N_1 = \zeta_1, \qquad N_2 = \zeta_2, \qquad N_3 = \zeta_3 \tag{2.6.14}$$

The residual of the basic equation is written in the following form.

$$G_i^* \equiv \iint_S N_i \left\{ \frac{\partial}{\partial x}\left[\nu_y \frac{\partial A}{\partial x}\right] + \frac{\partial}{\partial y}\left[\nu_x \frac{\partial A}{\partial y}\right] - \sigma\left[v_x \frac{\partial A}{\partial x} + v_y \frac{\partial A}{\partial y}\right] - \sigma \frac{\partial A}{\partial t} + J_0 \right\} dx\, dy \tag{2.6.15}$$

where the magnetic potential A is assumed in the following equation with the interpolating functions:

$$A = \sum_{i=1}^{nt} N_i \cdot A_i \tag{2.6.16}$$

By applying the formula of the integration of parts to the equation (2.6.15):

$$G_i^* = \iint_S \left\{ \frac{\partial}{\partial x}\left[N_i \nu_y \frac{\partial A}{\partial x} \right] + \frac{\partial}{\partial y}\left[N_i \nu_x \frac{\partial A}{\partial y} \right] \right\} dx\,dy$$

$$- \iint_S \left\{ \frac{\partial N_i}{\partial x}\left[\nu_y \frac{\partial A}{\partial x} \right] + \frac{\partial N_i}{\partial y}\left[\nu_x \frac{\partial A}{\partial y} \right] \right\} dx\,dy$$

$$+ \iint_S \left\{ -N_i \sigma \left[v_x \frac{\partial A}{\partial x} + v_y \frac{\partial A}{\partial y} \right] - N_i \sigma \frac{\partial A}{\partial t} + N_i J_0 \right\} dx\,dy \qquad (2.6.17)$$

in addition, according to the Green's theorem, the following relation is derived:

$$[The\ 1st\ term] = \iint_S \left\{ \frac{\partial}{\partial x}\left[N_i \nu_y \frac{\partial A}{\partial x} \right] + \frac{\partial}{\partial y}\left[N_i \nu_x \frac{\partial A}{\partial y} \right] \right\} dx\,dy$$

$$= \int_C N_i \left[\nu_y \frac{\partial A}{\partial x} dy - \nu_x \frac{\partial A}{\partial y} dx \right]$$

$$= 0 \qquad (2.6.18)$$

under the assumption of the natural boundary condition. Hence, if the new residual G_i is defined as follows:

$$G_i \equiv -G_i^* \qquad (2.6.19)$$

$$= \iint_S \left\{ \frac{\partial N_i}{\partial x}\left[\nu_y \frac{\partial A}{\partial x} \right] + \frac{\partial N_i}{\partial y}\left[\nu_x \frac{\partial A}{\partial y} \right] + \sigma N_i \left[v_x \frac{\partial A}{\partial x} + v_y \frac{\partial A}{\partial y} \right] + \sigma N_i \frac{\partial A}{\partial t} - N_i J_0 \right\} dx\,dy$$

$$= \sum_{R_i} \left[\iint_{S^{(e)}} \left\{ \frac{\partial N_{ie}}{\partial x}\left[\nu_y \frac{\partial A^{(e)}}{\partial x} \right] + \frac{\partial N_{ie}}{\partial y}\left[\nu_x \frac{\partial A^{(e)}}{\partial y} \right] + \sigma N_{ie} \left[v_x \frac{\partial A^{(e)}}{\partial x} + v_y \frac{\partial A^{(e)}}{\partial y} \right] + \sigma N_{ie} \frac{\partial A^{(e)}}{\partial t} - N_{ie} J_0 \right\} dx\,dy \right]$$

and the potential in an element is assumed:

$$A^{(e)} = \sum_{j=1}^{3} N_{je} A_{je} = \sum_{j=1}^{3} \zeta_j A_j \qquad (2.6.20)$$

then by applying the following relation to the integral of the residual:

$$\frac{\partial N_i}{\partial x} = \sum_{k=1}^{3} \frac{\partial N_i}{\partial \zeta_k}\frac{\partial \zeta_k}{\partial x} = \frac{1}{2S}\sum_{k=1}^{3} \beta_k \frac{\partial N_i}{\partial \zeta_k} = \frac{\beta_i}{2S}$$

$$\frac{\partial N_i}{\partial y} = \sum_{k=1}^{3} \frac{\partial N_i}{\partial \zeta_k}\frac{\partial \zeta_k}{\partial y} = \frac{1}{2S}\sum_{k=1}^{3} \gamma_k \frac{\partial N_i}{\partial \zeta_k} = \frac{\gamma_i}{2S}$$

the integral can be formulated as follows.

$$G_i = \sum_{R_i} \left[\iint_{S^{(e)}} \sum_{j=1}^{3} \left[\left\{ \frac{\partial N_i}{\partial x}\left[\nu_y \frac{\partial N_j}{\partial x} \right] + \frac{\partial N_i}{\partial y}\left[\nu_x \frac{\partial N_j}{\partial y} \right] + \sigma N_i \left[v_x \frac{\partial N_j}{\partial x} + v_y \frac{\partial N_j}{\partial y} \right] \right\} A_j + \sigma N_i \frac{\partial A}{\partial t} - N_i J_0 \right] dx\,dy \right]$$

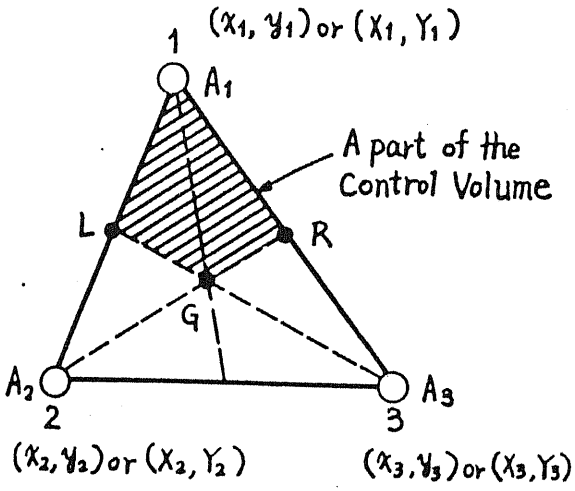

Figure 2.12. A triangular element.

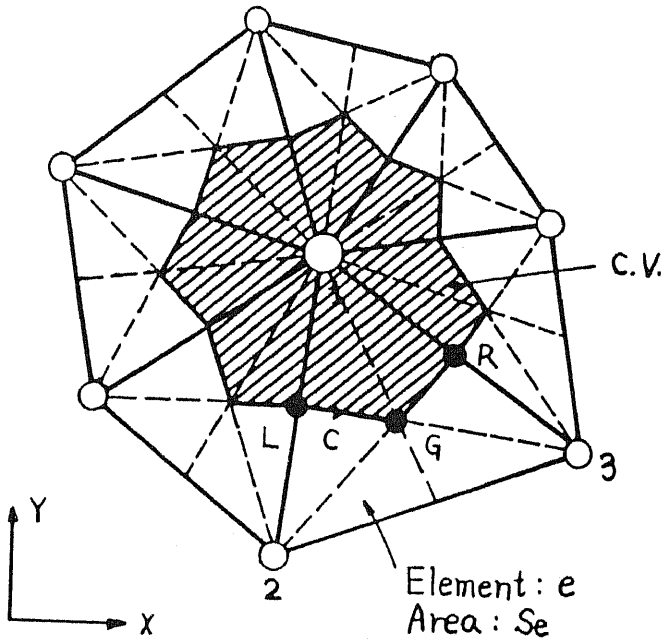

Figure 2.13. Triangular elements and a control volume.

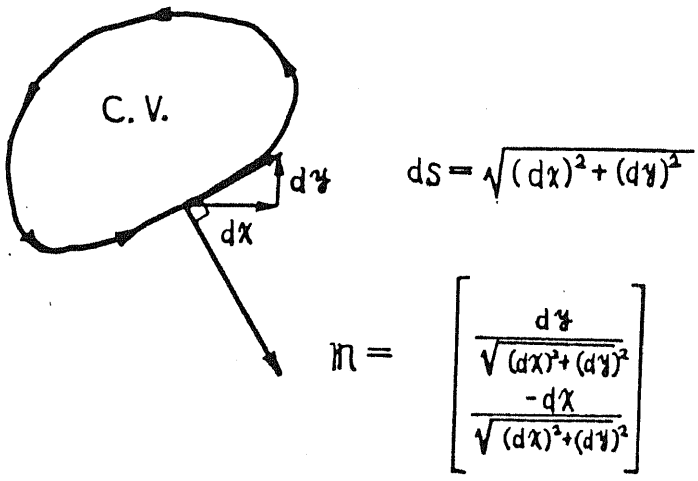

Figure 2.14. Line- and surface- integrals.

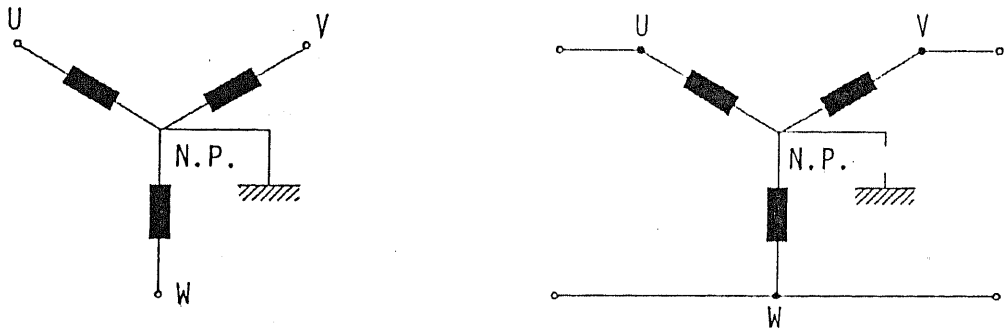

Figure 2.15. Three-phase circuits as multi- terminal system.

$$= \sum_{R_i}\left[\iint_{S(e)}\sum_{j=1}^{3}\left[\left\{\frac{1}{4S^2}\nu_y\beta_i\beta_j+\frac{1}{4S^2}\nu_x\gamma_i\gamma_j+\frac{1}{2S}\sigma\zeta_i\left(v_x\beta_i+v_y\gamma_j\right)\right\}A_j+\sigma\zeta_j\frac{\partial A}{\partial t}-\zeta_i J_0\right]dx\,dy\right] \quad (2.6.21)$$

$$= \sum_{R_i}\left[\iint_{S(e)}\left\{\left(\nu_y\frac{\beta_i}{2S}+\sigma v_x\zeta_i\right)\sum_{j=1}^{3}\frac{\beta_j}{2S}A_j+\left(\nu_x\frac{\gamma_i}{2S}+\sigma v_y\zeta_i\right)\sum_{j=1}^{3}\frac{\gamma_j}{2S}A_j-\zeta_i J_0+\sigma\sum_{j=1}^{3}\zeta_i\zeta_j\frac{\partial A_j}{\partial t}\right\}dx\,dy\right]$$

The simultaneous linear equations in an element is consequently derived by applying the formula $\iint_S \zeta_1^a\zeta_2^b\zeta_3^c\,dx\,dy = 2S\frac{a!\;b!\;c!}{(a+b+c+2)!}$ to the integral.

$$\left[\begin{array}{c} a_{ij} \\ =\frac{\beta_j(3\nu_y\beta_i+2S\sigma v_x)+\gamma_j(3\nu_x\gamma_i+2S\sigma v_y)}{12S} \end{array}\right]\begin{bmatrix}A_1\\A_2\\A_3\end{bmatrix}+\sigma S\begin{bmatrix}\frac{1}{6}&\frac{1}{12}&\frac{1}{12}\\\frac{1}{12}&\frac{1}{6}&\frac{1}{12}\\\frac{1}{12}&\frac{1}{12}&\frac{1}{6}\end{bmatrix}\begin{bmatrix}\frac{\partial A_1}{\partial t}\\\frac{\partial A_2}{\partial t}\\\frac{\partial A_3}{\partial t}\end{bmatrix}=\begin{bmatrix}\frac{J_0S}{3}\\\frac{J_0S}{3}\\\frac{J_0S}{3}\end{bmatrix} \quad (2.6.22)$$

2.6.1.2. Formulation based on the Ampere's law [2-7]

The same discretization is also possible by applying the Ampere's law directly to the analyzed region, *e.g.*, illustrated in the figure 2.13. The Ampere's law with the form of integration is:

$$\int_C \mathbf{H}\cdot d\mathbf{l} = \sum_{C_i}\int_{C_i}\mathbf{H}\cdot d\mathbf{l}$$

$$= \sum_{S_i}\int_{S_i} J_i\,dS \quad (2.6.23)$$

The input current consists of:

$$J_i = J_{0i} + J_{vi} + J_{ti} \quad (2.6.24)$$

where J_0, J_v, and J_t are current densities forced, and induced by velocity- and transformer- effects respectively. According to the linear interpolating (or shape-) function:

$$B_x = \frac{\partial A}{\partial y} = \sum_{j=1}^{3}\frac{\partial N_j}{\partial y} = \frac{\gamma_1A_1+\gamma_2A_2+\gamma_3A_3}{2S} = \gamma \quad (2.6.25)$$

$$B_y = -\frac{\partial A}{\partial x} = \sum_{j=1}^{3}\frac{\partial N_j}{\partial x} = -\frac{\beta_1A_1+\beta_2A_2+\beta_3A_3}{2S} = -\beta \quad (2.6.26)$$

Hence, the left hand side of the equation (2.6.23) in the first element is:

$$\int_{L\to R}\mathbf{H}\cdot d\mathbf{l} = \int_{L\to R}(H_x dx+H_y dy)$$

$$= \frac{1}{2}\left\{H_x(x_3-x_2)-H_y(y_2-y_3)\right\}$$

$$= \frac{1}{2}\left\{\nu_x B_x(x_3-x_2)-\nu_y B_y(y_2-y_3)\right\}$$

$$= \left[\nu_{xi}\frac{(x_3-x_2)^2}{4S_i} + \nu_{yi}\frac{(y_2-y_3)^2}{4S_i}\right]A_{1i}$$

$$+ \left[\nu_{xi}\frac{(x_3-x_2)(x_1-x_3)}{4S_i}+\nu_{yi}\frac{(y_2-y_3)(y_3-y_1)}{4S_i}\right]A_{2i}$$

$$+ \left[\nu_{xi}\frac{(x_3-x_2)(x_2-x_1)}{4S_i}+\nu_{yi}\frac{(y_2-y_3)(y_1-y_2)}{4S_i}\right]A_{3i} \qquad (2.6.27)$$

On the other hand, the right hand side is:

$$\iint_{S_i} J_0 \, dx\,dy = \frac{1}{3}S_i J_{0i} \qquad (2.6.28)$$

$$\iint_{S_i} J_{vi} \, dx\,dy = \iint_{S_i} -v\sigma\frac{\partial A}{\partial x} = \sum_{j=1}^{3}\frac{\sigma v \beta_i}{6}A_i$$

$$= -\left[v\sigma\frac{y_2-y_3}{6}\right]A_{1i}-\left[v\sigma\frac{y_3-y_1}{6}\right]A_{2i}-\left[v\sigma\frac{y_1-y_2}{6}\right]A_{3i} \qquad (2.6.29)$$

$$\frac{1}{\Delta t}\int_t^{t+\Delta t}\iint_{S_i} J_{ti} \, dx\,dy\,d\tau = -\frac{1}{\Delta t}\int_t^{t+\Delta t}\iint_{S_i}\sigma\frac{\partial A}{\partial t}dx\,dy\,d\tau$$

$$= -\sigma_i\frac{S_1}{3\Delta t}(A_1 - A_1^0) \qquad (2.6.30)$$

The discrete equation (2.6.39) in the next section is obtained by substituting the equations from (2.6.27) to (2.6.30) into (2.6.23), and if one sums up all the elements around the node one — in this case $i = 1, \ldots, 5$, one obtains completely the same discretized equations as (2.6.22).

2.6.2. Formulation based on the control volume method

2.6.2.1. Merits and demerits of the method

The following method is more complicated than the C.V.- methods in the previous sections for the following reasons.

(1) A coordinates transformation is necessary on every point in a moving region so that the X axis may be in the same direction as the speed.

(2) An exponential calculation is necessary on every point in the moving region for defining discretizing coefficients.

(3) The linear- and the exponential- interpolating function should be applied to points in standstill- and moving- regions respectively in order to avoid the numerical division by zero, where the zero-division was automatically avoided in the previous formulations on the rectangular coordinates with the *modified* exponential interpolating functions: one needs some attentions to it during a numerical programming.

The complexity is, however, not much larger than the conventional finite element methods. In addition, it is a strong point of the following control volume method that the false diffusion is always avoided thanks to the coordinates transformation.

2.6.2.2. Assumptions

(1) The integrated basic equation is:

$$\frac{\partial}{\partial x}\left[\nu_y \frac{\partial A}{\partial x}\right]+\frac{\partial}{\partial y}\left[\nu_x \frac{\partial A}{\partial y}\right]-\sigma\left[v_x \frac{\partial A}{\partial x}+v_y \frac{\partial A}{\partial y}\right]-\sigma \frac{\partial A}{\partial t} = -J_0 \qquad (2.6.31)$$

where the term of v_y is omitted from the equation (2.6.1) because of the coordinates transformation.

(2) The velocity v, the force current J_0 and the conductivity σ belong to each corner nodes, *i.e.*, each control volume. On the other hand, the magnetic reluctivity ν is defined at each boundary of control volumes, *i.e.*, each triangular element. That is to say, the reluctivity ν_e in a triangular element is defined with the values at the corner nodes ν_1, ν_2 and ν_3 as follows:

$$\nu_e = \frac{1}{1/\nu_1+1/\nu_2+1/\nu_3} = \frac{\nu_1\nu_2\nu_3}{\nu_1\nu_2+\nu_2\nu_3+\nu_3\nu_1} \qquad (2.6.32)$$

The control volume is surrounded by the lines connecting central points of sides and the weighting point of a triangle as illustrated in the figure 2.12. The subscripts of the nodes are defined counterclockwise, where the point $1i$ is the node representing the control volume. The basic equation is integrated in the control volume, which has been originally proposed by Winslow [2-9], for deriving a discrete equation. A triangular element contains parts of a control volume and its boundaries. (See the figure 2.12.) The discretized equation is derived by summing up the contribution of each element to the integral in a control volume, as described in the following subsections.

2.6.2.3. Formulation with linear interpolating function

For applying the weighted residual method, a basic equation is defined as follows:

$$R(A) \equiv -R^*(A) = -\frac{\partial}{\partial x}\left[\nu_y \frac{\partial A}{\partial x} - \sigma v_x A\right] - \frac{\partial}{\partial y}\left[\nu_x \frac{\partial A}{\partial y}\right] + \sigma \frac{\partial A}{\partial t} - J_0 \tag{2.6.33}$$

The equation (2.6.33) is multiplied by the same step- weighting function as in the equation (2.5.18). The complete implicit method will be applied concerning the time differential also in this case.

$$\frac{1}{\Delta t}\int_t^{t+\Delta t} \iint_{in\ a\ C.V.} R(A)\ dx\,dy\ d\tau = 0 \tag{2.6.33'}$$

When the following vector $\psi \equiv (\psi_x, \psi_y)^t$ is defined:

$$\psi_x \equiv \nu_y \frac{\partial A}{\partial x} = \nu_y \beta$$

$$\psi_y \equiv \nu_x \frac{\partial A}{\partial y} = \nu_x \gamma$$

the integral is written by supplying the Gauss' divergence theorem as follows:

$$\frac{1}{\Delta t}\int_t^{t+\Delta t} \iint_{in\ a\ C.V.} \left\{-\frac{\partial}{\partial x}\left[\nu_y \frac{\partial A}{\partial x}\right] - \frac{\partial}{\partial y}\left[\nu_x \frac{\partial A}{\partial y}\right]\right\} dx\,dy\ d\tau$$

$$= \iint_{in\ a\ C.V.} \nabla \cdot \psi\ dx\,dy$$

$$= -\int_C \psi \cdot \mathbf{n}\ dC \tag{2.6.34}$$

See the figure 2.14. Hence:

$$-\int_{L\to G\to R} \psi \cdot \mathbf{n}\ dC = -\int_{L\to G\to R} \psi_x\ dy - \int_{L\to G\to R} \psi_y\ dx$$

$$= -\int_{\frac{y_1+y_2}{2}}^{\frac{y_1+y_2}{2}} \nu_y \beta\ dy + \int_{\frac{x_1+x_2}{2}}^{\frac{x_1+x_3}{2}} \nu_x \gamma\ dx$$

$$= -\frac{\nu_y \beta (y_3 - y_2)}{2} + \frac{\nu_x \gamma (x_3 - x_2)}{2} \tag{2.6.35}$$

$$\frac{1}{\Delta t}\int_t^{t+\Delta t} \iint_{in\ a\ C.V.} \frac{\partial}{\partial x}(\sigma v_x A)\ dx\,dy\ d\tau = \iint_{in\ a\ C.V.} \sigma v_x \beta\ dx\,dy$$

$$= \sigma v_x \beta \cdot \frac{S}{3} \tag{2.6.36}$$

$$\frac{1}{\Delta t}\int_t^{t+\Delta t} \iint_{in\ a\ C.V.} \sigma \frac{\partial A}{\partial t}\ dx\,dy\ d\tau = \sigma \frac{(A_1 - A_1^0)}{\Delta t} \cdot \frac{S}{3} \tag{2.6.37}$$

$$\frac{1}{\Delta t}\int_{t}^{t+\Delta t}\iint_{in\ a\ C.V.} -J_0\,dx\,dy\,d\tau = -J_0\frac{S}{3} \tag{2.6.38}$$

The following relation is obtained by substituting the equations (2.6.35), (2.6.36), (2.6.37) and (2.6.38) into the equation (2.6.34).

$$\left[\frac{\nu_y\beta_1^2}{4S}+\frac{\nu_x\gamma_1^2}{4S}+\frac{\sigma v_x\beta_1}{6}+\frac{\sigma S}{3\Delta t}\right]A_1+\left[\frac{\nu_y\beta_1\beta_2}{4S}+\frac{\nu_x\gamma_1\gamma_2}{4S}+\frac{\sigma v_x\beta_2}{6}\right]A_2+\left[\frac{\nu_y\beta_1\beta_3}{4S}+\frac{\nu_x\gamma_1\gamma_3}{4S}+\frac{\sigma v_x\beta_3}{6}\right]A_3$$

$$=\frac{\sigma S}{3\Delta t}A_1^0+\frac{J_0S}{3} \tag{2.6.39}$$

The same equation as (2.6.22) is obtained by summing up all the elements around the node one. The global coefficient matrix can be obtained in the same way as an ordinary FEM.

2.6.2.4. Formulation considering effects of the velocity terms

2.6.2.4.1. Coordinates transformation

It is impossible to formulate directly the eddy current problem in which conductors have speeds in arbitrary directions. On the other hand, the flexibility of the analysis is required for general applications. With the contradicting requirement into mind, the local coordinates transformation is introduced so that the X-axis in an element may always be in the same direction as the local speed.

When the speed on the central node of a control volume is $\mathbf{v} = (v_x, v_y)^t$, the amplitude and the angle are defined: $\sqrt{v_x^2+v_y^2} \equiv V$, $\cos\theta = \frac{v_x}{V}$, and $\sin\theta = \frac{v_y}{V}$, in the case of $V \neq 0$. The local coordinates $[X,\ Y]^t$ is defined as follows:

$$\begin{bmatrix} X \\ Y \end{bmatrix} \equiv \begin{bmatrix} \cos\theta & \sin\theta \\ -\sin\theta & \cos\theta \end{bmatrix}\begin{bmatrix} x \\ y \end{bmatrix} \tag{2.6.40}$$

The reluctivity tensor is also transformed as follows:

$$\nu' = \begin{bmatrix} \cos\theta & \sin\theta \\ -\sin\theta & \cos\theta \end{bmatrix}\begin{bmatrix} \nu_x & 0 \\ 0 & \nu_y \end{bmatrix}\begin{bmatrix} \cos\theta & -\sin\theta \\ \sin\theta & \cos\theta \end{bmatrix}$$

$$= \begin{bmatrix} \nu_x\cos^2\theta+\nu_y\sin^2\theta & (\nu_y-\nu_x)\sin\theta\cos\theta \\ (\nu_y-\nu_x)\sin\theta\cos\theta & \nu_x\sin^2\theta+\nu_y\cos^2\theta \end{bmatrix} \equiv \begin{bmatrix} \nu_X & \nu_{XY} \\ \nu_{XY} & \nu_Y \end{bmatrix} \tag{2.6.41}$$

With the transformed reluctivity tensor, the following basic equation in the new local coordinates is derived.

$$\frac{\partial}{\partial X}\left[\nu_Y\frac{\partial A}{\partial X}-\sigma VA-2\nu_{XY}\frac{\partial A}{\partial Y}\right]+\frac{\partial}{\partial Y}\left[\nu_X\frac{\partial A}{\partial Y}\right]-\sigma\frac{\partial A}{\partial t} = -J_0 \tag{2.6.42}$$

2.6.2.4.2. Exponential interpolating function

In the same way as the equation (2.4.24), the following differential equation is introduced.

$$\sigma VA - \nu_Y \frac{\partial A}{\partial X} = 0 \tag{2.6.43}$$

The solution of this is used for the following definition of an interpolating function in an element.

$$A = A_0 \, e^{\frac{\sigma V}{\nu_Y} X} \tag{2.6.44}$$

The following interpolating function is assumed.

$$A_{inner} = \alpha' + \beta' \exp\frac{\sigma V}{\nu_Y} X + \gamma' Y \tag{2.6.45}$$

In the same way as the subsection 2.6.1.1., the following relations are derived:

$$A_{inner} = \sum_{s=1}^{3} \zeta'_s A_s \tag{2.6.46}$$

$$\zeta'_s = \frac{\left[\alpha'_s + \beta'_s \exp\frac{\sigma V}{\nu_Y} + \gamma'_s Y\right]}{2S'} \tag{2.6.47}$$

$$2S' = \alpha'_1 + \alpha'_2 + \alpha'_3 \tag{2.6.48}$$

$$S \equiv \frac{\left[X_2 Y_3 - X_3 Y_2 + X_3 Y_1 - X_1 Y_3 + X_1 Y_2 - X_2 Y_1\right]}{2} \tag{2.6.49}$$

$S \neq S'$ when $V \neq 0$

$$\alpha'_1 = e^{\frac{\sigma V}{\nu_Y} X_2} Y_3 - e^{\frac{\sigma V}{\nu_Y} X_3} Y_2 \qquad \alpha'_2 = e^{\frac{\sigma V}{\nu_Y} X_3} Y_1 - e^{\frac{\sigma V}{\nu_Y} X_1} Y_3 \qquad \alpha'_3 = e^{\frac{\sigma V}{\nu_Y} X_1} Y_2 - e^{\frac{\sigma V}{\nu_Y} X_2} Y_1$$

$$\beta'_1 = Y_2 - Y_3 \qquad \beta'_2 = Y_3 - Y_1 \qquad \beta'_3 = Y_1 - Y_2$$

$$\gamma'_1 = e^{\frac{\sigma V}{\nu_Y} X_3} - e^{\frac{\sigma V}{\nu_Y} X_2} \qquad \gamma'_2 = e^{\frac{\sigma V}{\nu_Y} X_1} - e^{\frac{\sigma V}{\nu_Y} X_3} \qquad \gamma'_3 = e^{\frac{\sigma V}{\nu_Y} X_2} - e^{\frac{\sigma V}{\nu_Y} X_1} \tag{2.6.50}$$

$$\alpha' = \frac{\alpha'_1 A_1 + \alpha'_2 A_2 + \alpha'_3 A_3}{2S'} \tag{2.6.51.a}$$

$$\beta' = \frac{\beta'_1 A_1 + \beta'_2 A_2 + \beta'_3 A_3}{2S'} \tag{2.6.51.b}$$

$$\gamma' = \frac{\gamma'_1 A_1 + \gamma'_2 A_2 + \gamma'_3 A_3}{2S'} \tag{2.6.51.c}$$

2.6.2.4.3. Discretized equation in the C. V.

In the same way as the section 2.6.2.3., the following basic equation is integrated:

$$R'(A) = -\frac{\partial}{\partial X}\left[\nu_Y\frac{\partial A}{\partial X}-\sigma VA-2\nu XY\frac{\partial A}{\partial Y}\right]-\frac{\partial}{\partial Y}\left[\nu_x\frac{\partial A}{\partial Y}\right]+\sigma\frac{\partial A}{\partial t}-J_0 \qquad (2.6.52)$$

as written in the equation (2.6.53):

$$\frac{1}{\Delta t}\int_t^{t+\Delta t}\iint_{in\ a\ C.V.} R'(A)\,dx\,dy\,d\tau = 0 \qquad (2.6.53)$$

When the following vector $\psi \equiv (\psi_x, \psi_y)^t$ is defined as follows:

$$\psi_X = \nu_Y\frac{\partial A}{\partial X}-\sigma VA-2\nu_{XY}\frac{\partial A}{\partial Y}$$

$$= -\left[\sigma V\alpha' + 2\nu_{XY}\gamma'\right]-\sigma V\gamma' Y \qquad (2.6.54)$$

$$\psi_Y = \nu_X\frac{\partial A}{\partial Y} = \nu_X\gamma' \qquad (2.6.55)$$

the integral is calculated with the following simple form.

$$\frac{1}{\Delta t}\int_t^{t+\Delta t}\iint_{in\ a\ C.V.}\left\{-\frac{\partial}{\partial x}\left[\nu_Y\frac{\partial A}{\partial x}-\sigma VA-2\nu_{XY}\frac{\partial A}{\partial Y}\right]-\frac{\partial}{\partial Y}\left[\nu_X\frac{\partial A}{\partial Y}\right]\right\}dX\,dY\,d\tau$$

$$= -\iint_{in\ a\ C.V.}\nabla\cdot\psi\,dX\,dY$$

$$= -\int_{L\to G\to R}\psi\cdot\mathbf{n}\,dC$$

$$= -\int_{\frac{Y_1+Y_2}{2}}^{\frac{Y_1+Y_3}{2}}\left\{-\left[\sigma V\alpha'+2\nu_{XY}\gamma'\right]-\sigma V\gamma' Y\right\}dY+\int_{\frac{X_1+X_2}{2}}^{\frac{X_1+X_3}{2}}\nu_X\gamma'\,dX$$

$$= \left[\sigma V\alpha'+2\nu_{XY}\gamma'\right]\frac{Y_3-Y_2}{2}+\sigma V\gamma'\frac{\left[2Y_1+Y_2Y_3\right]\left[Y_3-Y_2\right]}{4}+\frac{\nu_X\gamma'\left[X_3-X_2\right]}{2} \qquad (2.6.56)$$

The magnetic reluctivity in ordinary conductors is often homogeneous, therefore, $\nu_X=\nu_Y=\nu$ and $\nu_{XY}=0$ are assumed in the following discussion. Hence, the following simpler expression is obtained from the previous equation.

$$(2.6.56) = \frac{\left[Y_3-Y_2\right]\sigma V}{2}\alpha' + \frac{\sigma V\left[2Y_1+Y_2Y_3\right]\left[Y_3-Y_2\right]+2\nu\left[X_3-X_2\right]}{4}\gamma' \qquad (2.6.57)$$

The other terms can be calculated in the same way as the equations (2.6.37) and

(2.6.38).

$$\frac{1}{\Delta t}\int_{t}^{t+\Delta t}\iint_{in\ a\ C.V.}\sigma\frac{\partial A}{\partial t}\,dX\,dY\,d\tau=\sigma\frac{\left[A_1-A_1^0\right]}{\Delta t}\cdot\frac{S}{3} \tag{2.6.58}$$

$$\frac{1}{\Delta t}\int_{t}^{t+\Delta t}\iint_{in\ a\ C.V.}-J_0\,dX\,dY\,d\tau=-J_0\cdot\frac{S}{3} \tag{2.6.59}$$

Finally, the following discrete equation for a node in an triangular element is derived by substituting the equations (2.6.57), (2.6.58) and (2.6.59) into the equation (2.6.53).

$$a_1A_1+a_2A_2+a_3A_3=b \tag{2.6.60}$$

where

$$a_1=\frac{\sigma V\left[Y_3-Y_2\right]\left\{2\alpha'_1+\left[2Y_1+Y_2+Y_3\right]\gamma'_1\right\}+2\nu\left[X_3-X_2\right]\gamma'_1}{8S'}+\frac{\sigma S}{3\Delta t} \tag{2.6.61}$$

$$a_2=\frac{\sigma V\left[Y_3-Y_2\right]\left\{2\alpha'_2+\left[2Y_1+Y_2+Y_3\right]\gamma'_2\right\}+2\nu\left[X_3-X_2\right]\gamma'_2}{8S'}+\frac{\sigma S}{3\Delta t} \tag{2.6.62}$$

$$a_3=\frac{\sigma V\left[Y_3-Y_2\right]\left\{2\alpha'_3+\left[2Y_1+Y_2+Y_3\right]\gamma'_1\right\}+2\nu\left[X_3-X_2\right]\gamma'_3}{8S'}+\frac{\sigma S}{3\Delta t} \tag{2.6.63}$$

$$b=\frac{J_0+\sigma A_1^0/\Delta t}{3}S \tag{2.6.64}$$

The global coefficient matrix can be composed in the same way as an ordinary FEM.

2.6.2.5. Stationary state

For a stationary field analysis using $e^{j\omega t}$, the following parts are substituted in the previous equations.

$$\dot{a}_1\dot{A}_1+a_2\dot{A}_2+a_3\dot{A}_3=\dot{b} \tag{2.6.60'}$$

$$\dot{a}_1=\frac{\sigma V\left[Y_3-Y_2\right]\left\{2\alpha'_1+\left[2Y_1+Y_2+Y_3\right]\gamma'_1\right\}+2\nu\left[X_3-X_2\right]\gamma'_1}{8S'}+\frac{j\omega\sigma}{3}S \tag{2.6.61'}$$

$$\dot{b}=\frac{\dot{J}_0S}{3} \tag{2.6.64'}$$

2.7. Multi-terminal modeling of an asymmetrical LIM with a finite length

2.7.1. Basic principle

In order to investigate a relation between terminal voltages and line currents of a n-phase motor with asymmetric impedances generally, discussions based on a 2n-terminal network system is necessary, considering remarkable electromagnetic interferences between each phase.

For instance, a behavior of a three- phase motor on an operating point with a neutral point connection is modeled as a six- terminal network system shown in the figure 2.15. (a). Terminal-voltage- and line-current- vectors are defined as follows:

$$\dot{\mathbf{V}} = \left[\dot{V}_1,\ \dot{V}_2\ ,\ \ldots\ ,\ \dot{V}_n\right]^t \tag{2.7.1}$$

$$\dot{\mathbf{I}} = \left[\dot{i}_1,\ \dot{i}_2\ ,\ \ldots\ ,\ \dot{i}_n\right]^t \tag{2.7.2}$$

With the impedance matrix defined in the equation (2.7.3),

$$\dot{\mathbf{Z}} \equiv \begin{bmatrix} \dot{Z}_{1,1} & \cdots & \dot{Z}_{1,n} \\ \cdot & \cdots & \cdot \\ \cdot & \cdots & \cdot \\ \cdot & \cdots & \cdot \\ \dot{Z}_{n,1} & \cdots & \dot{Z}_{n,n} \end{bmatrix} \tag{2.7.3}$$

the voltage equations are written as follows:

$$\dot{\mathbf{V}} = \dot{\mathbf{Z}} \cdot \dot{\mathbf{I}} \tag{2.7.4}$$

where the motor's characteristics are ideally linear and a constant velocity of the secondary plate is given.

For a numerical simulation of a voltage source drive using a field-analysis program with current sources, the field distribution should be calculated with the following input-current vectors.

$$\dot{\mathbf{I}}_1 = \left[1.0e^{j0},\ 0,\ 0,\ \ldots\ ,\ 0\right]^t \tag{2.7.5}$$

$$\dot{\mathbf{I}}_2 = \left[0,\ 1.0e^{j0},\ 0,\ 0,\ \ldots\ ,\ 0\right]^t \tag{2.7.6}$$

$$\ldots\ \ldots\ \ldots\ \ldots\ \ldots\ \ldots$$

$$\dot{\mathbf{I}}_n = \left[0,\ 0,\ 0,\ 0,\ \ldots\ ,1.0e^{j0}\right]^t \tag{2.7.7}$$

Using resultant induced terminal voltages, the impedance matrix (2.7.2) can be determined. The admittance matrix is calculated by inversing the impedance matrix. Finally, the line currents corresponding to the given voltages are derived,

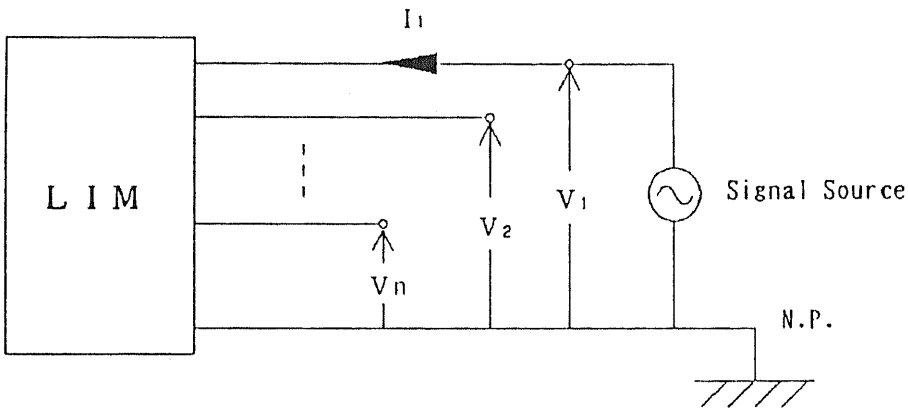

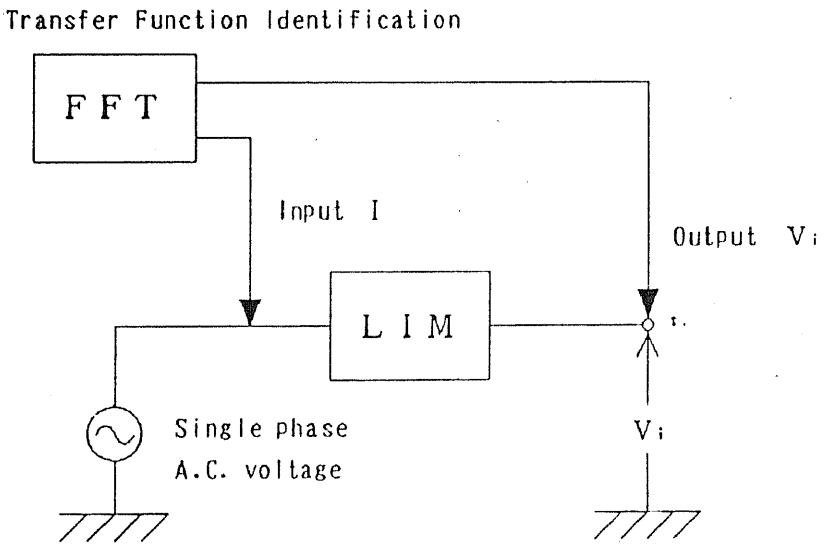

Figure 2.16. Impedance measurement with a single phase signal source.

and the field with voltage sources is calculated again much faster than the first analysis based on the superposition principle of a linear system.

In the case of impedance measurements, the same procedures should be applied with a single phase drive as shown in the figure 2.16.

If there is no neutral point connection like the figure 2.15. (b), *i.e.*, each line current is constrained by the Kirchhoff's first law, the motor should be treated as a four-terminal network — generally, as a 2(n-1) terminal network — due to less system freedom.

2.7.2. Physical meaning of the impedance matrix — Energy flow in a single phase drive

The energy flow in a motor is written as follows.

$$P_1 = P_{mech} + P_{loss} \tag{2.7.8}$$

Since the voltage between the terminal i and the neutral point is written from the equation (2.7.4) as follows,

$$\dot{V}_i = \sum_{j=1}^{n} \dot{Z}_{ij} \dot{i}_j \tag{2.7.9}$$

where $i = 1, 2, \ldots, n$. The average power put into the primary windings is written as follows.

$$\begin{aligned} P_1 &= \frac{1}{2} \mathrm{Re} \left[\sum_{i=1}^{n} \dot{V}_i \cdot \dot{I}_i^* \right] \\ &= \frac{1}{2} \sum_{i=1}^{n} \sum_{j=1}^{n} \mathrm{Re} \left[\dot{Z}_{ij} \cdot \dot{I}_j \cdot \dot{I}_i^* \right] \end{aligned} \tag{2.7.10}$$

I define a factor in the impedance matrix as $\dot{Z}_{ij} \equiv R_{ij} + j\omega L_{ij}$ here.

In a particular case †), where only a single phase AC current $\dot{I}_1$ is applied, as shown in the figure 2.16, *i.e.*, corresponding to the cases of the equation (2.7.4),

$$P_1 = \frac{1}{2} \mathrm{Re} \left[\dot{Z}_{11} \cdot \dot{I}_1 \cdot \dot{I}_1^* \right]$$

†) *T. Koseki and Hardo May* have compared their calculations at the TU Braunschweig, especially concerning a physical energy flow of a LIM, in the case of the equation (2.7.11). The two calculated results have agreed each other quite well based on the equation (2.7.12). The details will be described in the section 3.2.4.

$$= \frac{1}{2} |\dot{I}_1|^2 \cdot \mathrm{Re}\left[\dot{Z}_{11}\right]$$

$$= I_{1rms}^2 \cdot R_{11}. \qquad (2.7.11)$$

From the equations (2.7.4) and (2.7.6), the following equation is derived.

$$I_{1rms}^2 \cdot R_{11} = P_{loss} - F_{brake} \cdot v_2 \qquad (2.7.12)$$

In this way, it has been shown that the real parts of factors in an impedance matrix represent the energy flow in a motor. Some of them can be also negative in generator operations.

2.8. Three- phase serial- and parallel- connection

As written in the previous sections, impedances of a LIM can be described with an impedance matrix as a multi- terminal network in general. With this in mind, a concrete example is introduced in this section how to treat the serial- and parallel-connections with a LIM of twelve slots. Results of the calculations will be discussed in detail in the section 6.4.3.; the connections are illustrated in the figures 2.17.

The current vector **I**, the voltage vector **V** and the impedance matrix Z of the 24-terminal LIM of twelve slots are defined as follows:

$$\mathbf{I} \equiv \begin{bmatrix} \dot{i}_1 \\ \dot{i}_2 \\ \cdot \\ \cdot \\ \cdot \\ \dot{i}_{12} \end{bmatrix} \quad \mathbf{V} \equiv \begin{bmatrix} \dot{V}_1 \\ \dot{V}_2 \\ \cdot \\ \cdot \\ \cdot \\ \dot{V}_{12} \end{bmatrix} \quad Z = \begin{bmatrix} \dot{Z}_{1,1}, \ldots, \dot{Z}_{1,12} \\ \cdot \quad \cdot \quad \cdot \\ \cdot \quad \cdot \quad \cdot \\ \cdot \quad \cdot \quad \cdot \\ \dot{Z}_{12,1}, \ldots, \dot{Z}_{12,12} \end{bmatrix} \qquad (2.8.1)$$

The voltage equations are written with the vectors and the impedance matrix as follows:

$$\mathbf{V} = Z\,\mathbf{I} \qquad (2.8.2)$$

In the same way, the current- and voltage- vectors and the impedance matrix of the three- phase system are:

$$\mathbf{I}_{III} \equiv \begin{bmatrix} \dot{i}_1^{III} \\ \dot{i}_2^{III} \\ \dot{i}_3^{III} \end{bmatrix} \quad \mathbf{V}_{III} \equiv \begin{bmatrix} \dot{V}_1^{III} \\ \dot{V}_2^{III} \\ \dot{V}_3^{III} \end{bmatrix} \quad Z_{III} \equiv \begin{bmatrix} \dot{Z}_{1,1}^{III} & \dot{Z}_{1,2}^{III} & \dot{Z}_{1,3}^{III} \\ \dot{Z}_{2,1}^{III} & \dot{Z}_{2,2}^{III} & \dot{Z}_{2,3}^{III} \\ \dot{Z}_{3,1}^{III} & \dot{Z}_{3,2}^{III} & \dot{Z}_{3,3}^{III} \end{bmatrix} \qquad (2.8.3)$$

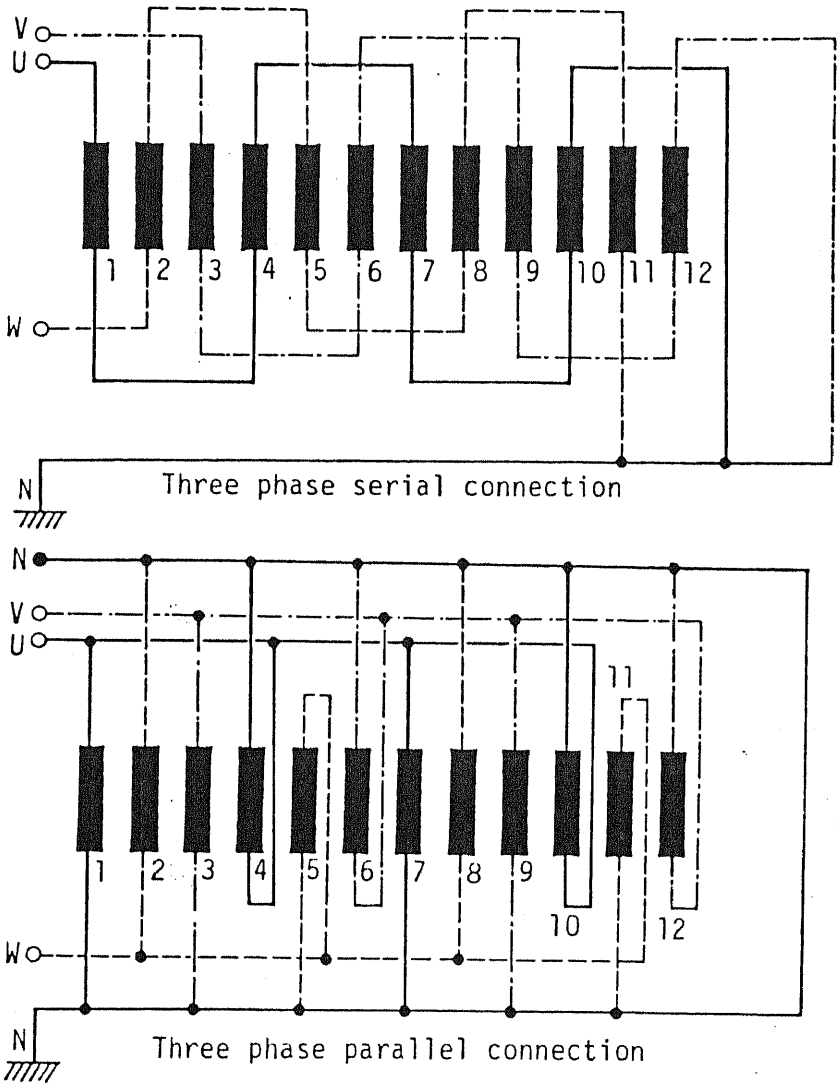

Figure 2.17. An example of a three- phase serial- and parallel- connections.

The voltage equations of the three- phase system are summarized in the following form:

$$\mathbf{V}_{III} = Z_{III}\,\mathbf{I}_{III} \tag{2.8.4}$$

The following connection 3×12 matrix is introduced for a description of the relation between the 24-terminal- and the three-phase- systems.

$$T \equiv \begin{bmatrix} 1 & 0 & 0 & -1 & 0 & 0 & 1 & 0 & 0 & -1 & 0 & 0 \\ 0 & 0 & 1 & 0 & 0 & -1 & 0 & 0 & 1 & 0 & 0 & -1 \\ 0 & -1 & 0 & 0 & 1 & 0 & 0 & -1 & 0 & 0 & 1 & 0 \end{bmatrix} \tag{2.8.5}$$

Serial connection

The current vectors are transformed with the connection matrix in the case of the serial connection illustrated in the figure 2.17 (a) as follows.

$$\mathbf{I} = T^t\,\mathbf{I}_{III} \tag{2.8.6}$$

$$\mathbf{V} = Z\,\mathbf{I}_{III} = Z\,T^t\,\mathbf{I}_{III} \tag{2.8.7}$$

Hence, the three- phase impedance matrix is calculated from the 24-terminal impedance matrix as follows:

$$\mathbf{V}_{III} = T\,\mathbf{V} = T\,Z\,T^t\,\mathbf{I}_{III} \tag{2.8.8}$$

$$Z_{III} = T\,Z\,T^t \tag{2.8.9}$$

$$\underset{\begin{bmatrix}1\le i\le 3\\ 1\le j\le 3\end{bmatrix}}{\dot{Z}_{ij}^{III}} = \sum_{l=1}^{12}\sum_{k=1}^{12} t_{il}\cdot\dot{Z}_{lk}\cdot t_{jk} \tag{2.8.10}$$

The three- phase currents are calculated by solving the three voltage equations as follows:

$$\mathbf{I}_{III} = Z_{III}^{-1}\,\mathbf{V}_{III} \tag{2.8.11}$$

The current of each slot is consequently calculated as follows:

$$\mathbf{I} = T^t\,\mathbf{I}_{III} \tag{2.8.12}$$

That is to say:

$$\underset{(1\le i\le 12)}{i_i} = \sum_{j=1}^{3} t_{ji}\cdot i_j^{III} \tag{2.8.13}$$

Parallel connection

In the case of the parallel connection illustrated in the figure 2.17. (b), you must solve the twelve voltage equations.

$$\mathbf{I}_{III} = T\,\mathbf{I} \tag{2.8.14}$$

$$\mathbf{V} = T^t\,\mathbf{V}_{III} \tag{2.8.15}$$

$$\mathbf{I} = Z^{-1}\,\mathbf{V} = Z^{-1}\,T^t\,V_{III} \tag{2.8.16}$$

The following three- phase input currents are calculated finally.

$$\mathbf{I}_{III} = T\,\mathbf{I} \tag{2.8.17}$$

$$i_i^{III} = \sum_{j=1}^{12} T_{ij} \cdot i_j \tag{2.8.18}$$

2.9. Voltage source transient simulation — solution of voltage equations with a transition matrix

For a transient analysis, the impedance matrix $\dot{Z}$ in the equation (2.7.3) is separated into the real- and imaginary- parts: $\dot{Z} = R + j\omega L$. The transient voltage equation is written with them as follows:

$$\mathbf{V} = L\left[\frac{d}{dt}\mathbf{I}\right] + R\,\mathbf{I}. \tag{2.9.1}$$

The inductance- and resistance- matrices are ideally constant, *i.e.*, independent of operations, if the machine had no end-effect. On the other hand, in the case of a real LIM of a finite length, which has a considerable end-effect, the impedance depends strongly on the operation, especially, on the secondary velocity. The matrices must, therefore, be written as time-dependent ones, *i.e.*, as $L_{(t)}$ and $R_{(t)}$.

From the equation (2.7.4), the voltage equation can be written as a first order ordinary differential equation of matrices:

$$\frac{d}{dt}\mathbf{I} = A_{(t)} \cdot \mathbf{I} + \mathbf{f}_{(t)} \tag{2.9.2}$$

where

$$A_{(t)} \equiv -L_{(t)}^{-1} \cdot R_{(t)}$$

$$\mathbf{f}_{(t)} = L_{(t)}^{-1} \cdot \mathbf{V}_{(t)}.$$

($A_{(t)}$: System matrix; $\mathbf{f}_{(t)}$: Input vector)

According to the theory of linear systems, the input current $\mathbf{I}_{(t)}$ on a voltage source transient drive is soluted using a transition matrix $\Phi_{(t,\,t')}$ of a linear homogeneous differential equation $\dot{\mathbf{x}} = A_{(t)} \cdot \mathbf{x}_{(t)}$ and an initial time t_0 as follows:

$$\mathbf{I}_{(t)} = \Phi_{(t,t_0)} \cdot \mathbf{I}_{(t_0)} + \int_{t_0}^{t} \Phi_{(t,\tau)} \cdot \mathbf{f}_{(\tau)}\, d\tau. \tag{2.9.3}$$

It, however, is so complicated to calculate numerically the $R_{(t)}$ and $L_{(t)}$ in the concrete by iterative algorithm of mechanical- and electromagnetic- analyses, that I assume a current- source drive in transient investigations of this research.

References

[2-1] P.P. Silvester and R.L. Ferrari: "Finite Element for Electrical Engineers", Cambridge University Press, 1983

[2-2] B. A. Finlayson: "The Method of Weighted Residuals and Variational Principles", Academic, New York, 1972

[2-3] S. V. Patanker: "Numerical Heat Transfer and Fluid Flow", Hemisphere Publishing Co., 1980

[2-4] The Mathematical Basis of PHOENICS-EARTH Computer Code, CHAM Ltd., 1981

[2-5] D. B. Spalding: "A Novel Finite-Difference Formulation for Differential Expressions Involving Both First and Second Derivatives, Int. J. Num. Methods Eng., Vol. 4, P. 551, 1972

[2-6] A. D. Gosman, W. M. Pun, A. K. Runchal, D. B. Spalding and M. Wolfshtein: "Heat and Mass Transfer in Recirculating Flows, Academic, New York, 1969

[2-7] H. May, W. Schmid und H. Weh: "Numerische Magnetfeldberechnung durch Diskretisierungsverfahren", Archiv für Elektrotechnik 69 (1986), pp.307-320, Springer-Verlag

[2-8] B. Heinrich: "Numerische Lösung eliptischer Differentialgleichungen mittels Diskretisierungsmethoden", Elektrie, Berlin 38 (1984) 7, pp. 251-253

[2-9] A.M. Winslow: "Numerical Solution of the Quasilinear Poisson Equation in a Nonuniform Triangle Mesh", Journal of Comp. Phys., vol. 1, p. 149

Chapter 3: Application of the analysis to a machine

Introduction

In the chapter 2, we saw the theoretical formulations for calculating electromagnetic phenomena in a LIM. To verify the theory, calculated results are compared with results derived with a classic machine theory, another numerical analysis based on the finite element method, and basic measurements. The studies were pursued under instruction of Professor Herbert Weh at the Technical University Braunschweig.

3.1. Model machine

I have built an experimental induction motor, whose secondary conductor is not a cage bar but an aluminum reaction plate, at the TU Braunschweig to verify the numerical calculations. The details of the measurements will be described in the section 3.5. The principal data of the machine are shown in the table 3.1, and the photograph is in the figure 3.1. The machine has totally 48 terminals; we can select four kinds of drives: four- pole- symmetric/ three- pole- asymmetric and six-phase/ three- phase- drives, by changing the connection from the outside. The structure of the winding is illustrated in the figure 3.2. I intended to simulate an asymmetric LIM drive with end-effects with the three- pole asymmetric operation, but the trial was not as successful as expected for the reasons described in the section 3.3.

For the comparison with a classic motor theory, the six- phase- four- pole symmetric drive is mainly discussed in the following section 3.2. The asymmetric drive is described in the section 3.3.

Table 3.1. Principal data of the experimental six- phase induction motor at the Technical University Braunschweig.

[STATOR]	
Phase number	6 (or 3)
Pole number	4 (or 3)
Conductors/ Phase /Pole	60 (or 120)
Outer diameter	340mm
Core width	240mm
Slot number	48
Pole pitch	188.50mm
Slot pitch	15.70mm
Slot width (exit)	2.3mm
Slot depth	27.7mm
[ROTOR]	
Core diameter	230mm
Rotor diameter with reaction plate	238mm
Mechanical gap length	1mm
Thickness of the reaction plate	4mm
Total gap length between cores	5mm
Core width	240mm
Overhang of the reaction plate	55mm

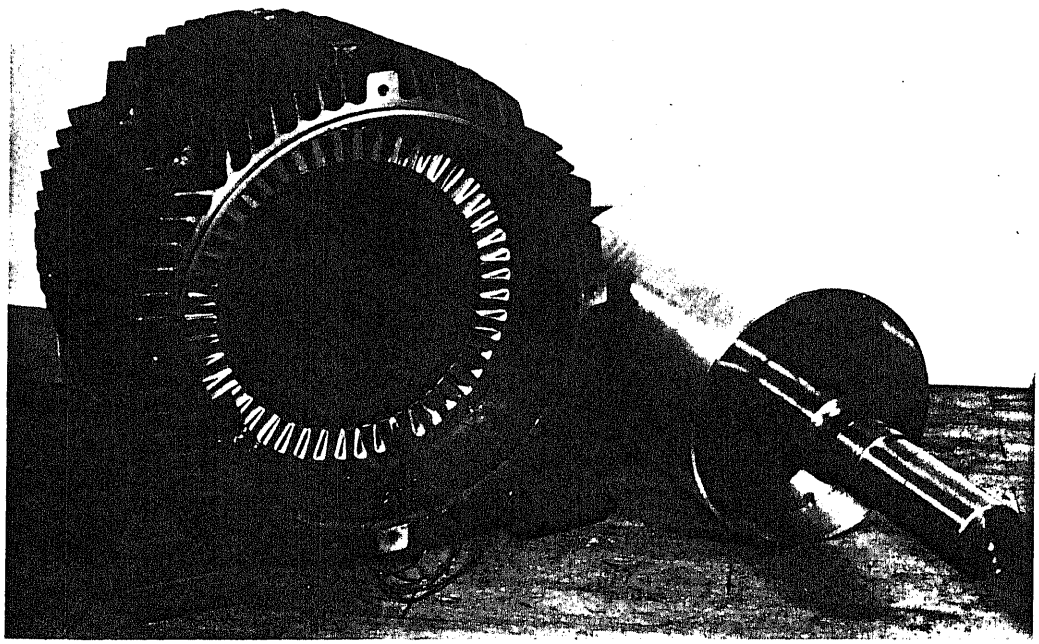

Figure 3.1. Experimental machine built at the TU Braunschweig.

3.2. Six- phase four- pole symmetric drive

3.2.1. Primary current vector loci [3-1] [3-2]

The complex admittances between the neutral point and a terminal are plotted in the figure 3.4 in the case of six- phase six- pole symmetrical drive where $f_1 = 30.0Hz$; it corresponds to the primary current vector loci where $V_{UN} = 1.0\,V$. It is generally known that the loci draw a circuit whose central point is on the imaginary axis in the case of $R_S = 0$ according to a conventional A.C.-motor theory. We can see that the calculated results are on a circle. Since the cross-section of the secondary aluminum reaction plate is much smaller than normal cage bars, the secondary resistance of the experimental machine is large, and the critical slip s_k is 1.0 (standstill state). We can identify constants in an equivalent circuit of an induction motor from the current vector loci as shown in the figure 3.5.

3.2.2. Comparison with classic analytical theory based on the equivalent current sheet method [3-2] [3-3]

In this subsection, I compare the calculated results with a simple conventional analytical field calculation (the current sheet method) based on the Ampere's law for verifying propriety of them. Along the path shown in the figure 3.6, the following basic equation is integrated:

$$\frac{\partial H}{\partial x} \cdot y_2 = A_s + A_r \tag{3.1}$$

where $A_r = -\sigma \cdot s \cdot v_1 y_1 B$. Details about formulations are neglected here [3-3], but the exciting current (the primary current on the no load operating point) is written as follows:

$$\begin{aligned} \hat{I}_{s0} &= \frac{p \times \pi \times \delta'' \times B_{\max|s=0}}{m_s \times N_{ph} \times \xi_s \times \mu_0} \\ &= \frac{2 \times \pi \times 5.13 \times 10^{-3} \times 0.44}{6 \times 240 \times 0.964 \times 4\pi \times 10^{-7}} \approx 8.1\ [A] \end{aligned} \tag{3.2}$$

where p is a pole-pair number, δ'' is an effective gap length, $B_{\max|s=0}$ is the maximum flux density in the gap in the no-load operation, m_s is a phase-number, N_{ph} is winding number per a phase, ξ_s is winding factor, μ_0 is a permeability of the space, $V_{UN|rms}$ is 354V, *i.e.*, $V_{UN|mag.} = 500\,V$, and the maximum magnetic flux density in the gap at the no-load operation is 0.44T from the figure 3.3.

On the other hand, the exciting current $\hat{I}_{s0}$ is calculated directly from the figure 3.4 as follows:

$$\hat{I}_{s0} = 0.016 \times \sqrt{2} \times 354 \approx 8.0\ [A]. \tag{3.3}$$

The result agrees with the calculation in the equation (3.2) well.

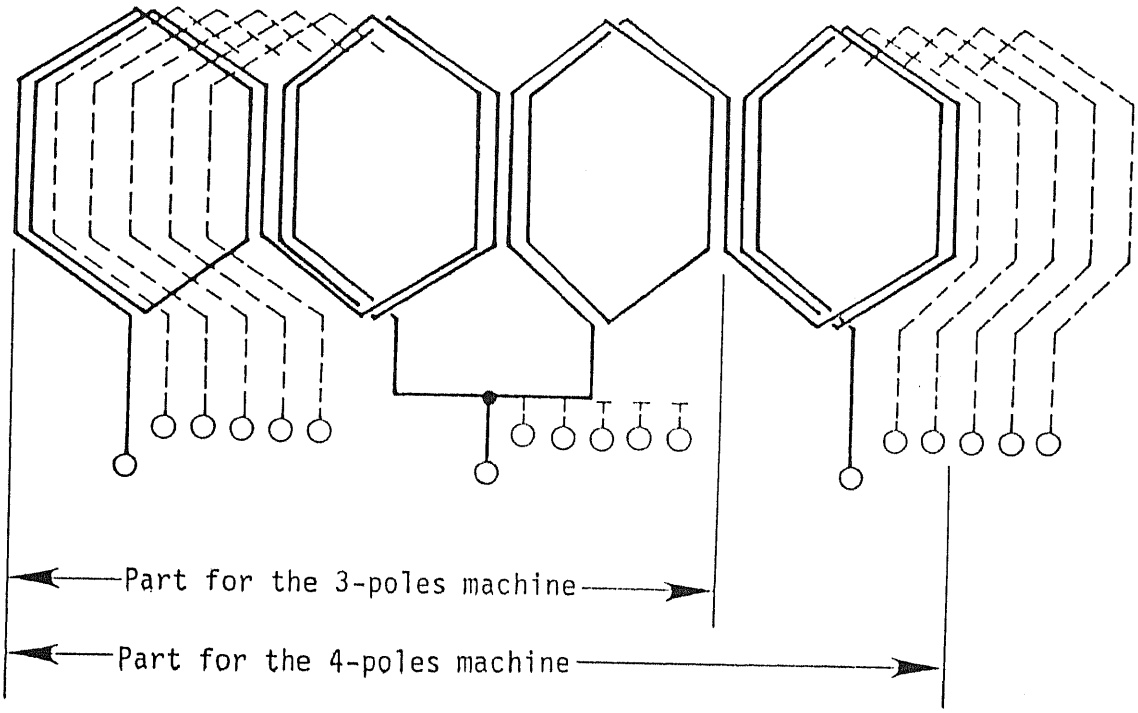

Figure 3.2. Structure of the windings.

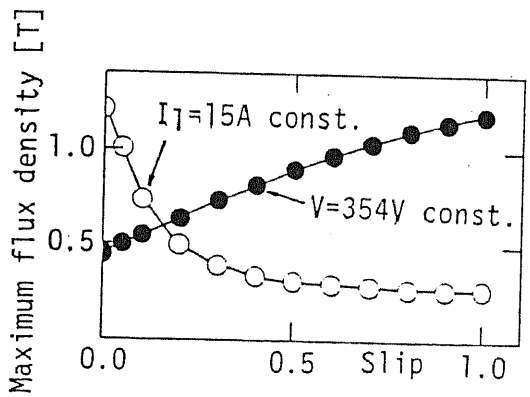

Figure 3.3. Maximum flux density in the gap in the six- phase four- pole symmetric drive (calculation).

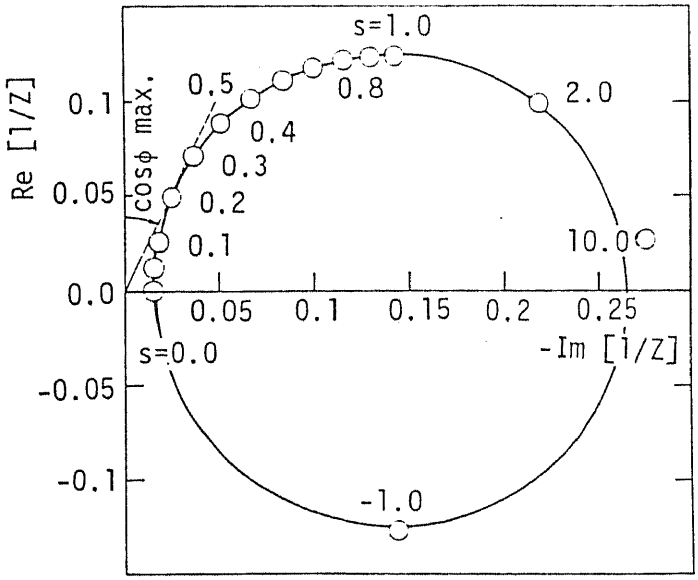

Figure 3.4. Primary current vector loci in the six- phase four- pole symmetric drive (calculation).

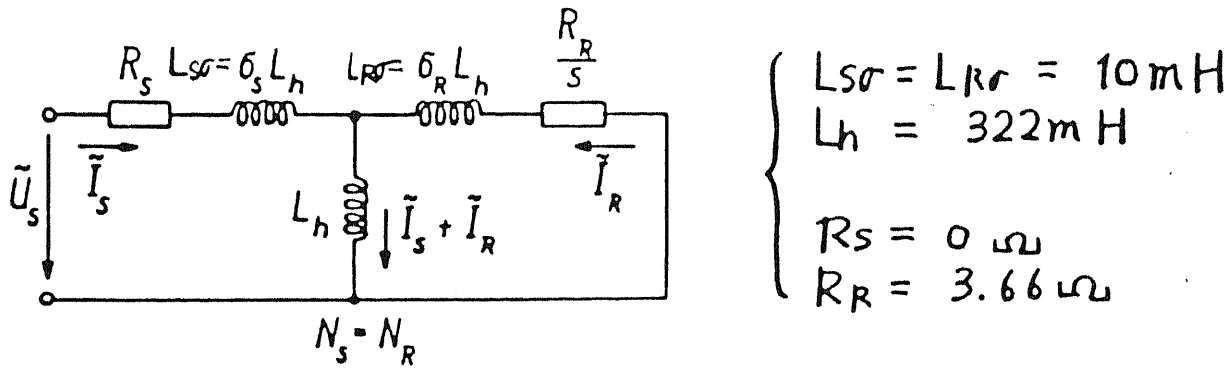

Figure 3.5. Equivalent circuit determined from the current vector loci.

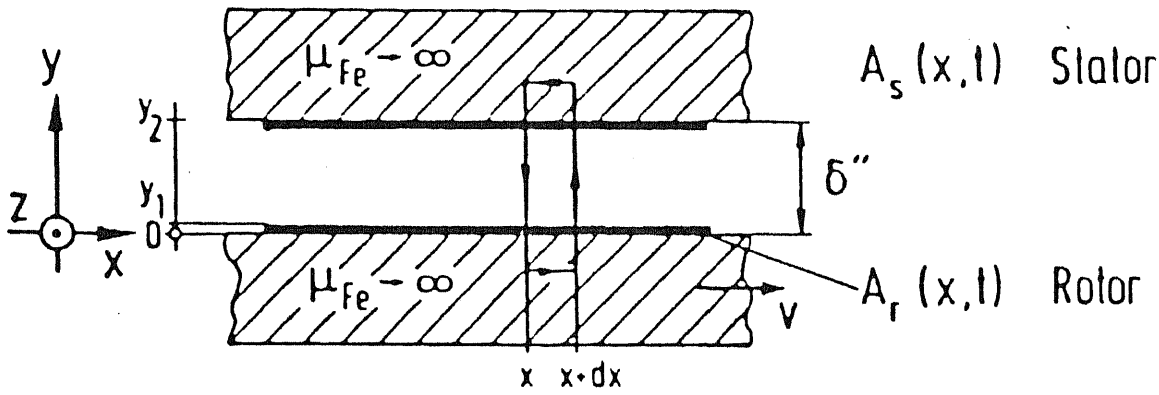

Figure 3.6. Classic analytical model of induction motor with current sheet.

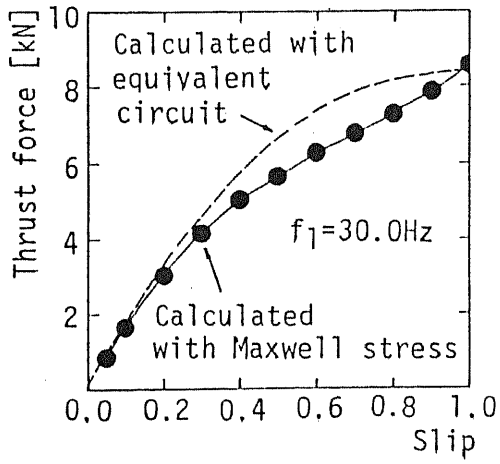

Figure 3.7. Slip characteristics of thrust force in the six- phase four- pole symmetric drive with a voltage source (V=354V const.).

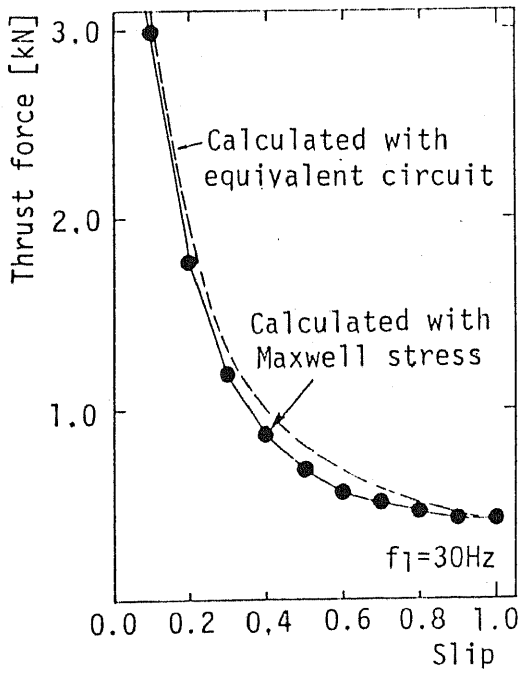

(a) Slip characteristics of thrust force in the six- phase four- pole symmetric drive with a current source (I=15A const.).

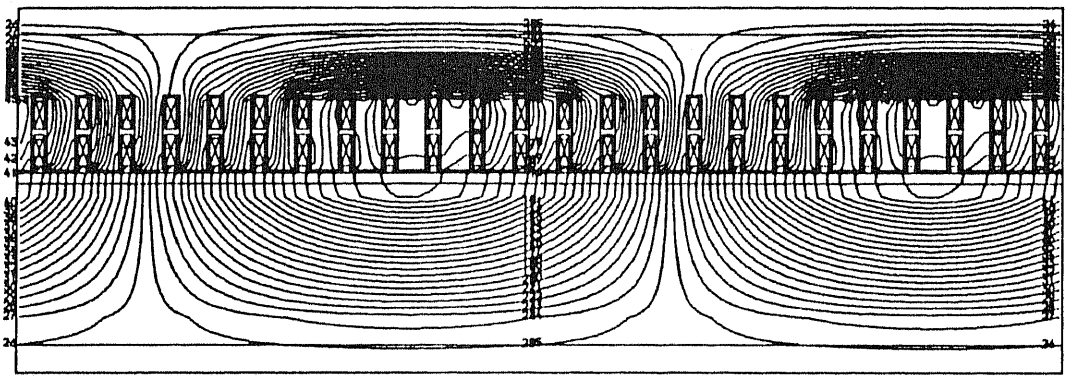

(b) Magnetic flux lines (Contour lines of magnetic vector potential)

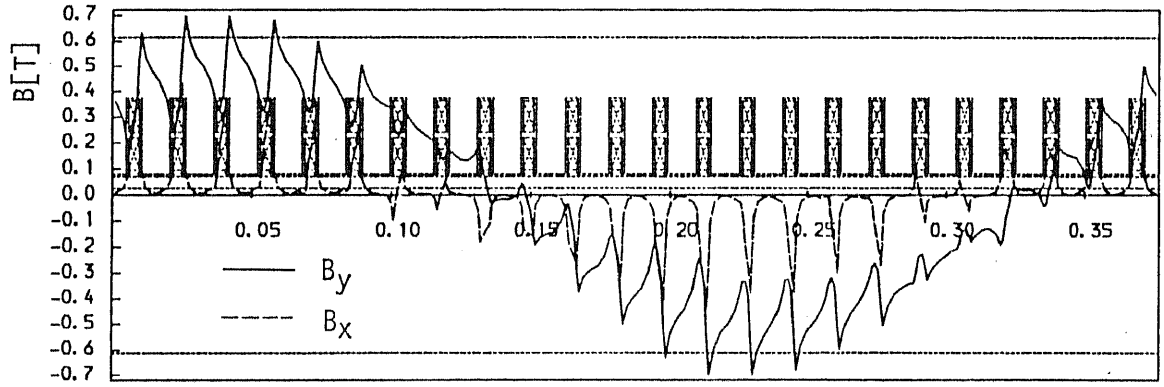

(c) Magnetic flux density in the gap (Instant value [T])

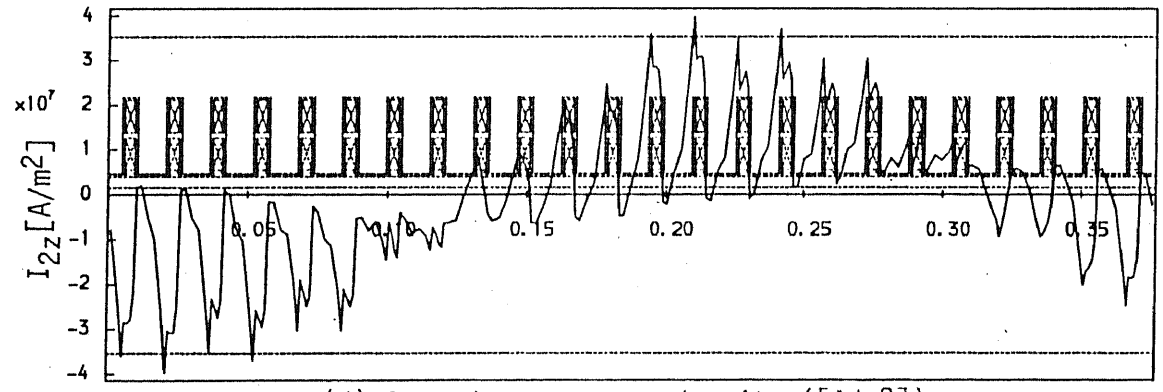

(d) Secondary current density ([A/m2])

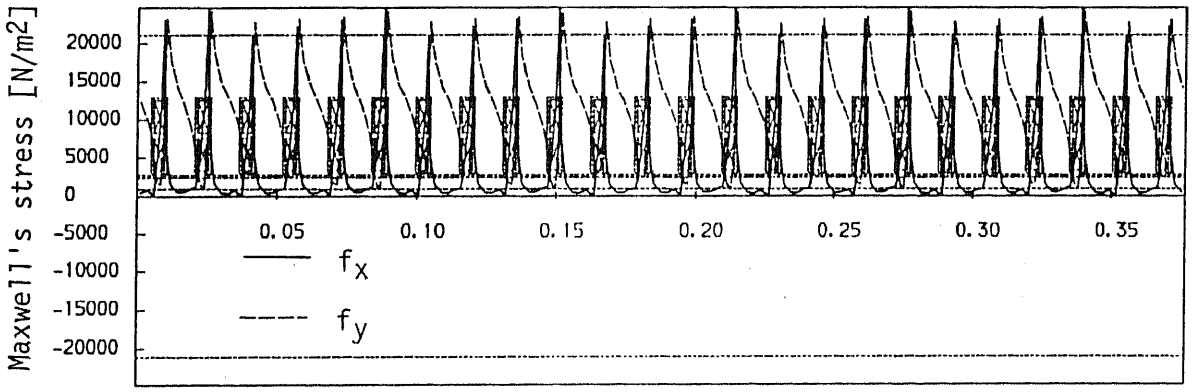

(e) Distribution of the Maxwell's stress tensors

Figure 3.8. Four- pole six- phase symmetrical drive with a current source ($I_1 = 15A$ *const.*, $f_1 = 30Hz$ and $s = 0.05$)

3.2.3. Thrust force and equivalent circuit

The thrust force of the four- pole symmetric machine without end-effect can be calculated in the same way using the Thevenin theorem as the torque calculation of normal rotary induction motors. [3-2] On the other hand, the forces can be calculated directly from the results of field analysis by integrating the Maxwell's stress tensors. The thrust forces, driven by current- and voltage- sources, have been calculated with the both of the methods and compared in the figures 3.7 and 3.8.

3.2.4. Comparison with other calculations by Mr. H. May

Hardo May and I compared our calculations of the same motor with different analysis methods at the TU Braunschweig to verify the analyses.

An example of the results is shown in the figure 3.9.

Furthermore, we checked the energy flows in the analyses. In May's analysis, the inductance of a conductor in each slot was calculated; an example of the results is referred in the table 3.2. He calculated also the secondary energy losses and the thrust force.

Table 3.2 Inductances of the primary conductors per one turn
(s= 0.1, f_1= 30.0Hz)
Secondary loss=7.06e-3 [W/m] : Fx=3.09e+3 [N/m]

Slot	1	2	3	4	5	6
Low	2.09e-5	8.31e-6	2.09e-5	8.31e-6	2.09e-5	8.31e-6
High	4.49e-5	3.54e-5	4.49e-5	3.54e-5	4.49e-5	3.54e-5

Slot	7	8	9	10	11	12
Low	2.09e-5	8.31e-6	2.09e-5	8.31e-6	2.09e-5	8.31e-6
High	4.49e-5	3.54e-5	4.49e-5	3.54e-5	4.49e-5	3.54e-5

From these data, the terminal impedance of a coil was calculated as follows:

$$j\omega L = 2\,\pi\, f_1\, N_s^2\, l_e \left[L_{1,low} + L_{11,high} + L_{2,low} + L_{12,high}\right] \times \frac{n_{pole\ pair}}{2_{parallel}}$$

$$= 2\,\pi \times 30 \times 30^2 \times 0.24 \times \left[2.09e{-}5 + 4.49e{-}5 + 8.31e{-}6 + 3.54e{-}5\right] \times \frac{2}{2} = 4.46[\Omega] \qquad (3.4)$$

$$R_{prim} = \frac{1}{i_{prim}^2} \cdot \left[P_{loss} + F_x \times v\right] \times l_e \times n_{pole} \times \frac{1}{n_{coil}}$$

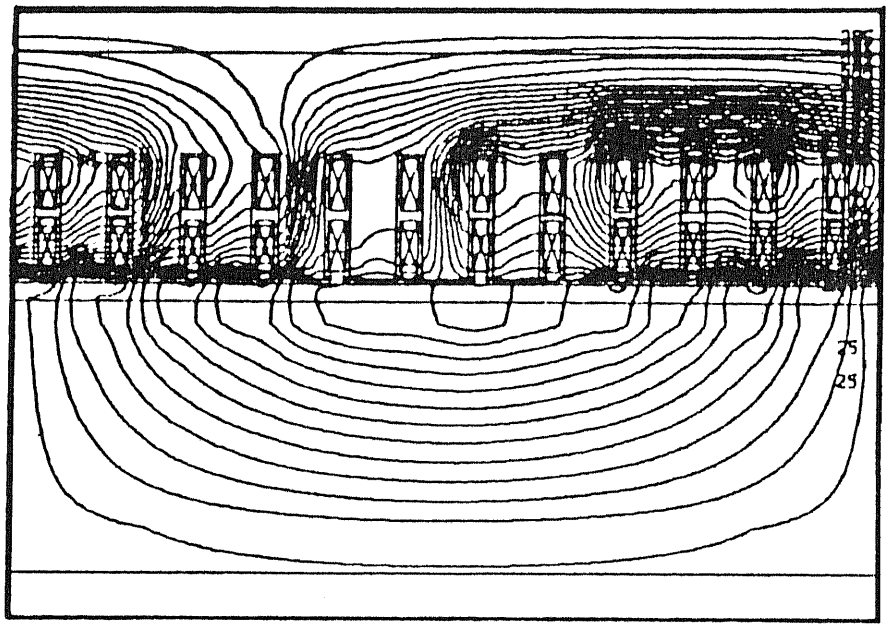

(a) Calculation by Koseki.

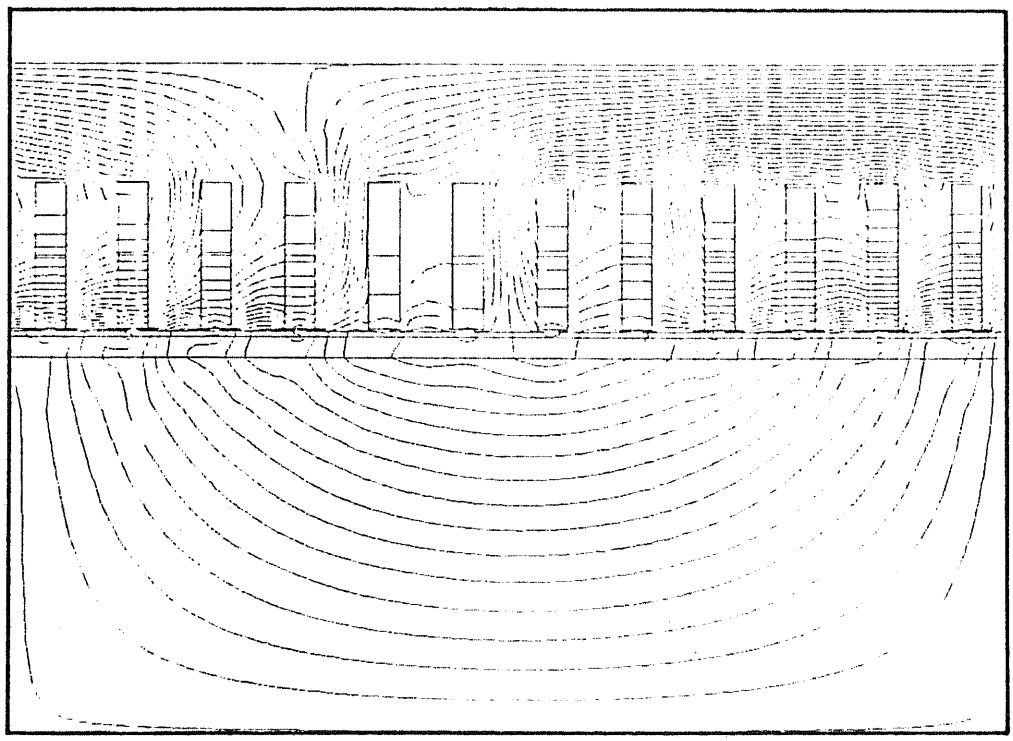

(b) Calculation by May.

Figure 3.9. Comparison between the two calculations ($f_1 = 30Hz$, $I_1 = 15A$, and $s = 1.0$).

$$= \frac{1}{30^2} \cdot \left[7.065e{-}3 + 3.09e{-}3{\times}0.9{\times}2{\times}30.0{\times}0.188\right] {\times}0.24{\times}4{\times}\frac{1}{6} = 6.5[\Omega] \qquad (3.5)$$

On the other hand, the thrust force per pole pitch was calculated on the same operating point: $F_x = 3.11e{+}3$ [N/m], in addition, $Z_{real} = 6.51[\Omega]$ and $Z_{imag} = 4.59[\Omega]$ with Koseki's analysis. The both results agree quite well.

3.3. Six- phase three- pole asymmetric drive

This driving mode was planned for the simulation of finite LIM drives with the end-effect, as shown in the figure 3.11. The primary current vector loci draw, however, confusing spiral curves shown in the figure 3.10: there are some abnormal points at the $s = -1.0$, (0.0,) 0.33, 0.5, and (1.0); we can see in the figures 3.12, 13, and 14 that the equivalent pole-pitch varies on those operating points because of the resonance of the magnetic circuit with interruption through the *"unused part"* of the yoke, which I did not intend. Consequently, the curves of thrust- and normal- forces, shown in the figures 3.15, are also complicated. The abnormality on the points $s = -1.0$ and 0.33 is especially conspicuous.

3.4. Transient analysis

Results of the transient calculation are shown in the subsection 4.2.2 or reference [3-4], but the results were not compared with the stationary analysis; the both of them should be in agreement, as described in [3-5].

3.5. Experiment

3.5.1. Purpose of the experiment

An experimental induction motor has been built at the TU Braunschweig as described in the section 3.1. The purposes of the measurements, intended at first, are as follows:

(1) the evaluation of propriety of the two- dimensional numerical program for the calculation of a field with eddy-currents in comparison with the measurement of basic characteristics of four- pole six- phase rotary induction motor with an aluminum- plate as a secondary conductor,

(2) investigation on the difference between six- phase- and three- phase- drives,

(3) identification of constants in the equivalent circuit of an induction motor in each case,

(4) comparison with the results calculated numerically,

(5) experimental investigation on three- pole linear induction motor using a half of the windings of the four- pole rotary machine as described in the subsection 3.3., particularly concentrating on measurements of unbalances between each phase and end effects, and

(6) experimental attempt to the application of the field oriented control scheme.

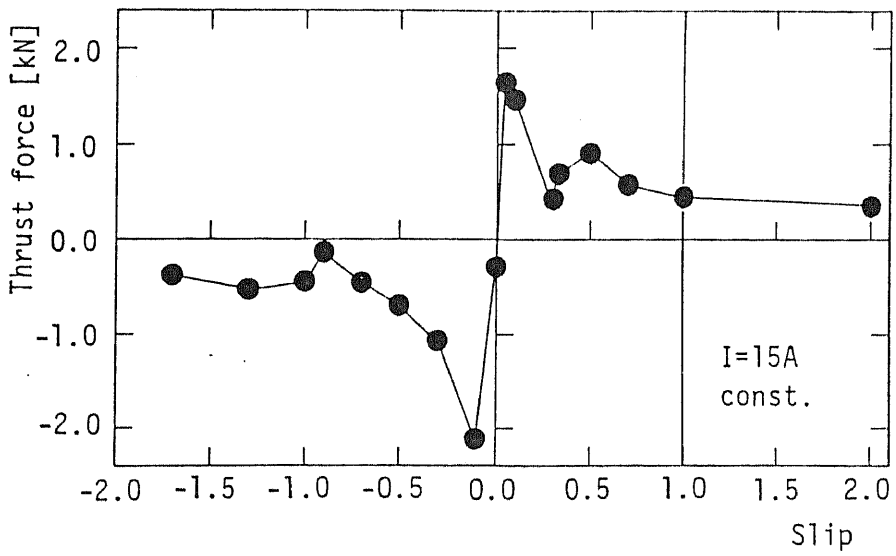

(a) Thrust force.

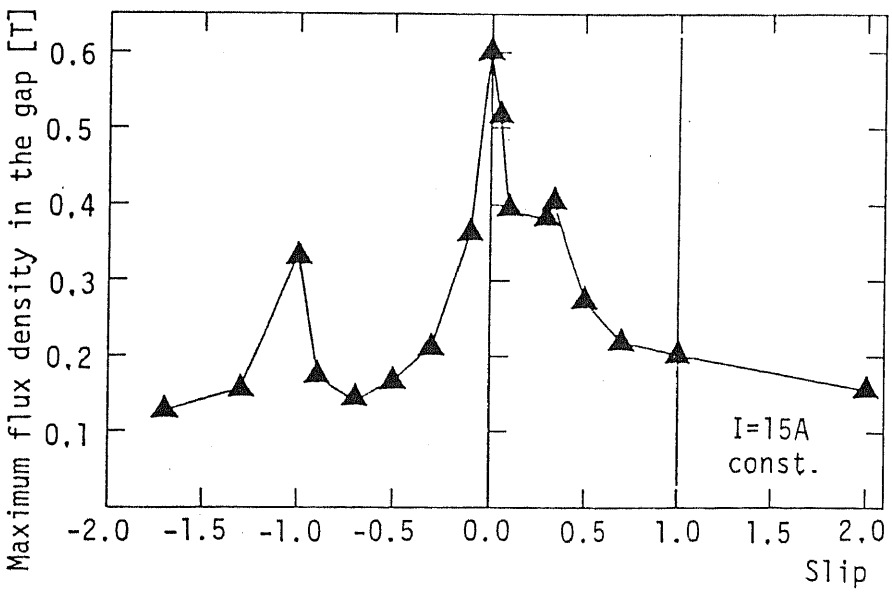

(b) Maximum gap flux density.

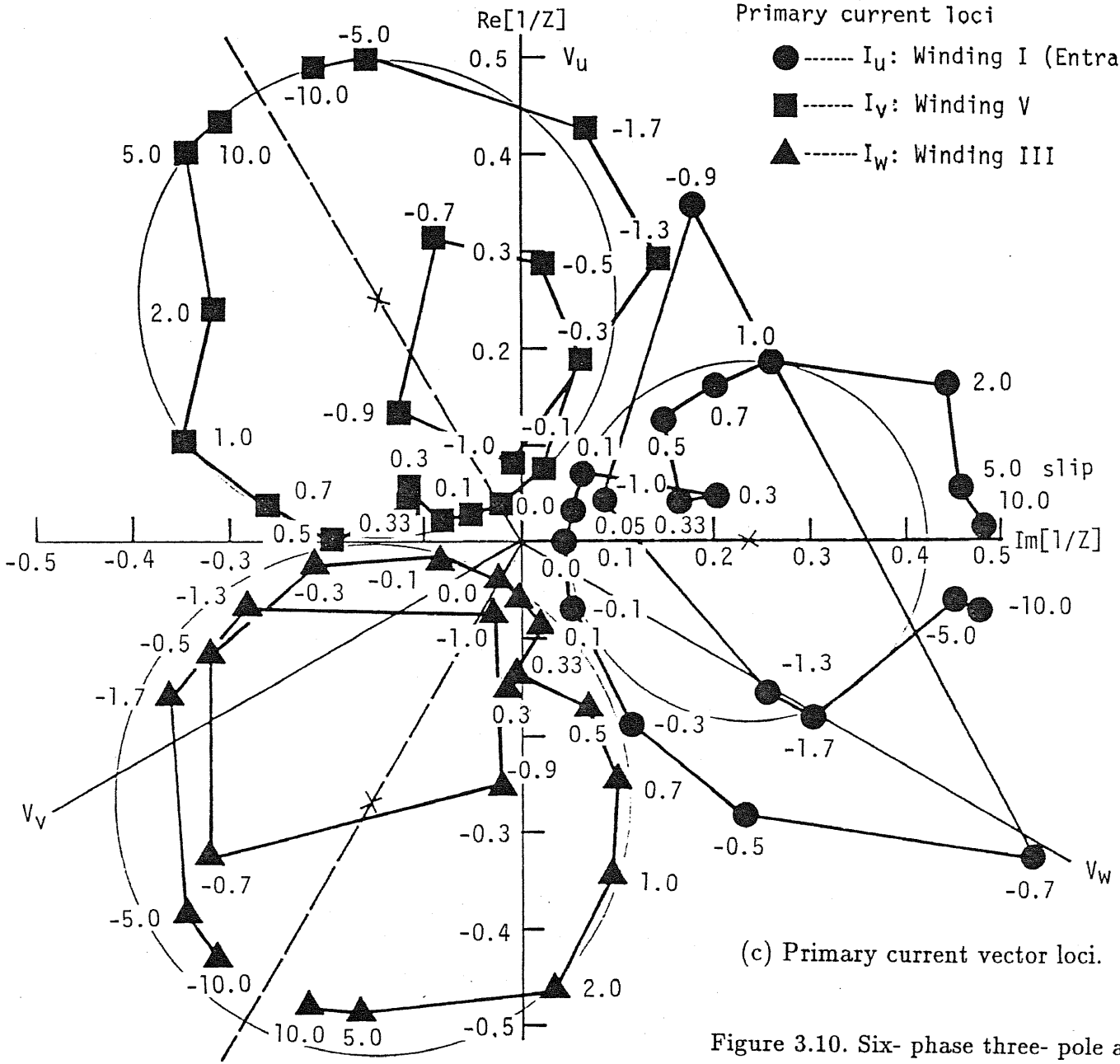

(c) Primary current vector loci.

Figure 3.10. Six- phase three- pole asymmetric drive (calculation).

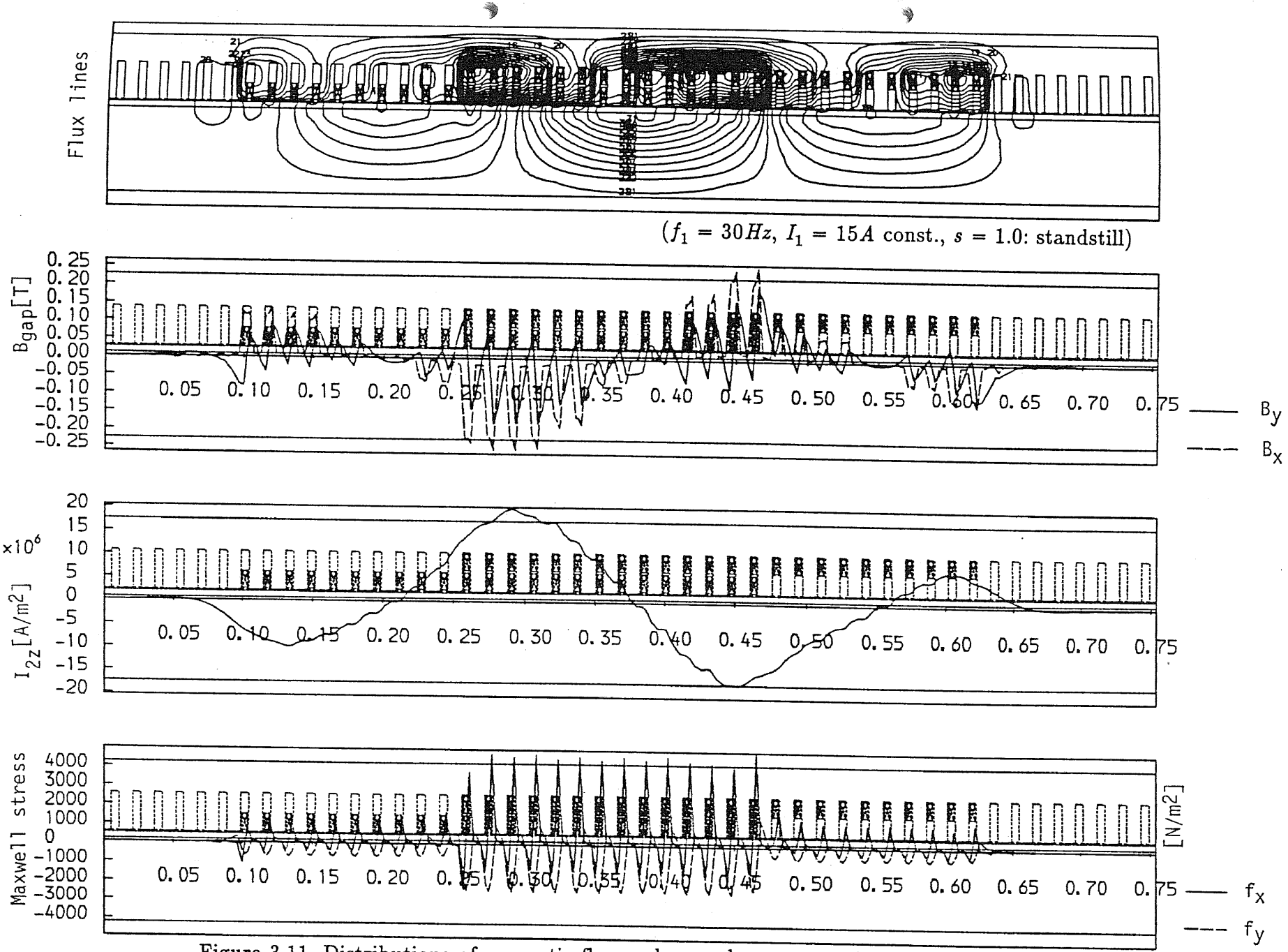

Figure 3.11. Distributions of magnetic flux and secondary current in the six- phase three- pole asymmetric drive (instant values).

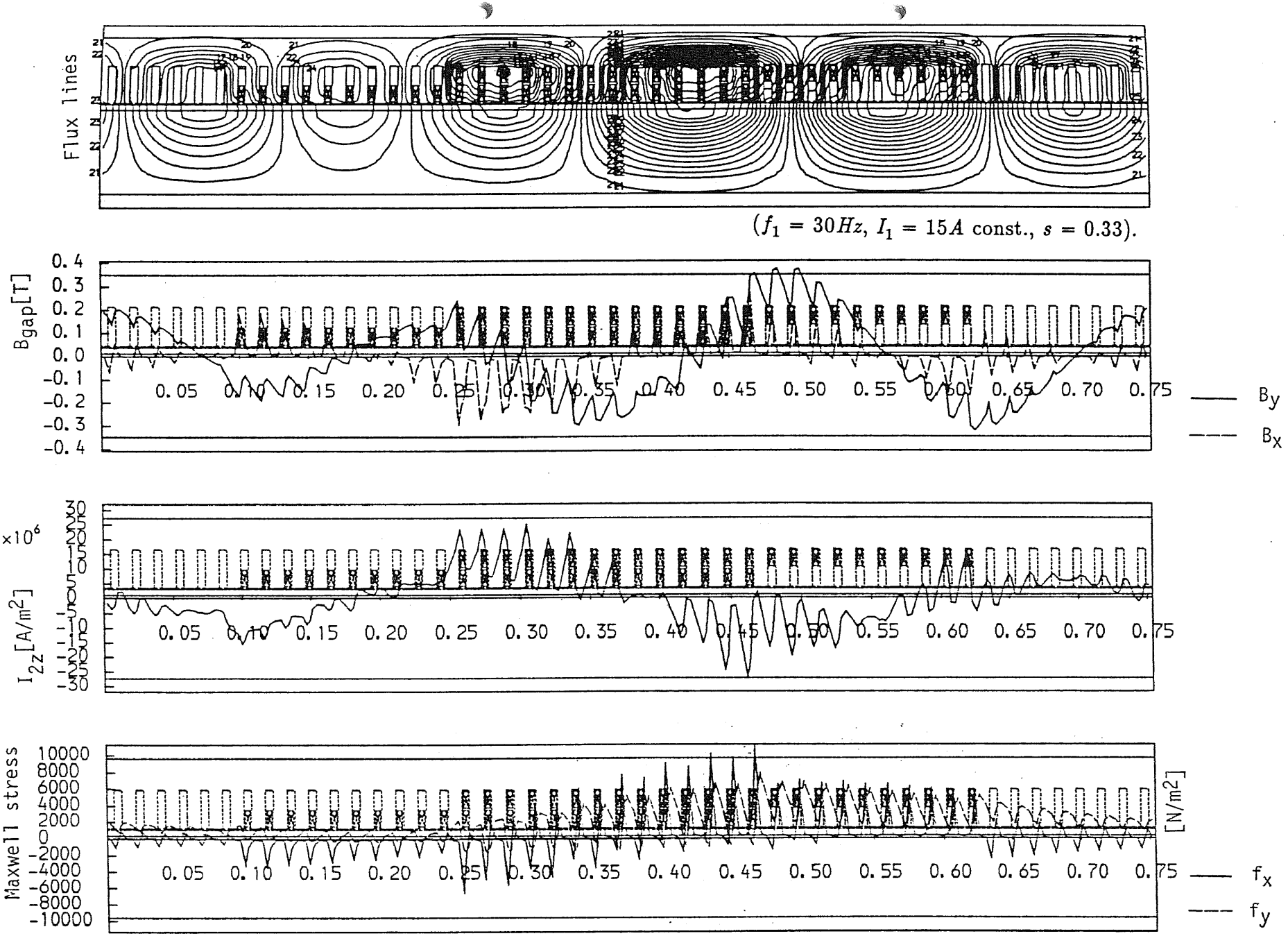

Figure 3.12. Distributions of magnetic flux and secondary current in the six- phase three- pole asymmetric drive (instant values).

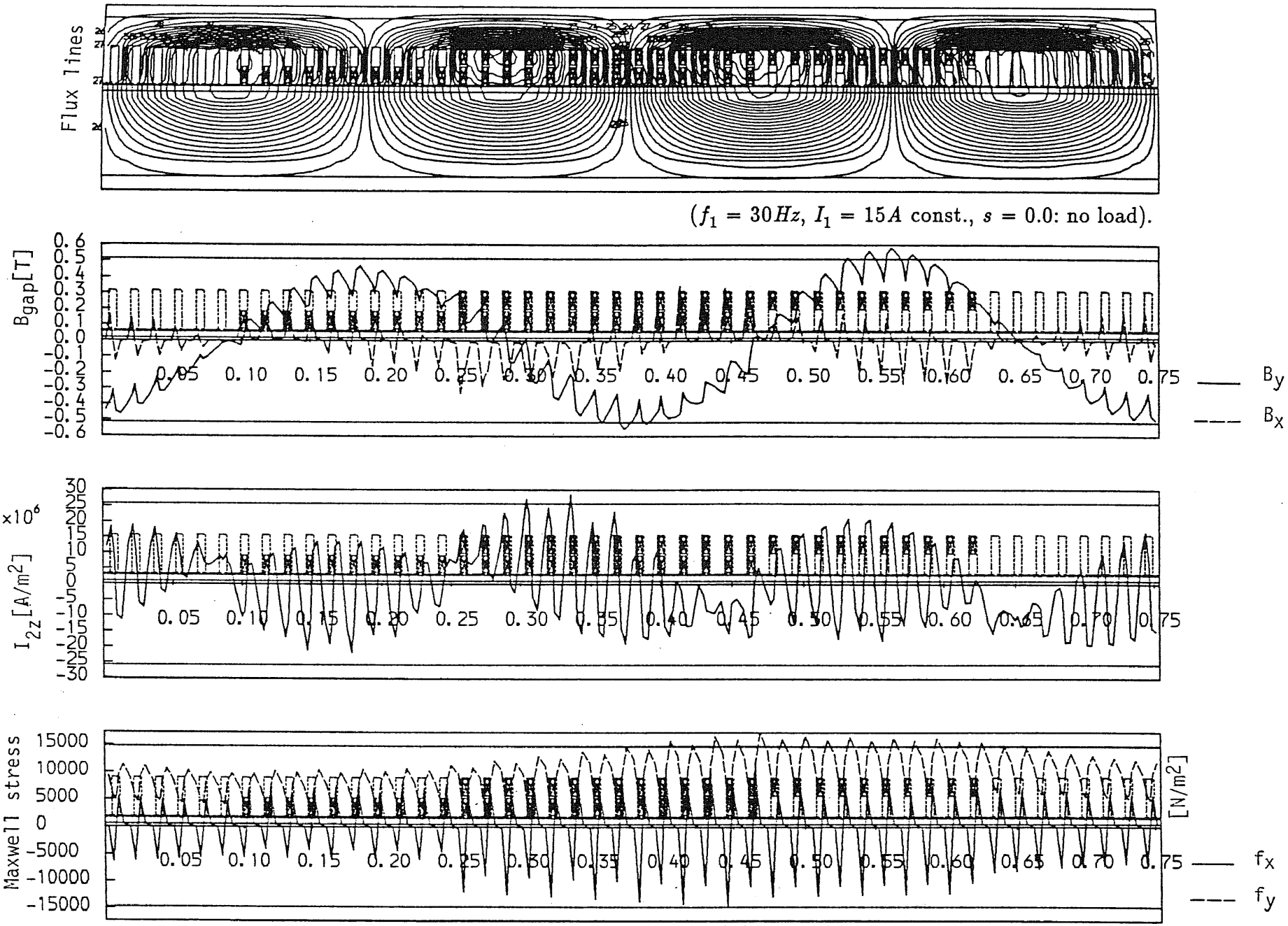

Figure 3.13. Distributions of magnetic flux and secondary current in the six- phase three- pole asymmetric drive (instant values).

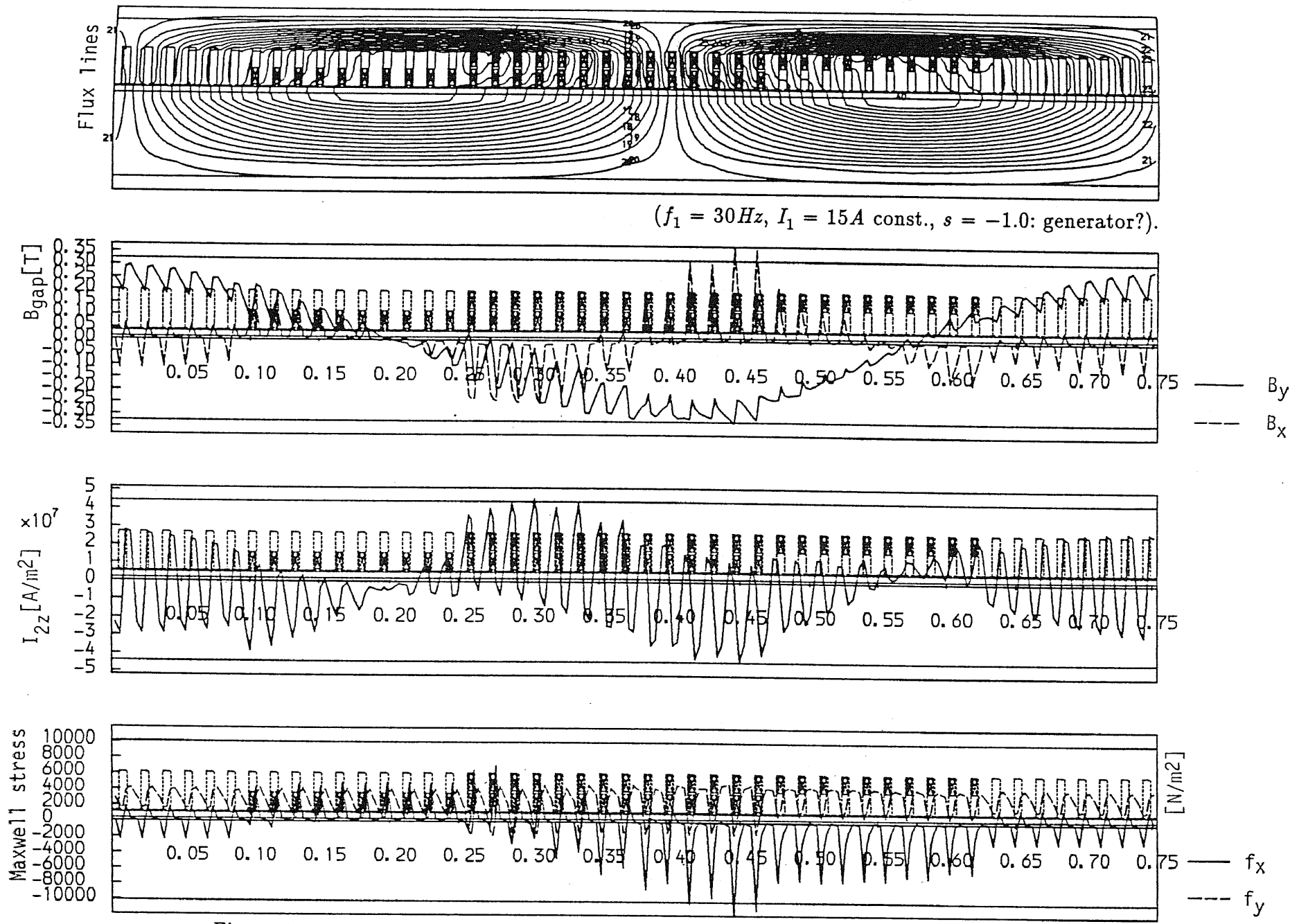

Figure 3.14. Distributions of magnetic flux and secondary current in the six- phase three- pole asymmetric drive (instant values).

Although the three- pole drives were measured, the purpose (5) has not been successful because of the interference of magnetic flux through the yoke as mentioned in the subsection 3.3. In addition to this, I had no time for the experimental attempt for the purpose (6) at the TU Braunschweig.

3.5.2. Procedure of the measurement

The machine has been already explained in the previous section. The experimental facilities for three- phase drive with a motor-generator and six- phase drive with a pair of three- phase PWM inverters are illustrated in the figures 3.15. and 3.16. It was impossible because of time harmonics with the PWM to measure the AC voltage and the output real power directly in the case of the inverter drive, therefore, the voltage and power were calculated from the DC- current I_d and voltage V_d shown in the figure 3.16, where the energy loss and voltage drop in the inverter were neglected, and the effect of asymmetry between phases could not be measured.

3.5.2.1. Three- phase four- pole symmetric drive with a motor-generator

The results measured and calculated with the two- dimensional analysis are shown in the figure 3.17 in the case of $f_1 = 30.0$ *Hz* and in the figure 3.18 in the case of $f_1 = 50.0$ *Hz*. The two- dimensional calculations of thrust forces show good agreements with the experiments under the assumption of current source drive. On the other hand, the measured impedances are larger than the calculation because of neglected impedances like primary resistance, primary leakage inductances at the coil-end portions, and some additional leakages, especially, we can see that the measured power factor is larger than the calculation on account of additional losses [3-6] in the high slip region.

3.5.2.2. Six- phase four- pole symmetric drive with an inverter

For the purpose (2), the figure 3.19 should be compared with the figure 3.17. The terminal impedance (magnitude) in the figure 3.17 is almost twice of the figure 3.19 owing to the serial connections. It is difficult to compare the two groups of figures, since the measurements of the six- phase drive could not be accurate enough for detailed discussions, on account of the difficulties of measurements due to harmonic waves with the inverter drives. Anyway, there seems to be no conspicuous difference between the two types of the drives in the measurements.

3.5.2.3. Three- phase three- pole asymmetric drive with the motor-generator

This experiment has not been successful for the reasons described in the subsection 3.3. We can see confusing torque curves in the figure 3.20, in particular, it was almost impossible to drive the motor faster than $s = 0.33$; the reason is supposed with the figures from 3.11 to 3.14. On account of the problem, I gave up the further measurements concerning the three- pole asymmetric drive, *i.e.*, a purely "linear" machine is necessary for evaluation of the end-effects.

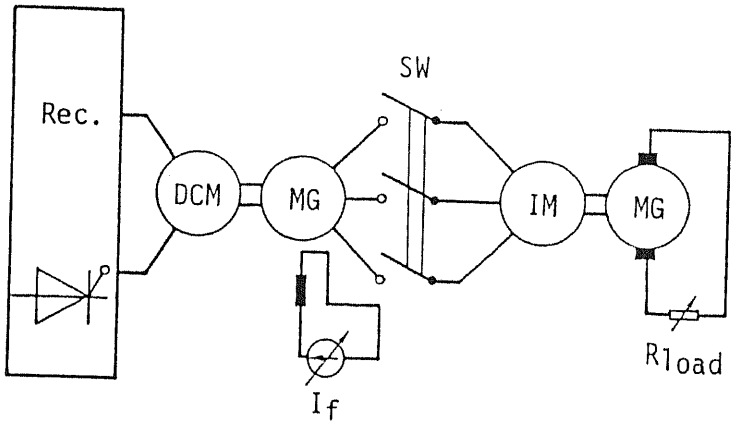

Figure 3.15. Equipment for experiments with a three- phase motor-generator.

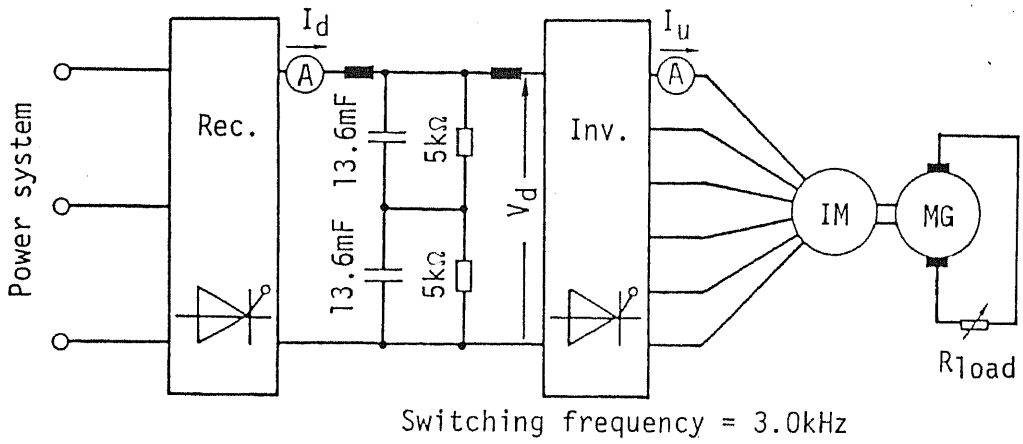

Figure 3.16. Equipment for experiments with six- phase inverters.

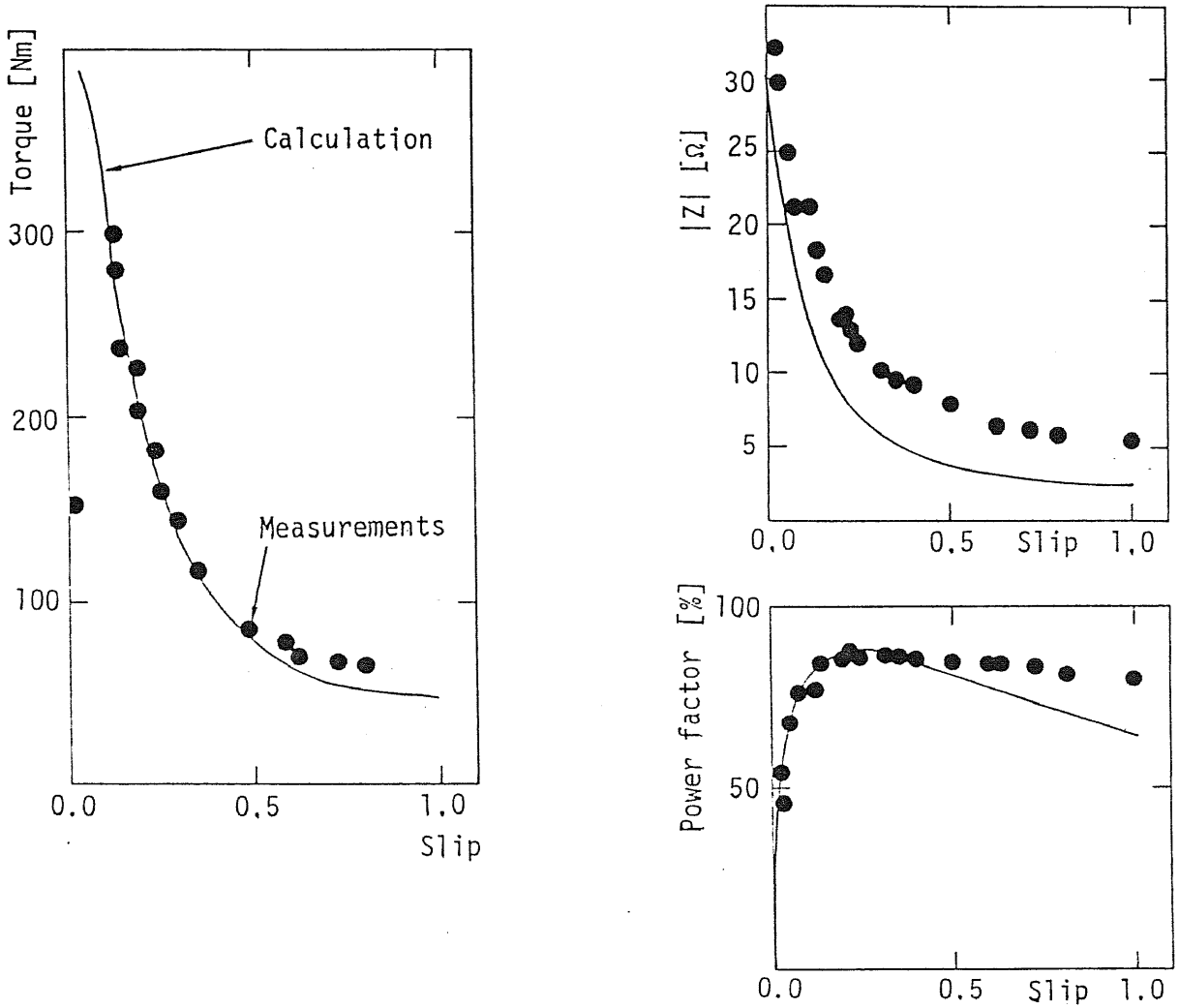

Figure 3.17. Four- pole three- phase drive $f_1 = 30Hz$ and $I_U = 30A$.

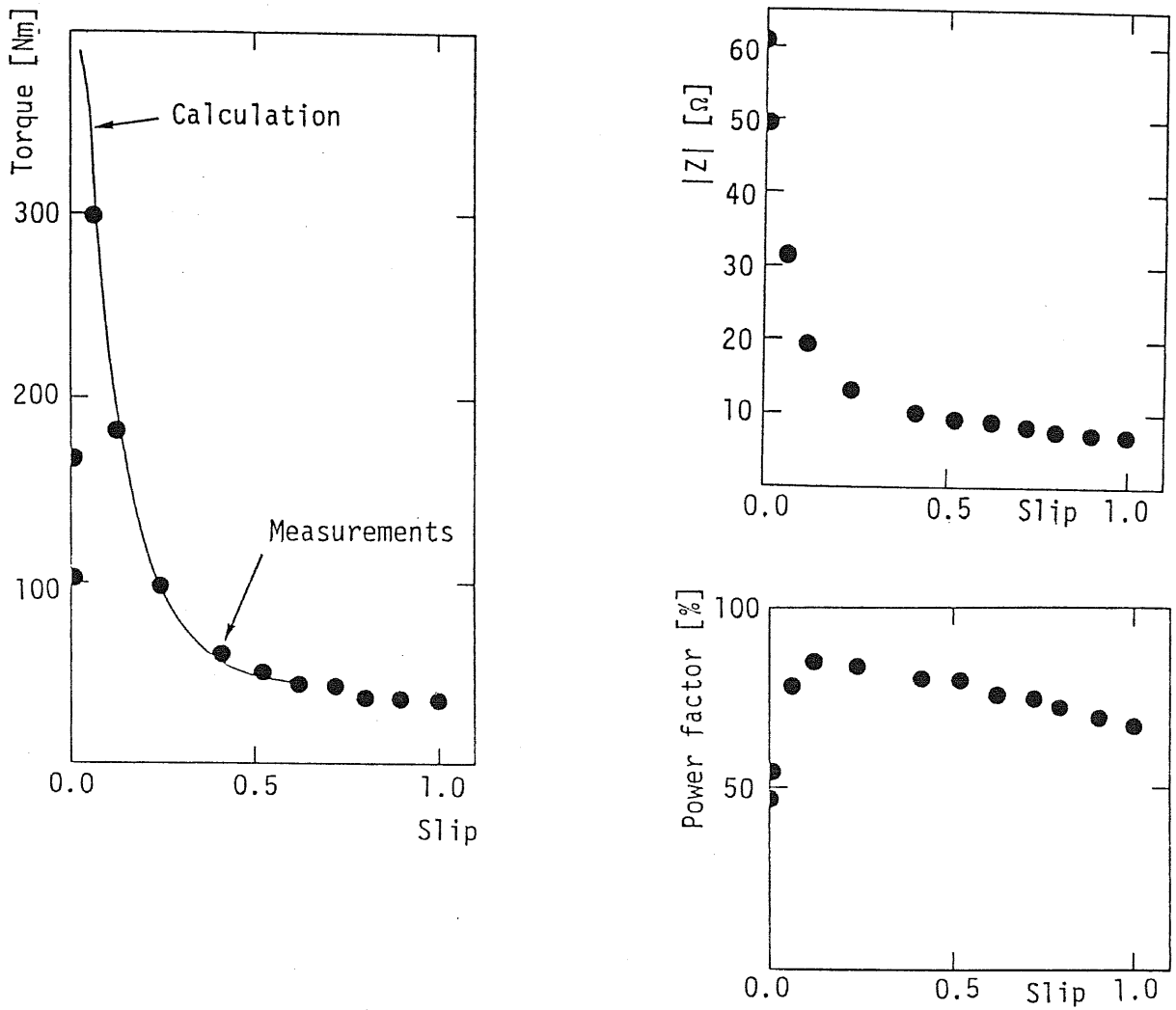

Figure 3.18. Four- pole three- phase drive $f_1 = 50Hz$ and $I_U = 30A$.

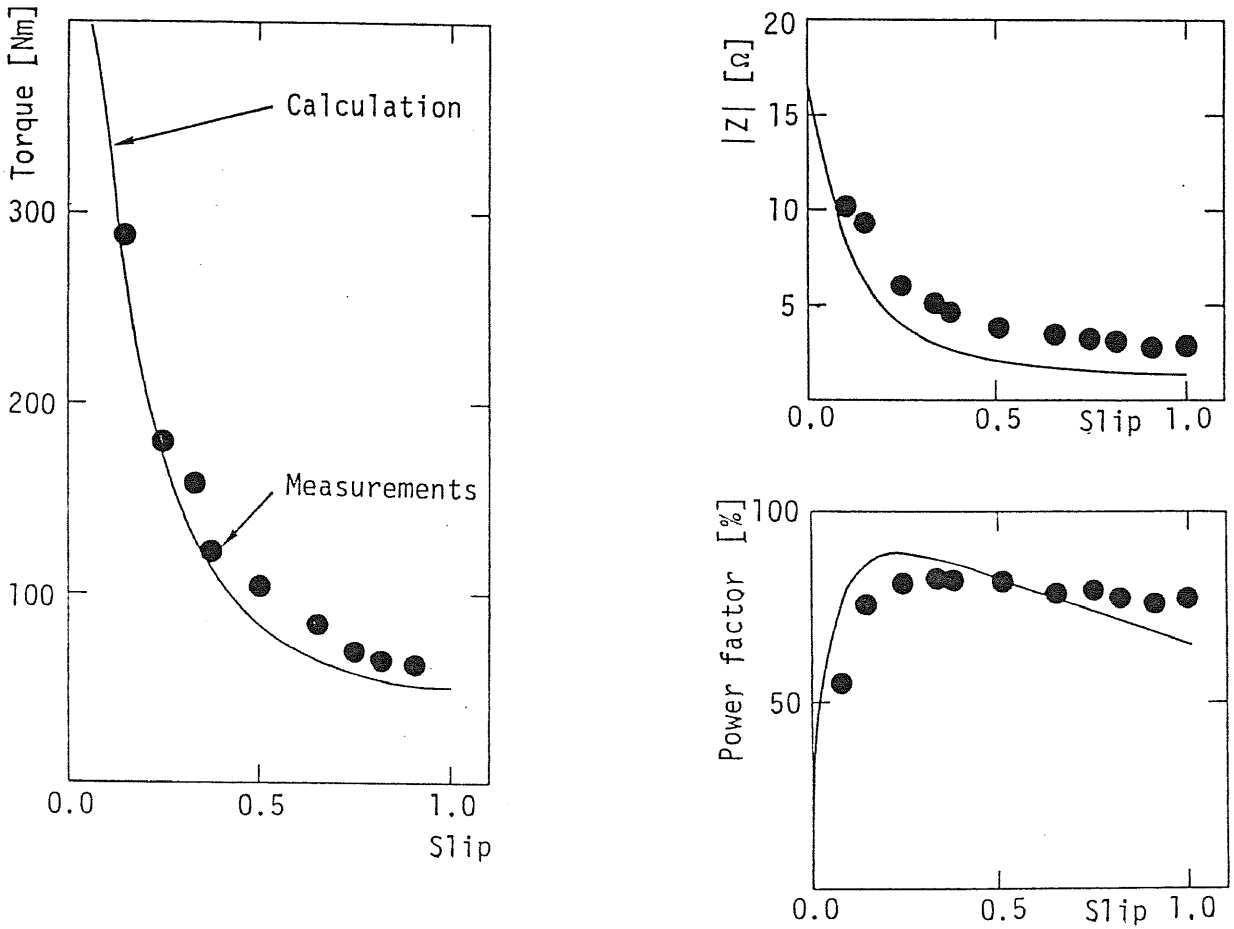

Figure 3.19. Four- pole three- phase drive $f_1 = 30Hz$ and $I_U = 30A$.

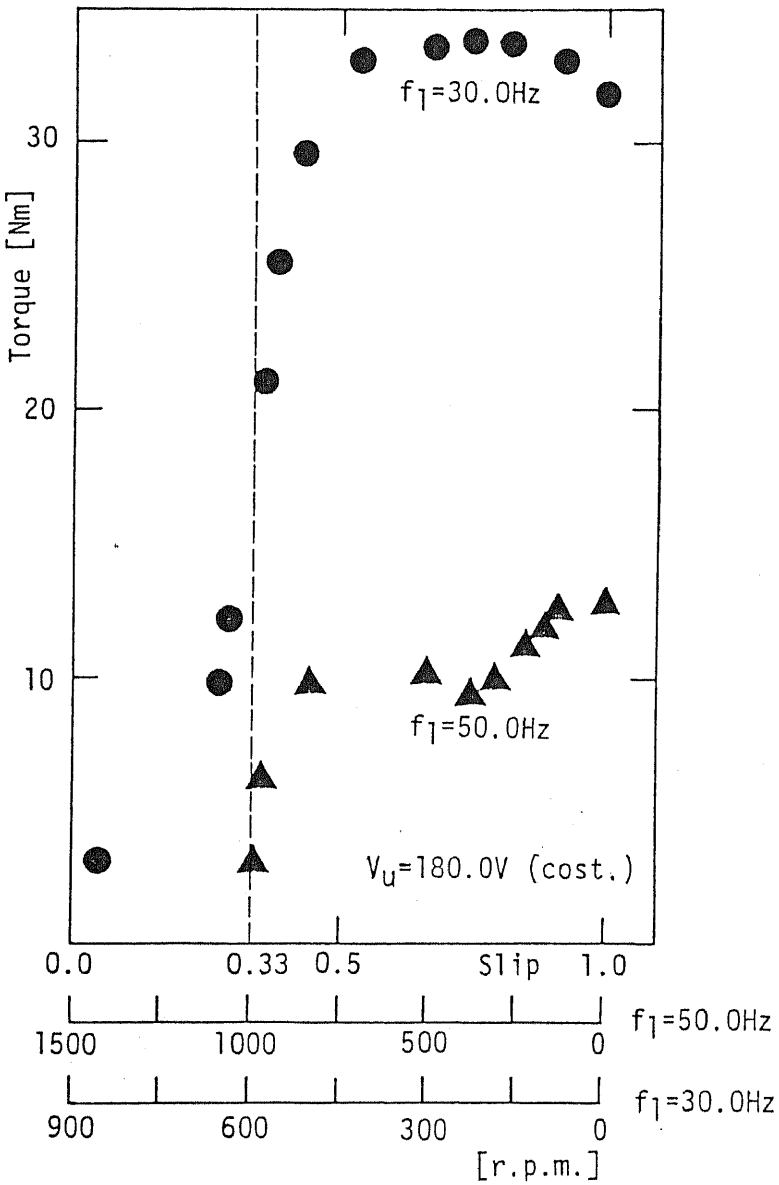

Figure 3.20. Thrust force in three- pole three- phase asymmetric drive: Measurements with a motor-generator.

3.6. Summary of results

- ☐ The calculations with the control volume method have been compared with some theoretical calculations based on classic machine theory and measurements; their agreement has been verified. This agreement is an essential condition of the further investigations described in the chapter 5.
- ☐ The calculated terminal impedances were, however, a little smaller than the real ones because of the two- dimensional modeling, which contains neither transverse edge-effect nor other additional leakage impedances.
- ☐ The calculation with the control volume method has been compared with another one based on the conventional finite element method; they have also agreed well with each other. In addition, a physical meaning of factors in the impedance matrix were investigated considering the energy flow in a machine.
- ☐ There was no substantial difference between the symmetric three- phase- and six- phase- drives.
- ☐ It was not successful to try the experimental simulation of LIMs with finite length with the asymmetric three- pole drives, since the interference of magnetic flux through the iron yoke in the non-active portion was not negligible.

References

[3-1] W. Leonhard: "Regelung in der elektrischen Antriebstechnik", Teubner Studienbücher — Elektrotechnik, 1974

[3-2] H. Eckhardt: "Grundzüge der elektrischen Maschinen", Teubner Studienbücher — Elektrotechnik/ Maschinenbau, 1982

[3-3] H. Mosebach: "Effekte der endlichen Länge und Breite bei asynchronen Linearmotoren in Kurzständer- und Kurzläuferbauform", doctoral dissertation at the TU Braunschweig (FRG), 1972

[3-4] T. Koseki, H. Ohsaki and E. Masada: "A Novel Control Scheme of a Linear Induction Motor", international Conference on Maglev 1989, Yokohama, pp. 345-350

[3-5] H. May and H. Weh: "Numerical Calculations on Magnetic Circuits", Journal of Magnetism and Magnetic Materials 19, 1980, pp. 301-319

[3-6] R.L. Russel and K.H. Norsworthy: "Eddy Current and Wall Losses in Screened Rotor Induction Motors", IEE Proc. A, 1968, 105, pp. 163-175

Chapter 4: Structure and switching scheme of FSLIMs

Introduction

A novel concept of the "flux synthesis" is introduced in this chapter. After introducing the concept and fundamental structure of the motor, results calculated with trial- and error- method are shown in detail in the sections 4.2. It will be suggested that a modified structure with multi- turn windings is necessary for constructing a test machine in reality, according to the calculation. We then proceed a discussion on mathematical scheme for deciding switching patterns based on the same idea as the impedance calculation in the section 2.7.

4.1 Flux synthesizing linear induction motor (FSLIM) [4-1]

A LIM is being used in public transport systems and automated factory lines. As a typical application of direct drives, LIMs are used in molten metal production processes, *e.g.,* pumping, stirring and braking. A sophisticated control of forces are required for high quality of the product in these processes.

In a conventional LIM, the power factor and the energy efficiency are low, and it takes long time to produce intended forces. Furthermore, the LIM has the end effect. Strategies against the effect are unfortunately limited because of the conventional three-phase construction. On the other hand, high speed power switching devices are available with reasonable costs at present; it is possible to use many switching devices as a part of an electric machine.

With the present technical situation in mind, **"Flux Synthesizing Linear Induction Motor (FSLIM)"** has been proposed as shown in the figure 4.1. Each slot has a conductor which carries bidirectional electric current whose magnitude is controlled with current control units: the units are bidirectional PWM switches connected with a pair of ideal DC-bus bars, whose capacity should be large enough to supply the primary motor current corresponding to arbitrary current reference values. That is to say, any desired waves of magnetic flux can be synthesized on the surface of the secondary conductive plate with an appropriate switching sequence of the current control units. There are, consequently, no constraints of three-phases windings.

With the FSLIM, we can precisely control not only the total force but also the distribution of it on the secondary conductor, *e.g.,* molten metal. It is also possible to produce forces for thrusting, braking, holding, and levitating the conductor with an appropriate switching scheme. On the other hand, the current capacity of the

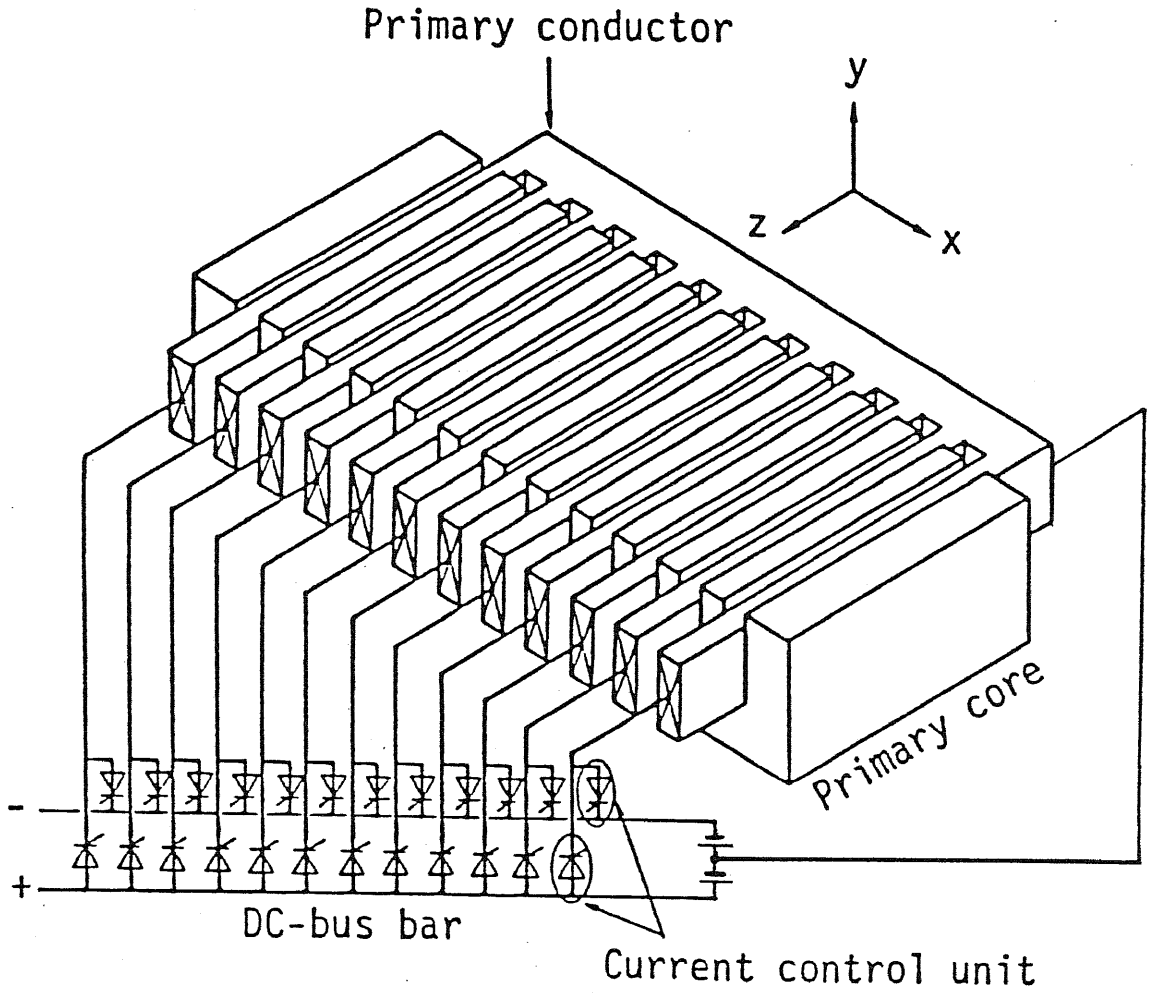

Figure 4.1. Primary side of a flux synthesizing linear induction motor with conductive bars.

switching devices should be much larger than those of conventional machines due to the single winding number. In addition, the controlling- and switching- schemes are inherently complicated; it is significant to investigate the appropriate switching sequences.

With this in mind, some basic characteristics with some switching patterns are calculated and discussed with a trial- and error- method in the next section. In order to synthesize intended magnetic flux in reality, mathematical formulation is, however, necessary to calculate the input- current or voltage corresponding to the reference flux distribution. The method is proposed in the section 4.3 using the principle of superposition of linear systems.

4.2. Basic calculations

4.2.1. Slip frequency characteristics of the thrust force for various switching patterns

The FSLIM model and the meshes for the numerical calculation with the C. V.-method are shown in the figure 4.2; dimensions of the FSLIM are described in the table 4.1.

Various primary currents' patterns are possible for the FSLIM. The power supply is restricted to multi-phase sinusoidal alternating current source for simplicity in this subsection; the five patterns show in the table 4.2 are selected as examples for basic calculations. Various pole pitches and phase numbers are tested. The current amplitude in a conductor is assumed to be constant in a cross-section of a conductive bar.

We see the results of slip frequency characteristics of the thrust force calculated with the five kinds of switching patterns and various secondary speeds in the figures 4.3 (a)-(e); the magnetic flux distribution in a case of the pattern I is shown in the figure 4.4. The curves on a graph should be the same at any speeds based on an ideal analysis model, *e.g.*, described in the section 5.1. The reality is, however, that the higher the speed is, the smaller the thrust force is. The effect is called "end effect" in general, and one of the purpose of the flux synthesis is to suppress the effect. Further discussions will be described in the section 5.1.

4.2.2. Transient calculations

A result of transient calculation is shown in the figures 4.5: all the initial values in the calculation were set to be zero, and the alternative current supply was assumed to be sinusoidal during the calculation time. We can see the initial transient deviation followed by an almost constant force on account of the ideal

Table 4.1. Dimension of the calculated FSLIM.

Primary side		
Motor length		385mm
Core height		70mm
Slot pitch		30mm
Slot width		15mm
Slot depth		30mm
(Core width		1.0m)
Permeability of core	ν_x	$500\mu_0$
	ν_y	$1000\mu_0$
Secondary side		
Mechanical gap length		5mm
Reaction plate Thickness		3mm
Core height		12mm
Permeability of core		$1000\mu_0$
Permeability of reaction plate		μ_0
Conductivity of reaction plate		$4.15\times10^7\Omega^{-1}m^{-1}$

Table 4.2. Primary current patterns.

Primary conductor's current pattern													
Pattern No.	Current in each primary conductor												pole pitch (m)
	1	2	3	4	5	6	7	8	9	10	11	12	
1	U	-W	V	-U	W	-V	U	-W	V	-U	W	-V	0.090
2	U	U	-W	-W	V	V	-U	-U	W	W	-V	-V	0.180
3	U	V	W	U	V	W	U	V	W	U	V	W	0.045
4	U	U	V	V	W	W	U	U	V	V	W	W	0.090
5	U	U	U	U	V	V	V	V	W	W	W	W	0.180

U V W : 3-phase alternating currents

Amplitude : 1414 A/conductor

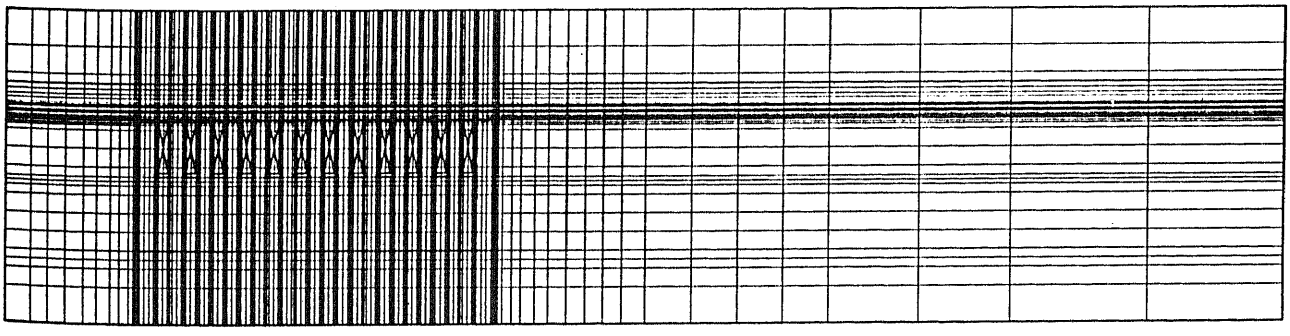

Figure 4.2. Example of two dimensional calculation of the FSLIM.

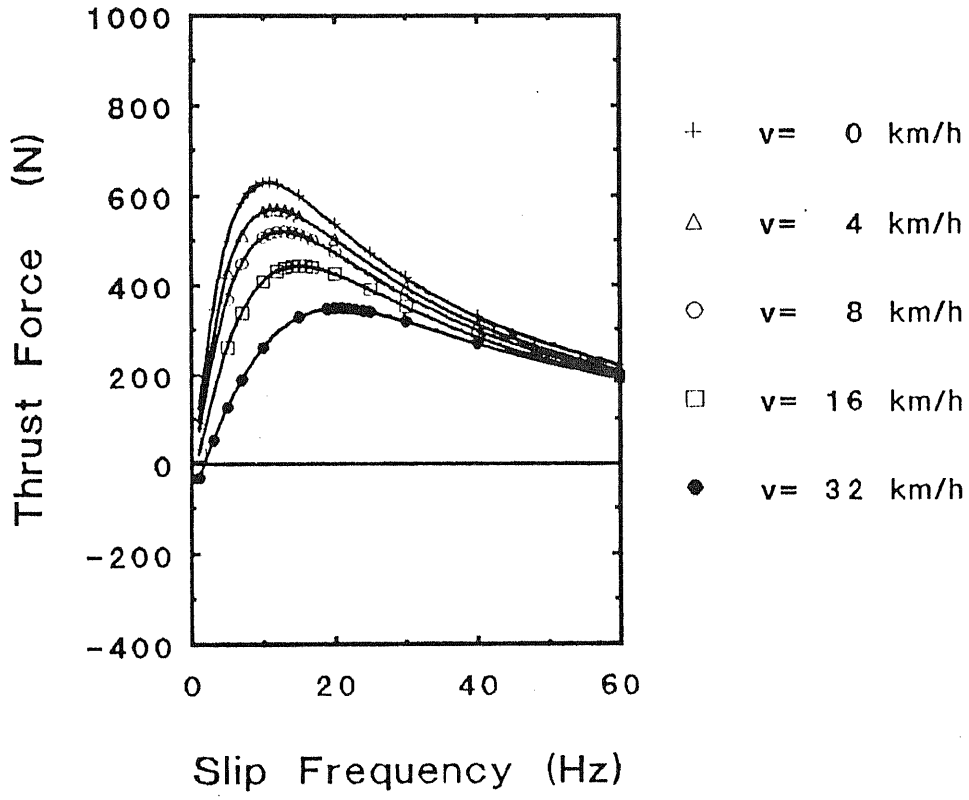

(a) Pattern I (six-phases, four-poles).

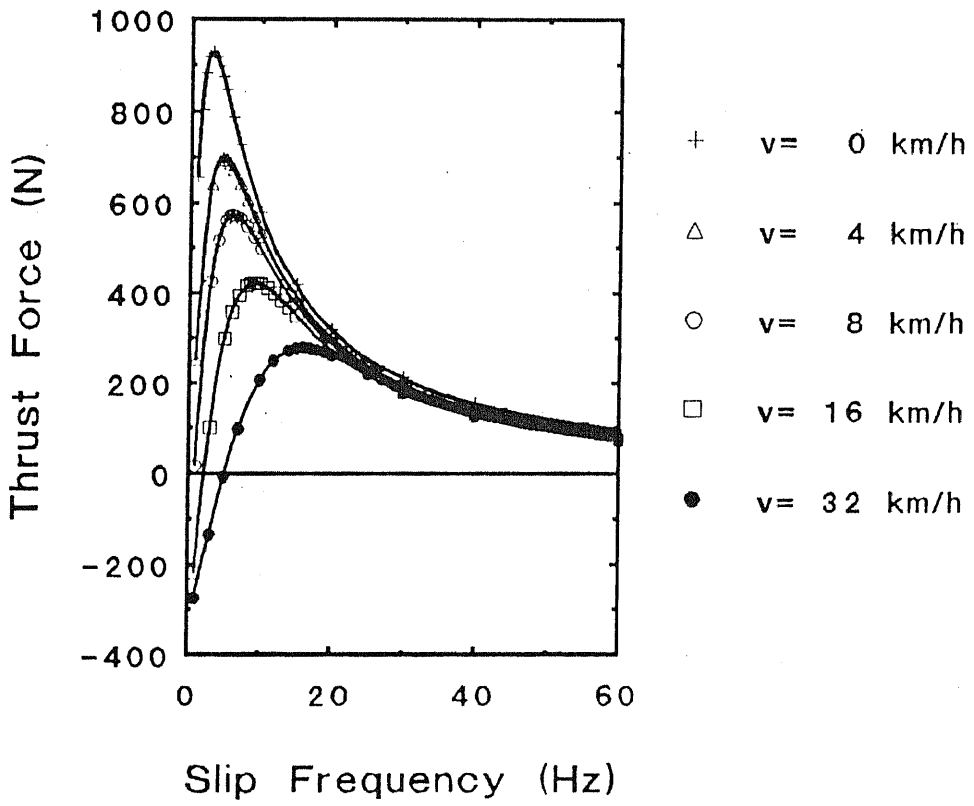

(b) Pattern II (six-phases, two-poles).

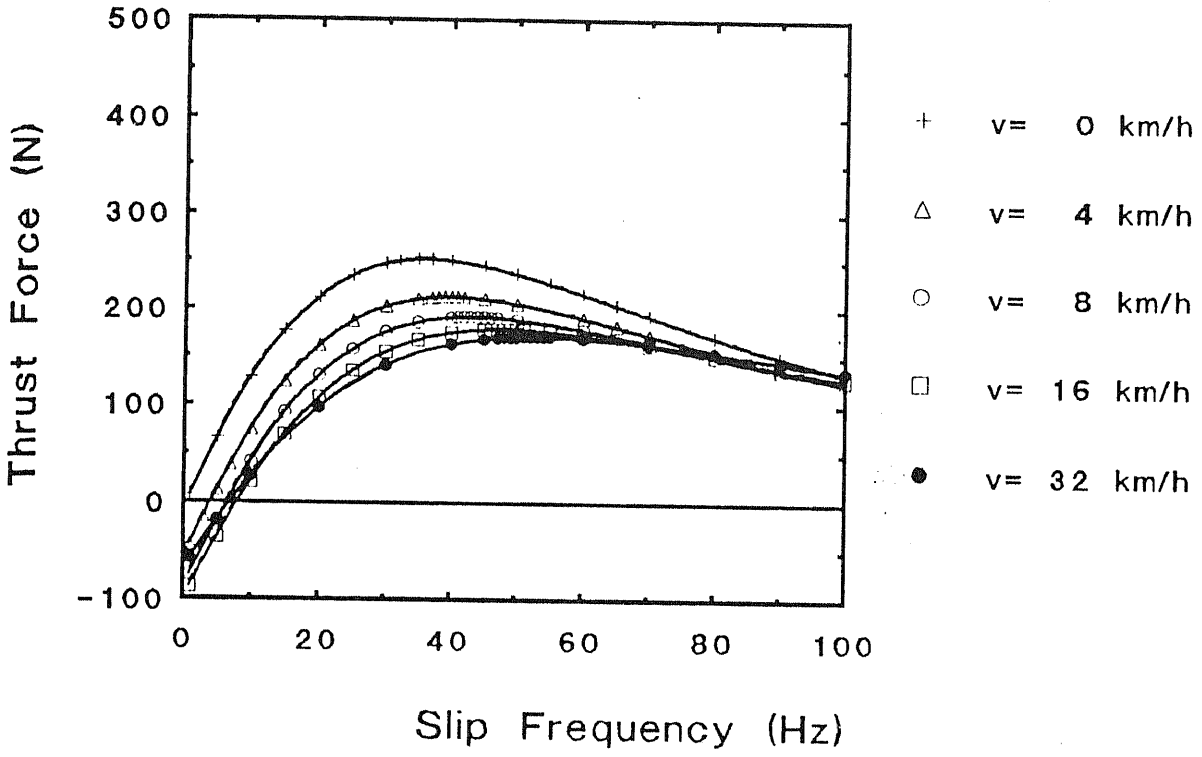

(c) Pattern III (three-phases, eight-poles).

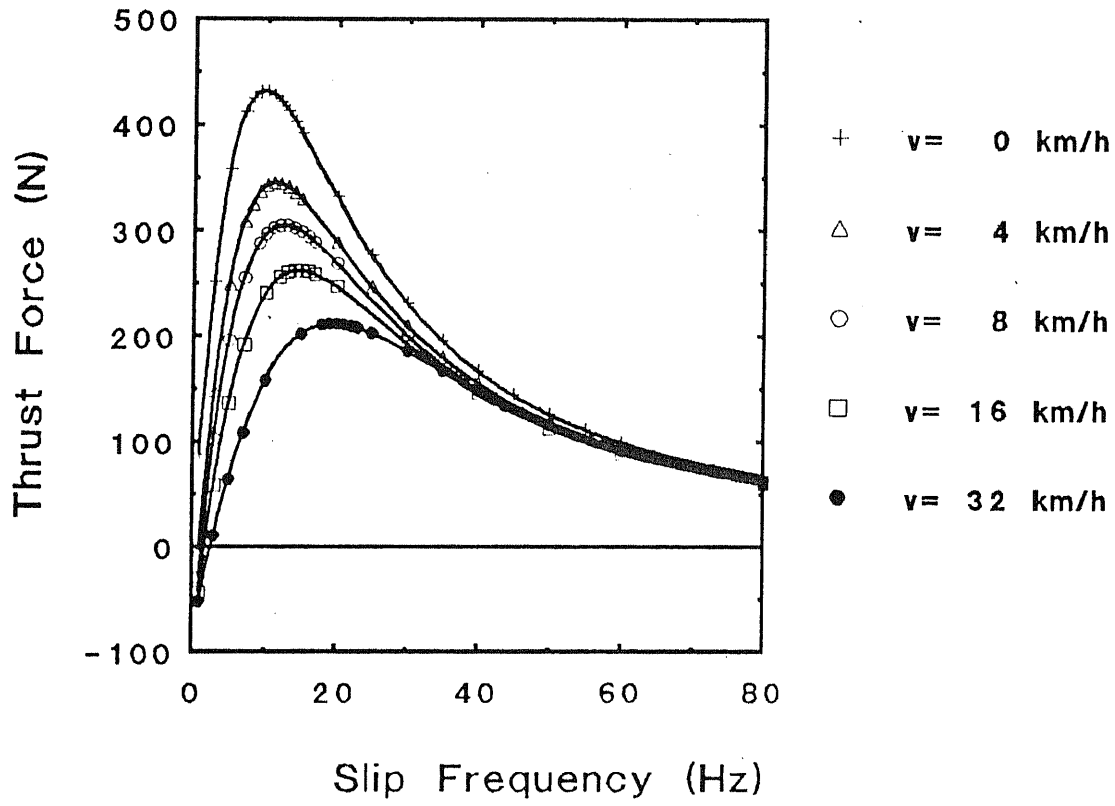

(d) Pattern IV (three-phases, four-poles).

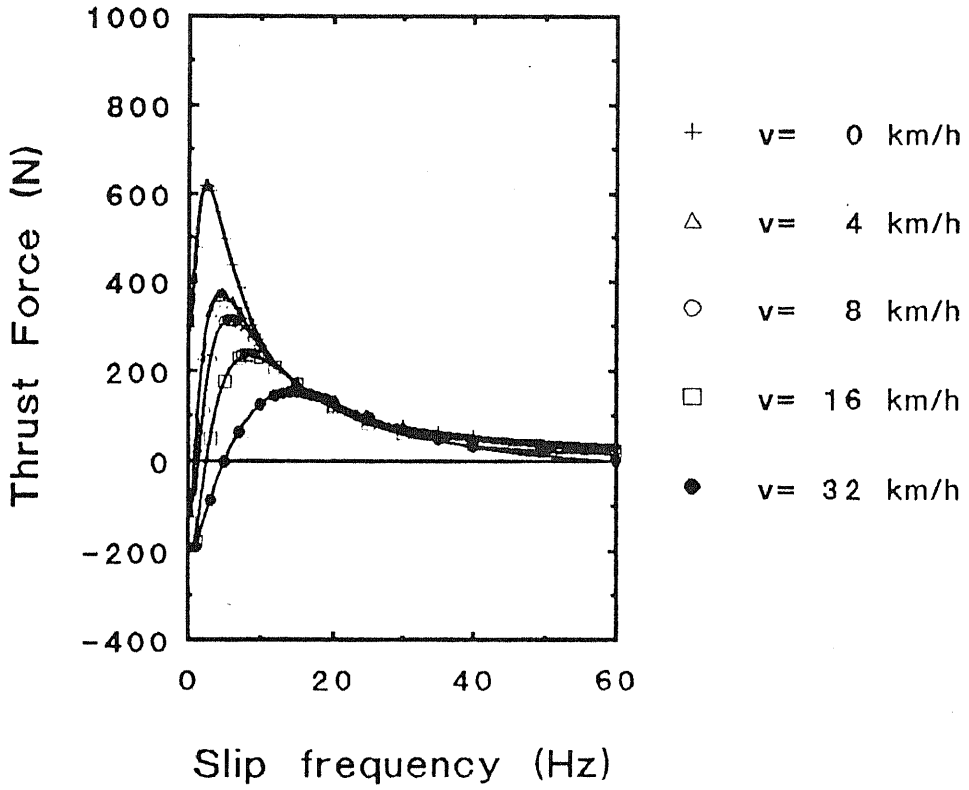

(e) Pattern V (three-phases, two-poles).

Figure 4.3. Slip frequency characteristics of thrust forces.

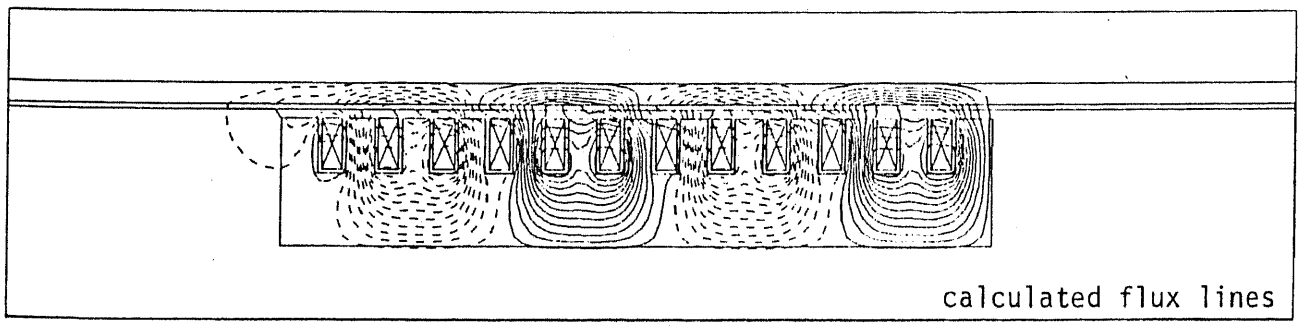

Figure 4.4. Magnetic flux distribution (Pattern I, $v_2 = 32km/h$).

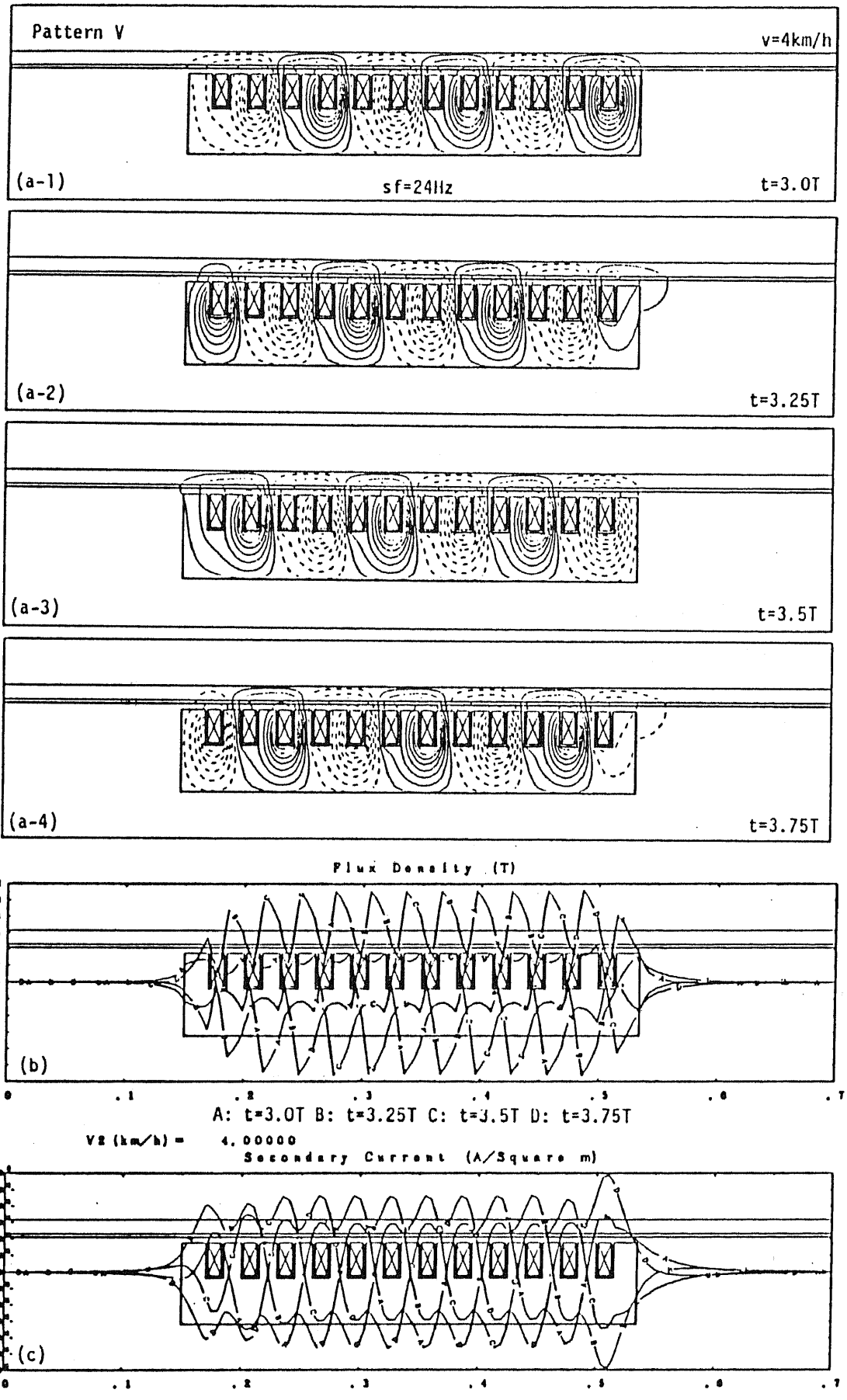

(a) Contour Lines of Magnetis Vector Potential
(b) Distribution of Magnetic Flux Density
(c) Distribution of Secondary Current Density

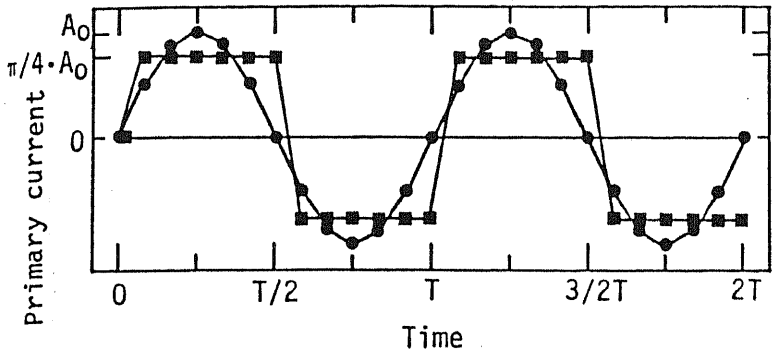

(d) Input current wave form (sinusoidal and square)

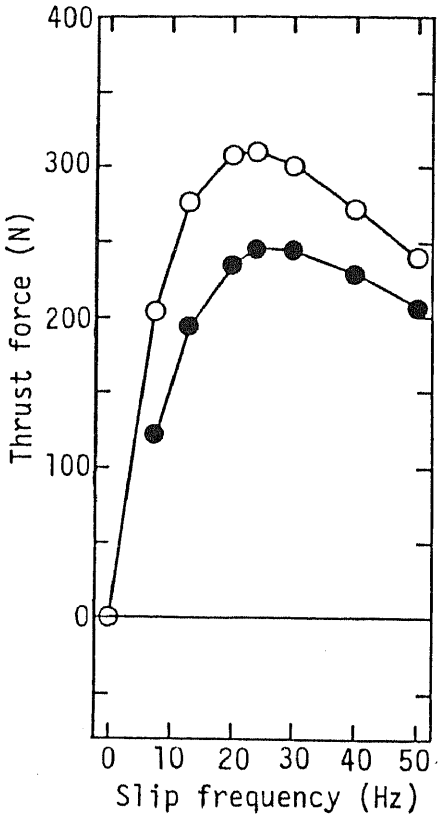

(e) sf- characteristics of thrust forces (time average)

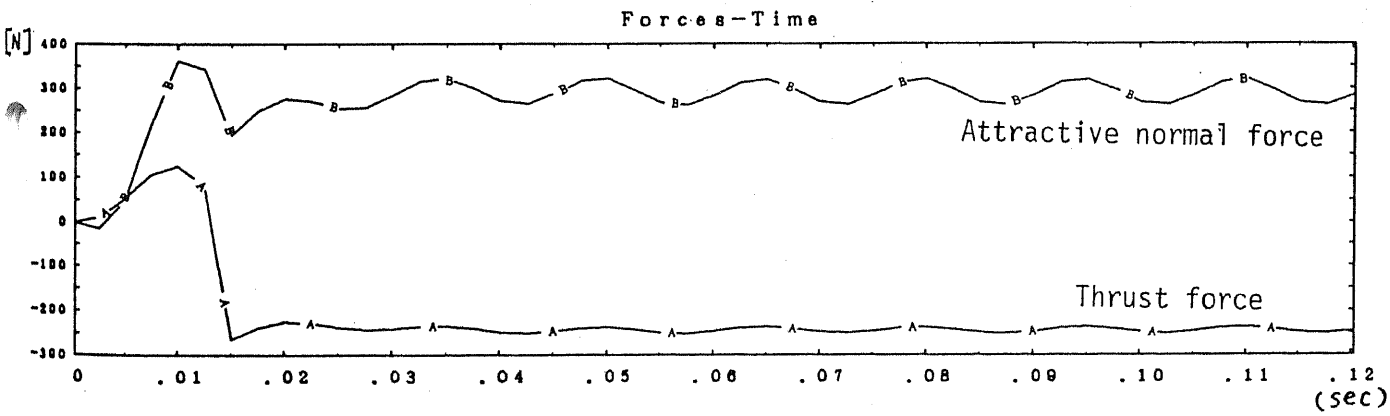

(f) Calculated forces from t=o to 4T (transient state; sf=24Hz)

Figure 4.5. An example of transient calculations.

Current form = SINUSOIDAL

sinusoidal current supplies.

4.2.3. Primary voltage induced in a conductor-bar

We see the voltages induced in the primary conductive bars in the case of the pattern I and $sf = 13.0Hz$ in the figure 4.6. The higher the speed of the secondary plate is, the larger the primary voltages are, since the primary frequency is larger at the higher speed. The voltage at the entry is smaller than in the central portion; it is more remarkable at higher speed. In other words, the primary currents at the entry portion are, conversely, larger than at the central one in the case of the voltage source.

The fatal problem of this virtual model machine is that the induced primary voltage is too small to design the power electronic switching units in practice: the largest on-stage voltage in the figure 4.6 is only $1V$ for the current of 1441A, which cannot be practically accepted. Some revisions of the motor structure are necessary; a tubular LIM will be used for the measurement in the chapter 5

4.2.4. Summary of basic calculations

The FSLIM is free of the restriction of the three- phase winding, therefore, an arbitrary magnetic flux wave can be synthesized in the air gap with appropriate switching sequences. The possibility to improve the motor characteristics will be verified with the basic calculation in the chapter 6; it is important to switch the current units so that the flux distribution may be as sinusoidal as possible.

From the basic calculations in this section, the following two problems have been noted:

(1) the so called end effects are serious especially for short FSLIMs like the model machine investigated here, since the effect depends substantially on the physical structure and dimensions of the machine itself, and

(2) the primary voltage is too small of the FSLIM with the single turn structure to design a realistic current supplying unit.

With (1) in mind, I will describe further calculations in the chapter 6. Although the FSLIM's structure with windings shown in the figure 4.7 could be attractive to avoid the problem (2), the analytical modeling will be difficult especially to consider the transverse edge effect, *i.e.*, remarkable leakage fluxes at the coil-end portions: the tubular FSLIM will, therefore, be calculated and measured in the next chapter as another practical alternative in spite of its limited possibilities of applications. Another merit of this type is that we need to consider neither compensation nor suppression of the normal force for a mechanical support in the gap.

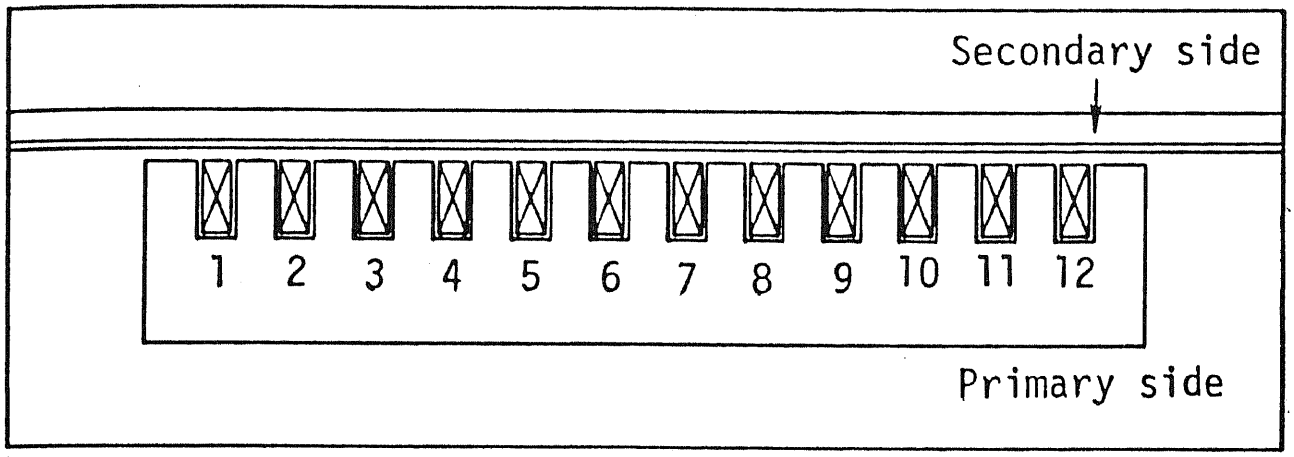

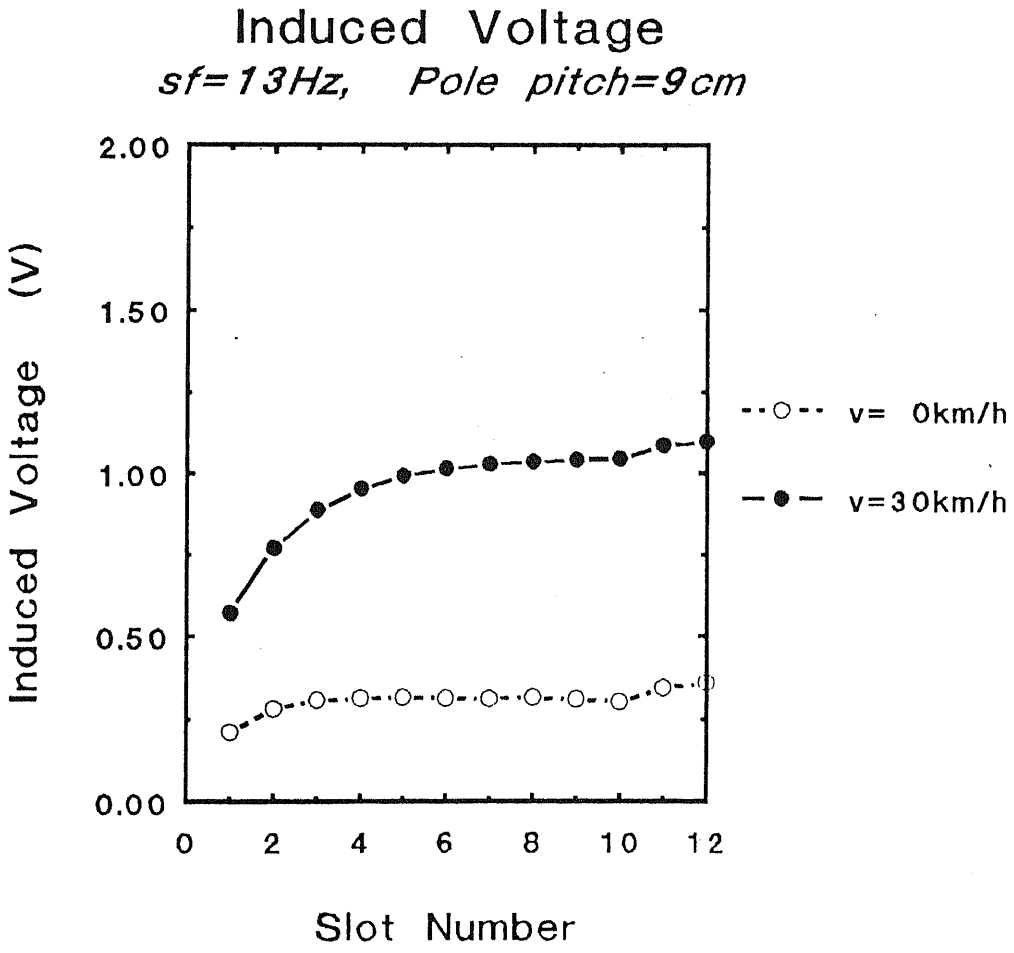

Figure 4.6. Voltage induced in primary conductors in each slot.

Anyway, such a trial- and error- investigation cannot be accepted for further concrete research, *i.e.*, a mathematically systematic approach is necessary for synthesizing the intended magnetic flux in reality. The method will be described in the following section using the principle of superposition of linear systems.

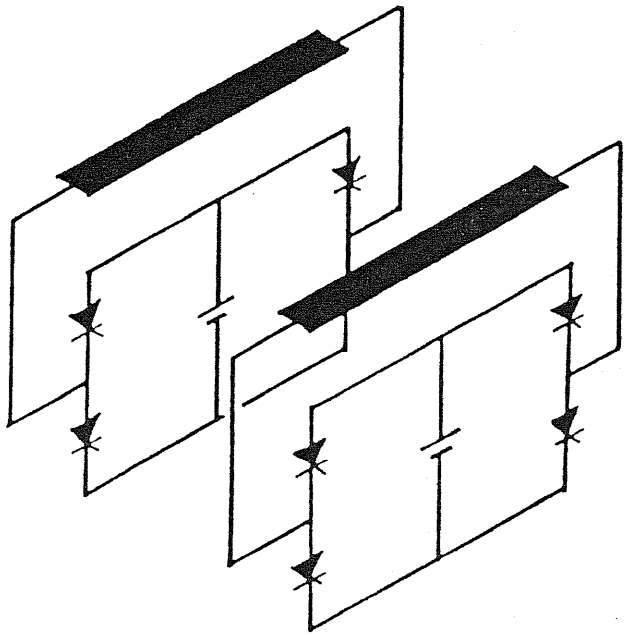

(a) Current supply
for each conductor

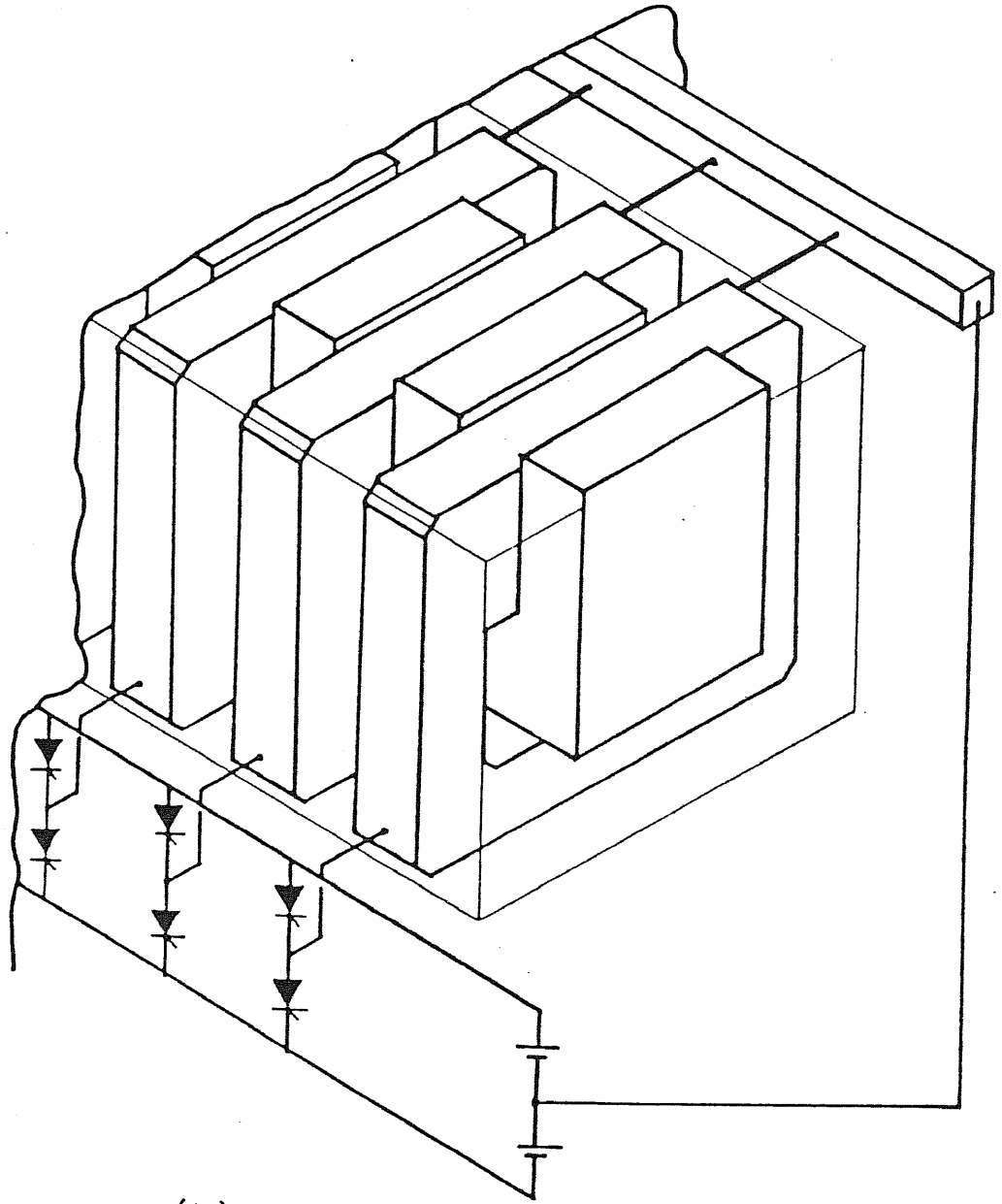

(b) A proposal of an FSLIM
with multi turn windings

Figure 4.7. Modified structure of the FSLIM with primary *winding.*

4.3. Decision scheme of switching patterns

4.3.1. Basic concept of the flux synthesis

First of all, the structure of the primary conductors of a FSLIM, whose neutral point is connected with the current source, is considered for simplicity. In this case, the freedom of the system is $2n$ where the $2n$ is the number of the independently controllable primary conductors. The distribution of the y- component of the magnetic flux density on 2n- points in the gap:

$$B_{y(1)},\ B_{y(2)},\ \ldots,\ B_{y(2n)}$$

or B_x and B_y on n- points:

$$B_{x(1)},\ B_{x(2)},\ \ldots,\ B_{x(n)}$$

$$B_{y(1)},\ B_{y(2)},\ \ldots,\ B_{y(n)}$$

can be arbitrarily decided, for instance, as shown in the figure 6.18 later. Considering that the thrust force of the motor is calculated with the equation (4.1) from the Maxwell's stress tensor, the latter alternative of point selection may me better.

$$F_x(t) = \frac{L}{\mu_0} \int B_y \cdot B_x \, dx \tag{4.1}$$

If the neutral point of the primary conductors is not connected with the current source, the freedom of the system is $2n-1$, because of an extra constraint to the primary current on account of the Kirchhoff's first law. There is, however, no intrinsic difference in the following mathematical formulations also in this case.

4.3.2. Stationary state with sinusoidal time dependency

Quasi- stationary state with the following assumptions can be analyzed with complex variables. ($e^{j\omega t}$- method)

(1) Currents and all the dependent variables vary sinusoidally with an angular frequency ω.

(2) The velocity of the secondary conductor is independent of the produced thrust force.

The current in each primary conductor and the magnetic flux density on each point are expressed with the complex vectors, which represent both amplitudes and phase differences, as follows:

$$\dot{\mathbf{I}} = \left[\dot{i}_1,\ \dot{i}_2,\ \ldots,\ \dot{i}_{2n}\right]^t \tag{4.2}$$

$$\dot{\mathbf{B}} = \left[\dot{B}_1,\ \dot{B}_2,\ \ldots,\ \dot{B}_{2n}\right]^t \tag{4.3}$$

The relation between the two vectors is formulated using a complex effect-coefficients-matrix P as follows:

$$\dot{P} \equiv \begin{bmatrix} \dot{P}_{1,1} & \cdots & \dot{P}_{1,2n} \\ \cdot & \cdots & \cdot \\ \cdot & \cdots & \cdot \\ \cdot & \cdots & \cdot \\ \dot{P}_{2n,1} & \cdots & \dot{P}_{2n,2n} \end{bmatrix} \tag{4.4}$$

$$\dot{\mathbf{B}} = \dot{P} \cdot \dot{\mathbf{I}} \tag{4.5}$$

That is to say,

$$\dot{\mathbf{B}}_i = \sum_{j=1}^{2n} \dot{P}_{ij} \cdot \dot{i}_j \qquad \left[i = 1, 2, \ldots, 2n \right] \tag{4.6}$$

where the dots $(\cdot)$ above the symbols mean complex variables.

If the electromagnetic field is calculated as shown in the figure 4.3 with the following input- current vector $\dot{\mathbf{I}}_1$:

$$\dot{\mathbf{I}}_1 = \left[1.0e^{j0}, 0, 0, \ldots, 0 \right]^t \tag{4.7}$$

then the calculated magnetic flux density vector $\dot{\mathbf{B}}_1$ is as follows:

$$\dot{\mathbf{B}}_1 = \left[\dot{P}_{1,1}, \dot{P}_{2,1}, \dot{P}_{3,1}, \ldots, \dot{P}_{2n,1} \right]^t \tag{4.8}$$

In the same way,

$$\begin{aligned} \dot{\mathbf{I}}_2 &= \left[0, 1.0e^{j0}, 0, 0, \ldots, 0 \right]^t \quad \rightarrow \quad \mathbf{B}_2 \\ \dot{\mathbf{I}}_3 &= \left[0, 0, 1.0e^{j0}, 0, \ldots, 0 \right]^t \quad \rightarrow \quad \mathbf{B}_3 \\ &\cdots\cdots\cdots\cdots\cdots\cdots\cdots\cdots \\ \dot{\mathbf{I}}_{2n} &= \left[0, 0, 0, 0, \ldots, 1.0e^{j0} \right]^t \quad \rightarrow \quad \mathbf{B}_{2n} \end{aligned} \tag{4.9}$$

all the factors of the matrix $\dot{P}$ can be calculated.

With the inverse matrix $\dot{Q} \equiv \dot{P}^{-1}$, the input current, to synthesize the intended flux density distribution $\dot{\mathbf{B}}_{design}$, are calculated as follows:

$$\dot{\mathbf{I}} = \dot{Q} \cdot \dot{\mathbf{B}}_{design} \tag{4.10}$$

It is also easy to calculate induced electromotive forces in primary conductors with the equation (4.11).

$$E_z = -\frac{\partial A_z}{\partial t} \tag{4.11}$$

Necessary input voltages in the case of a voltage source drive can, therefore, be calculated easily, too.

The mathematical algorithm is applicable also to a tubular LIM without intrinsic change.

4.3.3. Quasi- transient state

The quasi- transient state is defined here as follows:

(1) Currents and all the dependent variables vary unperiodically.

(2) The velocity of the secondary conductor is given independently of the produced thrust force.

The relation between the input currents and the magnetic flux densities is represented with a first- order time- differential equation, as written in the basic equation (2.2.3'). Hence, if $\dot{P}$s in (4.4) are separated into its real- and imaginary-parts as follows,

$$\dot{P} = P_r + j\omega P_i \tag{4.12}$$

the basic equation of the quasi- transient state corresponding to (4.5) is written as follows:

$$\mathbf{B}(t) = P_r\mathbf{I}(t) + P_i\frac{d\mathbf{I}(t)}{dt} \tag{4.13}$$

That is to say,

$$\frac{d\mathbf{I}(t)}{dt} = A\mathbf{I}(t) + \mathbf{f}(t) \tag{4.14}$$

$$A = -P_i^{-1}P_r \qquad (System\ matrix) \tag{4.15}$$

$$\mathbf{f}(t) = P_i^{-1}\mathbf{B}(t) \qquad (Input\ vector) \tag{4.16}$$

According to the theory of linear systems, the input current vector $\mathbf{I}(t)$ in the quasi- transient state is calculated using an initial time t_0 and the transition matrix $\Phi(t,t')$ in (4.18) of the homogeneous first order linear differential equation (4.17), as written in (4.19).

$$\frac{d\mathbf{x}(t)}{dt} = A\mathbf{x}(t) \tag{4.17}$$

$$\Phi(t,t') \equiv \exp\left[A(t-t')\right] \tag{4.18}$$

$$\mathbf{I}(t) = \Phi(t,t_0)\,\mathbf{I}(t_0) + \int_{t_0}^{t}\Phi(t,\tau)\,\mathbf{f}(\tau)\,d\tau \tag{4.19}$$

4.3.4. Transient state

The pure transient state is defined as follows:

(1) Current and all the dependent variables vary unperiodically.

(2) The velocity of the secondary conductor depends on the produced thrust force and mechanical loads.

In this case, the velocity v in (2.2.3') must be calculated from produced forces, *i.e.*, a numerical iterative procedure between electromagnetic- and mechanical- equations is inevitable. On account of this complexity, it will not be any more discussed in this paper.

References

[4-1] T. Koseki, H. Ohsaki and E. Masada: "A Novel Linear Induction Motor with an Arbitrary Magnetic Flux in the Air Gap", IPEC'90, pp. 913-918, Tokyo, April 1990

Chapter 5: Application of the field-coordinates oriented control scheme to the FSLIM

Introduction

The field- coordinates oriented control scheme has been developed and comprehensively applied to speed controls of induction motors, whose structure is inherently simple, and whose hardware and maintenance are, accordingly, cheap, on the basis of present improvement of power electronics, micro electronics, and modern control theories. On the other hand, conventional controls for LIMs have been quite simple at present; the on/off- control is applied to almost all the industrial transport lines, in addition, we can find some examples of the slip- frequency constant controls with VVVF inverters for vehicle propulsions. Although an accurate positioning and speed control are required to LIMs' drives these days, especially in industrial applications, responses of LIMs are unfortunately unsatisfying, since we cannot substantially know the exact state of the machines in the slip- frequency control without detection of the flux in the gap; responses to thrust force references have always delays due to the time constant "T_R" determined by the motor's inductance and secondary resistance, as described in the following subsections. The main purpose of this chapter is to establish a theoretical basis for applying the field-coordinates oriented control scheme to LIMs.

5.1. Modeling a linear induction motor for applying the field- coordinates oriented control

It is easy to accept the physical image of the field- coordinates oriented control model in the cases of rotary machines based on the coordinates transformation from the fixed α- and β- coordinates to the rotating d- and q- ones, but such a modeling based on the rotating space vector is not directly applicable to "linear" machines. In the following subsection, I will denote the formulations, not based on the physical image of the space vector, but the mathematical meaning of the complex expression of electromagnetic variables.

The frame work of the following formulation is based on the classic theory for rotary machines described by Prof. W. Leonhard [3-1] at the TU Braunschweig, who is the doctoral supervisor of F. Blaschke [5-1], with the following assumptions.

5.1.1. Physical model and assumptions

Assumptions for the analytical model illustrated in the figures 5.1 are as follows:

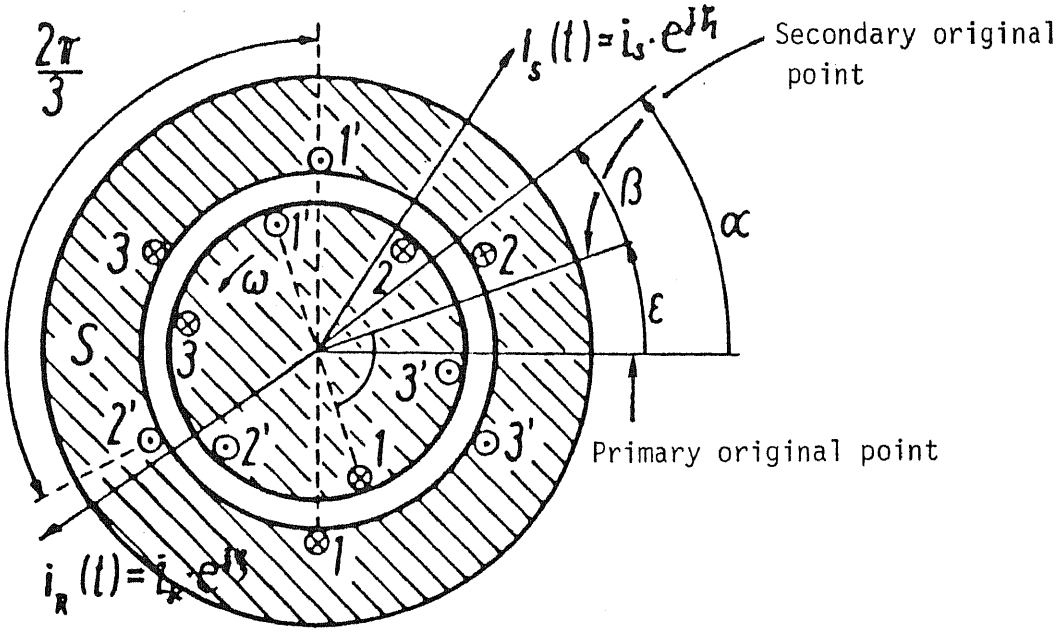

α: Angle seen from the stator side

β: Angle seen from the rotor side

ε: Rotary angle of the rotor seen from the stator

$\omega \equiv \dfrac{d\rho}{dt}$: Angular speed of the rotor

(a) Cross-section of a three- phase symmetric two- pole induction machine [3-1].

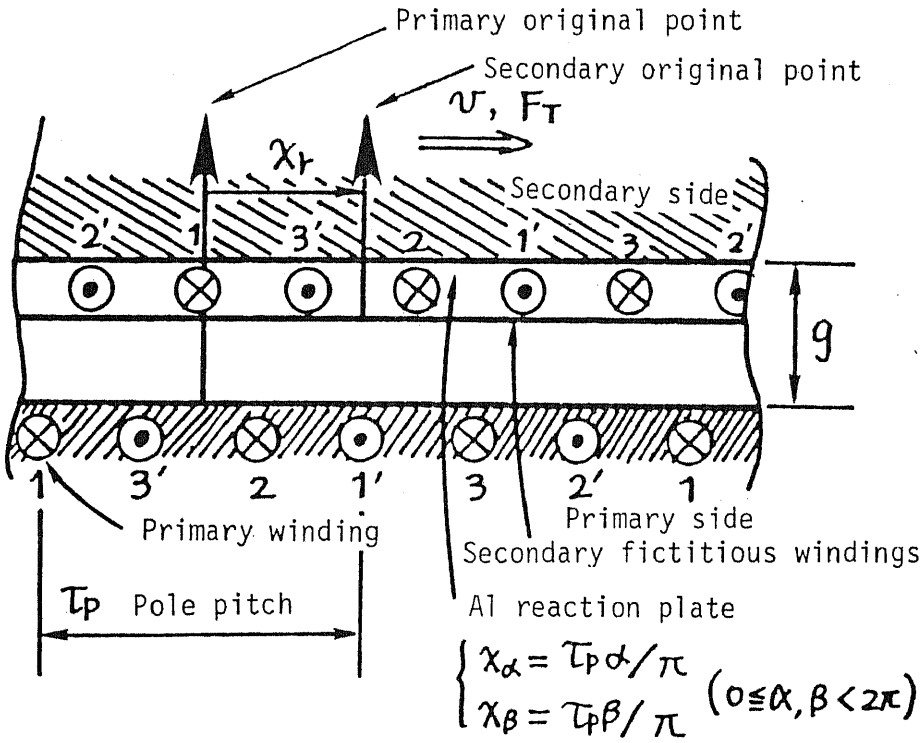

x_α: Position seen from the primary side

x_β: Position seen from the secondary side

x_r: Position of the secondary side seen from the primary side

$v \equiv \dfrac{dx_r}{dt}$: Speed of the secondary side

(b) The analysis model of an ideal LIM with infinite length corresponding to (a).

Figure 5.1. Basic model for calculations.

(1) the longitudinal end- and transverse edge- effects are neglected, since only the middle part of $2\tau_p$ length of a sufficiently long LIM is treated for simplicity;

(2) the permeabilities of the primary- and secondary- iron cores are infinitively large;

(3) the hysteresis- and eddy-current- losses in the cores are neglected;

(4) effects of the primary slots are neglected;

(5) distributions of the magnetomotive force, *i.e.*, 3-phases- windings are ideally sinusoidal and spatially symmetric; and

(6) there is no mechanical movement in the y- direction (up and down), *i.e.*, the gap length is constant.

The original point of the primary side (stator) locates on the central point between the primary windings 1 and 1'; in the same way, also the secondary original point, which should be in the region $0 \leq \frac{\pi}{\tau_p} x_\alpha < 2\pi$ on the primary coordinates, is set on the secondary side, as illustrated in the figure 5.1 (b).

5.1.2. Mathematical formulation of LIM's equations

On account of the symmetric 3-phases circuits, the stator currents $i_S(t)$ have the following relation.

$$i_{S1}(t) + i_{S2}(t) + i_{S3}(t) = 0 \tag{5.1}$$

According to the assumptions, the primary magnetomotive force in the gap is written as follows:

$$\Theta_S(x_\alpha, t) = N_S \left[i_{S1}(t)\cos\left[\frac{\pi}{\tau_p} x_\alpha\right] + i_{S2}(t)\cos\left[\frac{\pi}{\tau_p} x_\alpha - \frac{2}{3}\pi\right] + i_{S3}(t)\cos\left[\frac{\pi}{\tau_p} x_\alpha - \frac{4}{3}\pi\right]\right] \tag{5.2}$$

where N_S is the primary winding number per one pole. The sinusoidal functions should be expressed with the complex forms, *e.g.*, $\cos\alpha = \frac{1}{2}\left[e^{j\alpha} + e^{-j\alpha}\right]$. The equation (5.2) is then written as follows:

$$\Theta_S(x_\alpha, t) = \frac{1}{2} N_S \left[\mathbf{i}_S(t) e^{-j\frac{\pi}{\tau_p} x_\alpha} + \mathbf{i}_S^*(t) e^{j\frac{\pi}{\tau_p} x_\alpha} \right] \tag{5.3}$$

where the boldface characters mean complex variables and the $*$ means complex conjugate. $\mathbf{i}_S(t)$ corresponds to the space- and complex- vector in the theories for ordinary rotary machines.

$$\mathbf{i}_S(t) = \left[i_{S1}(t) + i_{S2}(t)e^{j\frac{2}{3}\pi} + i_{S3}(t)e^{j\frac{4}{3}\pi} \right]$$

$$= i_S(t) \cdot e^{j\zeta(t)} \tag{5.4.a}$$

where $\zeta(t)$ is the phase angle of the $\mathbf{i}_S$ seen from the original point of the primary side.

$$\mathbf{i}_S^*(t) = \left[i_{S1}(t) + i_{S2}(t)e^{-j\frac{2}{3}\pi} + i_{S3}(t)e^{-j\frac{4}{3}\pi} \right] \tag{5.4.b}$$

Θ_S is a real value, *i.e.*, it is physically observable. When $\mathbf{i}_S$ is expressed with the magnitude and the phase angle $\zeta(t)$:

$$\mathbf{i}_S(t) = i_S(t) \cdot e^{j\zeta(t)} \tag{5.5}$$

$i_S(t)$ corresponds to the instant maximum value of the spatial wave of the magnetomotive force, and $\zeta(t)$ is the phase angle of the maximum point of the magnetomotive force along the stator (see the figure 5.1.(a)).

$$\Theta_S(t) = N_S\, \mathbf{i}_S(t) \tag{5.6}$$

In the same way, we can describe mathematically the magnetomotive force produced by the fictitious secondary windings, which are moving with the speed $v(t)$ along the x- axis, seen from the secondary original point.

$$\Theta_R(x_\beta, t) = N_R \left[i_{R1}(t)\cos\left(\frac{\pi}{\tau_p}x_\beta\right) + i_{R2}(t)\cos\left(\frac{\pi}{\tau_p}x_\beta - \frac{2}{3}\pi\right) + i_{R3}(t)\cos\left(\frac{\pi}{\tau_p}x_\beta - \frac{4}{3}\pi\right)\right] \tag{5.7}$$

where N_R is the winding number of the fictitious secondary windings per one pole.

$$\mathbf{i}_R(t) = \left[i_{R1}(t) + i_{R2}(t)e^{j\frac{2}{3}\pi} + i_{R3}(t)e^{j\frac{4}{3}\pi} \right]$$

$$= i_R(t) \cdot e^{j\xi(t)} \tag{5.8.a}$$

and

$$\mathbf{i}_R^*(t) = \left[i_{R1}(t) + i_{R2}(t)e^{-j\frac{2}{3}\pi} + i_{R3}(t)e^{-j\frac{4}{3}\pi} \right] \tag{5.8.b}$$

where $\xi(t)$ is the phase angle of the $\mathbf{i}_R$ seen from the original point of the secondary side.

$$\Theta_R(x_\beta,\, t) = \frac{1}{2}N_R\left[\mathbf{i}_R(t)e^{-j\frac{\pi}{\tau_P}x_\beta} + \mathbf{i}_R^*(t)e^{j\frac{\pi}{\tau_P}x_\beta}\right] \tag{5.9}$$

Θ_R is a real value, too. The coordinates of the primary- and the secondary- sides have the following relation.

$$x_\beta = x_\alpha - x_r \tag{5.10}$$

$$\Theta_R(x_\alpha,x_r,t) = \frac{1}{2}N_R\left[\mathbf{i}_R(t)e^{-j\frac{\pi}{\tau_p}(x_\alpha-x_r)} + \mathbf{i}_R^*(t)e^{j\frac{\pi}{\tau_p}(x_\alpha-x_r)}\right] \tag{5.11}$$

These primary- and secondary- magnetomotive forces are superposed as follows.

$$\Theta(x_\alpha,x_r,t) = \Theta_S(x_\alpha,t) + \Theta_R(x_\alpha,x_r,t) \tag{5.12}$$

Since the permeabilities of the cores are assumed to be infinite, and the end-, edge-, and slotting- effects are neglected, the relation between the total magneto-motive force and the gap flux density depends only on the gap length g:

$$B_S(x_\alpha,x_r,t) = \frac{\mu_0}{2g}\left[\Theta_S(x_\alpha,t) + \kappa\Theta_R(x_\alpha,x_r,t)\right] \tag{5.13}$$

where μ_0 is a permeability of the space, κ is an effective coefficient of flux linkage between the primary- and the secondary- side considering flux leakages.

When we assume the ideal sinusoidal distribution of the windings, the average flux linkage (per a pole pair $2\cdot\tau_p$) of the primary winding of the first phase is calculated with the following double integral form:

$$\psi_{S1}(t) = \frac{1}{2}\frac{\pi}{\tau_P}N_S\int_{x_A=-\frac{\tau_p}{2}}^{\frac{\tau_p}{2}}\cos\frac{\pi}{\tau_p}x_A\cdot\left[\int_{x_\alpha=x_A-\frac{\tau_p}{2}}^{x_A+\frac{\tau_p}{2}} l_y B_S(x_\alpha,x_r,t)\, dx_\alpha\right] dx_A \tag{5.14}$$

where l_y is an effective transverse width of the LIM. The integral with x_α is due to the spatial distribution of the gap flux density along the x axis, and the other one with x_A is owing to the spatial sinusoidal distribution of the winding illustrated in the figure 5.3. (Since the total winding number integrated in a pole pitch is N_S turns, the distribution of the windings is written as $N_{S1}(x_n) = \frac{1}{2}\frac{\pi}{\tau_P}N_S\cos\frac{\pi}{\tau_p}x_A$, when the point A is the original point.) By substituting the equations (5.3), (5.11) and (5.13) into (5.14), ψ_{S1} is written as follows.

$$\psi_{Sa}(t) = \frac{N_S^2 l_y\mu_0\tau_p}{8g}\left[\mathbf{i}_S(t) + \mathbf{i}_S^*(t)\right] + \kappa\frac{N_S N_R l_y\mu_0\tau_p}{8g}\left[\mathbf{i}_R(t)e^{j\frac{\pi}{\tau_p}x_r} + \mathbf{i}_R^*(t)e^{-j\frac{\pi}{\tau_p}x_r}\right] \tag{5.15}$$

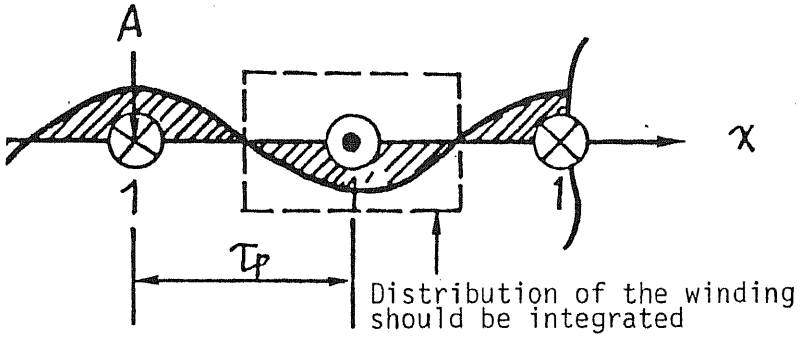

Figure 5.2. Ideal sinusoidal distribution of windings.

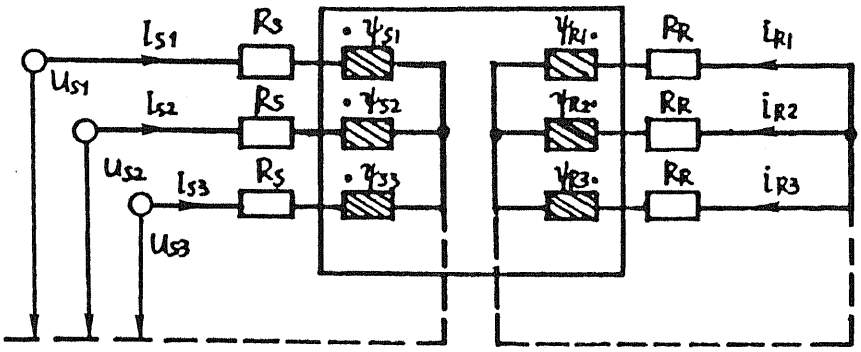

Figure 5.3. Relation between terminal voltages and flux linkage.

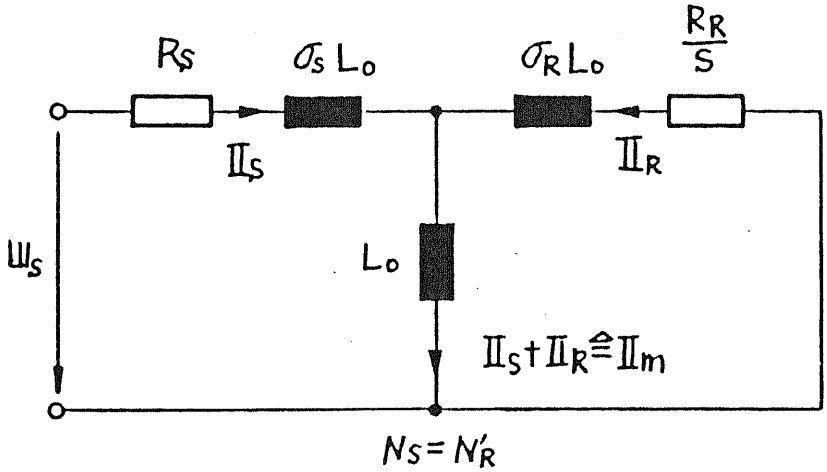

Figure 5.4. Equivalent circuit of an IM in the stationary state.

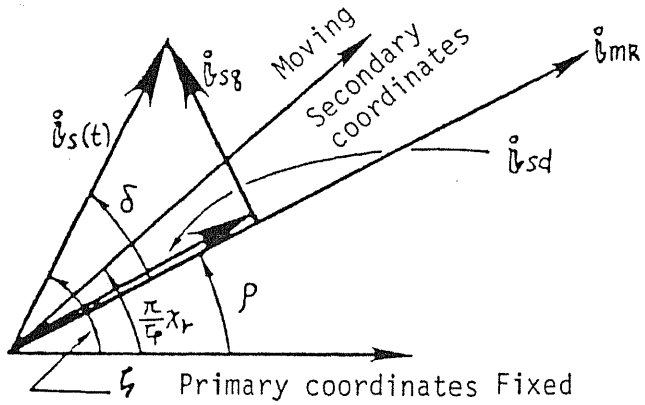

Figure 5.5. Relation among current complex vectors.

If the primary self inductance L_S and the mutual inductance between the primary- and secondary- windings M, which are average values per $2\tau_p$, are defined as follows:

$$\frac{N_S^2 l_y \mu_0 \tau_p}{8g} = \frac{1}{3} L_S \tag{5.16.a}$$

and

$$\frac{\kappa N_S N_R l_y \mu_0 \tau_p}{8g} = \frac{1}{3} M \tag{5.16.b}$$

then the equation (5.15) is written as follows.

$$\psi_{S1}(t) = \frac{1}{3} L_S \left[\mathbf{i}_S(t) + \mathbf{i}_S^*(t) \right] + \frac{1}{3} M \left[\mathbf{i}_R(t) e^{j\frac{\pi}{\tau_p} x_r} + \mathbf{i}_R^*(t) e^{-j\frac{\pi}{\tau_p} x_r} \right] \tag{5.17.a}$$

The same formulations are applied to the second- and third- phases.

$$\psi_{S2}(t) = \frac{1}{3} L_S \left[\mathbf{i}_S(t) e^{-j\frac{2}{3}\pi} + \mathbf{i}_S^*(t) e^{j\frac{2}{3}\pi} \right] + \frac{1}{3} M \left[\mathbf{i}_R(t) e^{j(\frac{\pi}{\tau_p} x_r - \frac{2}{3}\pi)} + \mathbf{i}_R^*(t) e^{-j(\frac{\pi}{\tau_p} x_r - \frac{2}{3}\pi)} \right] \tag{5.17.b}$$

$$\psi_{S3}(t) = \frac{1}{3} L_S \left[\mathbf{i}_S(t) e^{-j\frac{4}{3}\pi} + \mathbf{i}_S^*(t) e^{j\frac{4}{3}\pi} \right] + \frac{1}{3} M \left[\mathbf{i}_R(t) e^{j(\frac{\pi}{\tau_p} x_r - \frac{4}{3}\pi)} + \mathbf{i}_R^*(t) e^{-j(\frac{\pi}{\tau_p} x_r - \frac{4}{3}\pi)} \right] \tag{5.17.c}$$

$\psi_S(t)$ is defined here using the symmetry of the equations (5.17):

$$\psi_S(t) = \psi_{S1} + \psi_{S2} e^{j\frac{2}{3}\pi} + \psi_{S3} e^{j\frac{4}{3}\pi} \tag{5.18}$$

$$= L_S \mathbf{i}_S(t) + M \mathbf{i}_R(t) e^{j\frac{\pi}{\tau_p} x_r} \tag{5.19}$$

On account of:

$$1 + e^{j\frac{2}{3}\pi} + e^{j\frac{4}{3}\pi} = 0$$

the terms of complex conjugate are eliminated by themselves. The amplitude of $\psi_S(t)$ corresponds to the instant maximum value of the spatial wave of the flux,

and its angle is the phase angle of the maximum point of the flux along the stator from the original point of the primary side.

The flux linked with the secondary fictitious windings is calculated in the same way. The equation (5.3) is written using the equation (5.10) as follows:

$$\Theta_S(x_\alpha,x_r,t) = \frac{1}{2}N_S\left[\mathbf{i}_S(t)e^{-j\frac{\pi}{\tau_p}(x_\beta+x_r)} + \mathbf{i}_S^*(t)e^{j\frac{\pi}{\tau_p}(x_\beta+x_r)}\right] \tag{5.20}$$

This term makes a flux wave corresponding to the equation (5.13) on the surface of the secondary side together with secondary currents; the secondary flux density is as follows:

$$B_R(x_\beta,x_r,t) = \frac{\mu_0}{2g}\left[\Theta_R(x_\beta,t) + \kappa\Theta_S(x_\beta,x_r,t)\right] \tag{5.21}$$

By integrating sinusoidal distribution functions on the surface of the secondary conductor in the same way as the equation (5.14), and with the following definition of the secondary inductance per a pole-pair,

$$\frac{N_R^2 l_y \mu_0 \tau_p}{8g} = \frac{1}{3}L_R \tag{5.16.c}$$

the fluxes linked with the three- phase secondary fictitious windings are calculated as follows:

$$\psi_{R1}(t) = \frac{1}{3}L_R\left[\mathbf{i}_R(t) + \mathbf{i}_R^*(t)\right] + \frac{1}{3}M\left[\mathbf{i}_S(t)e^{-j\frac{\pi}{\tau_p}x_r} + \mathbf{i}_S^*(t)e^{j\frac{\pi}{\tau_p}x_r}\right] \tag{5.22.a}$$

$$\psi_{R2}(t) = \frac{1}{3}L_R\left[\mathbf{i}_R(t)e^{-j\frac{2}{3}\pi} + \mathbf{i}_R^*(t)e^{j\frac{2}{3}\pi}\right] + \frac{1}{3}M\left[\mathbf{i}_S(t)e^{-j(\frac{\pi}{\tau_p}x_r-\frac{2}{3}\pi)} + \mathbf{i}_S^*(t)e^{j(\frac{\pi}{\tau_p}x_r-\frac{2}{3}\pi)}\right] \tag{5.22.b}$$

$$\psi_{R3}(t) = \frac{1}{3}L_R\left[\mathbf{i}_R(t)e^{-j\frac{4}{3}\pi} + \mathbf{i}_R^*(t)e^{j\frac{4}{3}\pi}\right] + \frac{1}{3}M\left[\mathbf{i}_S(t)e^{-j(\frac{\pi}{\tau_p}x_r-\frac{4}{3}\pi)} + \mathbf{i}_S^*(t)e^{j(\frac{\pi}{\tau_p}x_r-\frac{4}{3}\pi)}\right] \tag{5.22.c}$$

The primary current vector seems to move backward in the equations (5.22), since it is observed from the moving secondary side.

The secondary magnetic flux is summed up in the same way as the primary circuit:

$$\psi_R(t) = \psi_{R1} + \psi_{R2}e^{j\frac{2}{3}\pi} + \psi_{R3}e^{j\frac{4}{3}\pi}$$

$$= L_R\mathbf{i}_R(t) + M\mathbf{i}_S(t)e^{-j\frac{\pi}{\tau_p}x_r} \tag{5.23}$$

Voltage equations are written based on (5.17) and (5.22) as follows; see the figure 5.3:

$$\begin{aligned} R_S i_{S1} + \frac{d\psi_{S1}}{dt} &= u_{S1}(t) \\ R_S i_{S2} + \frac{d\psi_{S2}}{dt} &= u_{S2}(t) \\ R_S i_{S3} + \frac{d\psi_{S3}}{dt} &= u_{S3}(t) \end{aligned} \tag{5.24}$$

where R_S is a line resistance per one phase, and forms of the voltages can be arbitrary.

$$\mathbf{u}_S(t) = u_{S1}(t) + u_{S2}(t)e^{j\frac{2}{3}\pi} + u_{S3}(t)e^{j\frac{4}{3}\pi} \tag{5.25}$$

With the equations (5.4) and (5.19):

$$R_S\mathbf{i}_S + \frac{d\psi_S}{dt} = R_S\mathbf{i}_S + L_S\frac{d\mathbf{i}_S}{dt} + M\frac{d}{dt}\left[\mathbf{i}_R e^{j\frac{\pi}{\tau_p}x_r}\right] = \mathbf{u}_S \tag{5.26}$$

With the following instant velocity of the secondary conductor $v \equiv \frac{dx_r}{dt}$, the equation (5.26) is written as follows:

$$R_S\mathbf{i}_S + L_S\frac{d\mathbf{i}_S}{dt} + M\frac{d\mathbf{i}_R}{dt}e^{j\frac{\pi}{\tau_p}x_r} + j\frac{\pi}{\tau_p}vM\mathbf{i}_R e^{j\frac{\pi}{\tau_p}x_r} = \mathbf{u}_S \tag{5.27}$$

The secondary current is separated into two terms in the equation (5.27); one is from the transformer electromotive force through the mutual inductance, and the other is from the speed electromotive force of the secondary conductor. By substituting the equation (5.17) into (5.24) and taking the equation (5.1) into account, we can obtain the following symmetrical relation among the primary voltages.

$$u_{S1}(t) + u_{S2}(t) + u_{S3}(t) = 0 \tag{5.28}$$

The secondary fictitious windings are short circuits and three- phase currents are balanced:

$$i_{R1}(t) + i_{R2}(t) + i_{R3}(t) = 0 \tag{5.29}$$

$$R_R i_{R1} + \frac{d\psi_{S1}}{dt} = 0$$

$$R_R i_{R2} + \frac{d\psi_{S2}}{dt} = 0 \qquad (5.30)$$

$$R_R i_{R3} + \frac{d\psi_{S3}}{dt} = 0$$

Voltage equations for the secondary side are written in the same way as the equation (5.26), using (5.8) and (5.23) as follows:

$$R_R \mathbf{i}_R + \frac{d\psi_R}{dt} = R_R \mathbf{i}_R + L_R \frac{d\mathbf{i}_R}{dt} + M \frac{d}{dt}\left[\mathbf{i}_S e^{-j\frac{\pi}{\tau_p}x_r}\right] = 0 \qquad (5.31)$$

Thus:

$$R_R \mathbf{i}_R + L_R \frac{d\mathbf{i}_R}{dt} + M \frac{d\mathbf{i}_S}{dt} e^{-j\frac{\pi}{\tau_p}x_r} + j\frac{\pi}{\tau_p} v M \mathbf{i}_S e^{-j\frac{\pi}{\tau_p}x_r} = 0 \qquad (5.32)$$

The following calculation of the thrust force is also important to connect the electric equations above with mechanical equations. The flux density on the surface of the secondary conductor, which is produced by the primary currents themselves, is derived from the equation (5.21) by seeing only the terms concerning Θ_S as follows:

$$B_{RS}(x_\beta, x_r, t) = \kappa \frac{\mu_0 N_S}{4g}\left[\mathbf{i}_S e^{-j\frac{\pi}{\tau_P}(x_\beta + x_r)} + \mathbf{i}_S^* e^{j\frac{\pi}{\tau_P}(x_\beta + x_r)}\right] \qquad (5.33)$$

There is no force corresponding to the "reluctance torque", on account of the constant gap length, *i.e.*, the term of the currents has no contribution to the calculation of the thrust force by themselves. The secondary current is calculated as follows, when the distribution of the secondary windings is assumed to be sinusoidal.

$$a_R(x_\beta, t) = \frac{1}{2}\frac{\partial \Theta(x_\beta, t)}{\partial x_\beta}$$

$$= -j\frac{N_R \pi}{4\tau_p}\left[\mathbf{i}_R e^{-j\frac{\pi}{\tau_p}x_\beta} - \mathbf{i}_R^* e^{j\frac{\pi}{\tau_p}x_\beta}\right] \qquad (5.34)$$

The thrust force per pole-pair $2\tau_p$ is integrated as follows:

$$F_T(t) = l_y \int_0^{2\tau_p} B_{RS}(x_\beta, x_r, t) \cdot a_R(x_\beta, t)\, dx_\beta \qquad (5.35)$$

By substituting the equations (5.33) and (5.34) into (5.35):

$$F_T(t) = \frac{2}{3}\left[\frac{\pi}{\tau_p}\right] M \cdot \mathrm{Im}\left[\mathbf{i}_S(t) \cdot \left[\mathbf{i}_R e^{j\frac{\pi}{\tau_p}x_r}\right]^*\right] \tag{5.36}$$

By assuming $N_R = N_S$, the inductances are represented using the following leakage factor as follows:

$$\begin{aligned} L_S &= (1+\sigma_S)\, L_0 \\ L_R &= (1+\sigma_R)\, L_0 \\ M &= L_0 \end{aligned} \tag{5.37}$$

where L_0 is a main inductance in an equivalent circuit of an IM, σ_S and σ_R are the primary- and secondary- leakage factors respectively.

Finally, the electric- and mechanical- basic equations are as follows:

$$R_S \mathbf{i}_S + L_S \frac{d\mathbf{i}_S}{dt} + L_0 \frac{d\mathbf{i}_R}{dt} e^{j\frac{\pi}{\tau_p}x_r} + j\frac{\pi}{\tau_p} v M \mathbf{i}_R e^{j\frac{\pi}{\tau_p}x_r} = \mathbf{u}_S \tag{5.38}$$

$$R_R \mathbf{i}_R + L_R \frac{d\mathbf{i}_R}{dt} + L_0 \frac{d}{dt}\left[\mathbf{i}_S e^{-j\frac{\pi}{\tau_p}x_r}\right] = 0 \tag{5.39}$$

$$m\frac{dx}{dt} = F_T - F_L = \frac{2}{3}\left[\frac{\pi}{\tau_p}\right] L_0 \cdot \mathrm{Im}\left[\mathbf{i}_S(t) \cdot \left[\mathbf{i}_R e^{j\frac{\pi}{\tau_p}x_r}\right]^*\right] - F_L(x_r, v, t) \tag{5.40}$$

$$\frac{dx_r}{dt} = v \tag{5.41}$$

where a mass attached to the mover is m, and an outer mechanical load is F_L. Since the equations with complex variables (5.38) and (5.39) are separated to their real- and imaginary- parts, the equations from the (5.38) to the (5.41) are six simultaneous nonlinear differential equations for one- dimensional mechanical movement.

5.1.3. Derivation of equivalent circuit of a symmetric IM

In order to derive an equivalent circuit of an ordinary induction machine, a symmetric three- phase ideally sinusoidal voltage source is assumed to be connected to the primary terminals in this subsection:

$$\begin{aligned} u_{S1}(t) &= \sqrt{2}\, U_S \cos(\omega_1 t + \phi_1) = \mathrm{Re}\left[\sqrt{2}\, U_S \cdot e^{j\phi_1} \cdot e^{j\omega_1 t}\right] \\ &= \frac{\sqrt{2}}{2}\left[\mathbf{U}_S \cdot e^{j\omega t} + \mathbf{U}_S^* \cdot e^{-j\omega t}\right] \end{aligned} \tag{5.42.a}$$

where $\mathbf{U}_S = U_S \cdot e^{j\phi_1}$, in the same way:

$$u_{S2} = \frac{\sqrt{2}}{2}\left[\mathbf{U}_S \cdot e^{\left(j\omega t - \frac{2}{3}\pi\right)} + \mathbf{U}_S^* \cdot e^{-\left(j\omega t - \frac{2}{3}\pi\right)}\right] \tag{5.42.b}$$

$$u_{S3} = \frac{\sqrt{2}}{2}\left[\mathbf{U}_S \cdot e^{\left(j\omega t - \frac{4}{3}\pi\right)} + \mathbf{U}_S^* \cdot e^{-\left(j\omega t - \frac{4}{3}\pi\right)}\right] \tag{5.42.c}$$

$$\mathbf{u}_S(t) = u_{s1} + u_{s2} \cdot e^{j\frac{2}{3}\pi} + u_{s3} \cdot e^{j\frac{4}{3}\pi}$$

$$= \frac{3}{2}\sqrt{2}\mathbf{U}_S \cdot e^{j\omega_1 t} \tag{5.43}$$

Terms of complex conjugates are eliminated by themselves. Since the primary currents are also symmetric, by substituting currents for $i_{S1}(t) = \frac{\sqrt{2}}{2}\left[\mathbf{I}_S \cdot e^{j\omega_1 t} + \mathbf{I}_S^* \cdot e^{-j\omega_1 t}\right]$ and so on, the primary current complex vector is simply written as follows:

$$\mathbf{i}_S(t) = \frac{3}{2}\sqrt{2}\mathbf{I}_S \cdot e^{j\omega_1 t} \tag{5.44}$$

On account of the stationary state, the secondary speed v is constant, and when the secondary angular speed is expressed as:

$$\omega = \frac{\pi}{\tau_p} v: \quad const. \tag{5.45}$$

the secondary slip angular speed is defined as follows:

$$\omega_2 = \omega_1 - \omega \tag{5.46}$$

With this in mind, by writing $i_{R1} = \frac{\sqrt{2}}{2}\left[\mathbf{I}_R \cdot e^{j\left(\omega_1 - \omega\right)t} + \mathbf{I}_R^* \cdot e^{-j\left(\omega_1 - \omega\right)t}\right]$ and so on, the secondary current complex vector is written as follows in the same way:

$$\mathbf{i}_R(t) = \frac{3}{2}\sqrt{2}\mathbf{I}_R \cdot e^{j\left(\omega_1 - \omega\right)t} \tag{5.47}$$

The following two voltage equations for a stationary operation are derived from the equations (5.38) and (5.39):

$$\left(R_S + j\omega_1\sigma_S L_0\right)\cdot\mathbf{I}_S + j\omega_1 L_0\left(\mathbf{I}_S + \mathbf{I}_R\right) = \mathbf{U}_S \tag{5.48}$$

$$\left(R_R + j\omega_2\sigma_R L_0\right)\cdot\mathbf{I}_R + j\omega_2 L_0\left(\mathbf{I}_S + \mathbf{I}_R\right) = 0 \tag{5.49}$$

The slip is defined as follows:

$$s = \frac{\omega_2}{\omega_1} = \frac{\omega_1 - \omega}{\omega_1} \tag{5.50}$$

By dividing both hand sides of the equation (5.49) by the slip, the following equation is derived, hence, the equivalent circuit of an induction motor in the figure 5.4 is illustrated considering the equations (5.48) and (5.51).

$$\left[\frac{R_R}{s}+j\omega_1\sigma_R L_0\right]\cdot\mathbf{I}_R + j\omega_1 L_0\left[\mathbf{I}_S+\mathbf{I}_R\right] = 0 \qquad (5.51)$$

5.1.4. Application of the field- coordinates oriented control theory

In this subsection, theoretical investigation on the following purposes is described with the basic formulation in the previous subsections:

(1) to supply asymmetric currents to n- conductors of the FSLIM so that the flux distribution in the gap may be sinusoidal, and

(2) to control instant value of thrust forces by applying the field- coordinates oriented control scheme to the FSLIM under the condition of the (1).

Concrete examples with simulations will be described in the next chapter, where also some basic measurements are compared with the calculations of a tubular LIM, normal forces of which need not to be considered.

The electrical and mechanical basic equations from (5.38) to (5.41) are based on the ideally symmetric LIM model without any end effects; the inherently significant assumptions are as follows.

- ☐ The stator gap-flux distribution is sinusoidal in the active region for the representation of the $\mathbf{i}_S(t)$ as a complex vector: "the stator flux" is defined here as the gap flux which were produced only by primary currents if the secondary conductivity were zero, *i.e.,* with no secondary current.
- ☐ The rotor gap-flux distribution is sinusoidal in the active region for the representation of the $\mathbf{i}_R(t)$ as a complex vector: "the rotor flux" is defined here as the gap flux which were produced only by secondary currents without any primary currents; it is a completely fictitious and unobservable value in reality, since the secondary currents are always induced by the primary alternative current.

It is difficult to control instant values of real LIMs properly, for the assumptions above are not valid in reality, but either the stator flux- or the total flux- distribution can be sinusoidal with controlling the FSLIM by supplying appropriate asymmetrical currents based on the scheme described in the chapter 4. We can never control the rotor current, *i.e.,* rotor flux. However, also the rotor current may be considerably sinusoidal in low speed operations by controlling and forming the stator flux sinusoidal. The application of the field- coordinate control scheme is possible under such conditions, though calculations for determining the current patterns are much more complicated than of ordinary induction motors, since we cannot

use simple calculating procedure based on the equivalent circuit in the previous subsection and $2\phi \rightarrow 3\phi$ transformation.

The control of instant values is substantially a transient phenomenon; a transient analysis program is necessary for simulating it in general. In the field- coordinates oriented control, however, transient phenomena with a large time constant are suppressed by keeping the *field excitation* constant as described in the following formulations. We can, consequently, make some basic investigations on the control scheme with a stationary simulation.

The thrust force per one pole-pair is quoted from the equation (5.40) as follows:

$$F'_{motor}(t) = \frac{2}{3}\left[\frac{\pi}{\tau_p}\right] L_0 \cdot \mathrm{Im}\left[\mathbf{i}_S(t) \cdot \left[\mathbf{i}_R e^{j\frac{\pi}{\tau_p}x_r}\right]^*\right] \tag{5.52}$$

In the equation (5.52), the secondary current $\mathbf{i}_R$ is an unobservable value; the term $\mathbf{i}_R \cdot e^{j\frac{\pi}{\tau_p}x_r}$ should be expressed with other values. The following magnetizing current $\mathbf{i}_{mR}$ is, hence, introduced on the stator coordinates, by dividing both hand sides of the equation (5.23) by the main inductance L_0, and multiplying it by $e^{j\frac{\pi}{\tau_p}x_r}$.

$$\mathbf{i}_{mR}(t) = \mathbf{i}_S(t) + \left[1+\sigma_R\right]\mathbf{i}_R(t) \cdot e^{j\frac{\pi}{\tau_p}x_r} = i_{mR}(t) \cdot e^{j\rho(t)} \tag{5.53}$$

By substituting the equation (5.53) into (5.52), the force is written as follows:

$$\begin{aligned} F'_{motor}(t) &= \frac{2}{3}\left[\frac{\pi}{\tau_p}\right]\frac{L_0}{1+\sigma_R} \cdot \mathrm{Im}\left[\mathbf{i}_S \cdot (\mathbf{i}_{mR} - \mathbf{i}_S)^*\right] \\ &= \frac{2}{3}\left[\frac{\pi}{\tau_p}\right]\frac{L_0}{1+\sigma_R} \cdot \mathrm{Im}\left[\mathbf{i}_S \cdot \mathbf{i}_{mR}\right] \\ &= \frac{2}{3}\left[\frac{\pi}{\tau_p}\right]\frac{L_0}{1+\sigma_R} \cdot i_{mR} \cdot \mathrm{Im}\left[\mathbf{i}_S \cdot e^{-j\rho}\right] \end{aligned} \tag{5.54}$$

where $\rho(t)$ means a position of the maximum total flux wave linked with the secondary conductor seen from the primary original point. With the figure 5.5 in mind:

$$\mathbf{i}_S \cdot e^{-j\rho} = i_S \cdot e^{(\zeta-\rho)} = i_S \cdot e^{j\delta} \tag{5.55}$$

$$= i_{Sd} + j \cdot i_{Sq} \tag{5.56}$$

where the angle $\delta(t)$ is defined: $\delta(t) \equiv \zeta(t) - \rho(t)$.

$$i_{Sd} = \mathrm{Re}\left[\mathbf{i}_S \cdot e^{-j\rho}\right] = i_S \cos\delta \tag{5.57}$$

$$i_{Sq} = \mathrm{Im}\left[\mathbf{i}_S \cdot e^{-j\rho}\right] = i_S \sin\delta \tag{5.58}$$

With the coefficient $k \equiv \dfrac{\dfrac{2}{3}\left(\dfrac{\pi}{\tau_p}\right)\cdot L_0}{\left(1+\sigma_R\right)}$ (5.59), the force is written simply as follows:

$$F'_{motor}(t) = k \cdot i_{mR} \cdot i_{Sq} \tag{5.60}$$

This i_{mR} is controlled by adjusting the primary current component i_{Sd}, the response of which has a relatively large delay with the time constant $T_R \equiv \dfrac{(1+\sigma_R)}{R_R} L_0$. On the other hand, the response of the other primary current component i_{Sq} is expected to be fast, *i.e.*, it has no delay as described below. i_{mR} and i_{Sq} correspond to field- and armature- currents respectively in an analogy of a DC machine. Mathematical basis of these characteristics are described below.

From the equation (5.38),

$$R_R \mathbf{i}_R + L_0 \frac{d}{dt}\left[\left(1+\sigma_R\right)\mathbf{i}_R + \mathbf{i}_S \cdot e^{-j\frac{\pi}{\tau_p}x_r}\right]$$

$$= R_R \mathbf{i}_R + L_0 \frac{d}{dt}\cdot \mathbf{i}_{mR} \cdot e^{-j\frac{\pi}{\tau_p}x_r} = 0 \tag{5.61}$$

By using the following time constant,

$$T_R \equiv \frac{L_R}{R_R} = \left(1+\sigma_R\right)\cdot\frac{L_0}{R_R} \tag{5.62}$$

the equation (5.61) is written as follows:

$$T_R \frac{d\mathbf{i}_{mR}}{dt} + \left[1 - j\frac{\pi}{\tau_p} v T_R\right]\cdot \mathbf{i}_{mR} = \mathbf{i}_S \tag{5.63}$$

Angular speeds of $\mathbf{i}_{mR}$ and $\mathbf{i}_S$ are as follows:

$$\frac{d\rho}{dt} = \omega_{mR}(t) \tag{5.64}$$

$$\frac{d\zeta}{dt} = \omega_S(t) = \omega_{mR} + \frac{d\delta}{dt} \tag{5.65}$$

By multiplying both hand sides of the equation (5.61) by $e^{-j\rho}$, on account of:

$$\frac{d}{dt} i_{mR} = \frac{d}{dt}\left[\mathbf{i}_{mR} \cdot e^{-j\rho}\right] = e^{-j\rho}\frac{d}{dt}\mathbf{i}_{mR} - j\omega_{mR} \cdot e^{-j\rho}\mathbf{i}_{mR}$$

$$= e^{-j\rho}\frac{d}{dt}\mathbf{i}_{mR} - j\omega_{mR} i_{mR} \tag{5.66}$$

$$e^{-j\rho}\frac{d\mathbf{i}_{mR}}{dt} = \frac{di_{mR}}{dt} + j\omega_{mR} i_{mR}$$

the following relation is derived consequently.

$$T_R\frac{di_{mR}}{dt} + j\omega_{mR} T_R i_{mR} + \left[1 - j\frac{\pi}{\tau_p} v T_R\right] = \mathbf{i}_S \cdot e^{-j\rho} \tag{5.67}$$

By separating this equation to the real- and the imaginary- parts:

$$T_R\frac{di_{mR}}{dt} + i_{mR} = i_{Sd} \tag{5.68}$$

$$\frac{d\rho}{dt} = \omega + \frac{i_{sq}}{T_R i_{mR}} = \omega + \omega_2 \tag{5.69}$$

where $\omega(t) \equiv \frac{\pi}{\tau_p} v(t)$ and $\omega_2(t) \equiv \frac{i_{Sq}}{T_R i_{mR}}$.

As a result, the basic equations for the field-coordinates oriented control scheme consist of (5.38), (5.39), (5.50), (5.68) and (5.69).

With the control procedure illustrated in the figure 5.6 in mind, We can calculate the relation between the concrete currents references to each conductor and the components of the primary current vector i_{Sd} and i_{Sq} using the phase angle of the gap flux $\rho(t)$ based on the method described in the section 4.2..

As shown in the figure 5.6, the most important in the control scheme is to separate i_{Sd} and i_{Sq}, and to control them independently: i_{Sq} can respond primary input currents immediately while i_{mR} is compelled to follow the input current i_{Sd} with the delay of T_R, which is determined by the hardware of the motor. In other words, the control of i_{Sq} means a precise control of the slip frequency with keeping i_{mR}, *i.e.*, i_{Sd} constant, as written in the equation (5.69).

The constant i_{mR}, therefore, is assumed in the following discussion. From the equation (5.68) of the field excitation,

$$i_{mR} = i_{Sd}: \quad const. \tag{5.68'}$$

(5.69) of the synchronous speed,

$$\omega_S(t) = \frac{d\rho}{dt} = \omega + \frac{i_{Sq}}{T_R i_{Sd}} = \omega + \omega_2 \tag{5.69'}$$

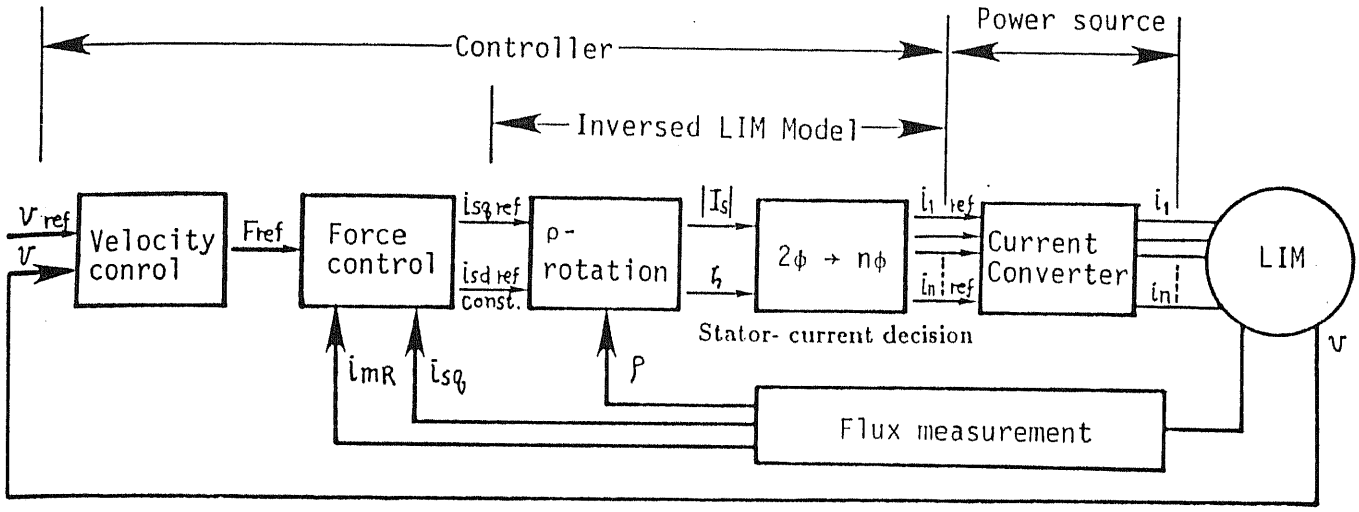

Figure 5.6. Block diagram of a speed control based on the field- coordinates oriented control scheme.

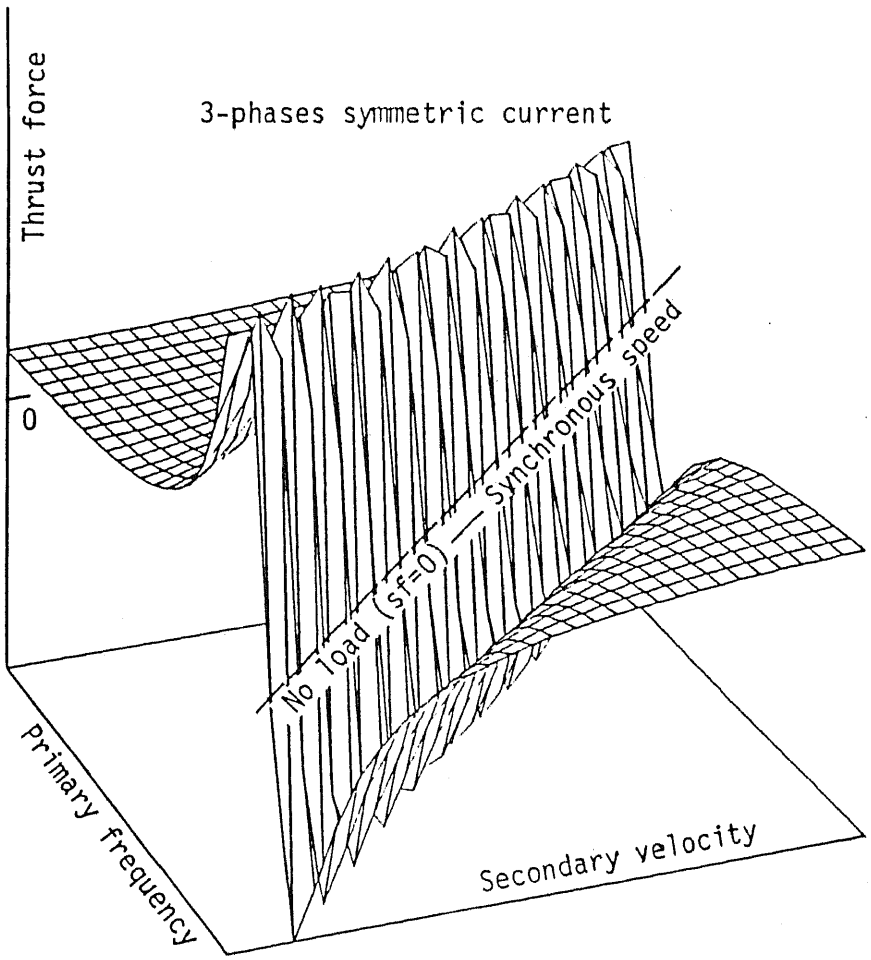

Figure 5.7. Operating points of a LIM — speed and primary frequency.

and the figure 5.5,

$$i_{Sq} = i_{Sd} \tan\delta$$

the thrust force is written as follows:

$$F_{motor} = k\, i_{Sd} i_{Sq} = k\, i_{Sd}^2 \tan\delta = k \cdot T_R \cdot i_{Sd}^2 \cdot \omega_2 \tag{5.70}$$

The thrust force, consequently, is in proportion to the slip frequency ω_2 in the case of that i_{Sd} is kept constant, as shown in the figure 5.9. The adequate condition for the field- coordinates oriented control scheme are summarized as follows.

- ☐ The spatial distribution of the gap flux density in the active region is sinusoidal.
- ☐ The thrust force characteristics is — *or can practically approximate to be* — a single-valued function of the "slip frequency".

Operation of real LIMs depends on both the primary frequency and the secondary velocity as shown in the figure 5.7 due to the end effect. With this in mind, I should draw the force — slip frequency characteristics on several lines of *sf-constant* in the figure 5.8 in order to verify the practical propriety of the assumptions. It can be verified, owing to the equation (5.70), if the curves like the figure 5.9 are drawn under the condition of $B_{\max} = const.$.

For transient simulations and design of the controller, it is necessary to identify the constants k and T_R: they can be easily calculated from the equivalent circuit in the case of the ordinary rotary induction motors. There are, however, no equivalent circuits of asymmetric LIMs with finite length; it is impossible to decide the constants analytically. They should, hence, be determined based on results of numerical analyses as follows.

From the equations (5.68') and (5.69'),

$$F_{motor} = k\, i_{Sd} i_{Sq} = k\, i_S^2 \cos\delta \sin\delta = \frac{k i_S^2 \sin 2\delta}{2} \tag{5.71}$$

$$\omega_2 = \frac{1}{T_R} \tan\delta \tag{5.72}$$

Hence, when $i_S = const.$, the phase difference angle δ is $\delta = 45°$ at the point of $F_{\max}$ in the figure 5.10.

$$k = \frac{2\, F_{\max}}{i_S^2} \tag{5.73.a}$$

$$T_R = \frac{1}{\omega_{2\,\max}} \tag{5.73.b}$$

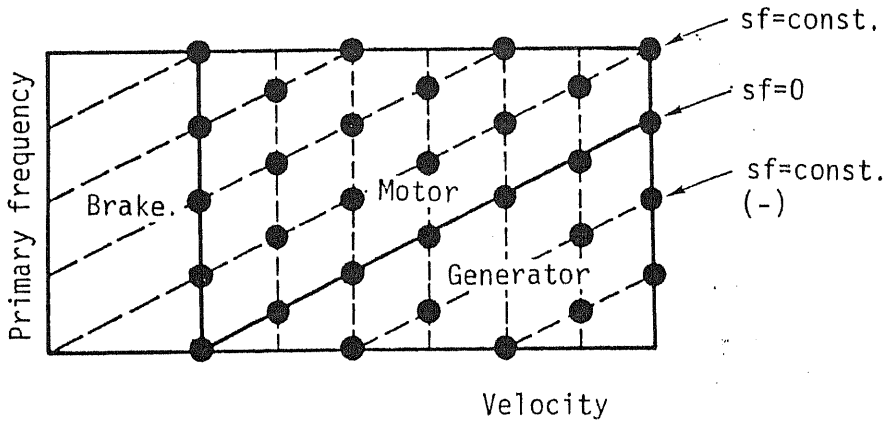

Figure 5.8. Systematic view of the operating points: sf- constant lines on the speed — frequency plane.

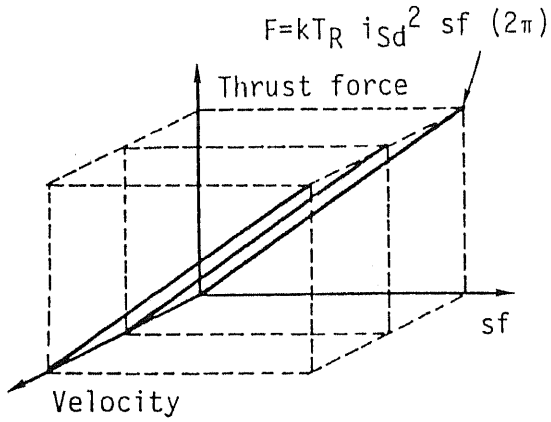

Figure 5.9. Expected sf — thrust force characteristics in the case of $i_{mR} = const.$

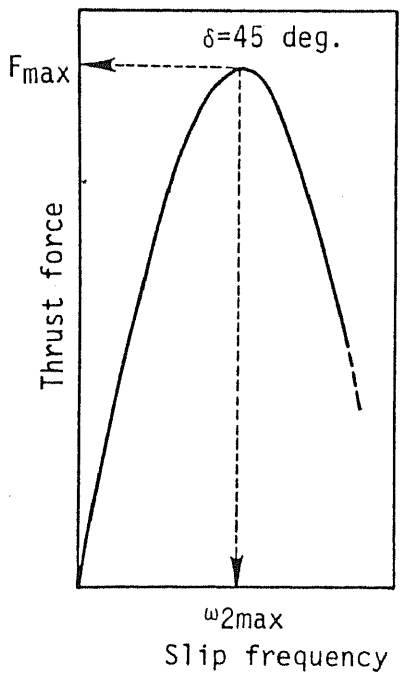

Figure 5.10. Expected sf — thrust force characteristics in the case of $i_S = const.$: how to decide k and T_R.

$$F_{motor} = k i_{Sd} = k i_{Sd}^2 \tan\delta = k i_{Sd}^2 T_R (2\pi) \cdot sf \qquad (5.73.c)$$

The current reference values are calculated with the $2\phi \rightarrow n-\phi$ transformation by applying the scheme in the chapter 4.

5.2. Qualitative discussions on:

5.2.1. Terminal voltages

It is important to check amplitudes of terminal voltages to construct the machine drive system illustrated in the figure 5.6 with a realistic inverter. With the leakage factor defined as $\sigma \equiv 1 - \dfrac{1}{(1+\sigma_R)(1+\sigma_S)}$ and equations (5.38) and (5.53), the following equation is derived.

$$\mathbf{u}_S(t) = R_S + \sigma L_S \frac{d\mathbf{i}_S}{dt} + (1-\sigma) L_S \frac{d\mathbf{i}_{mR}}{dt} \qquad (5.74)$$

In the case of the stationary state driven with sinusoidal inputs, $\omega_{mR} = \omega_1 = const.$, $i_S = const.$ and $i_{mR} = const.$, the equation (5.74) is:

$$\mathbf{U}_S(t) = \left[R_S + j\omega_1 \sigma L_S\right] \mathbf{I}_S + j\omega_1 \left[1-\sigma\right] L_S \mathbf{I}_{mR} \qquad (5.75)$$

It is essential to keep the margin of the voltage corresponding to $\sigma L_S \dfrac{d\mathbf{I}_S}{dt}$ for control, so that we can change i_{Sq}. Since the inductances L_S of LIMs are larger than of ordinary rotary induction motors, the trade-off relation, between the response speed and the rated voltage of converters, is a problem in practice.

The larger ω_1 corresponding to the speed of the motor is, the smaller the voltage margin for the control is in the equation (5.75). The field weakening with smaller i_{Sd} may, therefore, be inevitable in a high speed drive, where the steady thrust force is smaller.

5.2.2. Normal force

The control of only the thrust force has been investigated in the subsections above: perturbations of the normal force, which is substantially larger than the thrust one in general, can be a large disturbance for suspension systems. In the equation (5.69), the field- coordinates oriented control scheme, where i_{mR} is kept large and constant, means a precise control of the slip frequency near the no-load operating point s=0 — the braking is always a generator-brake in the operation. The normal force is a strong attractive force, in addition, even a small change of the thrust force, *i.e.*, an instant value of the slip frequency may cause a relatively large perturbation of the normal force. In order to keep the gap length constant, a stiff suspension system is required for a single sided LIM. I will, therefore, investigate a

tubular LIM in the following sections, in order to avoid the problem.

5.2.3. Detection of gap flux

It is almost impossible to design a flux observer of a LIM, the equivalent circuit of which cannot be identified. On the other hand, it is much easier to attach flux sensors in the surface of the primary side of a LIM than rotary machines. The flux detector in the figure 5.6 should, therefore, be based on a direct measurement of the gap flux distribution. Though the precise detection of the flux phase angle $\rho(t)$ is important in the control scheme, a real gap flux distribution is not very sinusoidal on account of spatial harmonics of slots as illustrated in the figures in the next chapter; it is practically important *technical* issue to investigate how to detect ρ of the basic wave of the gap flux, considering both arrangements of the flux sensers and signal processing techniques.

5.3. Algorithm for a simulation of controlling a transient state of symmetric normal LIM — based on a numerical field analysis

We will see concrete iterative procedures for a transient simulation of a LIM under the field- coordinates oriented control based on the numerical analyses in this section, where no mechanical load but a mass is assumed for simplicity. The model and definition of coordinates in this section are shown in the figure 5.11, and an example of time diagrams for the simulation is illustrated in the figure 5.12.

5.3.1. Preliminary excitation mode

It is required to prepare field excitation before the controlled drive at first, on account of the time constant T_R of the field current i_{mR} in the equation (5.68); this procedure is called as a preliminary excitation mode here. In the figure 5.12 (a), i_{mR} is increasing to I_{Sd}: *const.* from $t = 0$ to t_0, while ρ is kept zero. The basic equation during this mode illustrated in the figure 5.13 is:

$$T_R \frac{di_{mR}}{dt} + i_{mR} = I_{Sd} \tag{5.76}$$

where $i_{Sd} = I_{Sd}$: *const. i.e.,* $i_{Sq} = 0$ and the initial condition is $i_{mR}(0) = 0$. The solution is:

$$i_{mR}(t) = I_{Sd}\left[1 - e^{-\frac{t}{T_R}}\right] \tag{5.77}$$

When t_0 is sufficiently large, $i_{mR}(t_0)$ is closed to I_{Sd}, for instance, $i_{mR}(4T_R) = 0.982\ I_{Sd}$. Further simulations for the controlled mode can be executed with this initial condition.

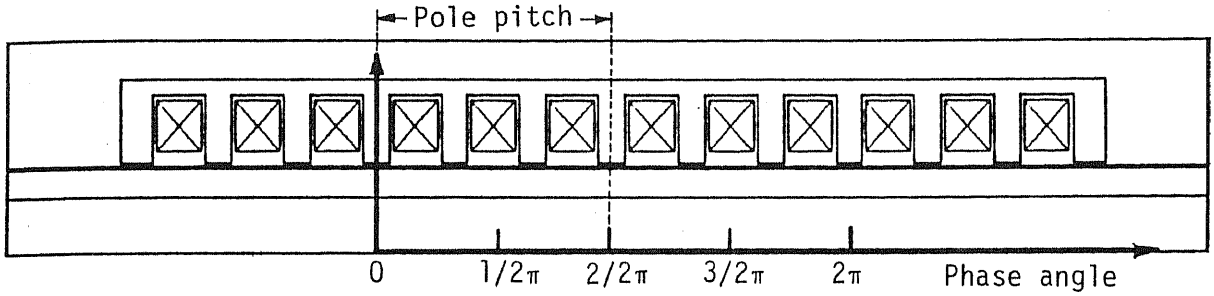

Figure 5.11. Model and coordinates for application of the field- coordinates oriented control scheme to an FSLIM.

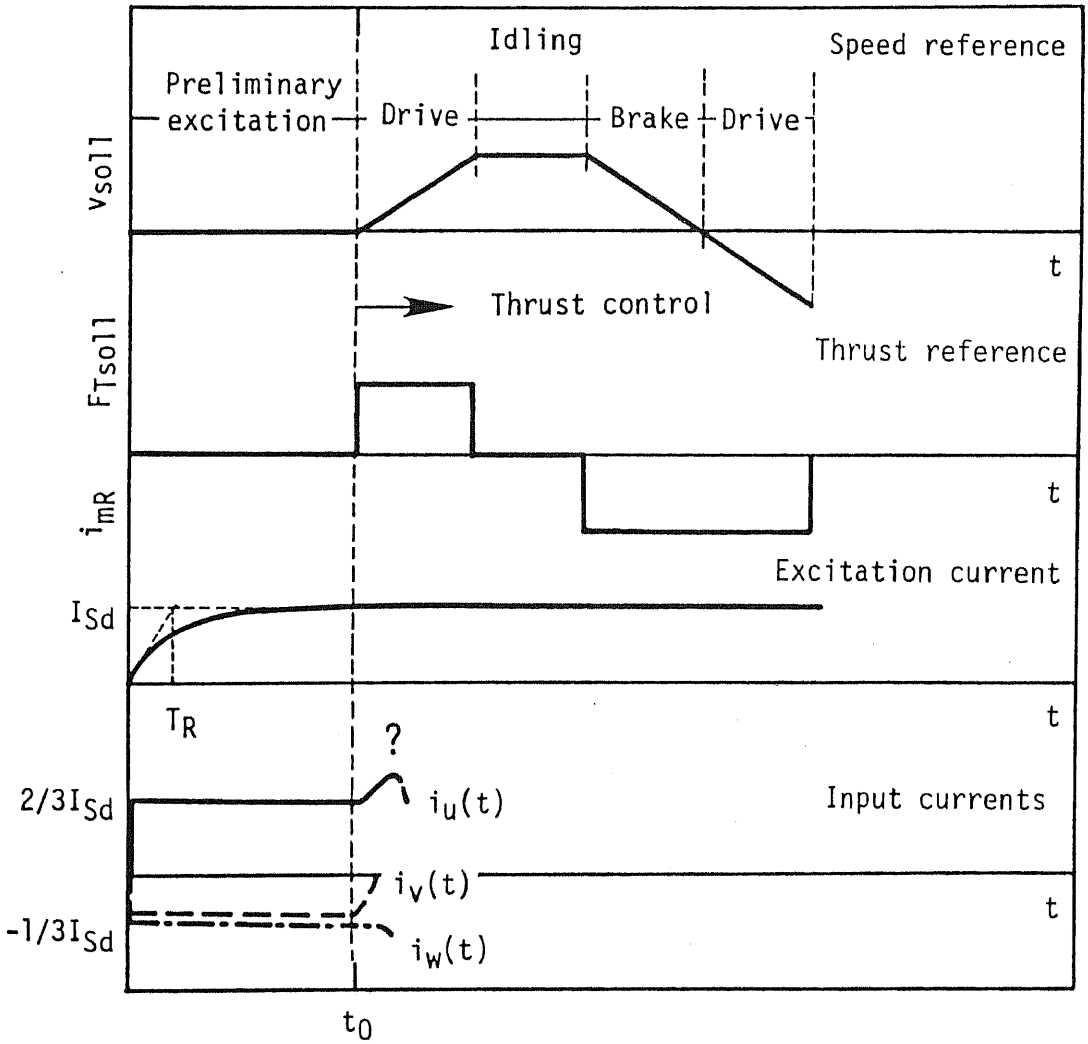

Figure 5.12. Transient simulation of the field- coordinates oriented control without mechanical loads.

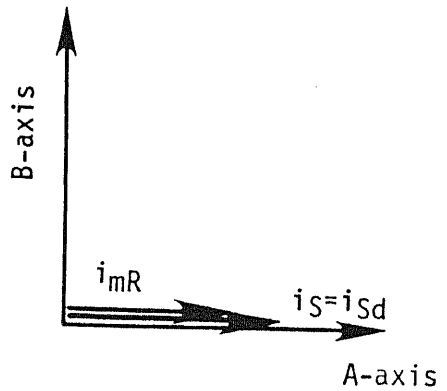

Figure 5.13. Preliminary excitation mode.

The input currents are concretely calculated according to the procedure described in the section 4.3.: in a special case of the symmetric three- phase drive, the initial condition is realized considering $i_{Sd} \equiv I_{Sd}$, $i_{Sq} \equiv 0$ and $\rho = 0$ as follows.

$$i_{Su} = \frac{2}{3} I_{Sd}, \quad i_{Sv} = i_{Sw} = -\frac{1}{3} I_{Sd} \tag{5.79}$$

5.3.2. Thrust control mode

In this mode, the field current is always kept constant, $i_{mR} = I_{Sd}$. It is essential to identify the position of the maximum flux $\rho(t)$ at any steps for deciding input currents. It is calculated by integrating the following equation in the simulation.

$$\frac{d\rho(t)}{dt} = \frac{\pi}{\tau_P} v(t) + \frac{1}{T_R I_{Sd}} i_{Sq} \tag{5.80}$$

From the equation (5.60):

$$i_{Sq}(t) = \frac{F_{Tsoll}(t)}{k \cdot I_{Sd}} \tag{5.81}$$

With $\rho(t) \equiv 0$ from $t = 0$ to t_0 in mind, the equation (5.80) is integrated as follows:

$$\rho(t) = \frac{\pi}{\tau_P} \int_{t_0}^{t} v(t)\, dt + \frac{1}{k T_R I_{Sd}^2} \int_{t_0}^{t} F_{Tsoll}\, dt \tag{5.82}$$

where $0 \leq \rho < 2\pi$ in the figure 5.11. It is not required to consider the change of the secondary resistance due to high temperature, in this calculation for simplicity.

In a special case of no mechanical load, the equation (5.83) is written as follows.

$$\rho(t) = \frac{\pi}{\tau_P} x_r(t) + \frac{1}{k T_R I_{Sd}^2} \cdot \frac{1}{M} v_{soll}(t) \tag{5.83}$$

Since the both I_{Sd} and $i_{Sq}(t)$ are known, the input current can be determined with the $2\phi \rightarrow n-\phi$ transformation described in the section 4.3. In the special case of the symmetric three- phase drive, the line currents are calculated as follows:

$$i_{Su}(t) = \frac{2}{3} I_{Sd} \cos\rho(t) - \frac{2}{3} i_{Sq}(t) \sin\rho(t) \tag{5.84.a}$$

$$i_{Sv}(t) = I_{Sd}\left\{-\frac{1}{3}\cos\rho(t) + \frac{\sqrt{3}}{3}\sin\rho(t)\right\} + i_{Sq}(t)\left\{\frac{1}{3}\sin\rho(t) + \frac{\sqrt{3}}{3}\cos\rho(t)\right\} \tag{5.84.b}$$

$$i_{Sw}(t) = I_{Sd}\left\{-\frac{1}{3}\cos\rho(t) - \frac{\sqrt{3}}{3}\sin\rho(t)\right\} + i_{Sq}(t)\left\{\frac{1}{3}\sin\rho(t) - \frac{\sqrt{3}}{3}\cos\rho(t)\right\} \tag{5.84.c}$$

All the algorithm is summarized in the figure 5.14.

5.3.3. Calculation of terminal voltages

After determining the input currents, the primary terminal voltages can be calculated according to the procedures described in the subsection 2.4.6. referring the figures 2.7.

In the special case of the three- phase symmetric induction motors, the primary terminal voltages are calculated from the equation (5.38) as follows. Since $\mathbf{i}_R$ cannot be measured, it should be calculated from the equation (5.53).

$$\mathbf{i}_R e^{j\frac{\pi}{\tau_P}x_r} = \frac{1}{1+\sigma_R}\left[\mathbf{i}_{mR} - \mathbf{i}_S\right] \tag{5.85}$$

$$\begin{aligned}
\mathbf{u}_S &= R_S\mathbf{i}_S + L_S\frac{d\mathbf{i}_S}{dt} + \frac{L_0}{1+\sigma_R}\frac{d}{dt}\left[\mathbf{i}_{mR}-\mathbf{i}_S\right] \\
&= R_S\mathbf{i}_S + \left[L_S-\frac{L_0}{1+\sigma_R}\right]\frac{d}{dt}\left\{i_{Sa}(t)+j\,i_{Sb}(t)\right\}\frac{L_0}{a+\sigma_R}\frac{d}{dt}\left\{I_{Sd}e^{j\rho(t)}\right\} \\
&= R_S\left\{i_{Sa}(t)+j\,i_{Sb}(t)\right\} + \sigma L_S\frac{d}{dt}\left\{i_{Sa}(t)+j\,i_{Sb}(t)\right\} \\
&\quad + \left[1-\sigma\right]L_S I_{Sd}\frac{d}{dt}\left[e^{j\rho(t)}\right]
\end{aligned} \tag{5.86}$$

The time differential operator $\frac{d}{dt}$ is expressed with "$\cdot$":

$$\frac{d}{dt}(i_{Sa}(t)) = -I_{Sd}\cdot\sin\rho\cdot\dot{\rho} - \dot{i}_{Sq}\cdot\sin\rho - i_{Sq}\cdot\cos\rho\cdot\dot{\rho}$$

$$\frac{d}{dt}(i_{Sb}(t)) = I_{Sd}\cdot\cos\rho\cdot\dot{\rho} + \dot{i}_{Sq}\cdot\cos\rho - i_{Sq_\rho}\cdot\dot{\rho}$$

$$\frac{d}{dt}(e^{j\rho(t)}) = -\dot{\rho}\cdot\sin\rho + j\cdot\dot{\rho}\cdot\cos\rho$$

With this in mind,

$$u_{Sa}(t) = R_S i_{Sa} - L_S I_{Sd}\dot{\rho}\sin\rho - \sigma L_S i_{Sq}\dot{\rho}\cos\rho - \sigma L_S\dot{i}_{Sq}\sin\rho \tag{5.87.a}$$

$$u_{Sb}(t) = R_S i_{Sb} + L_S I_{Sd}\dot{\rho}\cos\rho - \sigma L_S i_{Sq}\dot{\rho}\sin\rho + \sigma L_S\dot{i}_{Sq}\cos\rho \tag{5.87.b}$$

The primary resistance R_S is assumed zero in the example shown in the next subsection. The terminal voltages are derived as follows:

$$U_{UN} = \frac{2}{3}U_{Sa} \tag{5.88.a}$$

$$U_{VN} = -\frac{1}{3}U_{Sa} + \frac{\sqrt{3}}{3}U_{Sb} \tag{5.88.b}$$

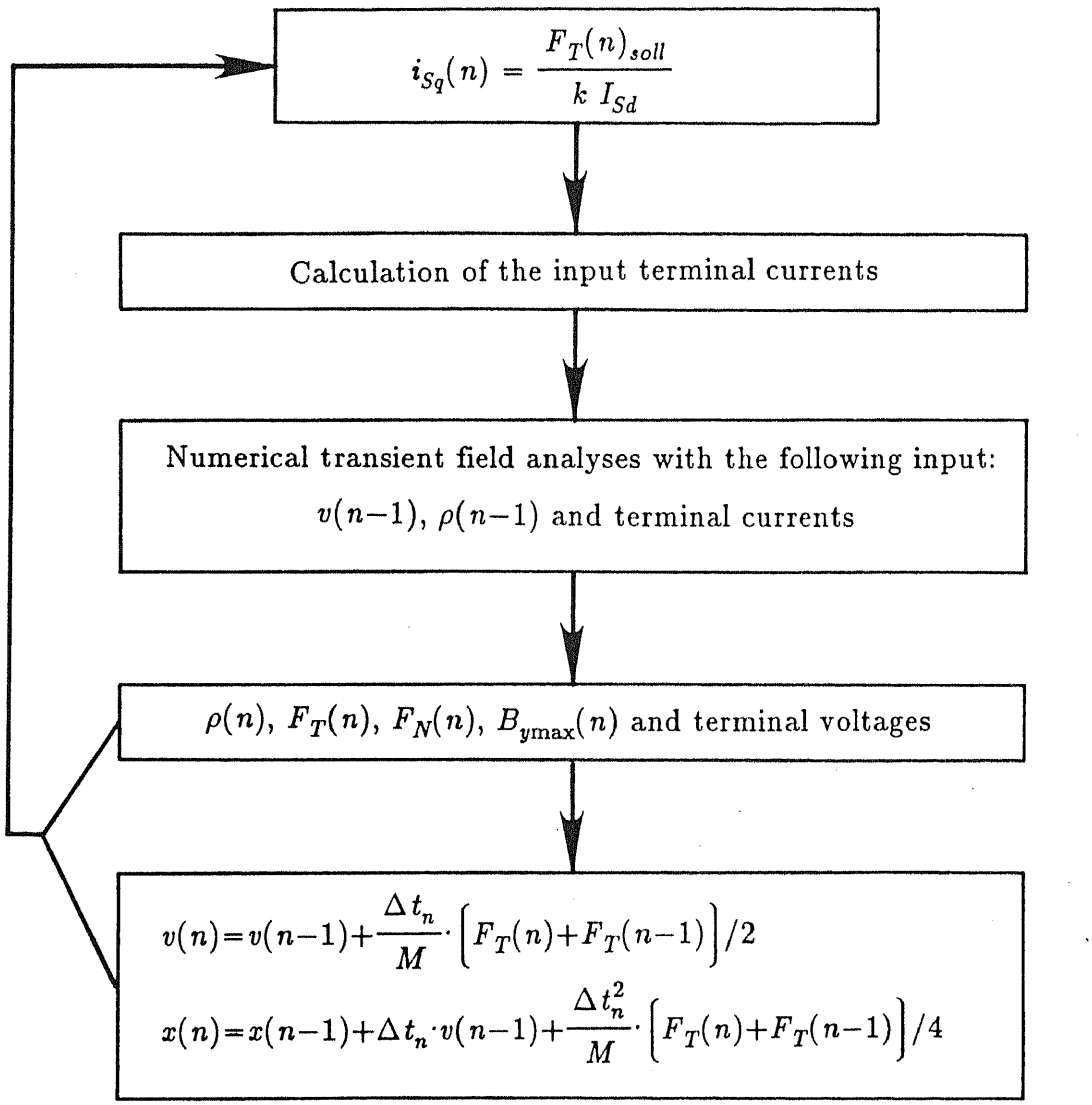

Figure 5.14. Flow-chart of the simulation with the numerical field analysis.

$$U_{WN} = -\frac{1}{3}U_{Sa} - \frac{\sqrt{3}}{3}U_{Sb} \tag{5.88.c}$$

and the input power is:

$$W(t) = U_{UN}\cdot i_{SU} + U_{VN}\cdot i_{SV} + U_{WN}\cdot i_{SW} \tag{5.89}$$

5.3.4. A calculated example

A calculated example of the algorithm is shown in this subsection with the test machine at the TU Braunschweig described in the chapter 3. From the calculation in the chapter 3, the equivalent circuit in the figure 5.15 (a) has been derived for three- phase four- pole drive in the case of $f_1 = 30Hz$ *const.*.

$$L_R = L_S = 3.2\times10^{-1}[\mathrm{H}]$$

$$\sigma_S = \sigma_R = 9.7/310 = 3.13\times10^{-2}$$

$$\tau_p = 1.885[\mathrm{m}]$$

$$\pi = 3.1416$$

$$T_R = \frac{L_R}{R_R} = 9.14\times10^{-2}[\mathrm{s}]$$

$$\tan\delta = 2\pi T_R f_1\cdot s = 17.2s$$

$$\sigma = 1-\frac{1}{(1+\sigma_R)(1+\sigma_S)} = 5.98\times10^{-2}$$

and

$$k = \frac{2}{3}\frac{\pi}{\tau_p}\frac{L_0}{1+\sigma_R} = 3.34[\mathrm{N/A^2}] \tag{5.90}$$

The thrust force in the case of $I_S = 30[\mathrm{A}]_{rms\ const.}$ is calculated in the following form from the equation (5.71):

$$F = kI_{Sd}\,I_{Sq} = \frac{k}{2}\sin2\delta\cdot I_S^2$$

$$= \frac{kI_S^2}{2}\frac{2\tan\delta}{1+\tan^2\delta}$$

$$= \frac{1.0344\times10^5 s}{1+295.84s^2}[\mathrm{N}] \tag{5.91}$$

The forces calculated from the equation (5.91) are compared with the direct numerical calculation in the chapter 3 in the figure 5.15 (b). The results of the transient simulation are shown in the figures 5.16. The references of the speed and the thrust force illustrated in the figures (a) and (b) correspond to the figure 5.12.

The preliminary excitation mode is in the first one second in this simulation. The magnetizing current converges to the reference value sufficiently well in the figure (c).

Since a current source converter is assumed as a power source, the terminal primary currents are constant during the preliminary excitation mode as shown in the figure (d), while the primary terminal voltages are zero because of $R_S = 0$. The primary electrical input power in the figure (f) was calculated by summing up the multiplication of the currents and the voltages. The input power is proportional to the speed, for the thrust force is kept constant. No input power, *i.e.*, no loss is calculated during the no load operation from $t = 2$ to 3 [s] due to the ideal modeling and $R_S = 0$; we should naturally consider additional losses in a real operation. The resultant position was calculated and drawn in the figure (g) under the assumption of no mechanical load.

References

[5-1] F. Blaschke: "Das Verfahren der Feldorientierung zur Regelung der Drehfeldmaschine", doctoral dissertation at the TU Braunschweig, 1974, FR Germany

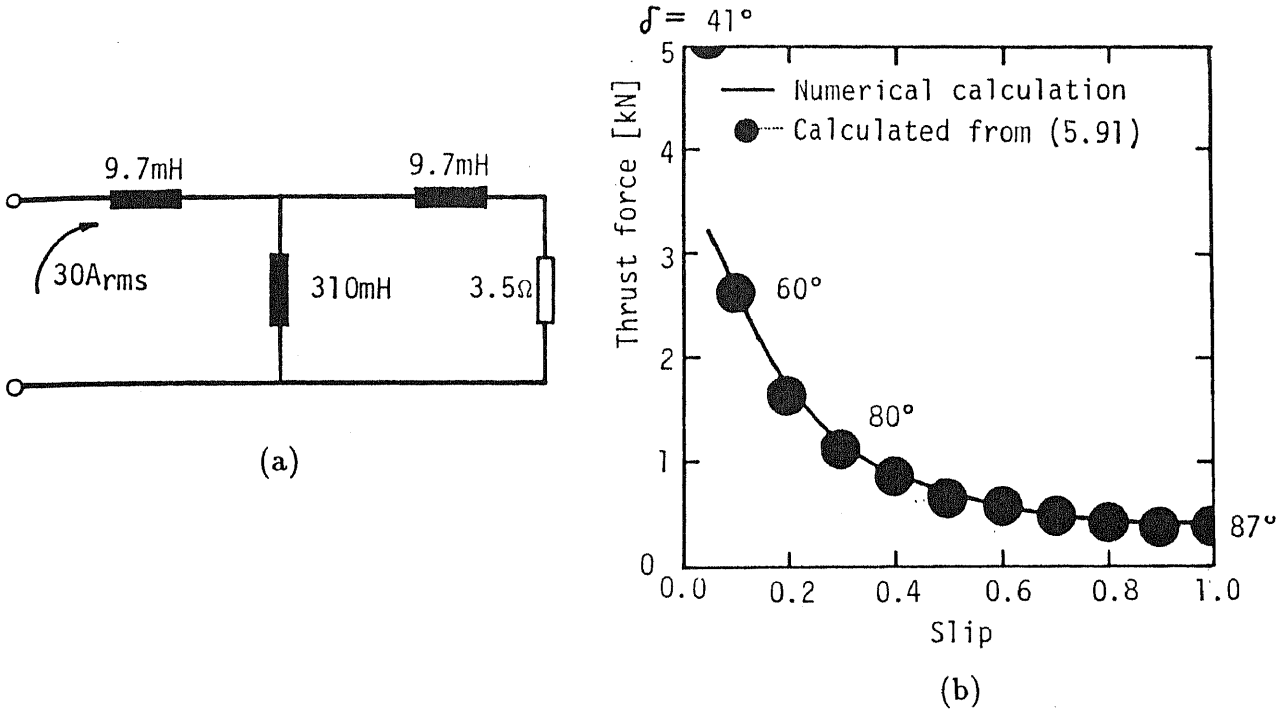

Figure 5.15. (a) Equivalent circuit of the test machine in the chapter 3 in the three- phase four- pole drive determined with the numerical field analysis.

(b) Thrust forces calculated with the field analysis directly and with the equivalent circuit from the equation (5.91)

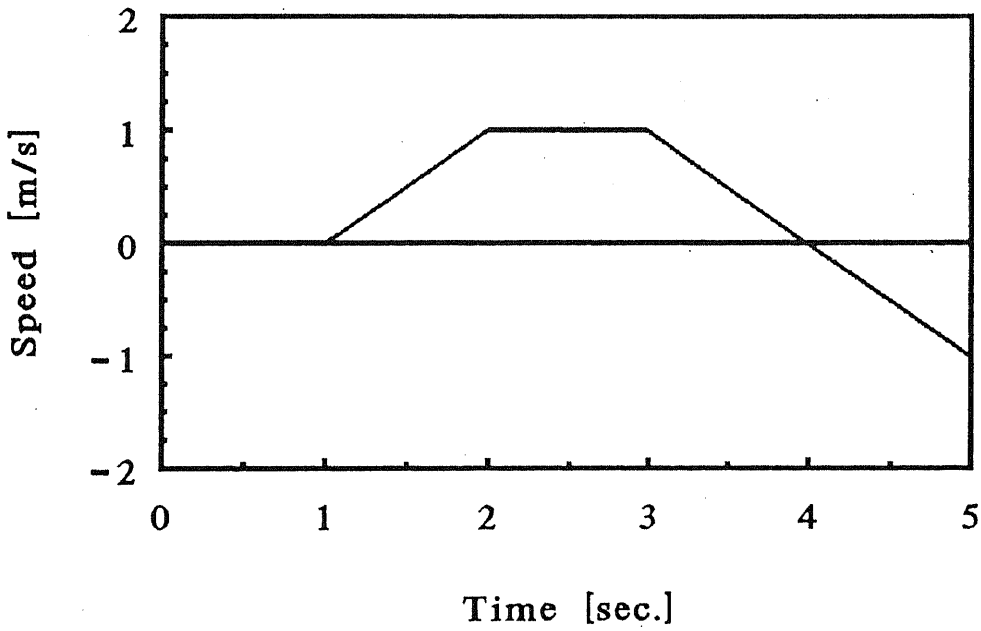

(a) Reference speed.

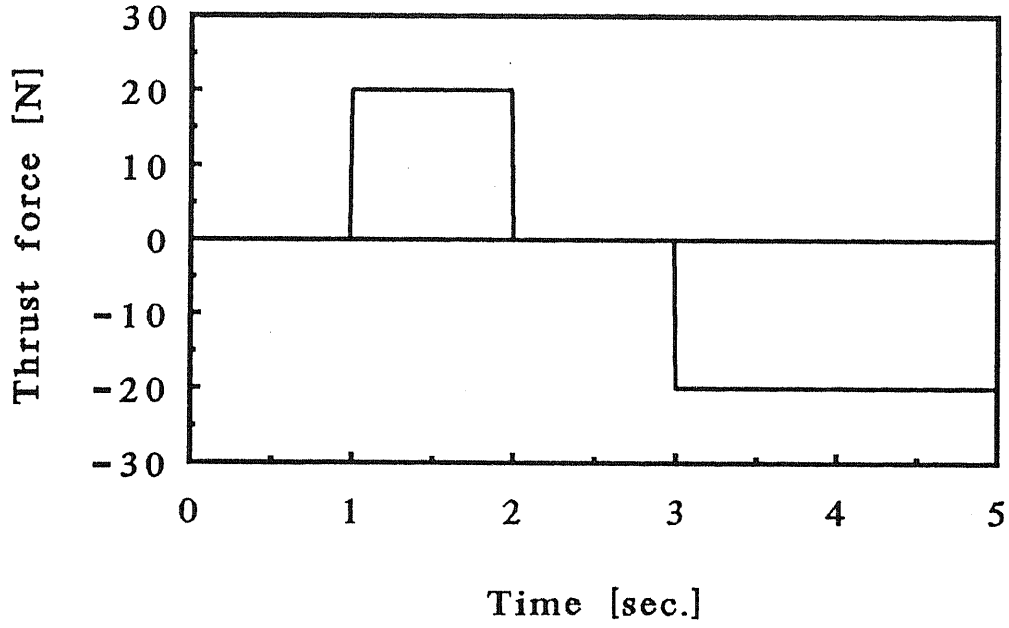

(b) Reference thrust force.

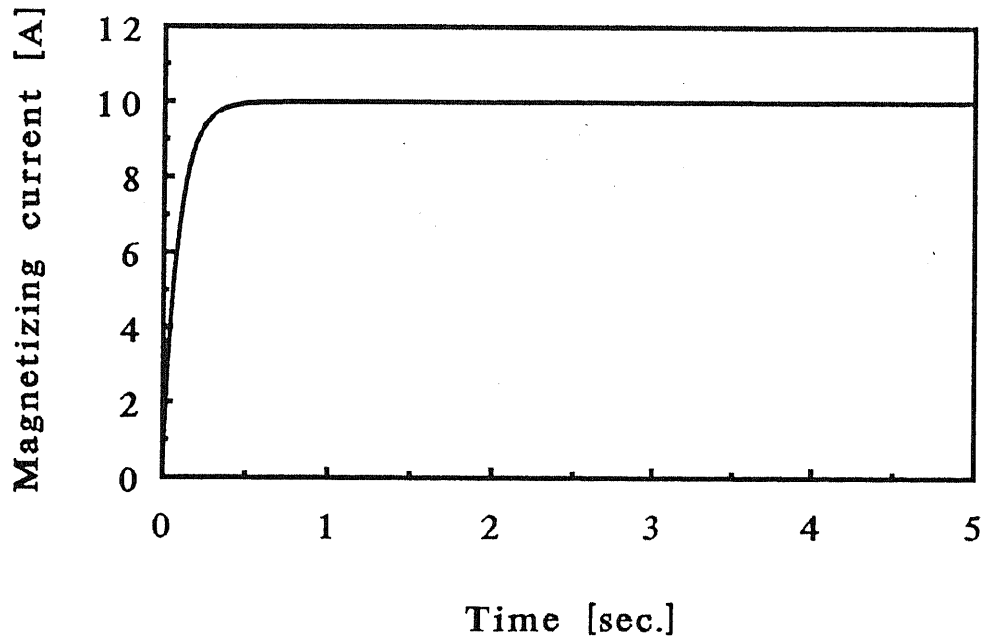

(c) Magnetizing current.

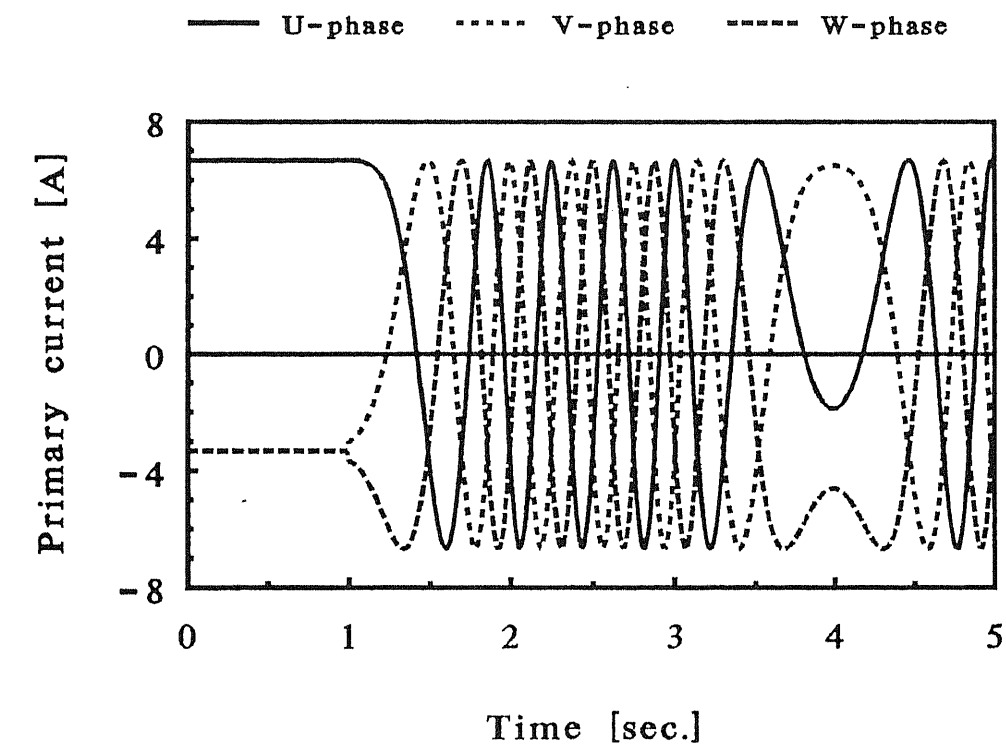

(d) Primary current.

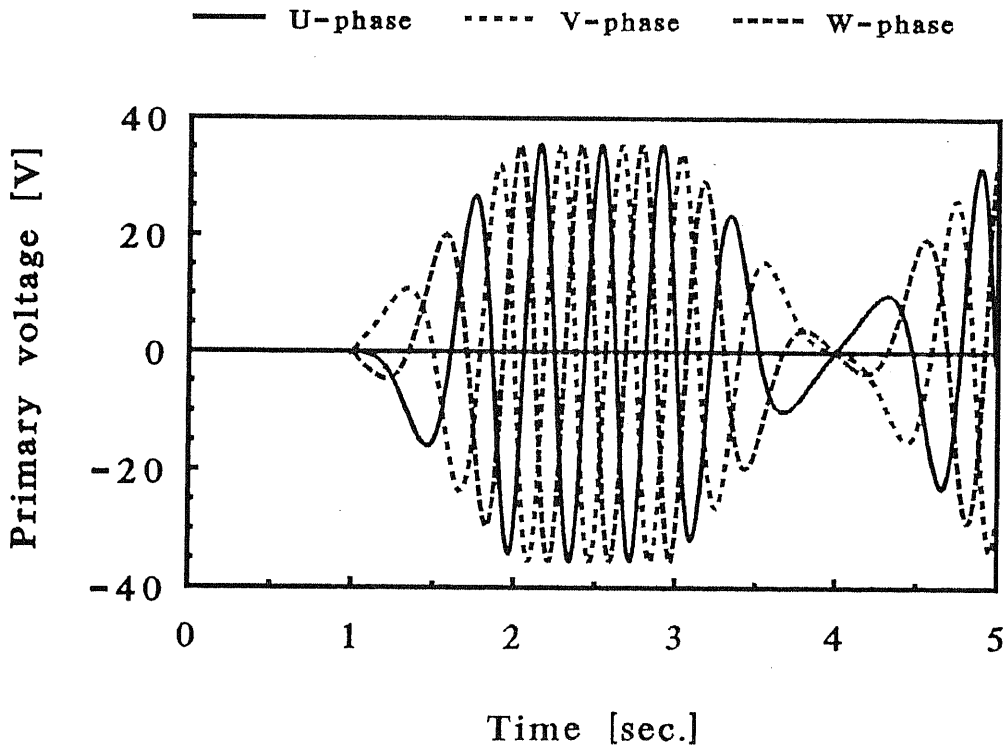

(e) Primary terminal voltage.

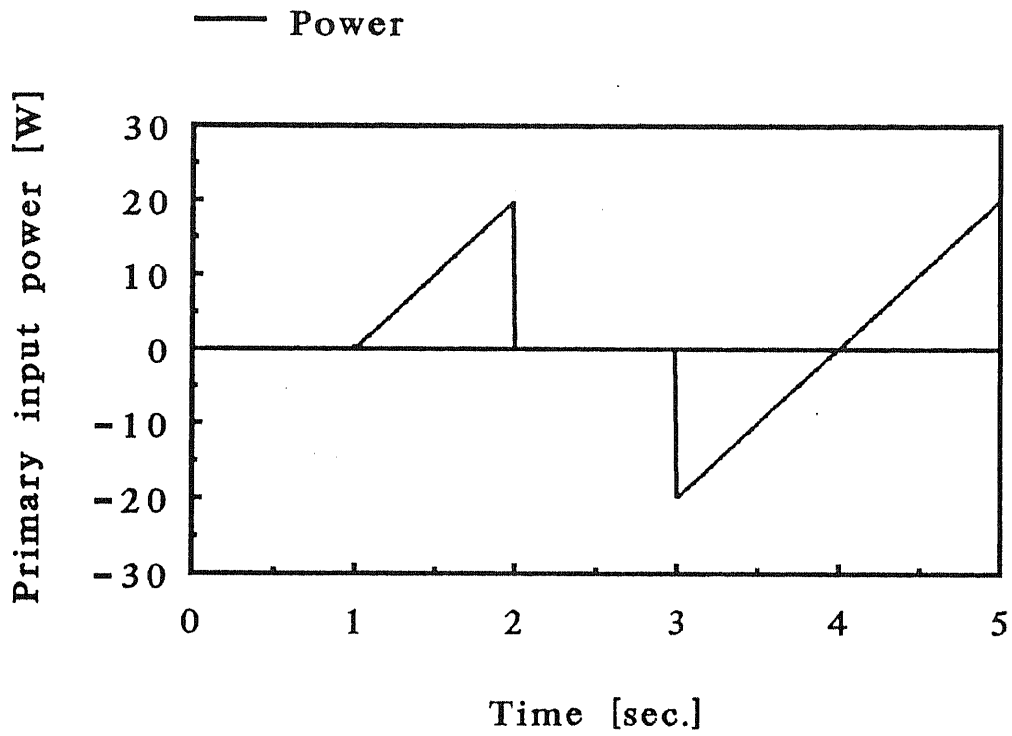

(f) Primary input power.

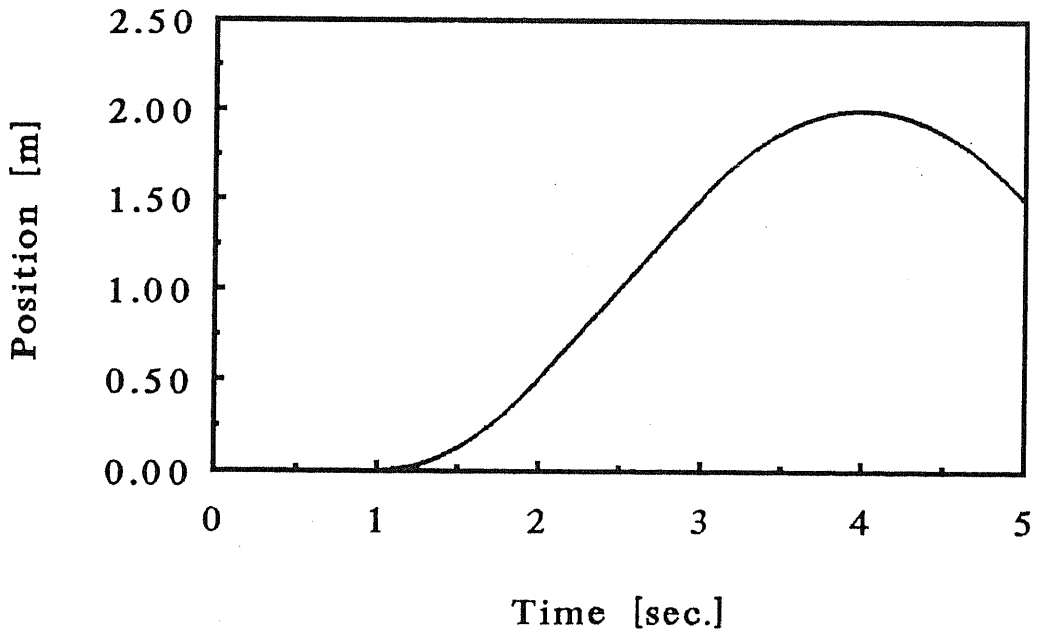

(g) Position of the mover.

Figure 5.16. An example of the transient simulation.

Chapter 6: Investigation with a tubular test machine

Introduction

We will check all the theories prepared in the chapters 2, 4, and 5 by applying them to a tubular test LIM in this chapter. The numerical field calculation on the cylindrical coordinates is verified by comparing the analysis with measurements with a three-phase power source. Key points in the results are:

(1) comparison between characteristics with- and without- end effect,

(2) difference between three-phase serial- and parallel- connections,

(3) energy efficiency with- and without- the flux synthesis, and

(4) possibility of the field-coordinates oriented control scheme with the flux synthesis.

6.1. Test machine — tubular LIM

As described in the subsection 4.2.4, a tubular FSLIM was used for the numerical and experimental studies in practice. The test machine was borrowed to me by Mr. Karita in the Shinko Electric Mfg. Co.. The motor and the peripherals for measurements are shown in the figure 6.1. Important technical data are noted in the table 6.1.

Table 6.1 Investigated tubular LIM

Slot width	13.0 mm
Slot pitch	19.5 mm
Slot depth	11.4 mm
Slot number	12
Winding number	150 turns/slot
Inner diameter of the primary	29.2 mm
Secondary plate	Copper
Thickness of the secondary plate	0.4 mm
Secondary core height	2.5 mm
Gap length between cores	(0.4+0.6) mm
Measured R_S	1.1Ω

The cross-section of a primary winding is 3.18×10^{-1}[mm^2]; the normal current $I_{1n,rms}$ has been decided as $2A$ by assuming the maximum current density approximately 8.0[A/mm^2].

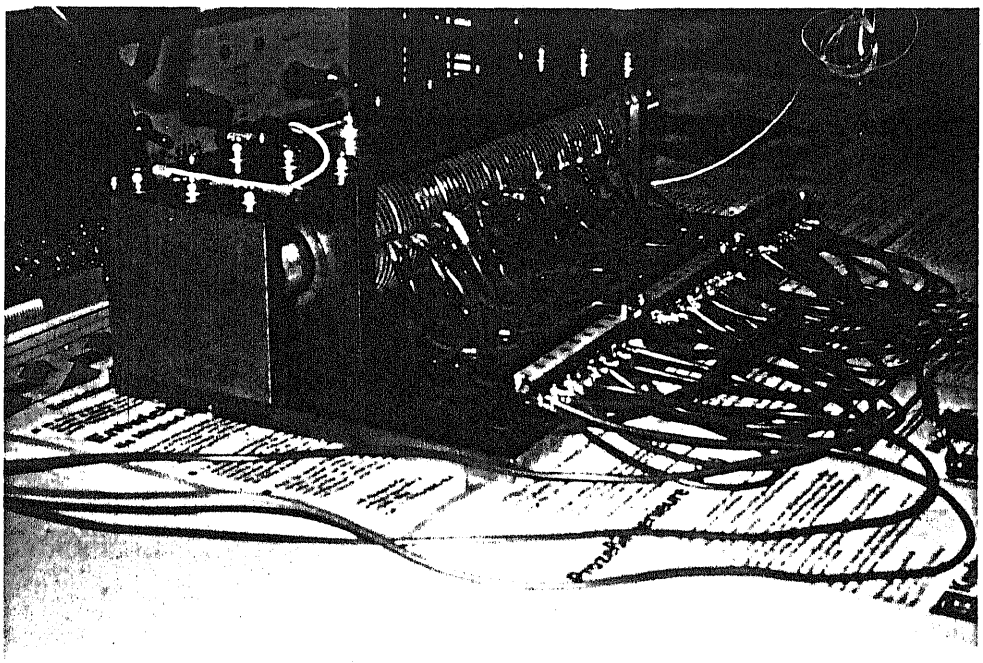

(a) Photograph of the test machine.

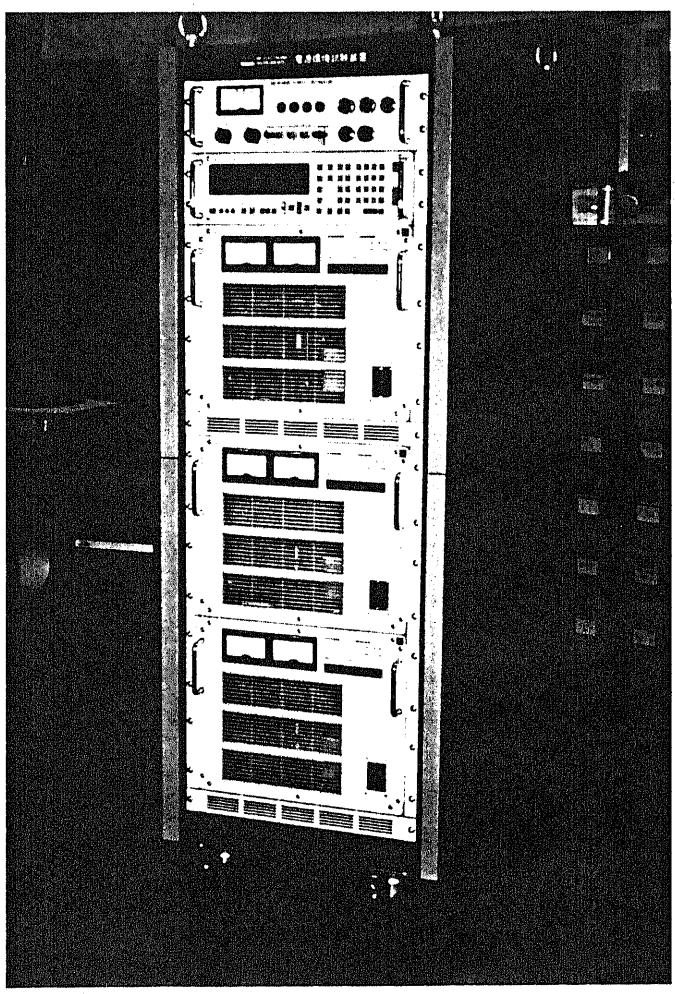

(b) Photograph of the power amplifier.

6.2. Preliminary calculation (1) — with current sources

I calculated the cases with current sources of amplitude of $2A_{rms}$ and phase differences of 60°, in order to decide the capacities of the power supply unit and of a load cell for sensing the thrust force. In these cases, three slot pitches equal to one pole pitch.

The both of the cases with- and without- end effect were calculated for basic comparisons; examples of the calculations are illustrated in the figures 6.4 and 6.5. We can see from the figure 6.2.(a) that we need a voltage source of approximately 10V for each slot at the standstill drive. A clean sinusoidal wave form of the input voltages is required for a theoretical comparison between calculations and measurements, on the other hand, the capacity of the power source needs not to be large: a linear power amplifier will be used in the experimental study in the section 6.4.3. The maximum phase difference between the current and the voltage is approximately 80° in the case of a symmetrical drive without the end effect as shown in the figure, but it is larger than 90° in the case of asymmetric drives with the end effect in some slots as we will see in the figure 6.3 (f).

Characteristics of the thrust force in a standstill drive with the current sources are shown in the figure 6.2 (c). The maximum thrust force is produced at sf = 35Hz; the secondary time constant of the motor is calculated on account of the equation (5.73.b): $T_R = 4.55\times10^{-3}$ sec. The short time constant is due to the thin secondary plate, *i.e.,* the large secondary resistance and the small gap length. We can see also the end effect on the thrust force: the force is reduced to approximately eighty percent by the effect of finite length of the LIM in comparison with the case of the infinite length. From these calculations, I decided the capacity of the load cell as five kilogram-weights. The gap flux density with end effect seems larger in the figure 6.2. (d), but it is due to local concentration of the gap flux caused by an asymmetric magnetic path; it does not mean that the average magnetization is stronger with the end effect.

The running characteristics of the $f_1 = 20\,Hz$ *const.* are shown in the figure 6.2, where the synchronous speed is 2.34m/s. In the figure 6.3 (a), the less the slip is, the smaller the thrust force is, since the secondary resistance is large. The curve of the force, prognosticated from the ideal model with a sinusoidal current sheet in the chapter 5, is also illustrated in the figure; the thrust force at the synchronous speed should be zero in the ideal model, but the forces calculated numerically is much less than the model. We should pay attention to that the difference between the cases with- and without- end effect is much smaller than the reduction from the ideal model, in other words, the harmful effect of slot harmonics may be a dominant factor of the deterioration of the running characteristics. In fact, we can

see in the figures 6.4 and 6.5 relatively large harmonics of the secondary current, which does not contribute to the drive but causes energy loss in the secondary plate. We can expect some improvements with an appropriate flux synthesis against the end effect, but the compensation of the slot harmonics is inherently impossible. The test machine, unfortunately, has relatively large slot harmonics and the field distribution in the gap, hence, is not clean on account of small slot numbers, open slots and small gap length. It should be emphasized here that sophisticated and careful design of a motor itself is anyway important also for an effective application of the flux synthesis. A drive with a longer pole pitch is a solution for forming a clean gap flux distribution, *e.g.,* the two- pole drive discussed in the section 6.6, but for the long pole pitch, we need a thicker yoke. The pole pitch is not only the issue of the current supply, but also of the design of motor's hardware. It should also be enphasized here, that the drag force with the slot harmonics would be much smaller if the secondary conductor were cage or windings, which would constrain the path of the secondary current, as in ordinary rotary machines.

The deterioration of LIM characteristics was considered to be simply due to the end effect *hitherto,* but we must also pay attention to the effect of the continuous secondary conductor and spatial harmonics of the gap flux distribution.

It is difficult, unfortunately, to verify the merits of the flux synthesizing schemes using the test machine investigated in this chapter, because the slot harmonics cannot be compensated by any flux syntheses inherently and we cannot, therefore, have the no load operating point on account of the drag force at the synchronous speed, but we will — or must — try further discussions with it.

The input- and output- powers, and the energy efficiencies are plotted in the figures 6.4 (b) and (c) respectively. The maximum energy efficiency is achieved at low speed: $s \approx 0.6$, and it is anyway low because of the large secondary resistance and the end effect.

Terminal voltages, amplitudes and phase angles of the impedances are illustrated in the figure 6.3 (d), (e) and (f) respectively on a couple of operating points. The terminal voltages are exactly proportional to the impedances in this case, since the terminal currents are assumed constant. The impedance at the entrance is small, and *vice versa* at the exit; we can see power flows from the motor to the power source in the twelfth winding due to the end effect. In the third graphs of the figures 6.4 and 6.5, we can see effects of the slot harmonics. The end effect is conspicuous especially in the fourth figures.

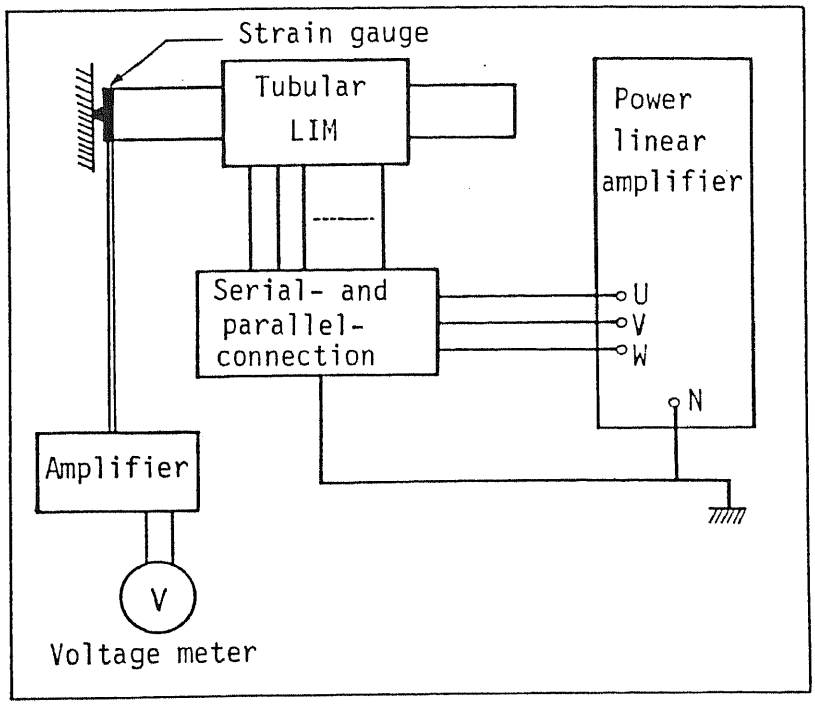

(c) Structure of the experimental equipment.

Figure 6.1. Equipment for the experiments.

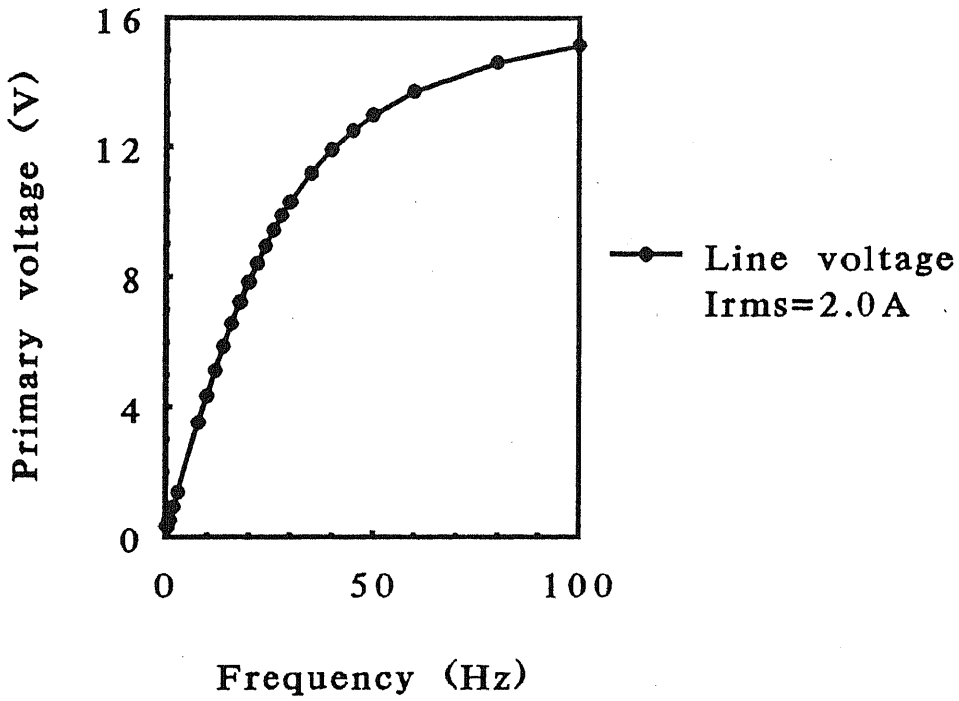

(a) Primary terminal voltage (without end effect).

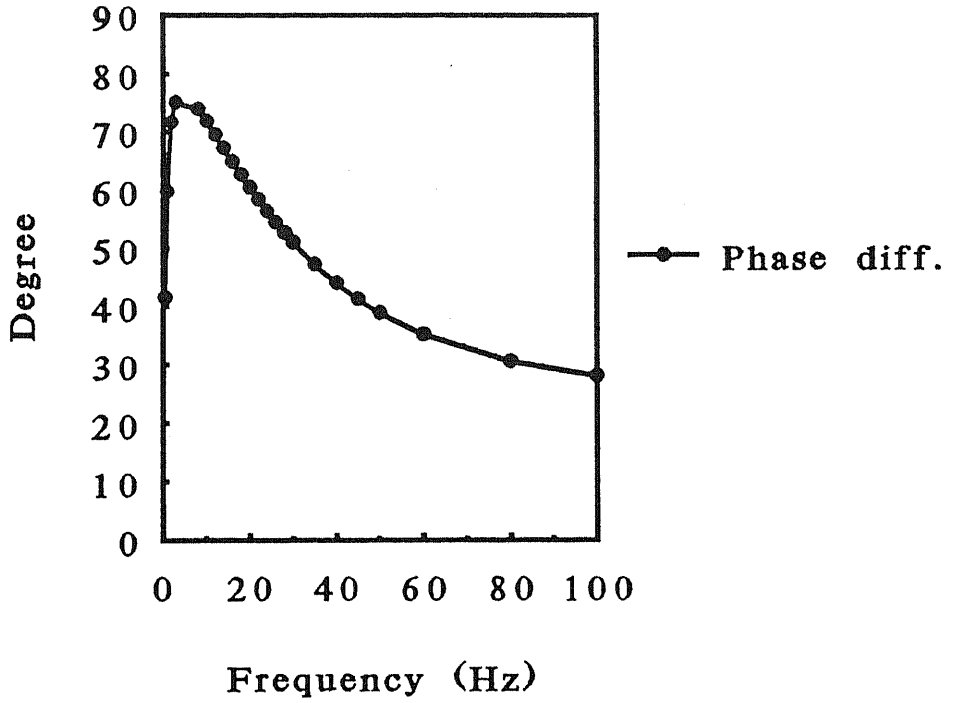

(b) Phase angle of impedance.

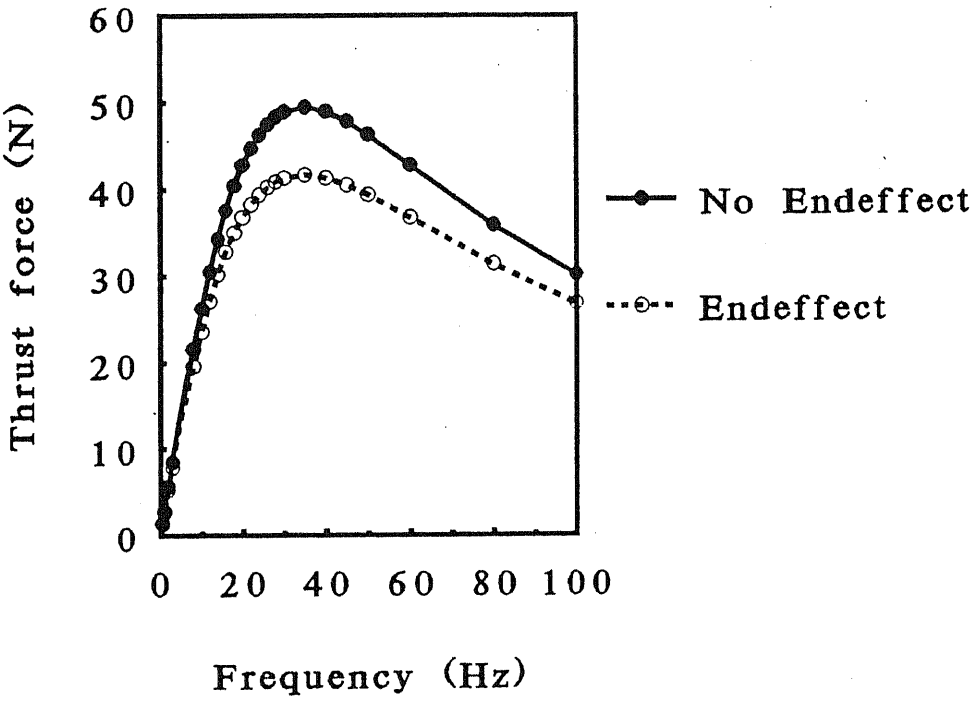

(c) Thrust force.

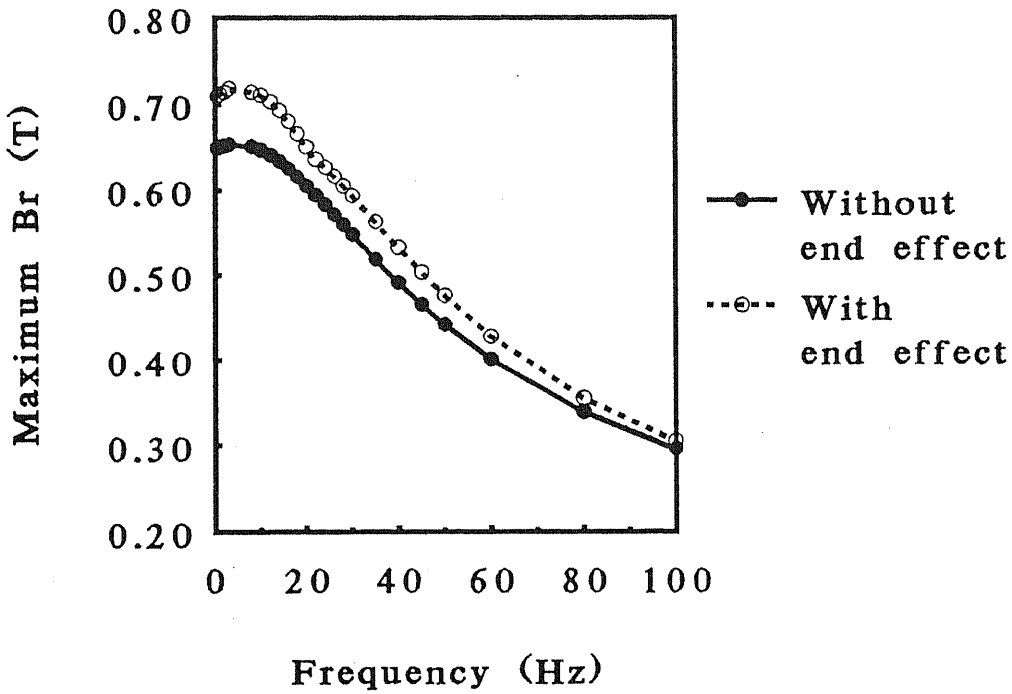

(d) Maximum flux density.

Figure 6.2. Standstill drive $I_{rms} = 2.0A$ *const.*

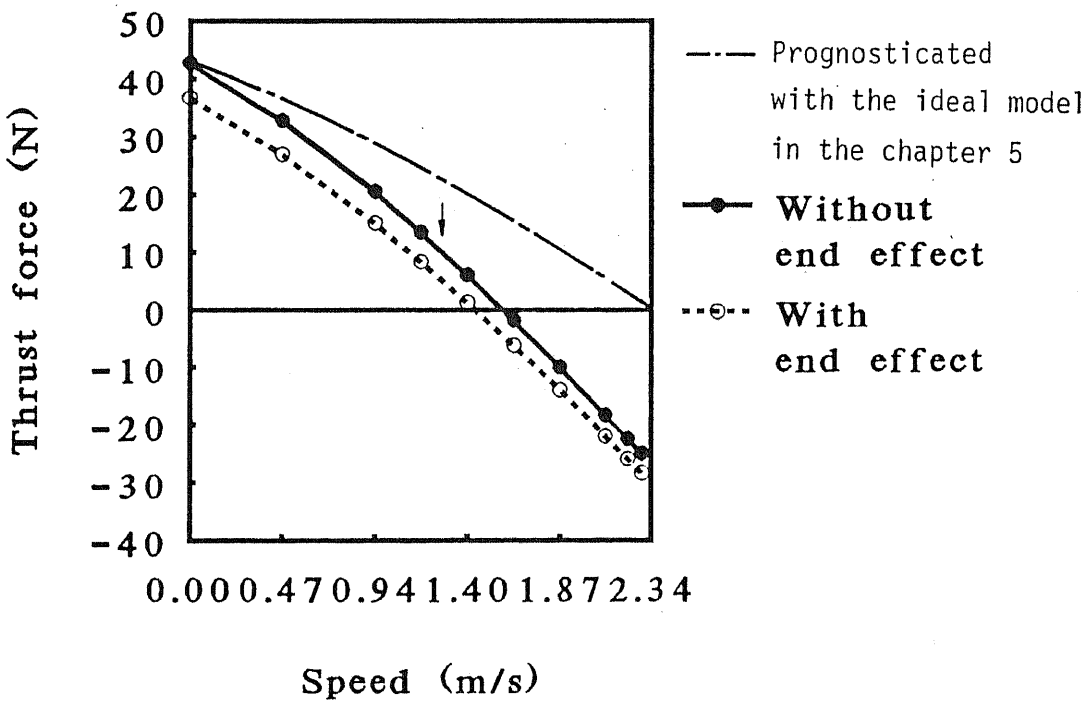

(a) Thrust force.

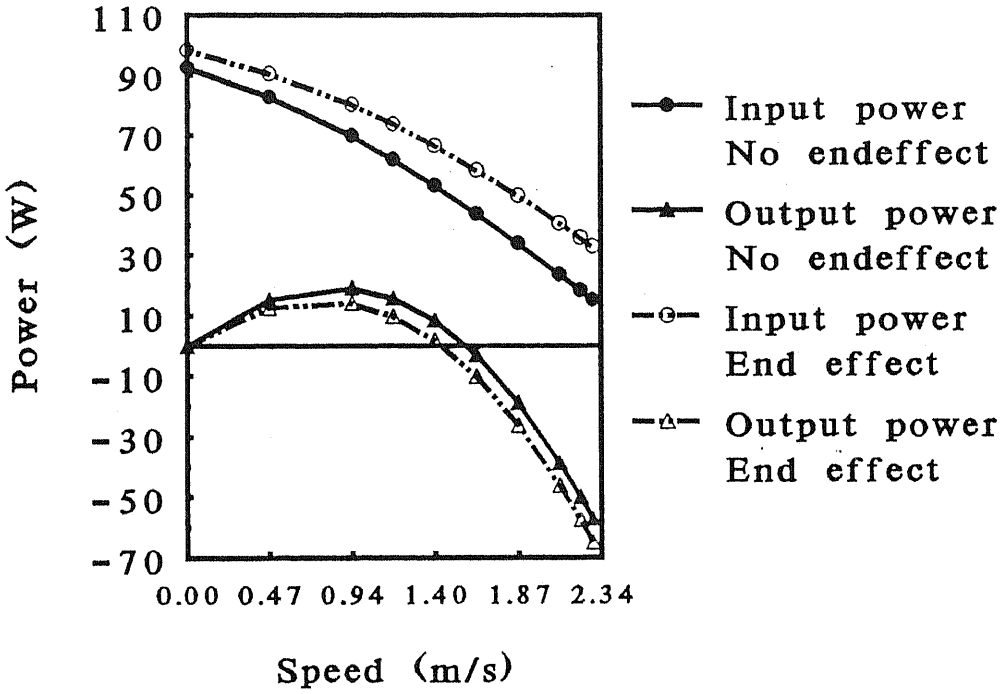

(b) Input- and output- powers.

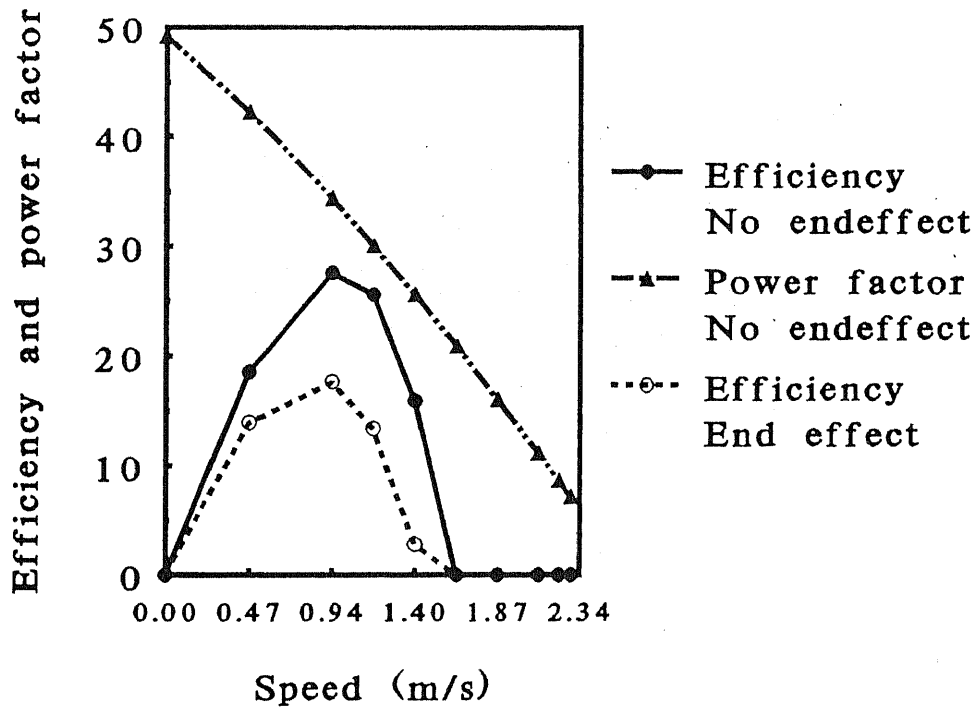

(c) Power factor and energy efficiency.

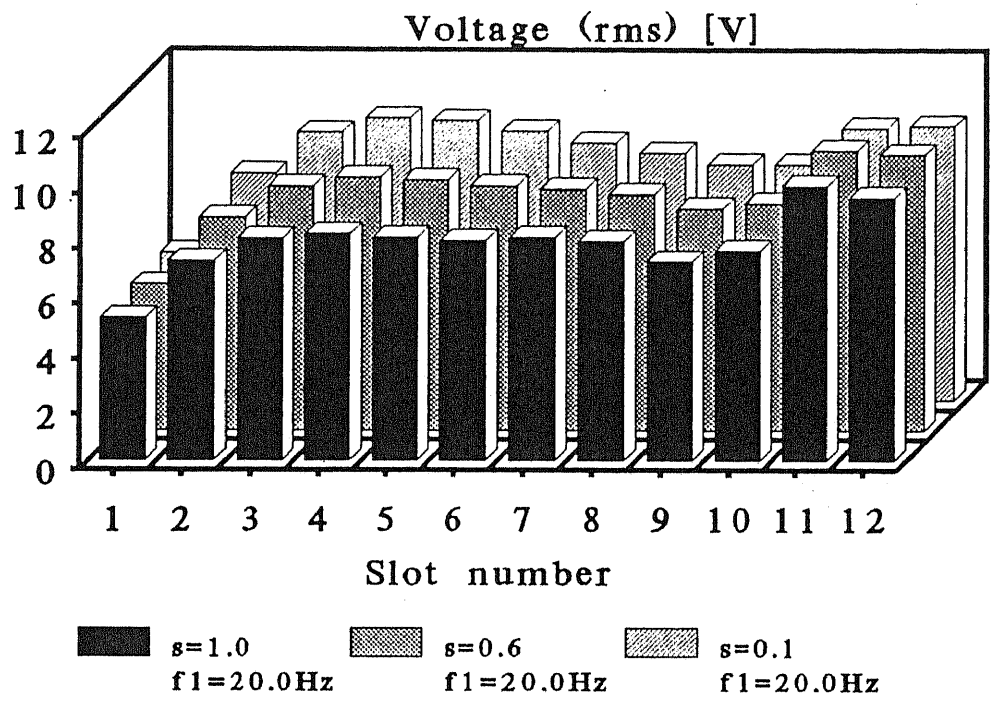

(d) Voltage in each winding.

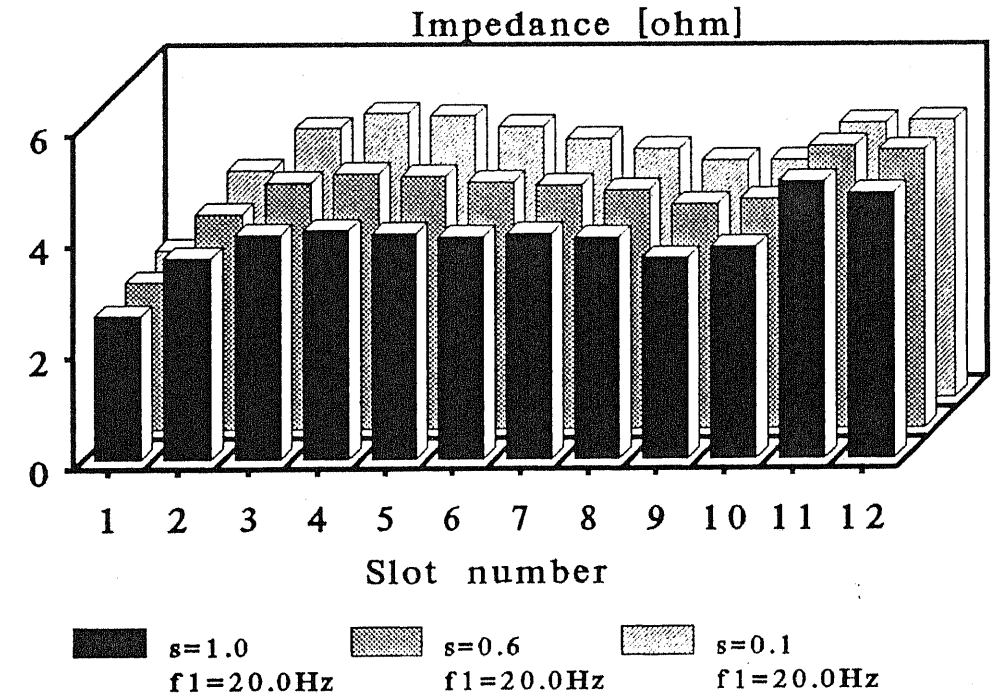

(e) Absolute value of impedance in each winding.

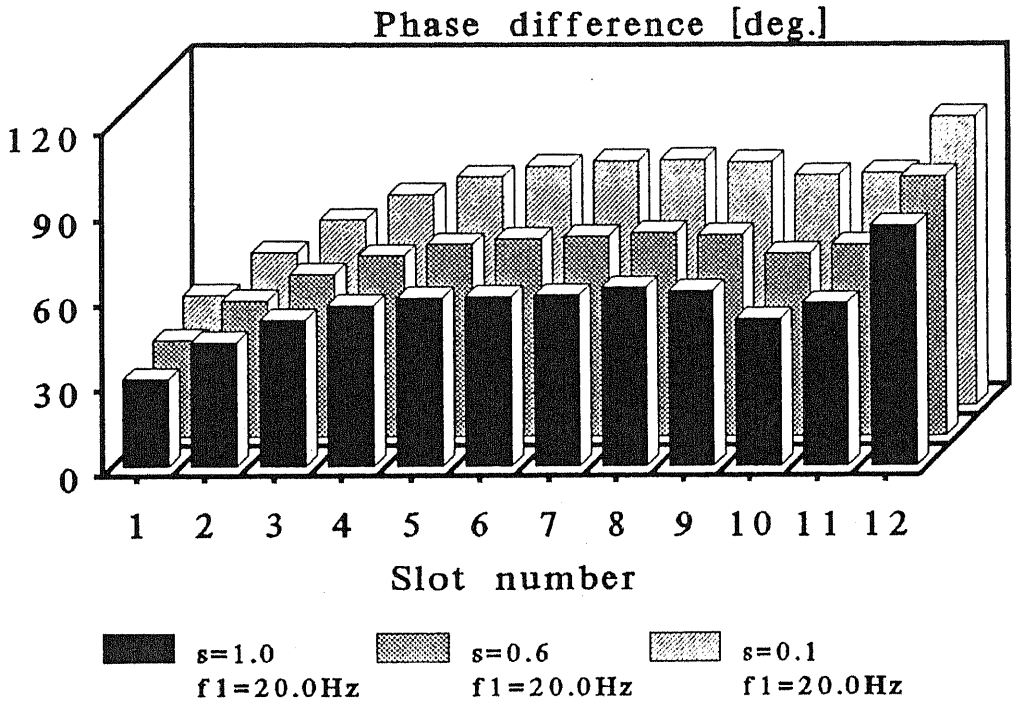

(f) Phase angle of impedance in each winding.

Figure 6.3. Drive with current sources ($f_1 = 20Hz$ *const.* and $I_{rms} = 2.0A$ *const.*).

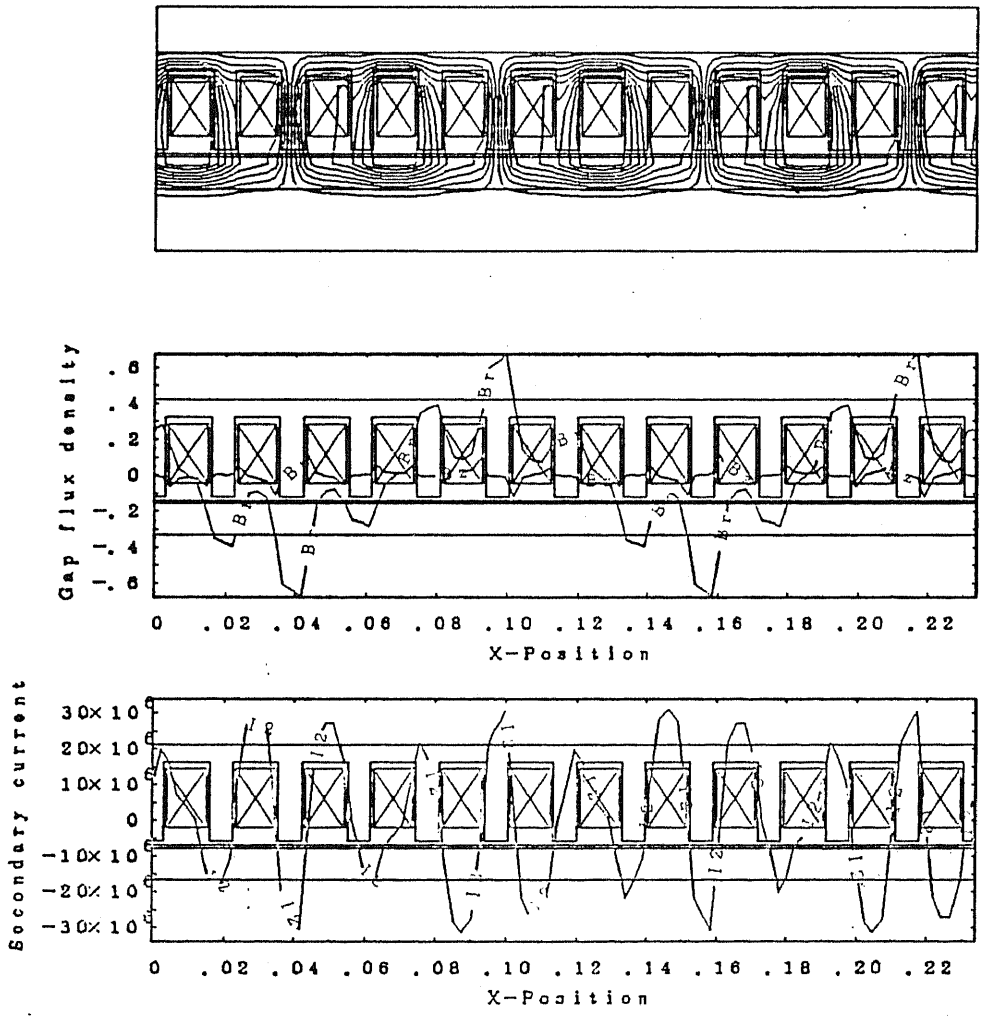

Figure 6.4. Calculated results ($I_{rms} = 2.0A$ *const.*, $s = 0.1$, and without end effect).

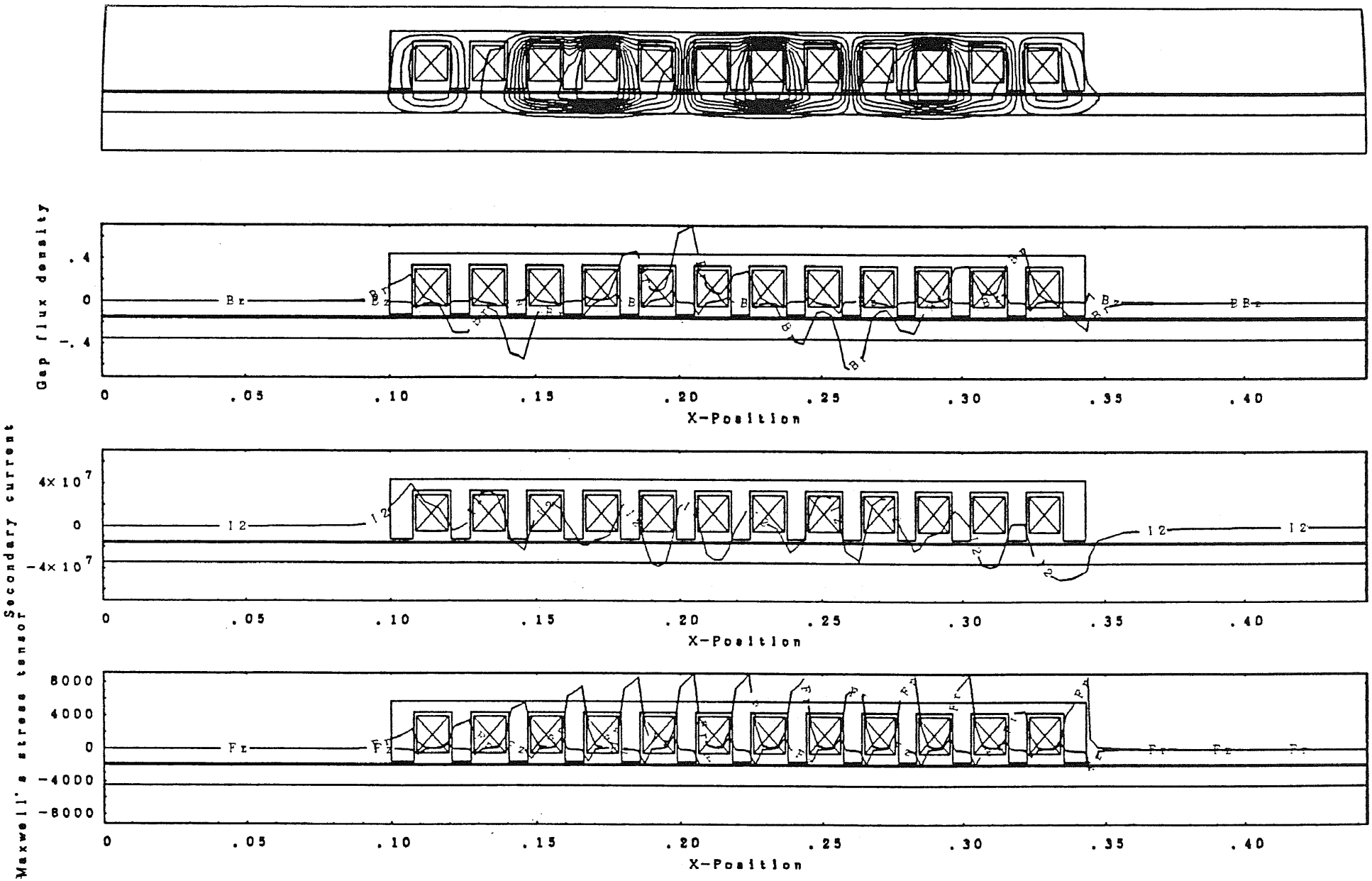

Figure 6.5. Calculated results ($I_{rms} = 2.0A$ *const.*, $s = 0.1$, and end effect).

6.3. Preliminary calculation (2) — general comparison among current-source-, voltage-source-, and flux-synthesizing- drives

The three kinds of the drives — current-source-, voltage-source- and flux-synthesizing- drives — without end effects are compared in this section for a prospect of further discussion.

The currents, the voltages and the gap flux density on the sampling points (see the figure 6.18 (c)) are kept constant $2.0A_{rms}$, $8.8V_{rms}$ and $0.68T_{amp}$ in the current-source-, voltage-source- and flux-synthesizing- drives respectively. Since an infinitely long motor without end effect is assumed in the calculations, there is no substantial difference among the three types of drives: in the case of asymmetric drives of the motor with finite length, discussed in the following sections, the three are inherently different, conversely.

We can see in the figure 6.6 (a) that the primary current flows too much at low frequencies in the drive with the constant voltage on account of low impedances. It should be noted that the voltage- and the thrust-force- curves of the flux synthesis are straight in the figures 6.6 (b) and (c) as prognosticated from the equation (5.73.c); the power source must raise the primary currents with the increase of the slip frequency to keep the gap flux density constant against the secondary reaction as shown in the figure 6.6 (a). The flux synthesis should be realized in low slip frequency region anyway, since the input power increases rapidly with the raise of the slip frequency as we see in the figure 6.6 (d).

The results in the figures 6.2 (c), 6.6 (b) and (c) will be used to decide the coefficient k in the equation (5.71) in the section 6.7.

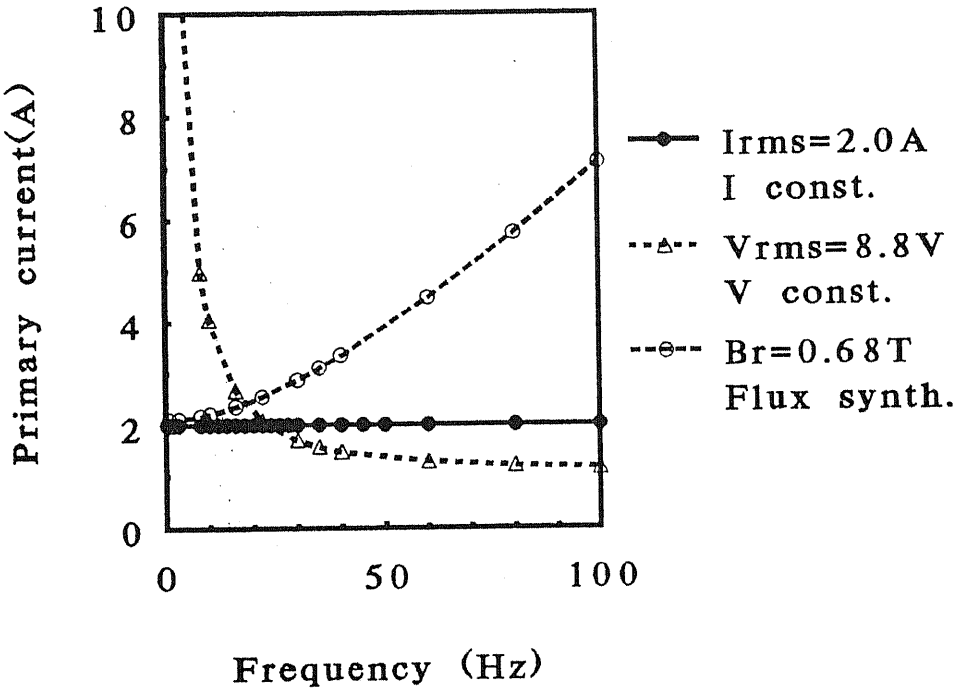

(a) Current.

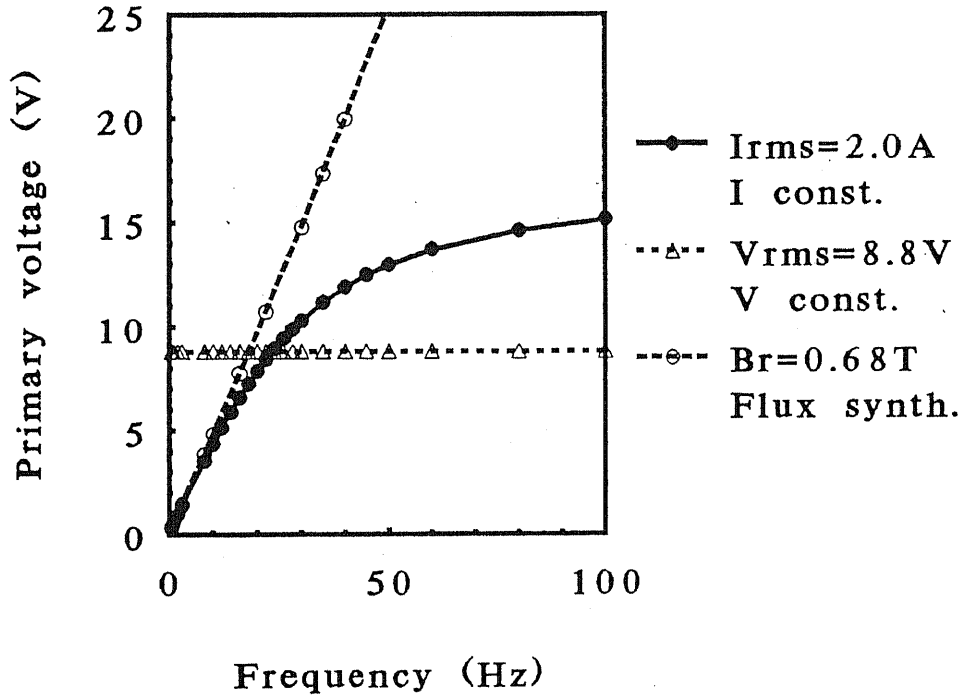

(b) Voltage.

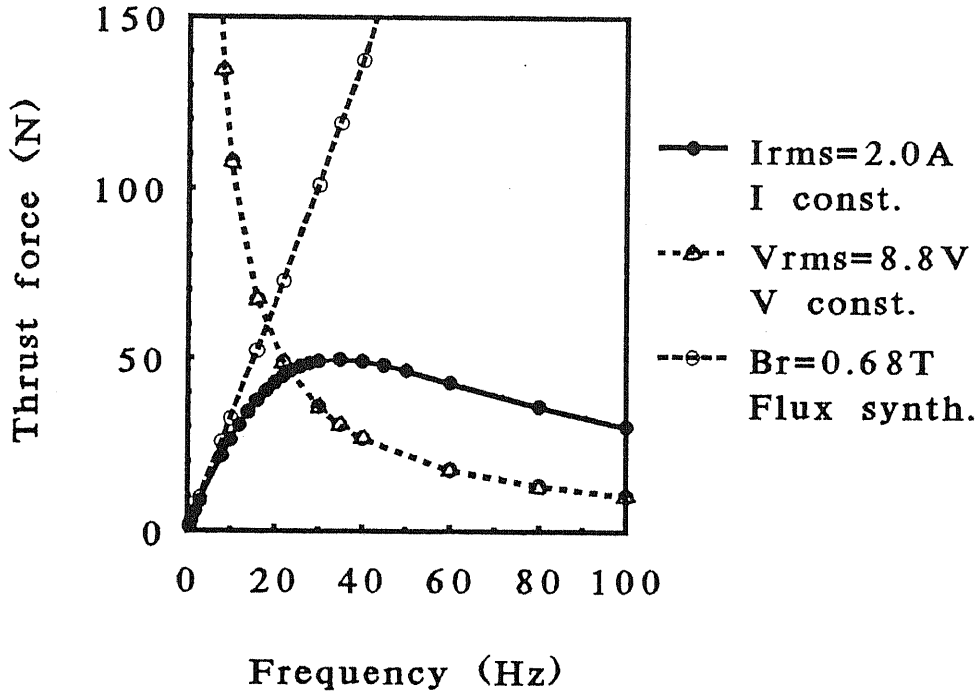

(c) Thrust force.

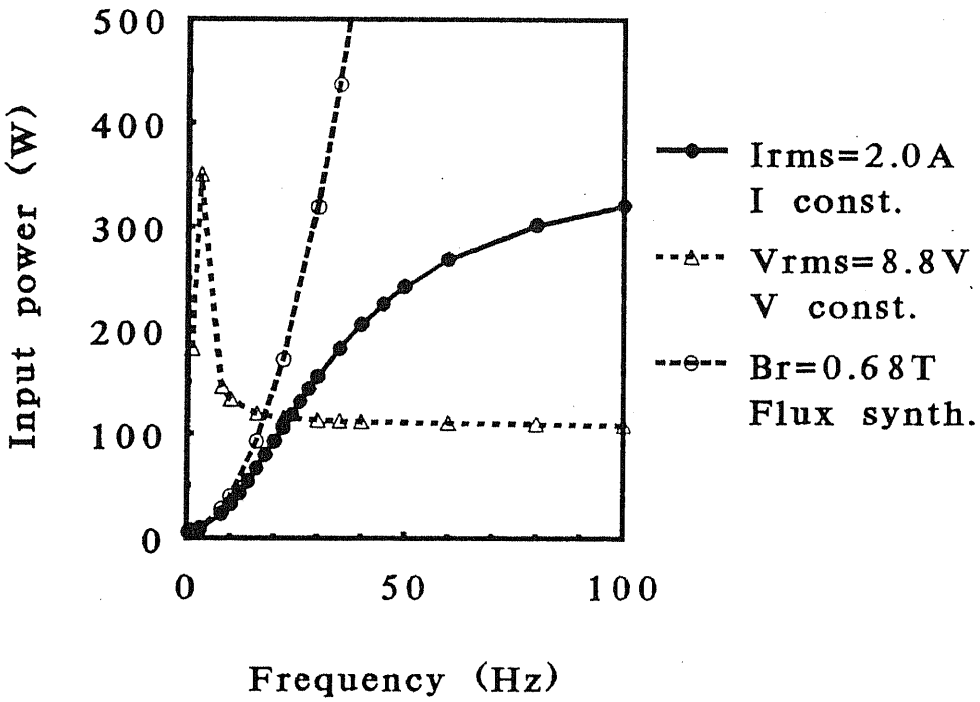

(d) Input power.

Figure 6.6. Comparison among the three kinds of drives.

6.4. Voltage source drive

6.4.1. Comparison between LIMs with- and without- end effect

The calculated thrust forces are plotted in the figure 6.7: there is almost no difference between the standstill drives with- and without- end effect, but the reduction of the thrust force on account of the end effect is larger than the case of the current source drive in the figure 6.3 (c) when the secondary side moves.

6.4.2. Comparison between three- phase serial- and parallel- connections

6.4.2.1. Experiment

The tubular machine shown in the figure 6.1 (a) was tested by using the three-phase power amplifier in the figure 6.1 (b) with the serial- and parallel- connections in the figure 6.8. The purpose of the measurements is as follows:

(1) to verify the calculations of the tubular LIM with the control volume method on the cylindrical coordinates, and

(2) to compare the serial- and parallel- connections.

The results measured at standstill tests have been plotted on the figures 6.9 and 6.10.

6.4.2.2. End effect and the connections (1) — force, impedance and efficiency

From the figures 6.9 and 6.10, we can see that:

(1) the agreement between the measurements and the calculations is much better than the case of the LIM calculated with the two- dimensional analysis discussed in the chapter 3, and that

(2) there is no remarkable difference between the serial- and parallel- connections if we see only the resultant forces or the three- phase impedances.

Running characteristics were also calculated: examples of the calculations are illustrated in the figure 6.11 and 6.12. The distribution of the Maxwell stress tensor is more rugged with the serial connection, but no one recognizes a substantial difference between the two kinds of connections either by seeing the results illustrated in the figures 6.13.

According to the serial connection illustrated in the figure 6.8 (b), the line currents are the same every three slots in the figure 6.14 (a), *e.g.*, the currents in the first, fourth, seventh and tenth slots. The serial connection transmits the asymmetry of impedances at the end portions to the inner part of the motor as we see in the figures 6.14 (c) and (d). Conversely, the end effect stays locally at the end portions in the case of the parallel connection: the impedances from the second- to the eleventh- slots are almost homogeneous in the figures 6.15. On the other hand, the

end effect is concentrated in the first and the last slots: the sudden change of the magnetic circuit at the end portions is harmful to motor characteristics.

6.4.2.3. End effect and the connection (2) — input power

The tendency discussed in the previous subsection is more obvious if we see the input power into each slot illustrated in the figures 6.16. That is to say, the drive with the parallel connection is not better than with the serial one due to the harmful effect concentrated into the both end portions, if the homogeneous voltages are applied to all the slots. We can, however, relux the sudden change of the magnetic characteristics at the end portion by applicating an appropriate voltage to each slot independently with the structure illustrated in the figure 4.10; an example will be introduced in the next section. In this case, we could improve the motor characteristics remarkably, because the impedances, *i.e.,* electromagnetic characteristics in the inner part of the motor are inherently homogeneous in a LIM with the parallel connection, *i.e.,* with a voltage applied independently to each slot as we saw in this section.

For comparison, the LIM with doubled length was calculated and the results are illustrated in the figures 6.16 (c) and 6.17. On account of the doubled length, the ruggedness of the input powers among the slots is relaxed but not completely, in the case of the serial connection. Conversely, the projection of the input power at the first slot is the same as in the figure 6.16 (b). The suppression of the local projection, therefore, is important anyway for improving motor's characteristics.

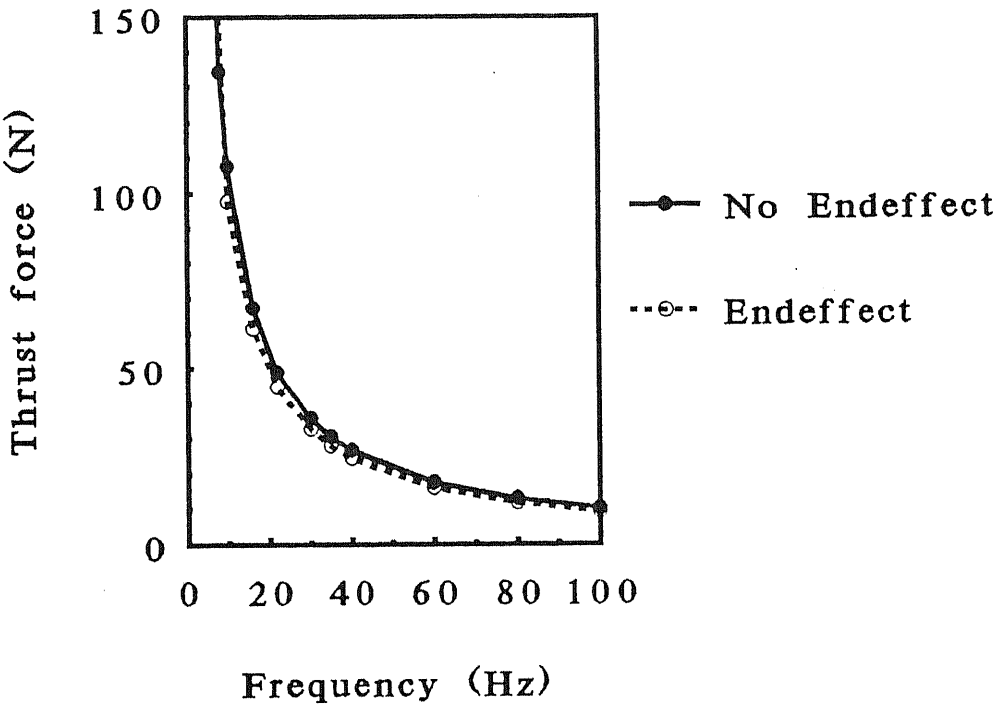

(a) Standstill drive.

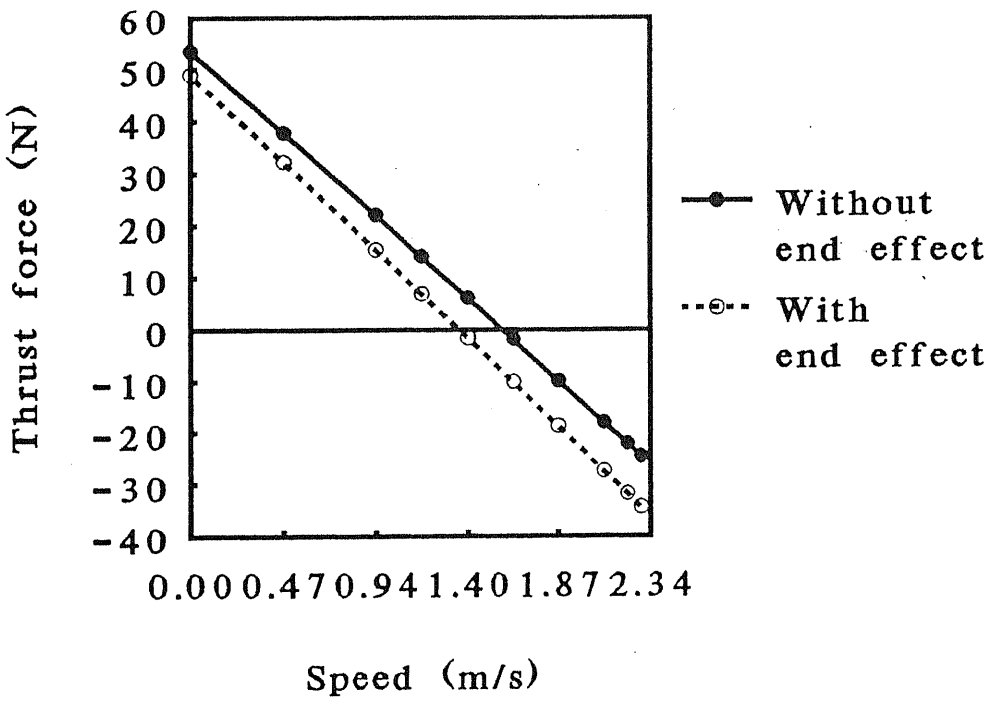

(b) $f_1 = 20Hz$ *const.*

Figure 6.7. Thrust force characteristics with voltage sources. (V = 8.8V/Slot)

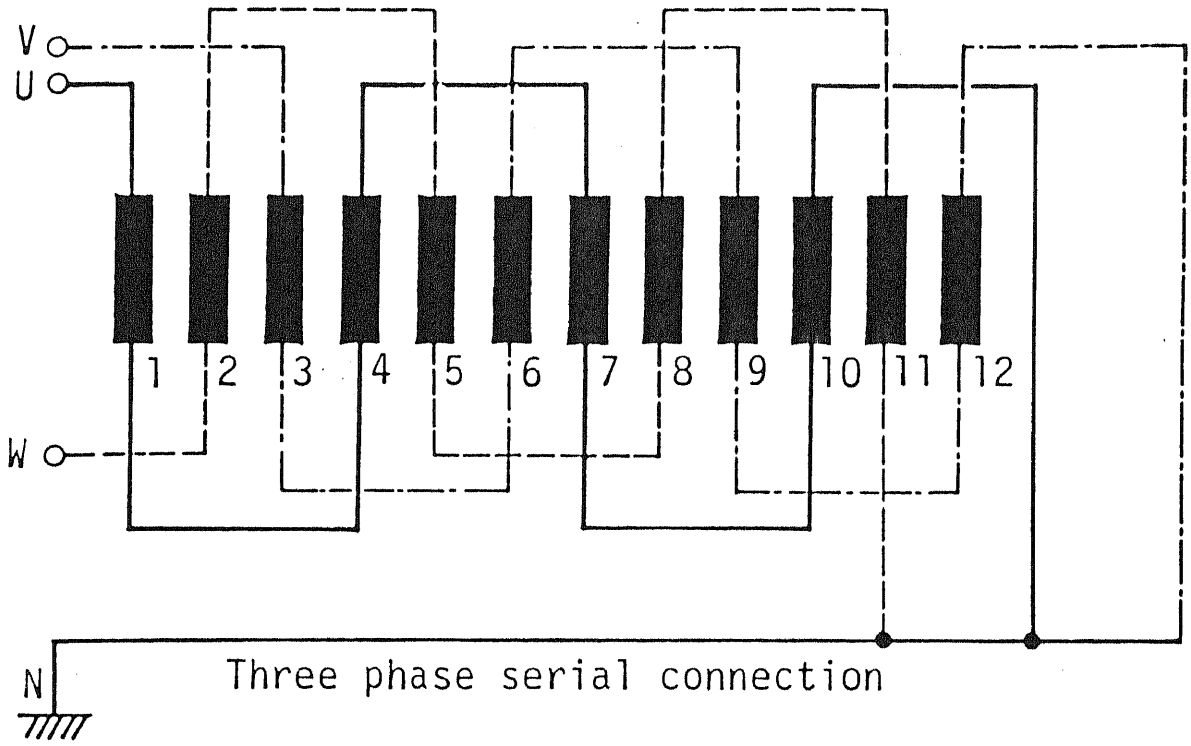

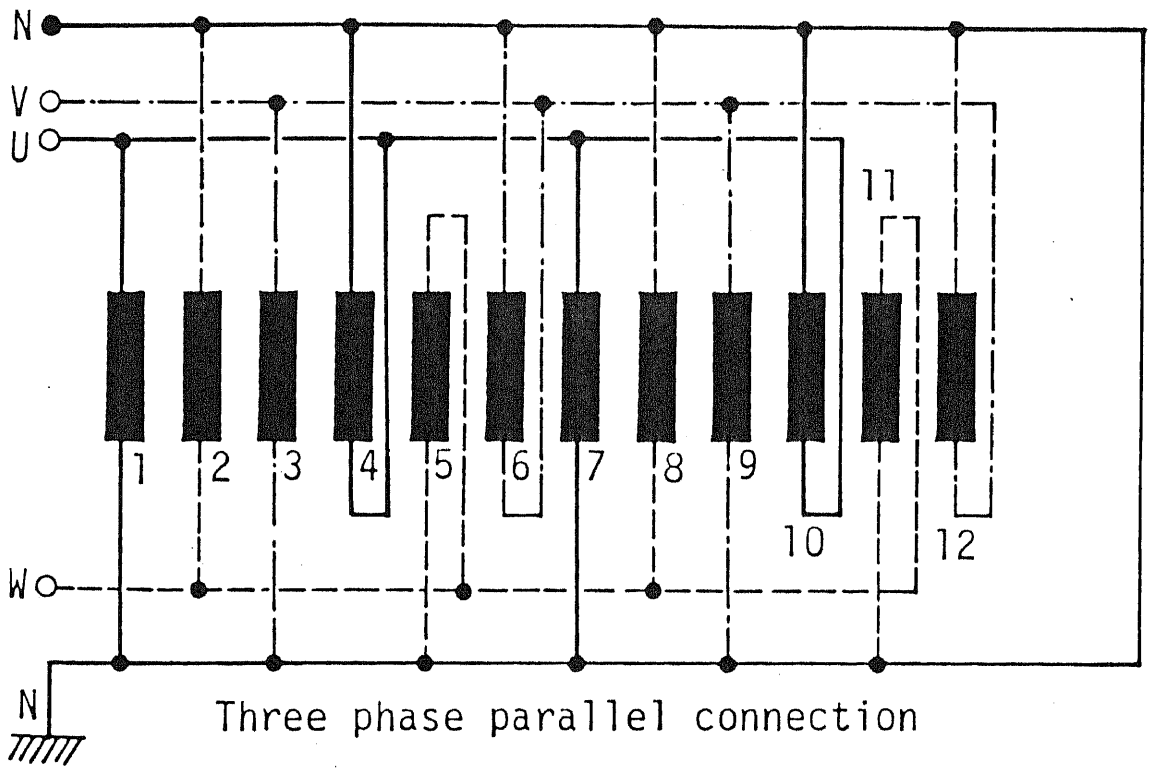

Figure 6.8. Three- phase serial- and parallel connections.

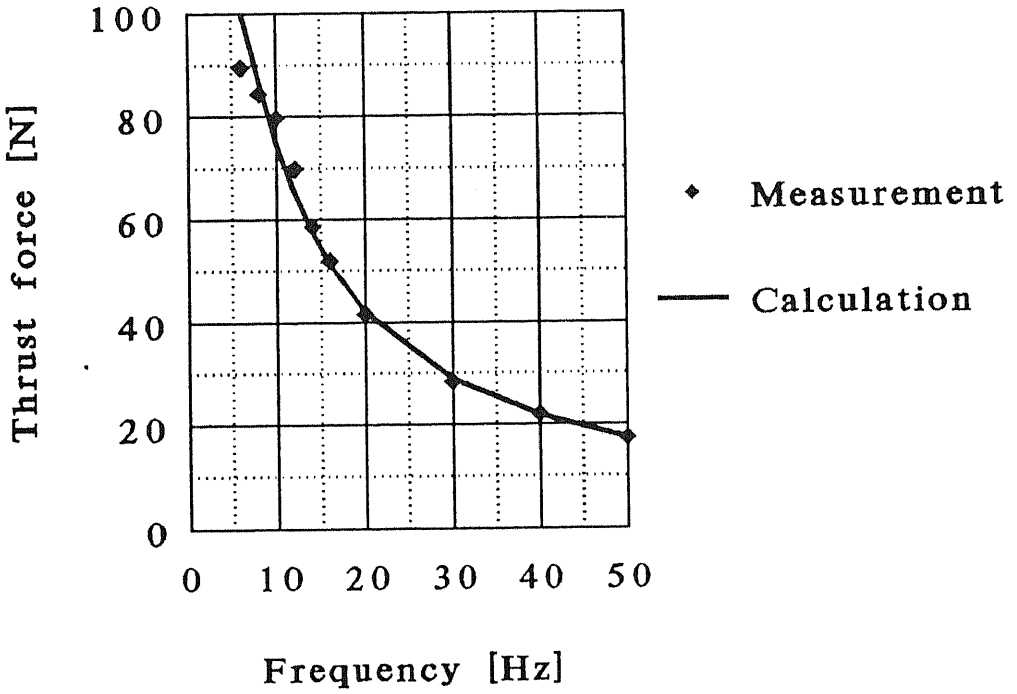

(a) Thrust force.

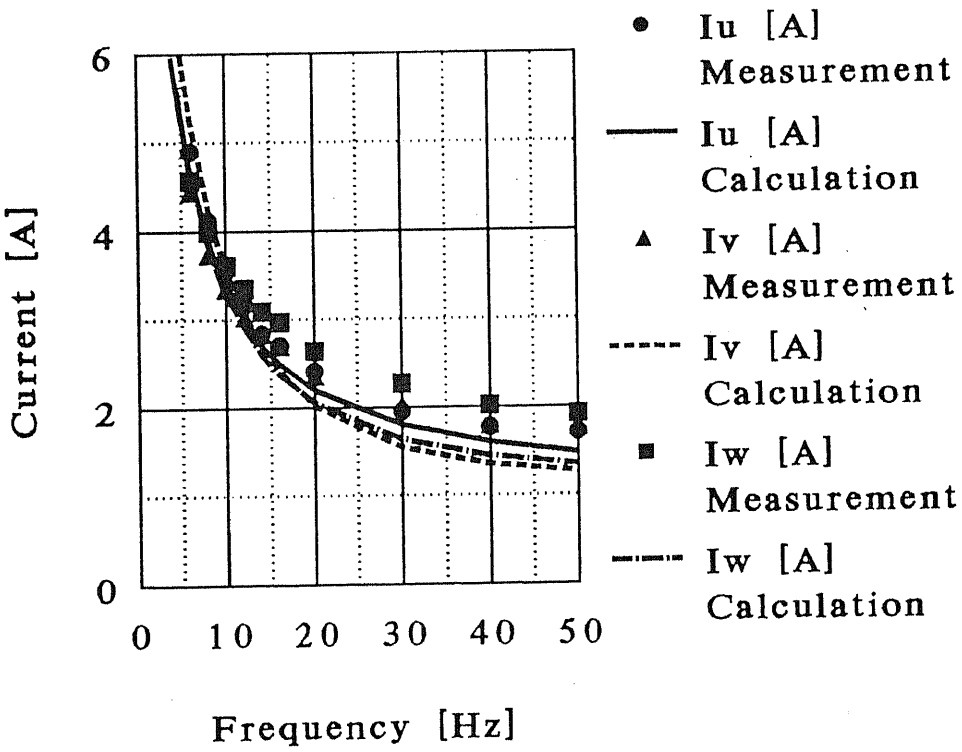

(b) Three- phase currents.

Figure 6.9. Measured- and calculated- results with serial connection. (V = 35.2V)

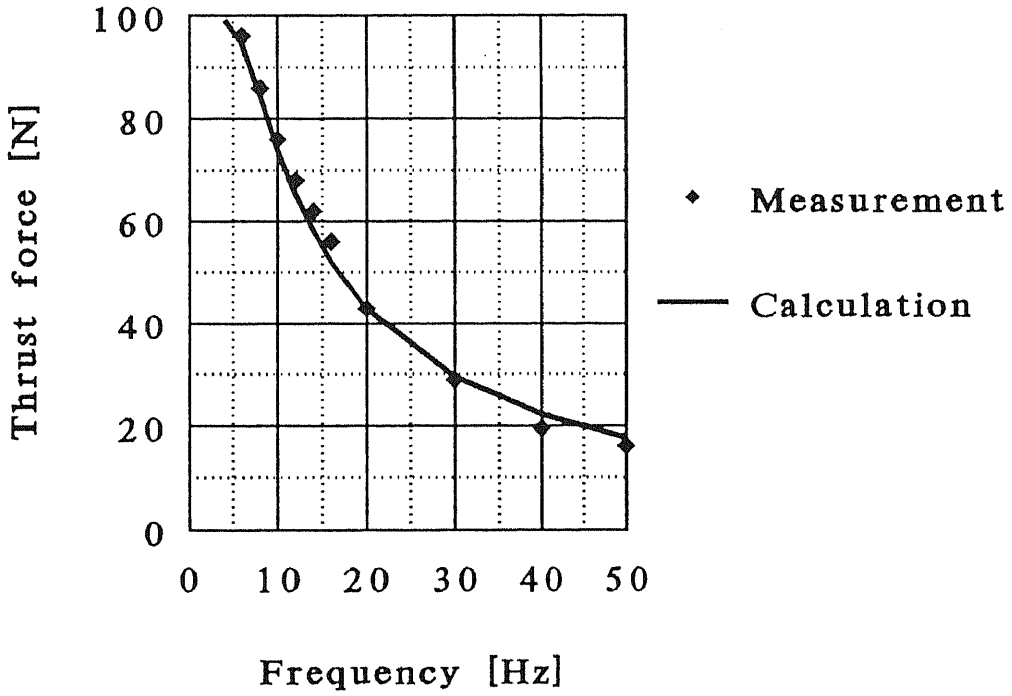

(a) Thrust force.

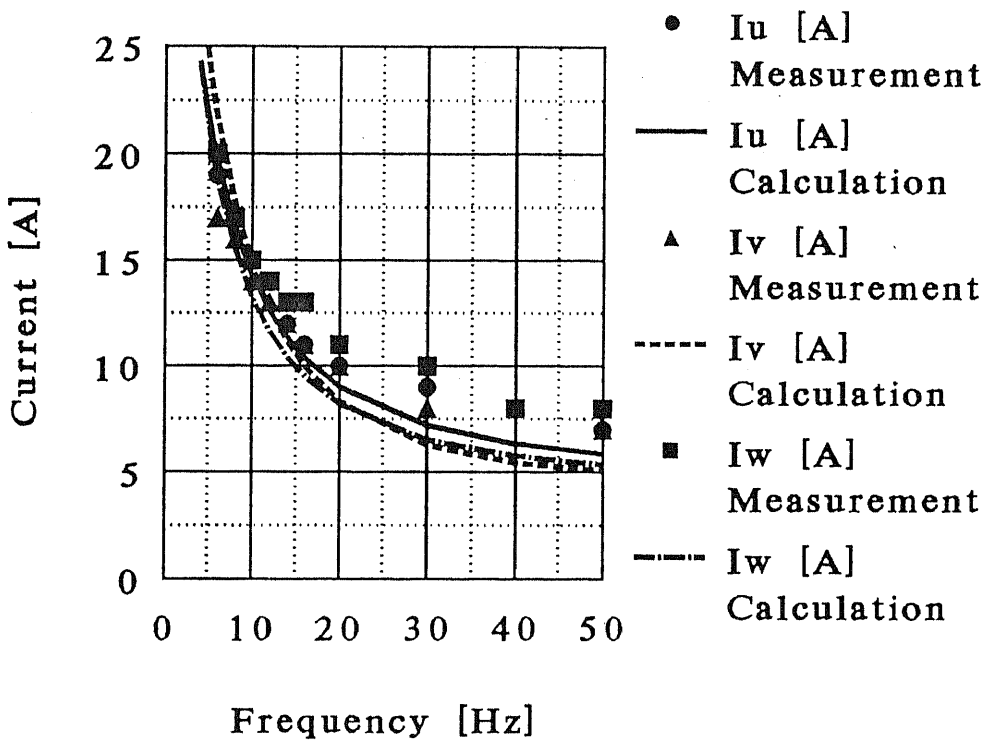

(b) Three- phase currents.

Figure 6.10. Measured- and calculated- results with parallel connection.
(V = 8.8V)

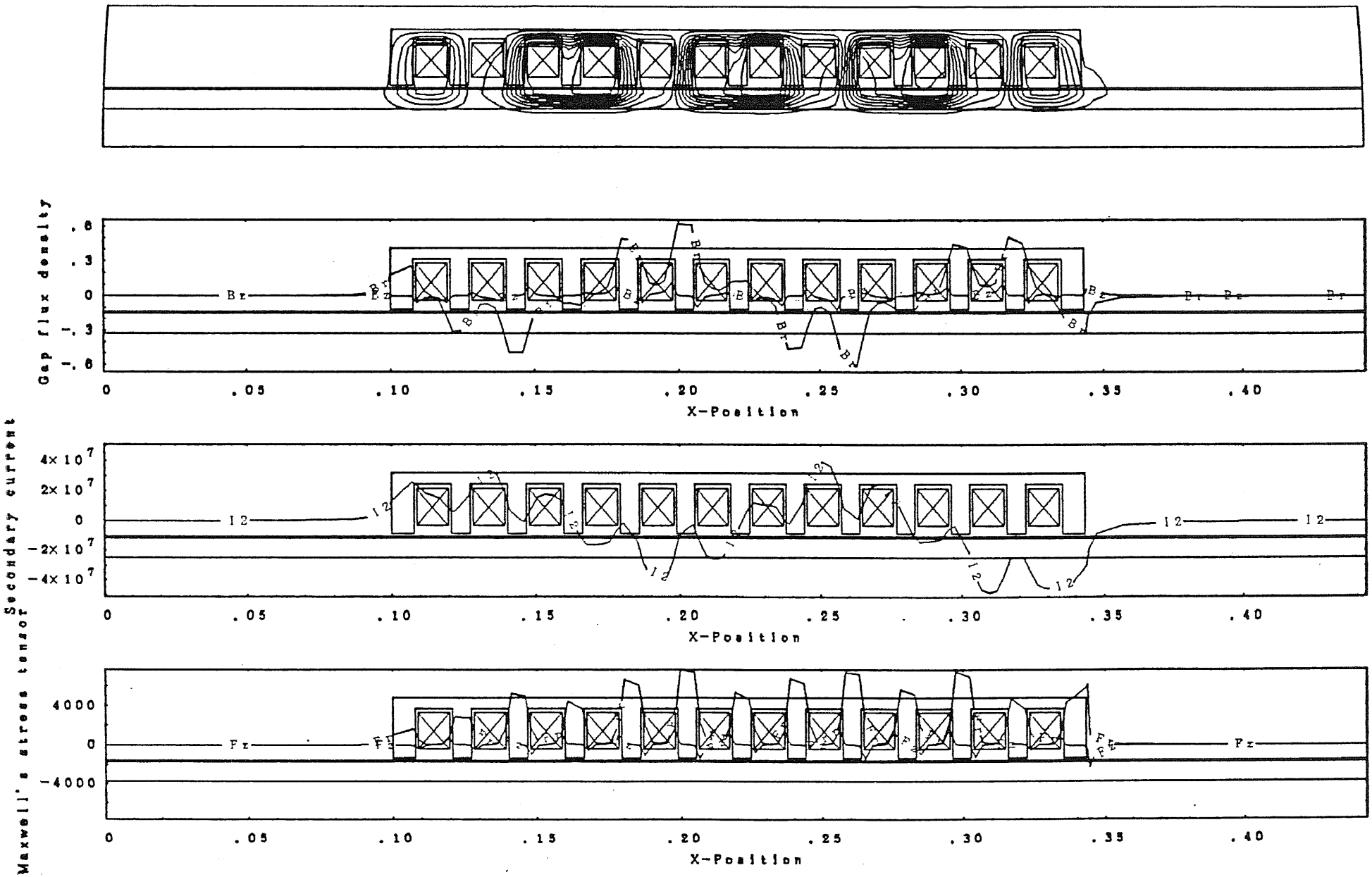

Figure 6.11. Calculated results of the serial connection ($s = 0.6$ and $f_1 = 20Hz$).

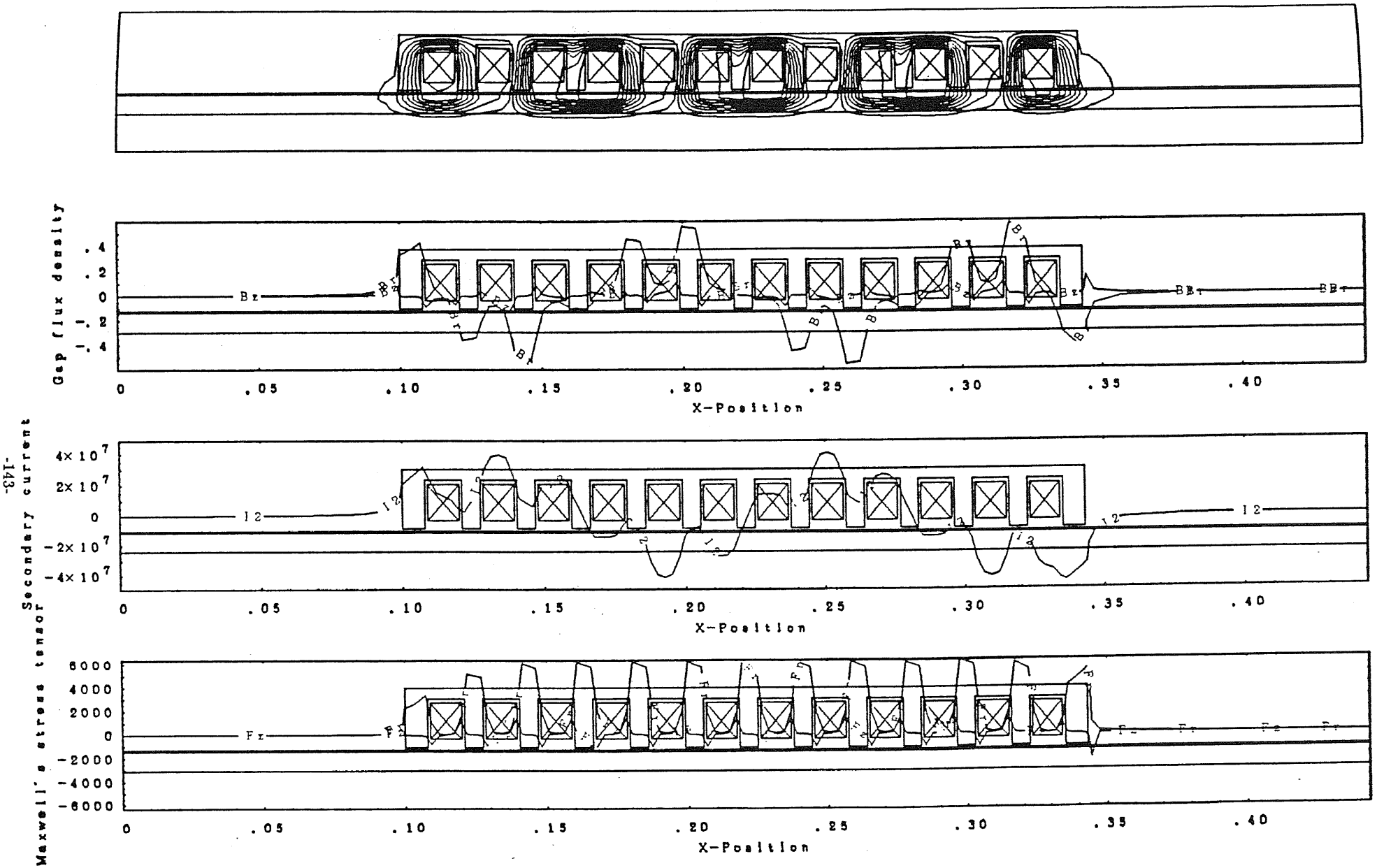

Figure 6.12. Calculated results of the parallel connection. ($s = 0.6$ and $f_1 = 20Hz$).

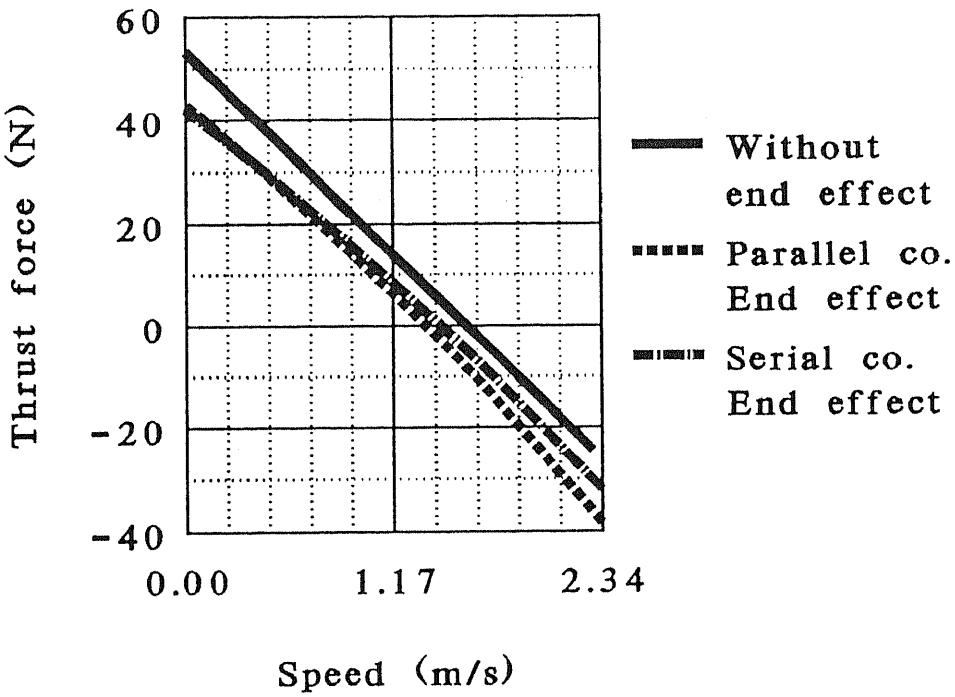

(a) Thrust force.

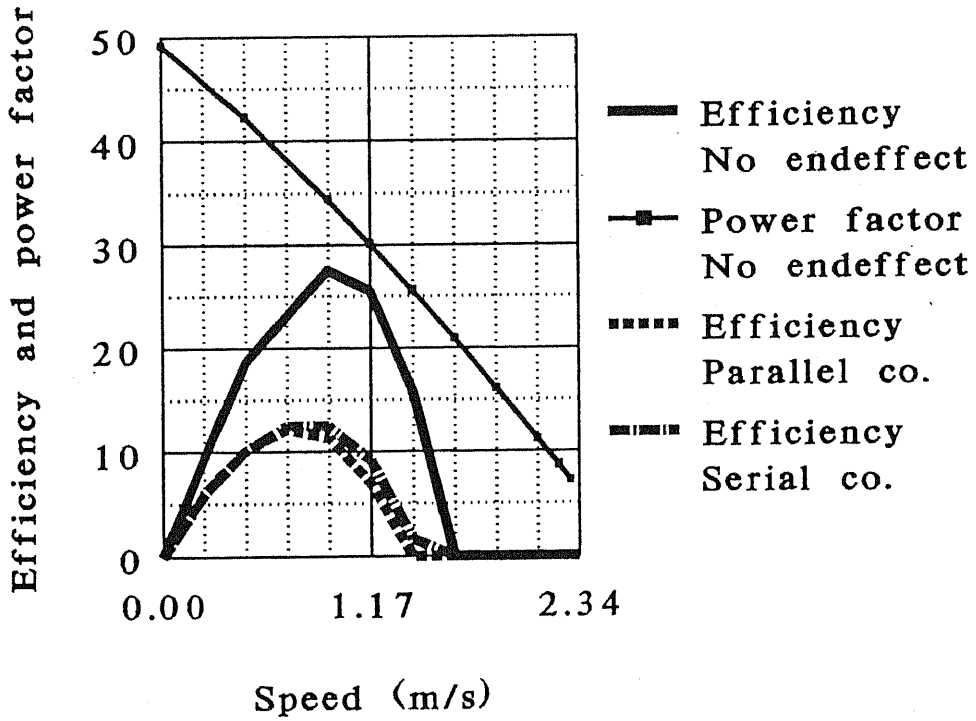

(b) Power factor and energy efficiency.

Figure 6.13. Comparison of running characteristics between serial- and parallel-connections. (V_{ser} = 35.2V and V_{par} = 8.8V)

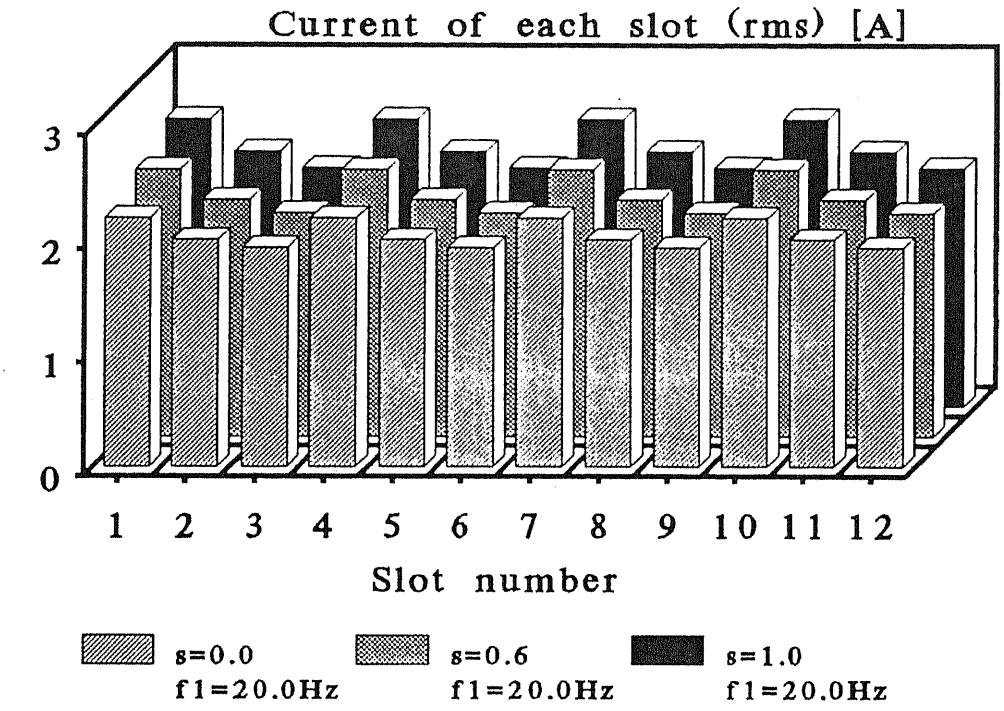

(a) Current.

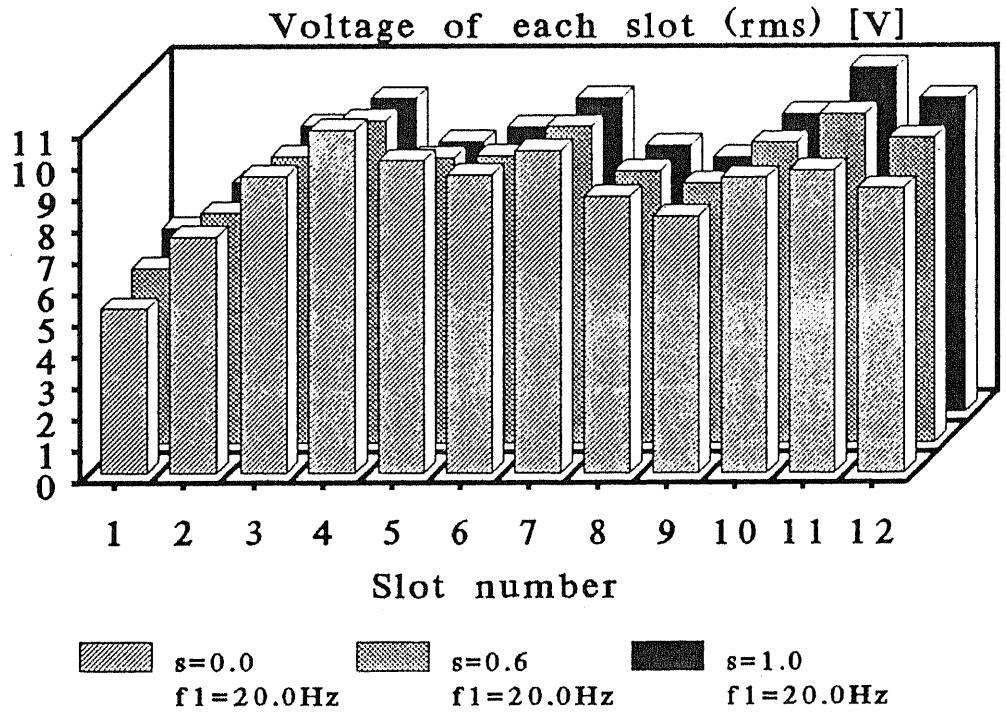

(b) Voltage.

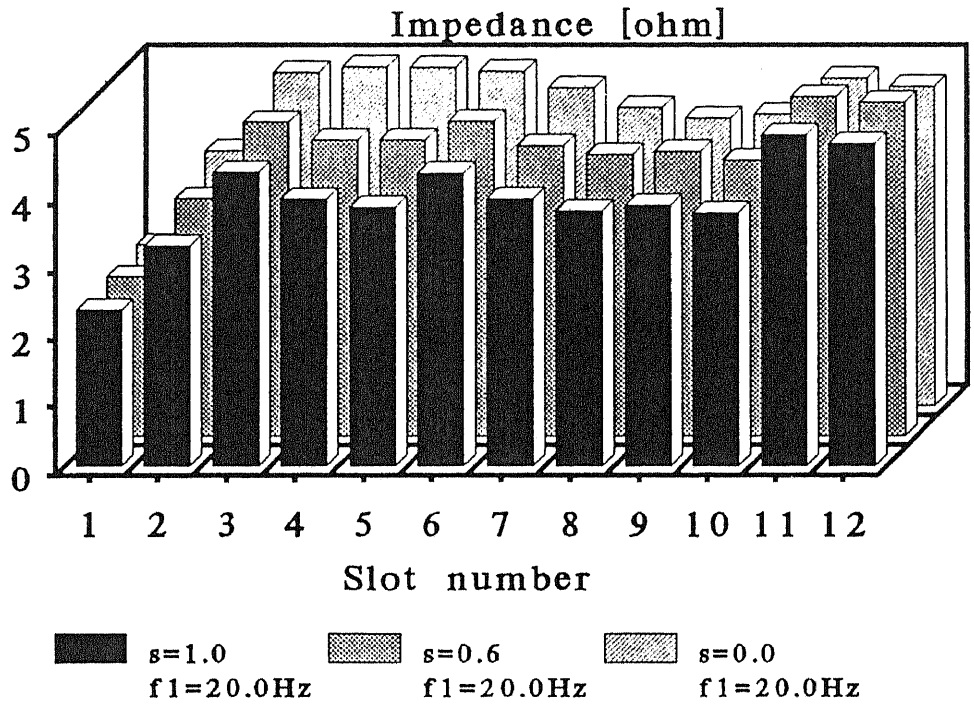

(c) Absolute value of impedance.

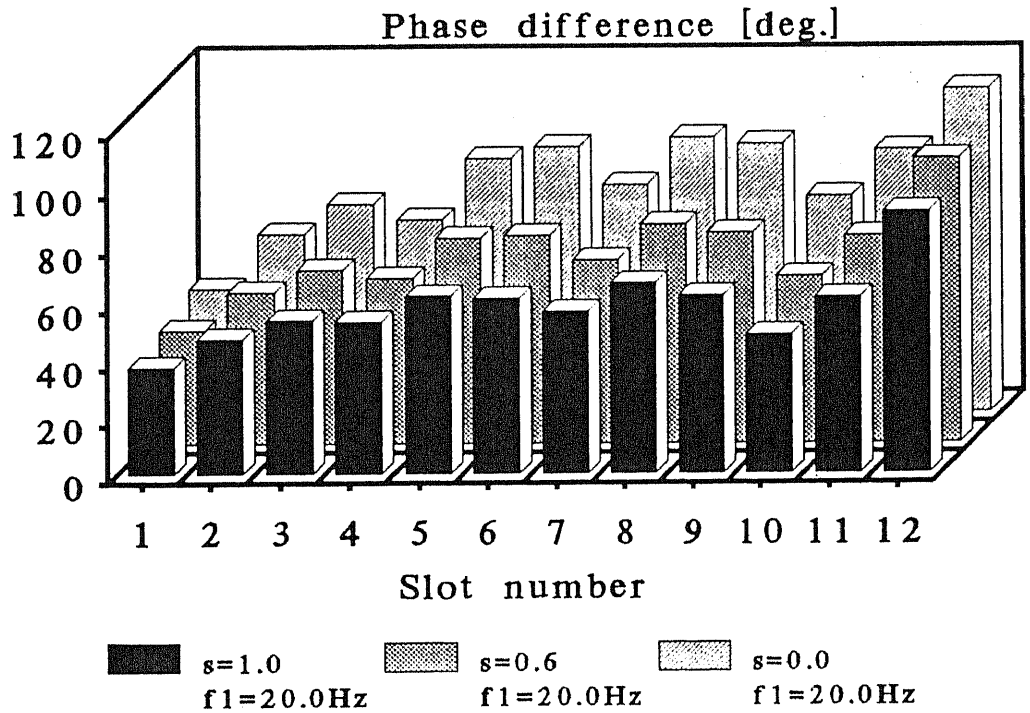

(d) Phase angle of impedance.

Figure 6.14. Serial connection: values in each slot. (V = 35.2V)

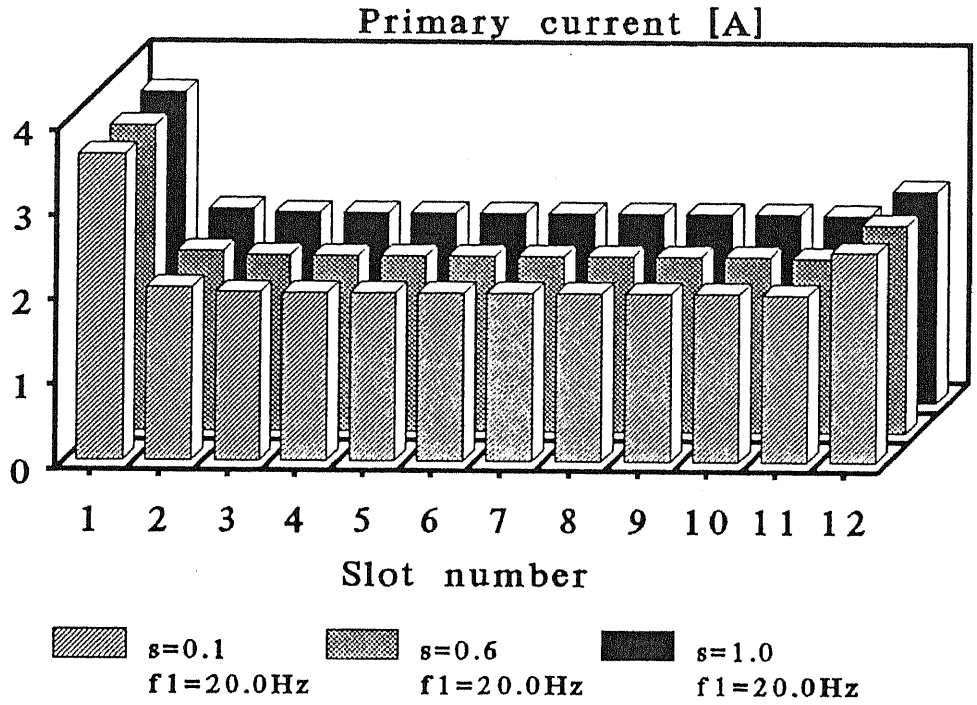

(a) Current.

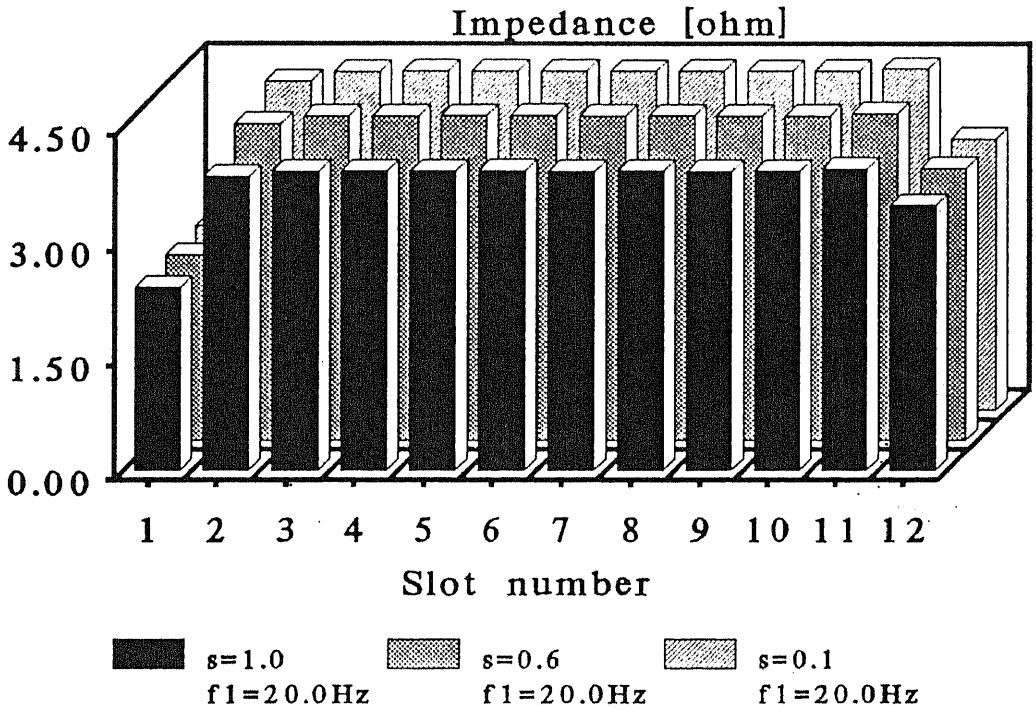

(b) Absolute value of impedance.

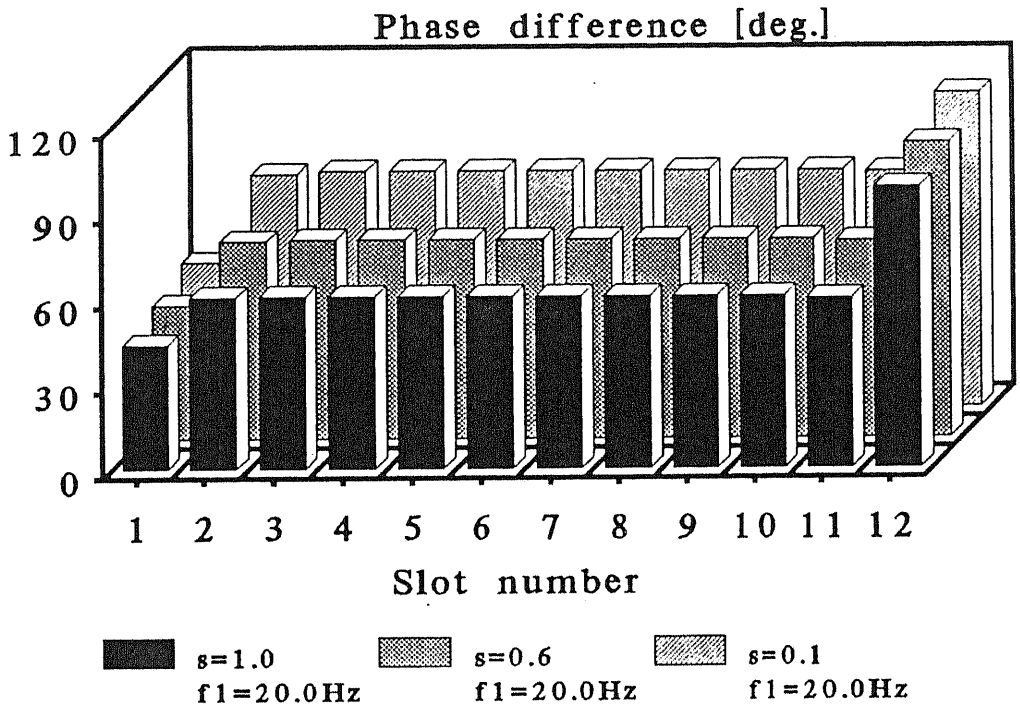

(c) Phase angle of impedance.

Figure 6.15. Parallel connection: values in each slot. (V = 8.8V)

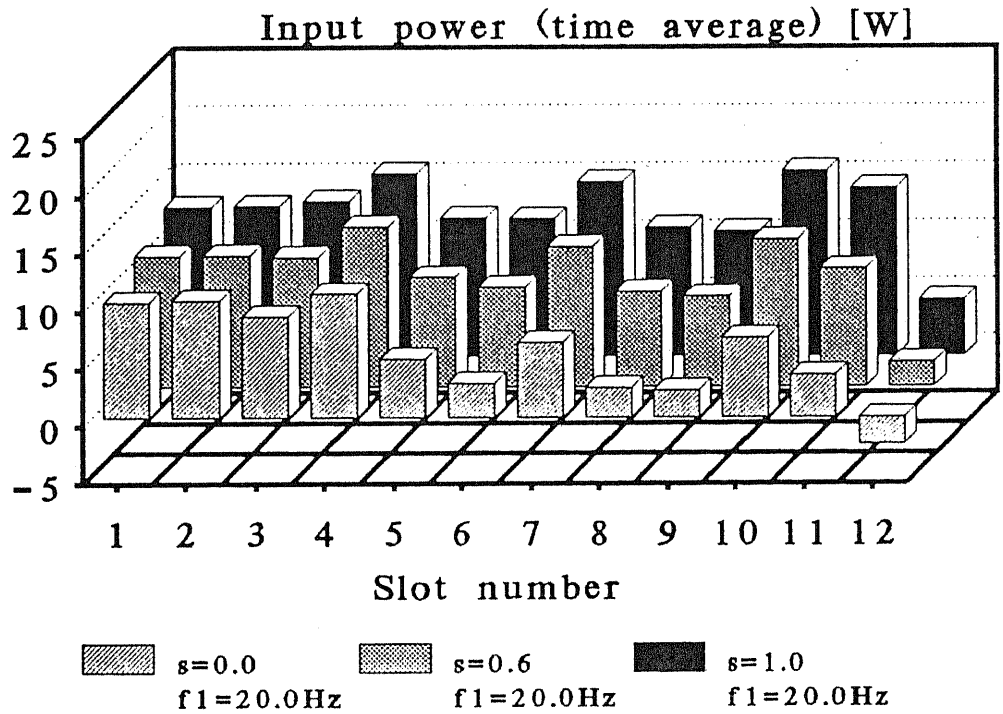

(a) Serial connection.(V = 35.2V)

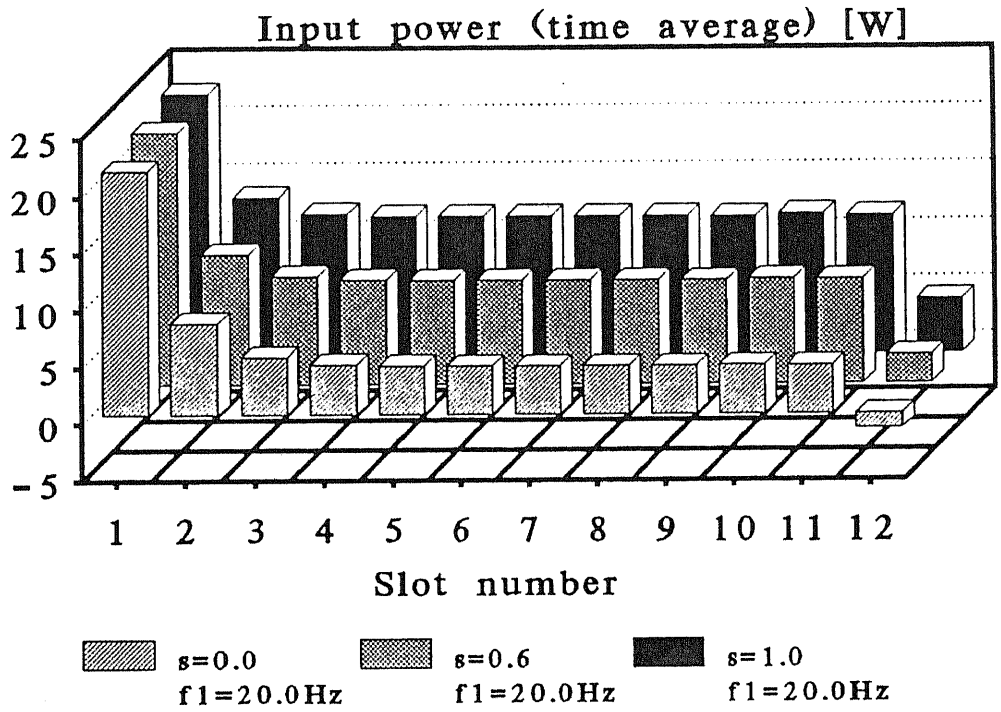

(b) Parallel connection.(V = 8.8V)

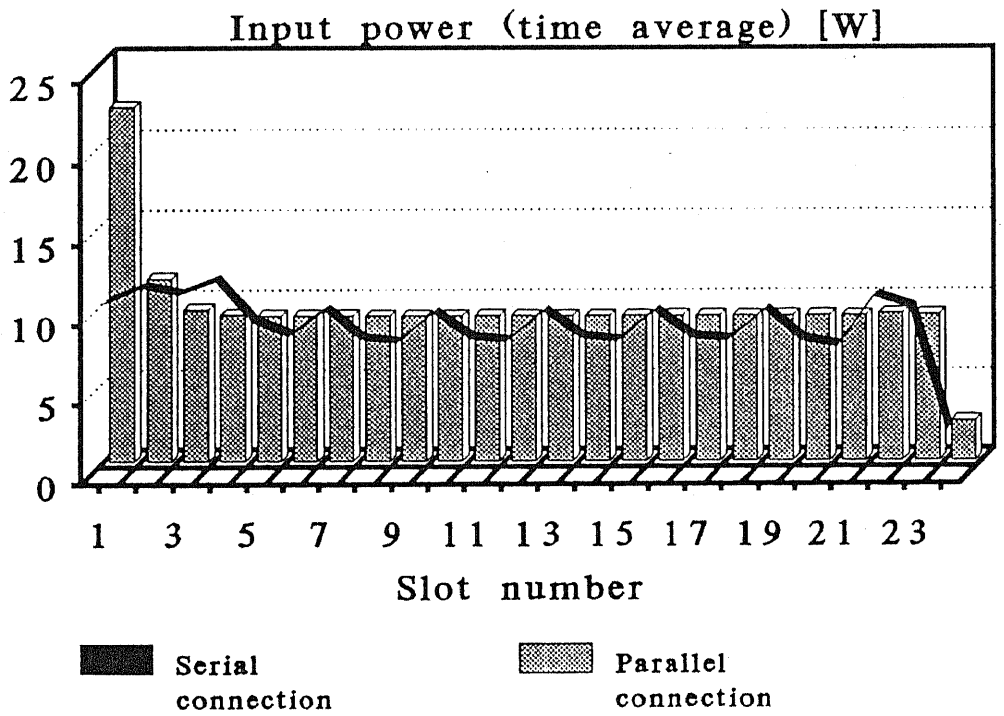

(c) Comparison between serial- and parallel- connections with doubled length.

Figure 6.16. Input power into each winding.

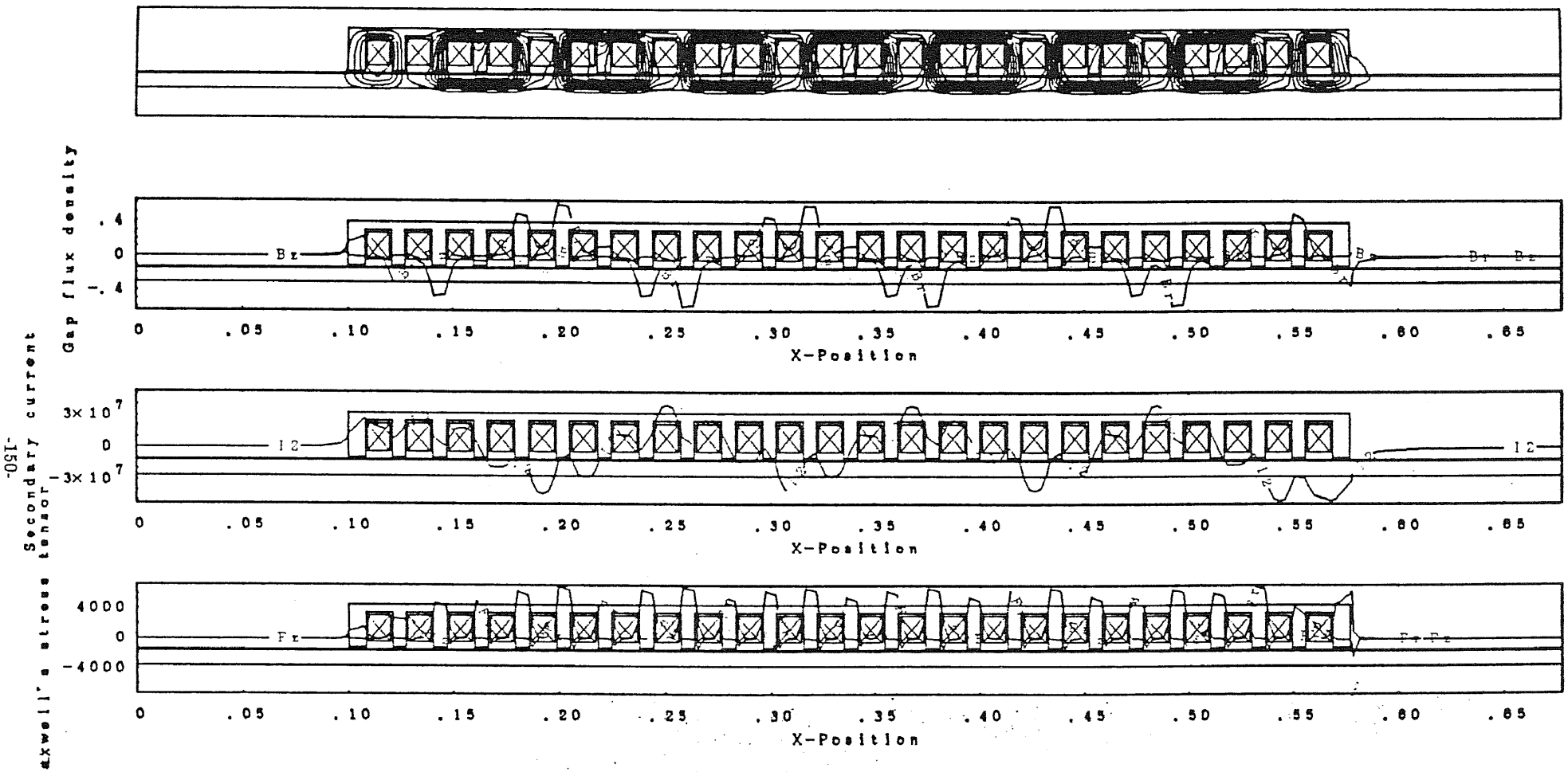

(a) Serial connection.($V = 70.4$V)

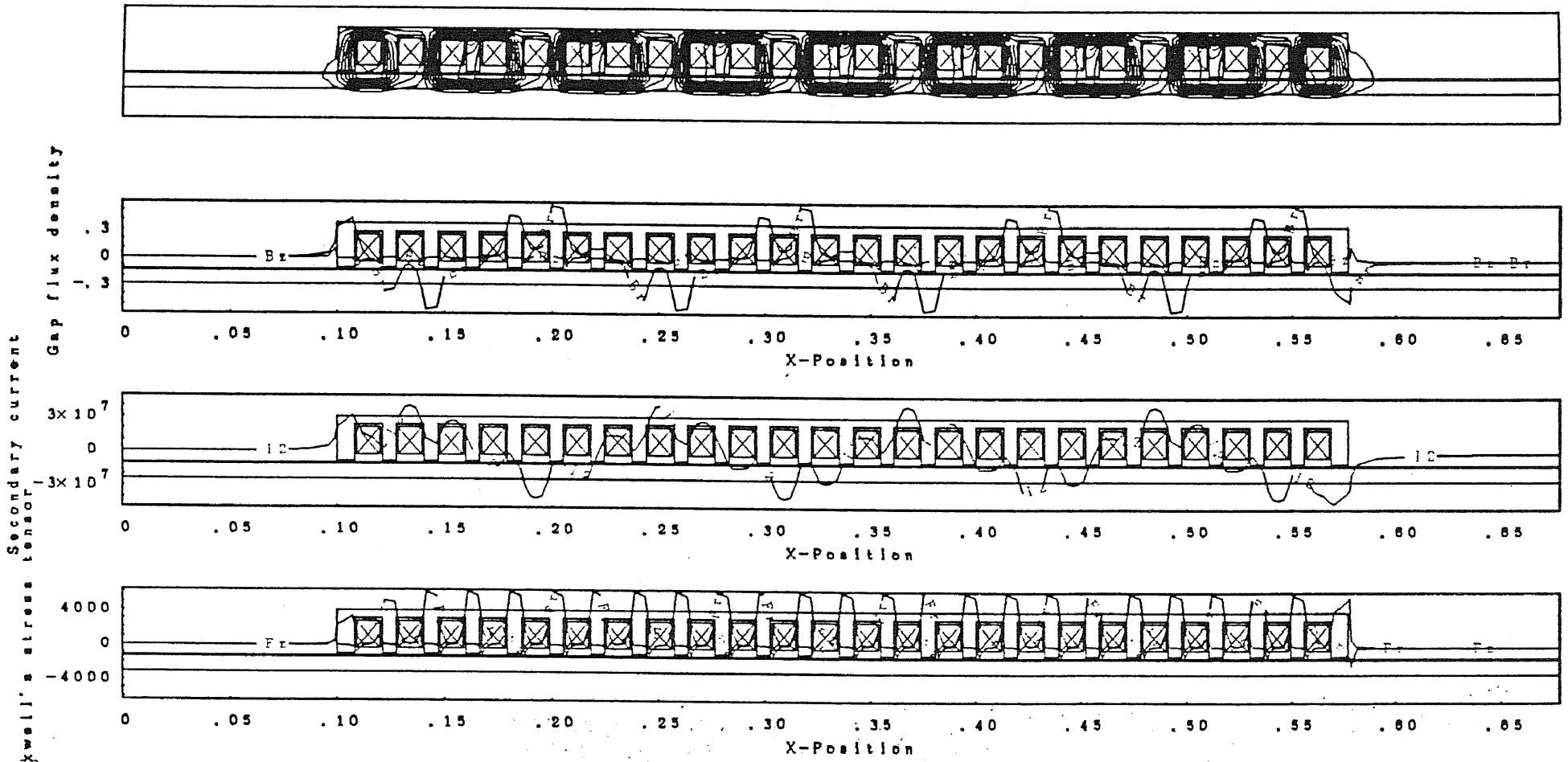

(b) Parallel connection.($V = 8.8$V)

Figure 6.17. Flux distribution. ($s = 0.6$ and $f_1 = 20.0$Hz)

6.5. Various flux synthesizing methods

The following three kinds of flux synthesizing method will be calculated, verified and compared with the case without end effect in this section. The gap flux distributions are synthesized, so that the flux density B_r may be spatially sinusoidal on the sampling points illustrated in the figure 6.18. Since the test machine has twelve independent primary windings, there are twelve degrees of freedom for control. The twelve points of the flux synthesis (1) in the figure 6.18 (a) were selected by rote, therefore, the arrangements of the points are asymmetric. To avoid the asymmetry, two points were set on the central slot in the flux synthesis (2) as we see in the figure 6.18 (b). On the other hand, eleven sampling points were set and the last freedom was used for fulfilling the constraint of $\sum_{n=1}^{12} i_{1,n} = 0$ in the flux synthesis (3) illustrated in the figure 6.18 (c).

Flux lines, gap flux density, secondary current and distribution of the Maxwell stress have been calculated and illustrated in the figures 6.19-21. Zero phase current is conspicuous in the flux synthesis (1) as we see in the figure 6.19 (c). The curves of the thrust force for (slip) frequency are straight lines as prognosticated with the equations (5.73). The thrust force of the flux syntheses (2) and (3) are approximately eighty percent of the case of no end effect. If we see the energy consumption and running characteristics illustrated in the figures 6.22 (b)-(e), it is immediately recognized that we can accept only the method (3). It should be emphasized that the energy efficiency is improved with the flux synthesis (3) as we can see by comparing the figure 6.22 (e) with the figure 6.13 (b).

Also the figures 6.22 (f)-(h) support the previous arguments. The spatial ruggedness of the method (1) must cause energy loss and requirements of redundant power supplies, hence, it is not acceptable. Conversely, the remarkable projection of the input to the first slot in the figures 6.15 has been reluxed and the spatial distribution has, accordingly, been much improved by applying the flux synthesizing method (3).

We will, therefore, always assume the method (3) for flux synthesis in the following discussion.

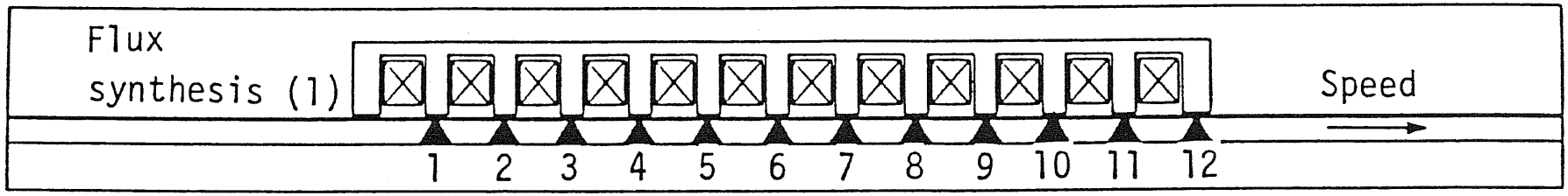

(a) Flux synthesis (1).

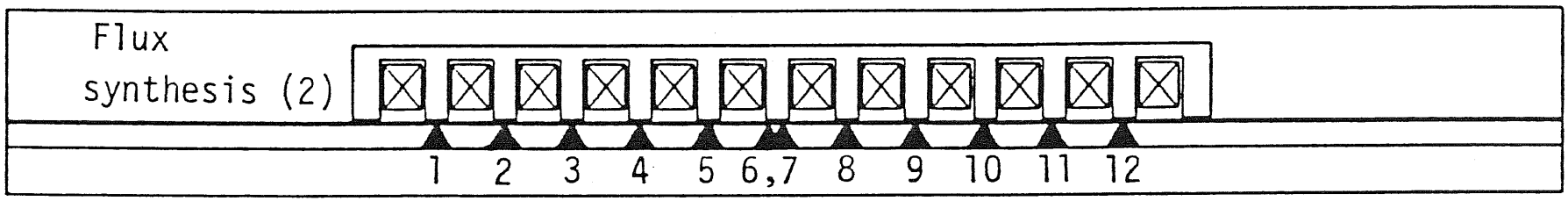

(b) Flux synthesis (2).

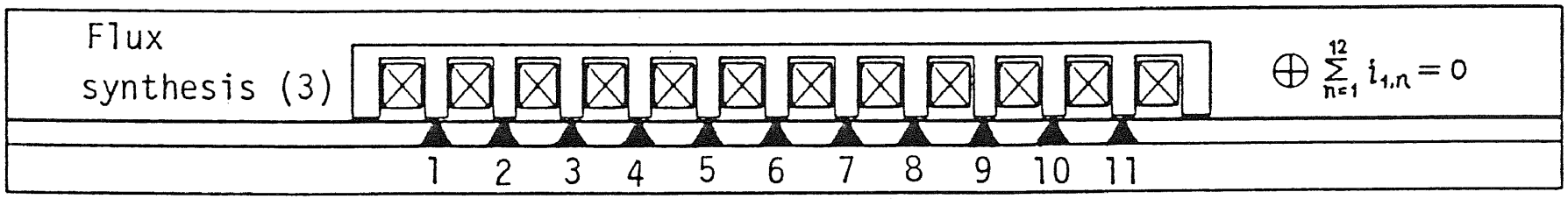

(c) Flux synthesis (3).

Figure 6.18. Sampling points for flux syntheses.

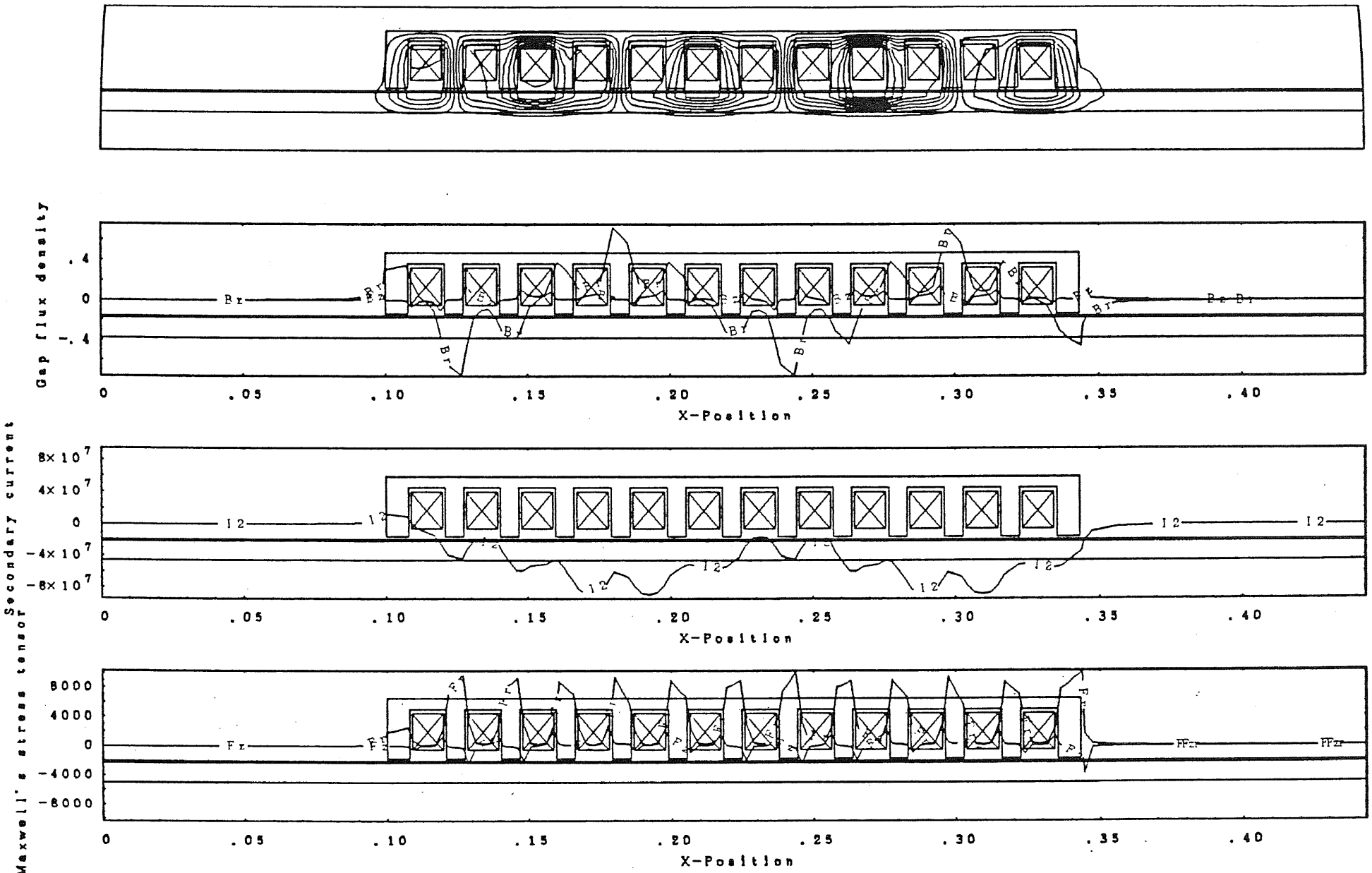

Figure 6.19. Calculated results of the flux synthesis (1) ($s = 0.6$ and $B_r = 0.68T$ *const.*)

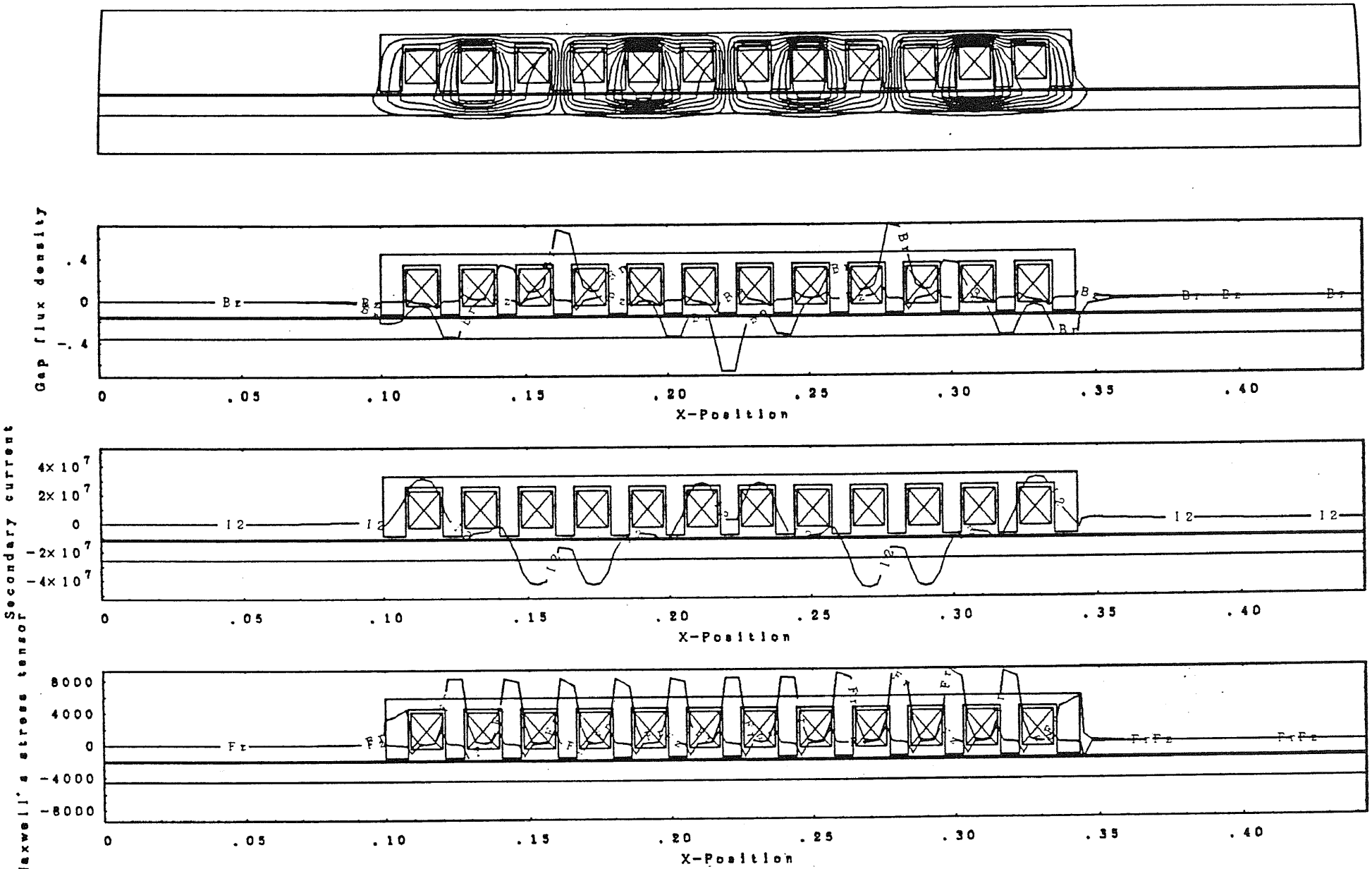

Figure 6.20. Calculated results of the flux synthesis (2) ($s = 0.6$ and $B_r = 0.68T$ *const.*)

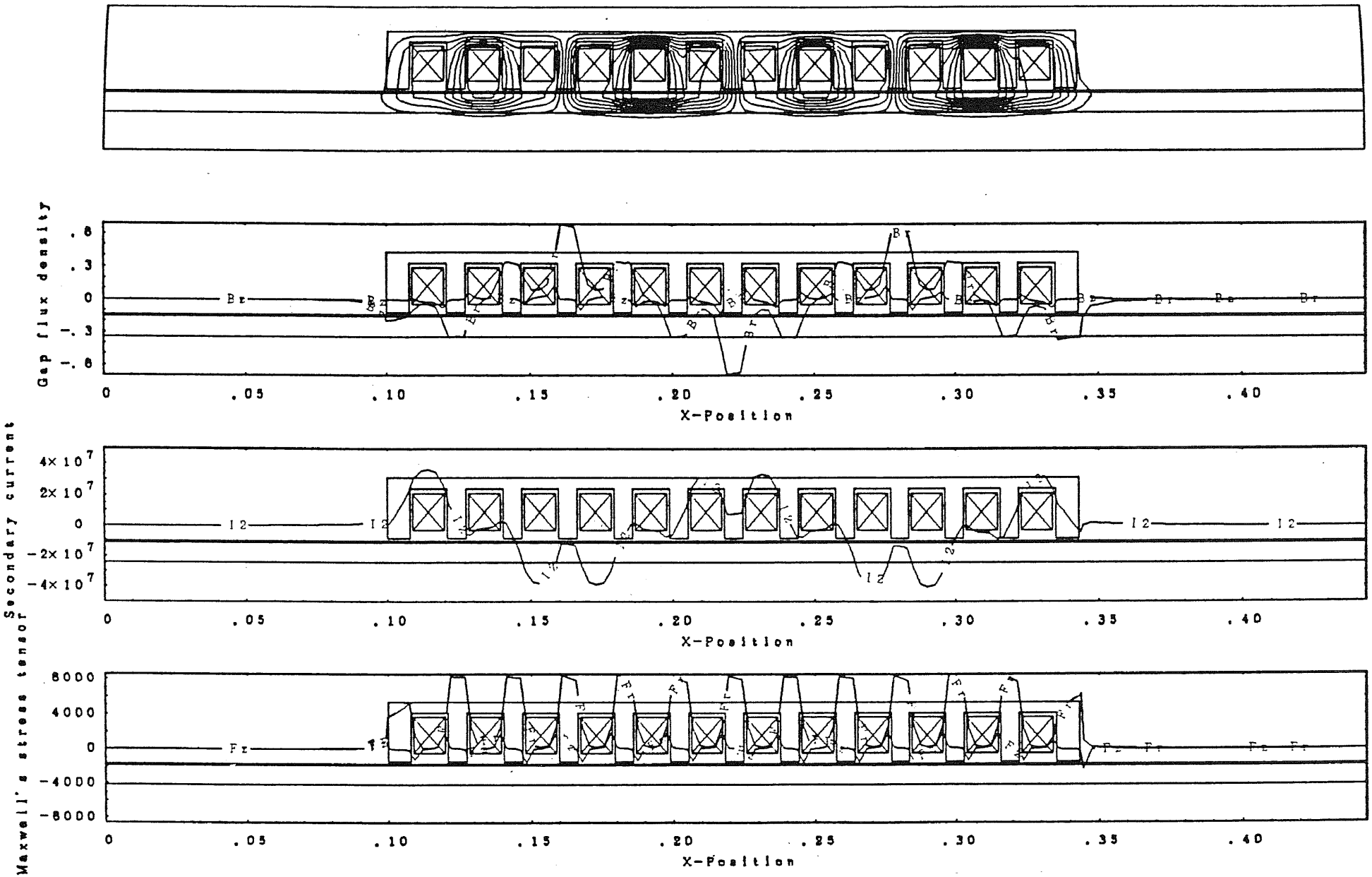

Figure 6.21. Calculated results of the flux synthesis (3) ($s = 0.6$ and $B_r = 0.68T$ *const.*)

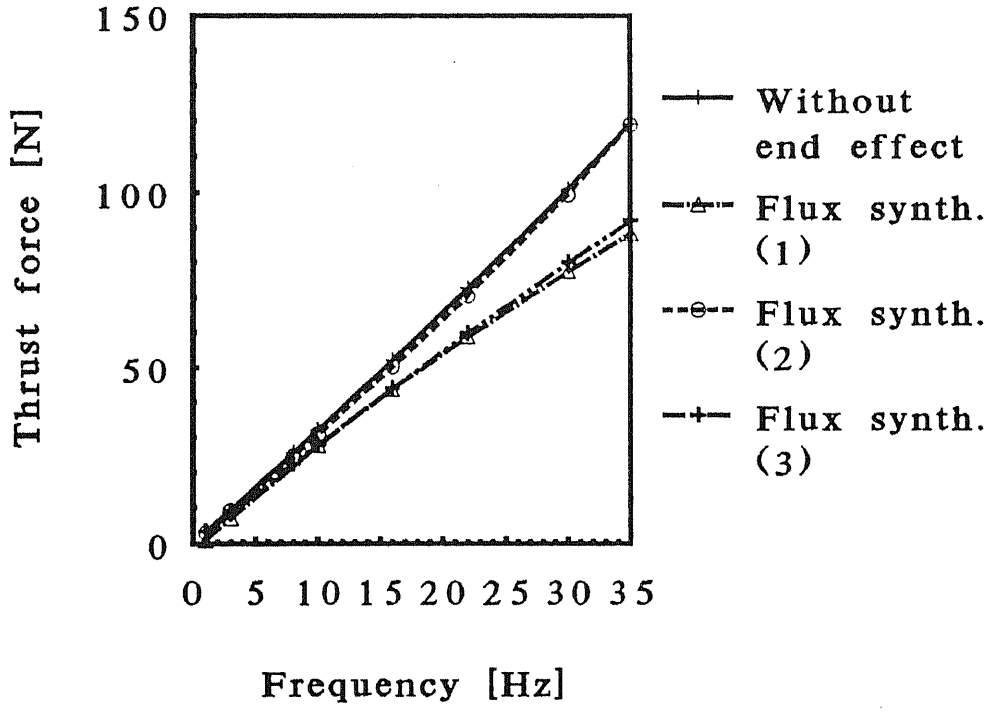

(a) Thrust force in standstill drive.

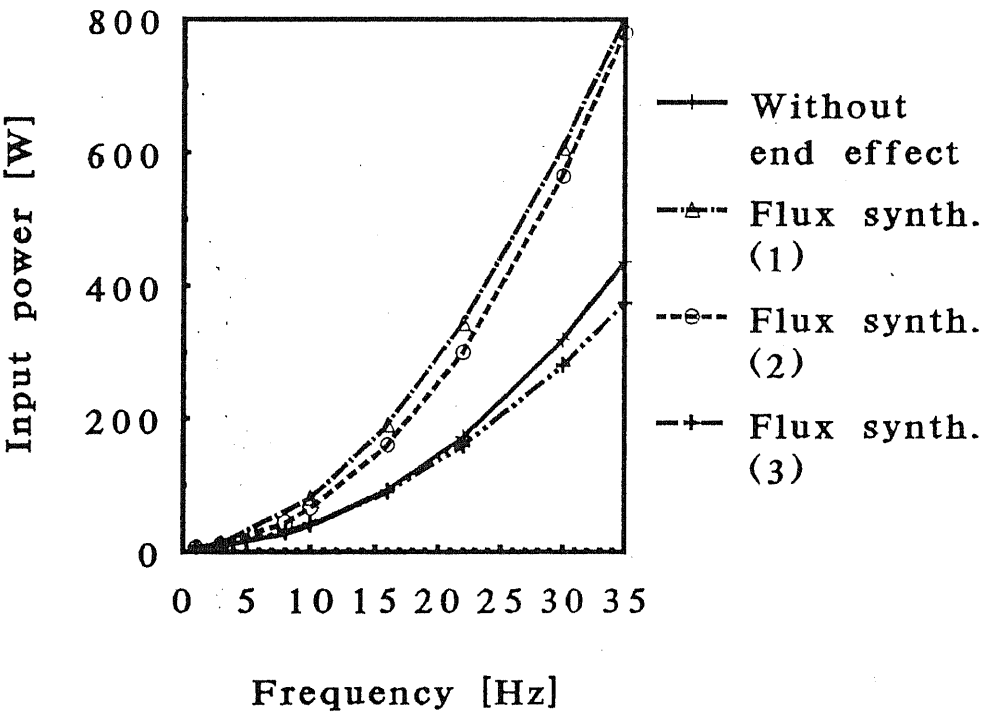

(b) Input power in standstill drive.

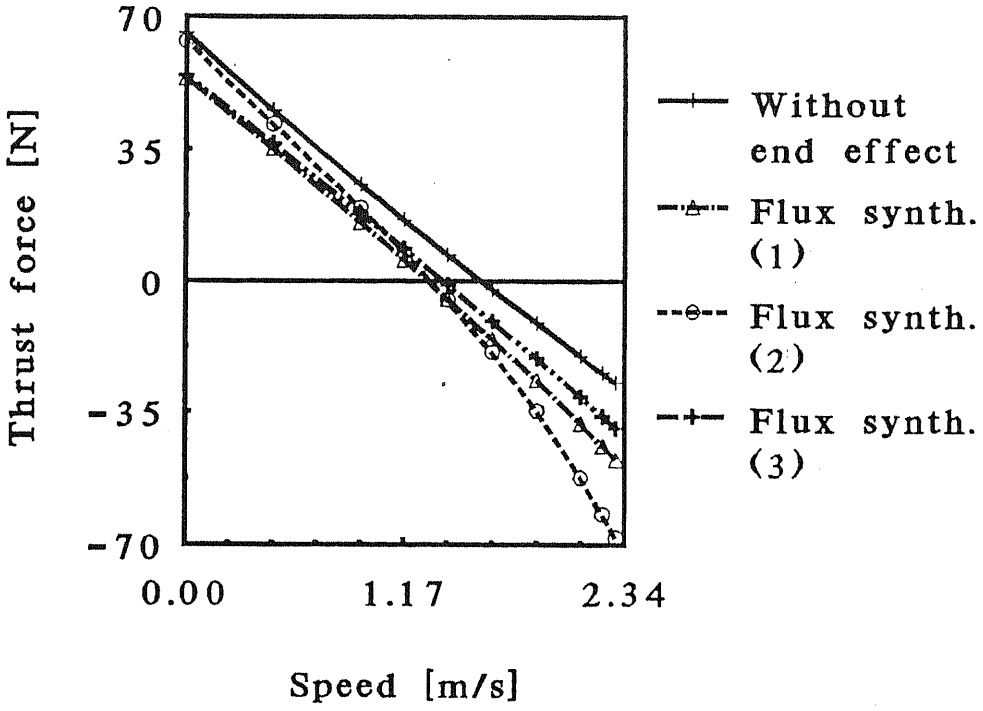

(c) Thrust force at $f_1 = 20Hz$.

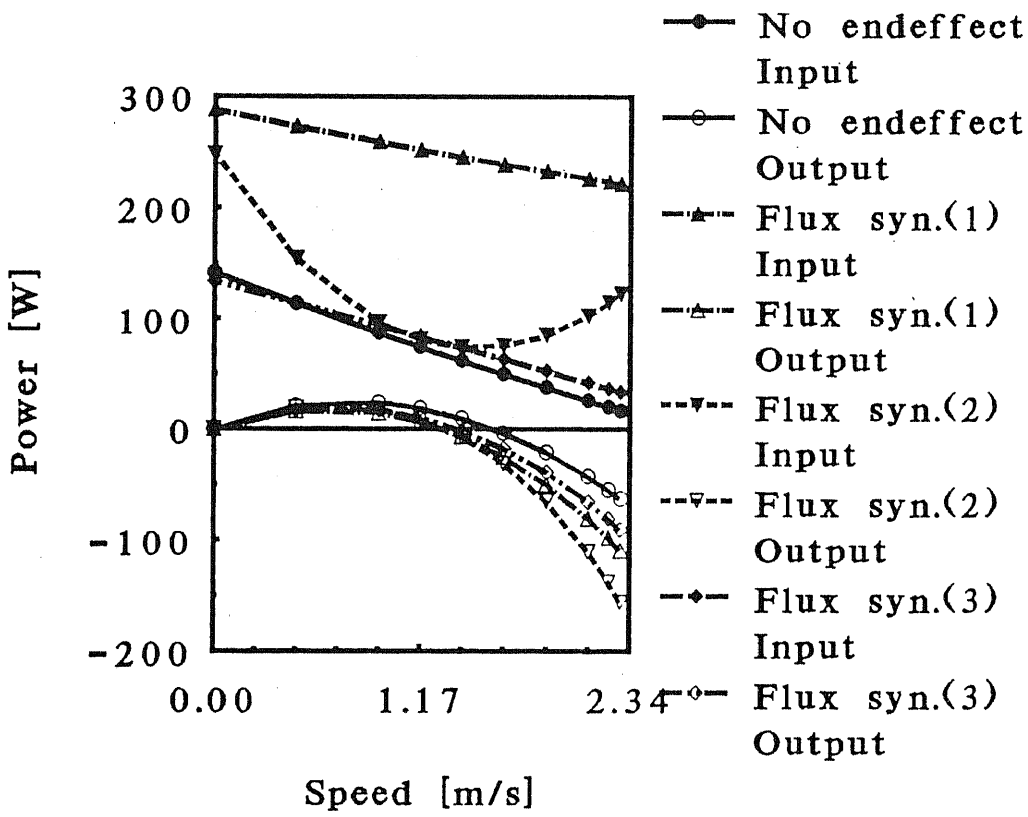

(d) Input- and output- powers at $f_1 = 20Hz$

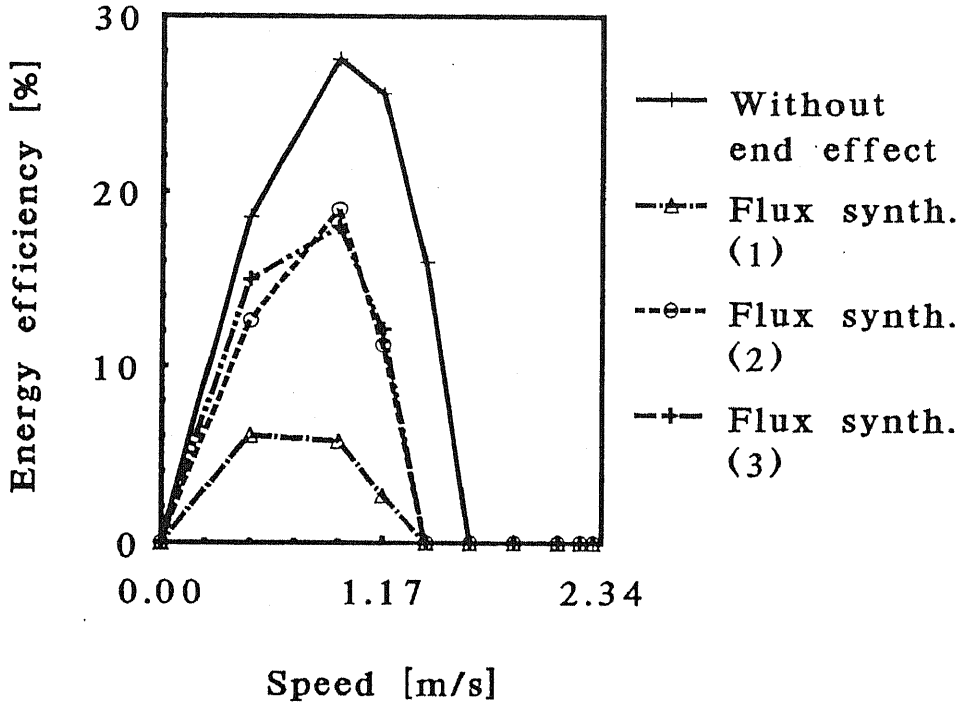

(e) Energy efficiency at $f_1 = 20Hz$ *const.*

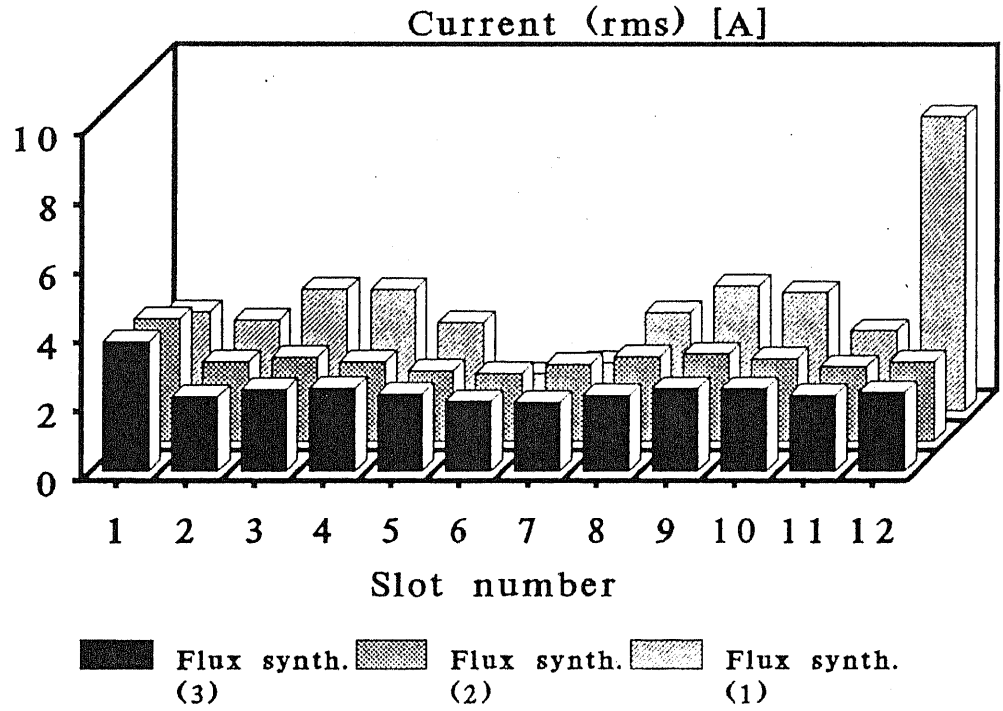

(f) Current in each slot (*rms* value, $B_r = 0.68T$ *const.*, $s = 0.6$ and $f_1 = 20Hz$).

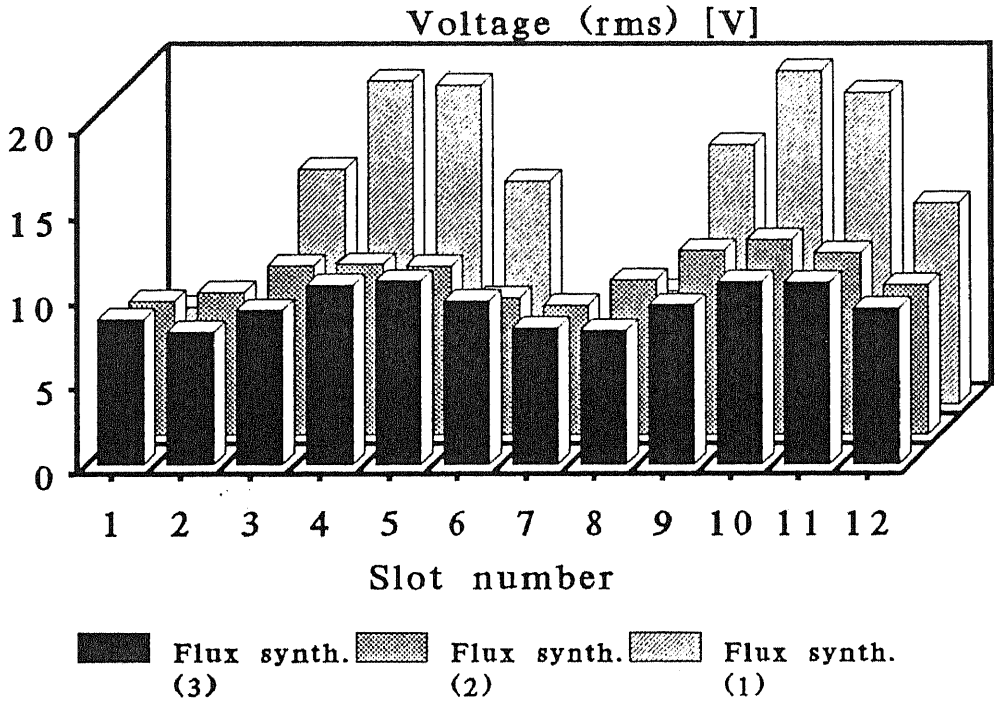

(g) Voltage in each slot (*rms* value, $B_r = 0.68T$ *const.*, $s = 0.6$ and $f_1 = 20Hz$).

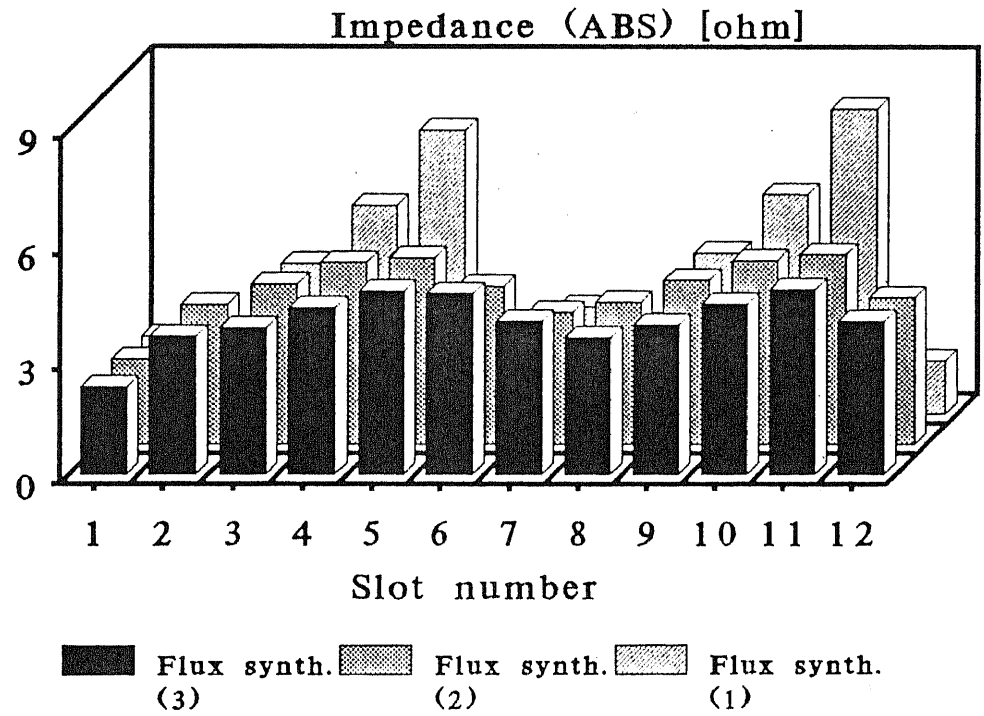

(h) Absolute value of impedance in each slot ($B_r = 0.68T$ *const.*, $s = 0.6$ and $f_1 = 20Hz$).

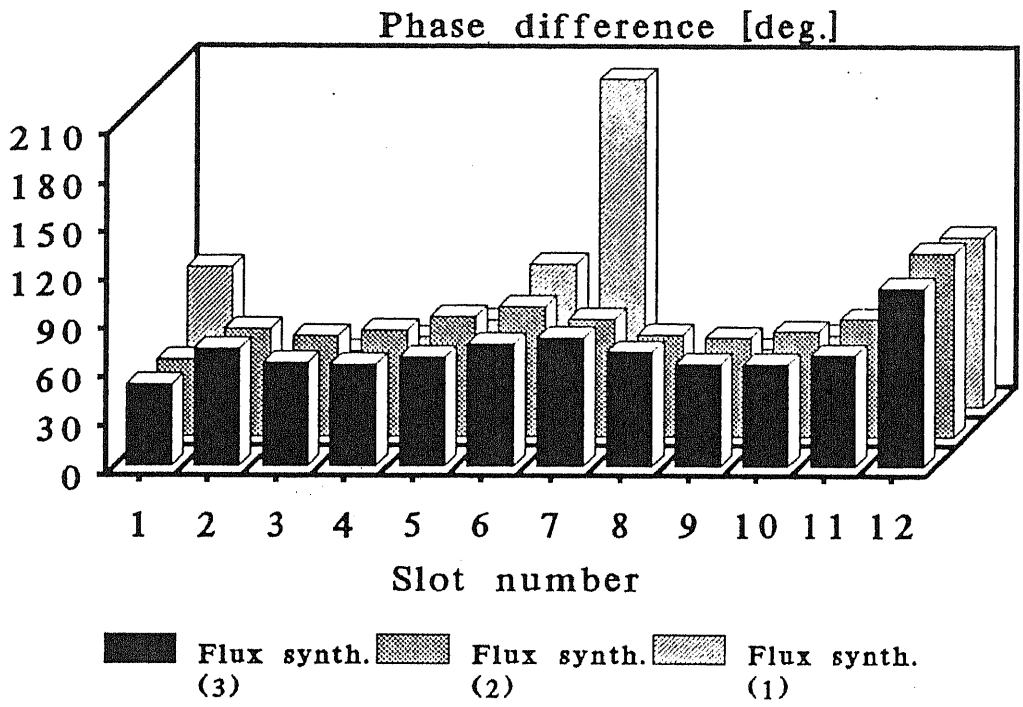

(i) Phase angle of impedance in each slot ($B_r = 0.68T$ *const.*, $s = 0.6$ and $f_1 = 20Hz$).

Figure 6.22. Comparison among the three kinds of flux syntheses.

6.6. Effects of pole pitch

It is well known that the longer a pole pitch is, the better motor characteristics we have in general. The pole pitch is, however, not only an issue of driving but also of a hardware of a motor itself: a thicker yoke is necessary for longer pole pitch, and the longer pole pitch requires low frequency of a power supply, which reduces power density per weight, for the same speed, Hence, decision of the pole pitch is a quite important and complicated issue of motor design.

We will, however, try to calculate motor characteristics with the doubled pole pitch as an conceptional experiment for comparison with the previous sections here. The applied frequency was assumed ten hertz for the condition of the same speed. The gap flux density $B_r = 0.814\mathrm{T}$ and the voltage $V = 10.14\mathrm{V}$ were decided so that the input energy in the standstill drive may be approximately the same as the former calculations.

The harmful effect of the slot harmonics is reluxed with a longer pole pitch as shown in the 6.23, hence, thrust force without end effect can be kept positive in the higher speed region than the former calculations, as shown in the figures 6.24 (a) and (b). The energy efficiency in the figure 6.24 (c) is also improved in the case of no end effect. However, the difference between with- and without- end effect is larger than the former calculations due to the structure with only one pole pair. We can see in the figure 6.25 that the spatial ruggedness cannot be reluxed effectively even with the flux (3) in this case. Consequently, we cannot expect a good behavior anyway with the short structure with two poles.

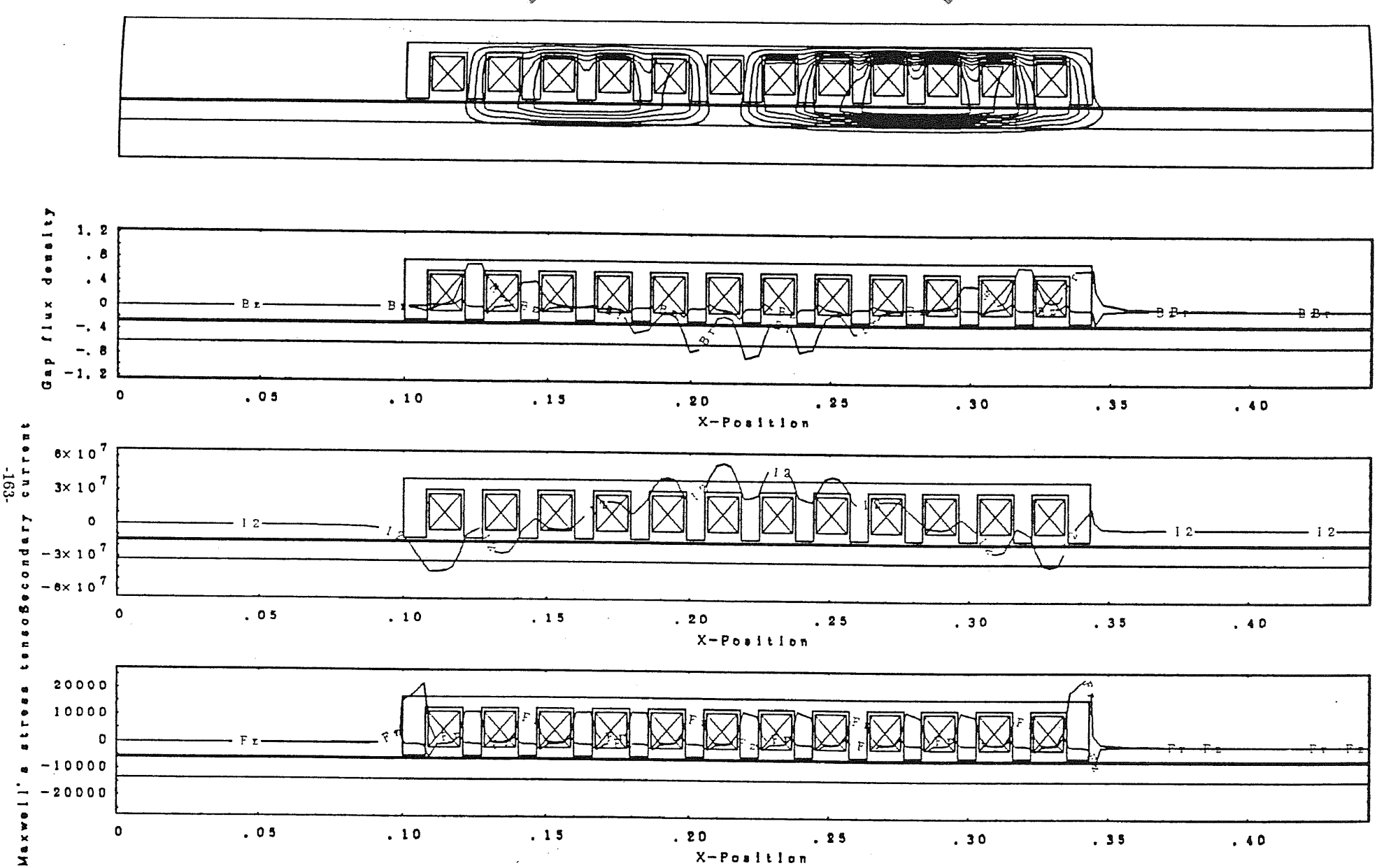

Figure 6.23. Calculated result of a drive with doubled pole pitch. (B_r = 0.814T, f_1 = 10.0Hz, and s = 0.6)

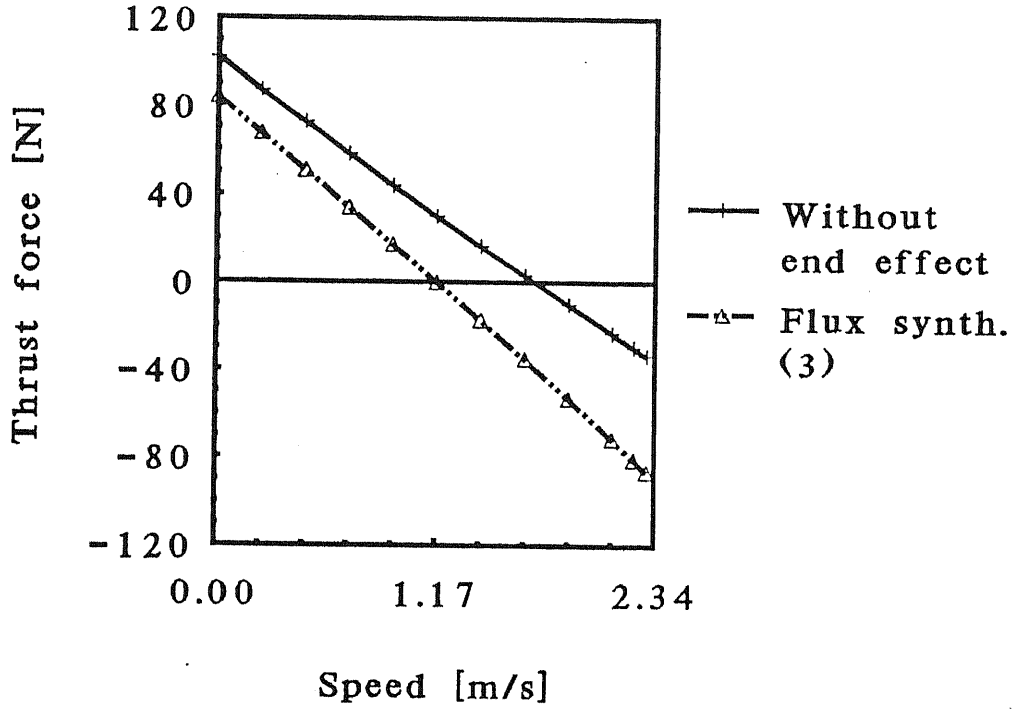

(a) Thrust force.

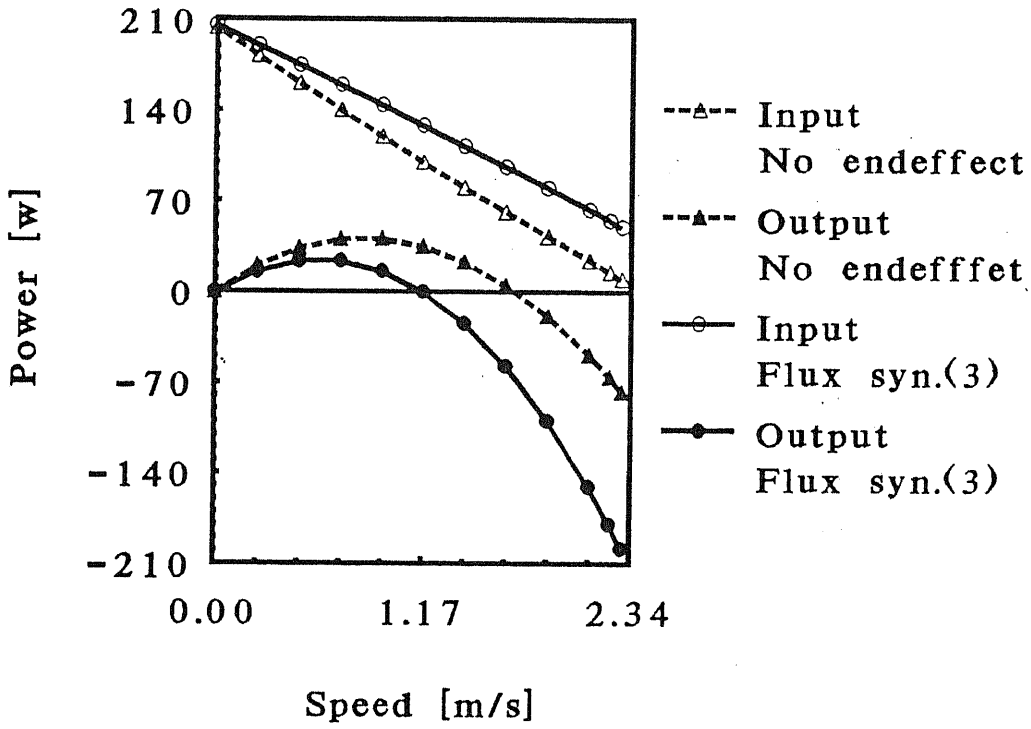

(b) Input- and output- powers.

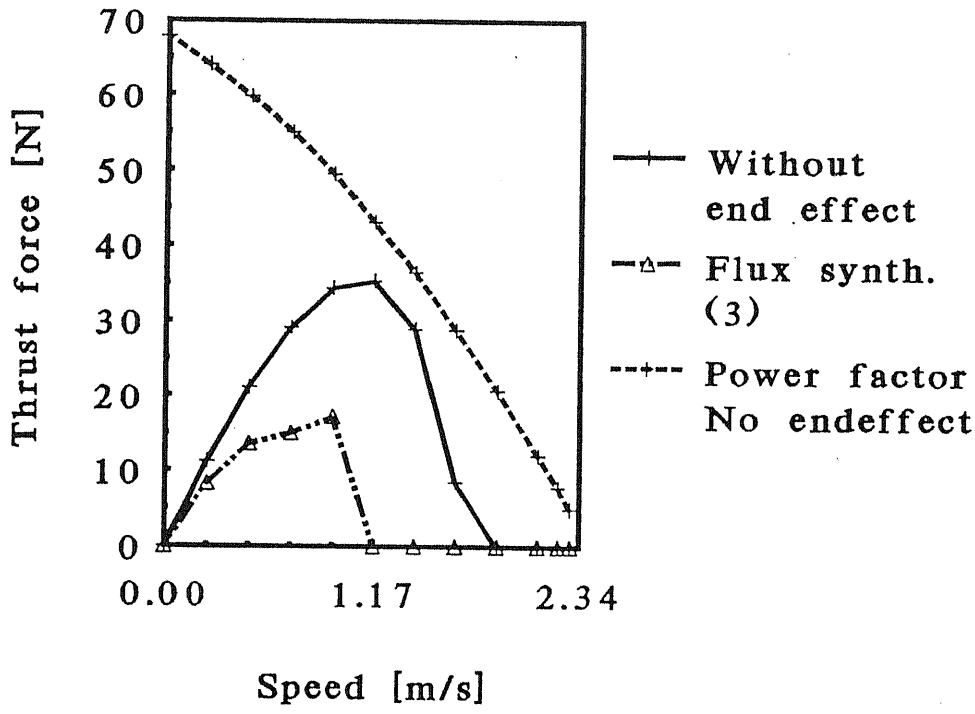

(c) Energy efficiency.

Figure 6.24. Two- pole machine with doubled pole pitch: comparison between the drives with- and without- end effect ($B_r = 0.814T$ *const.*, and $f_1 = 10.0Hz$).

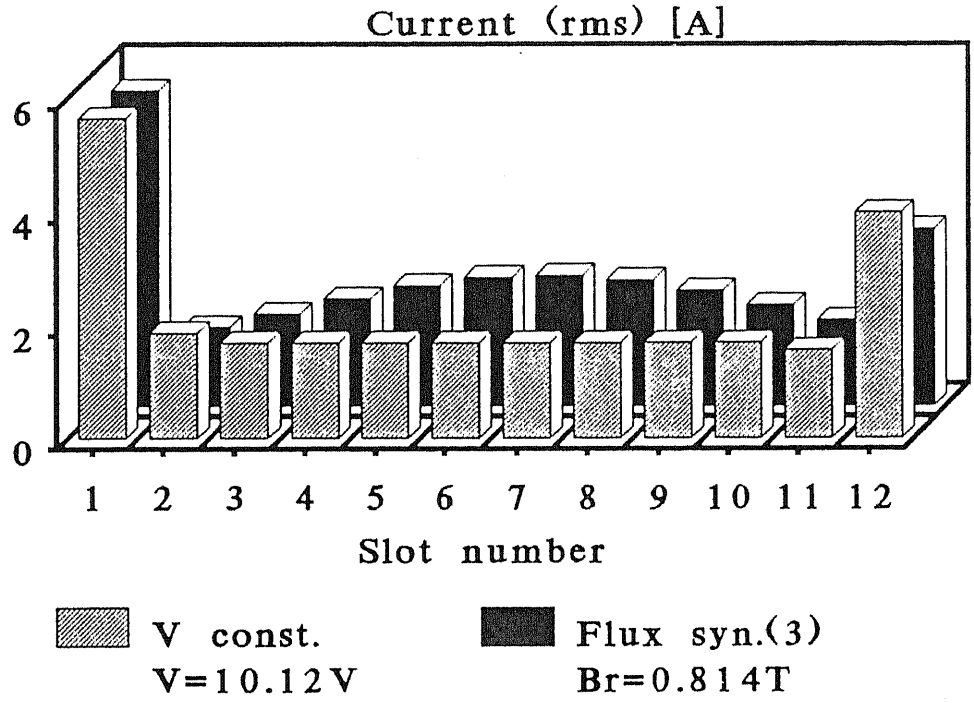

(a) Current in each slot.

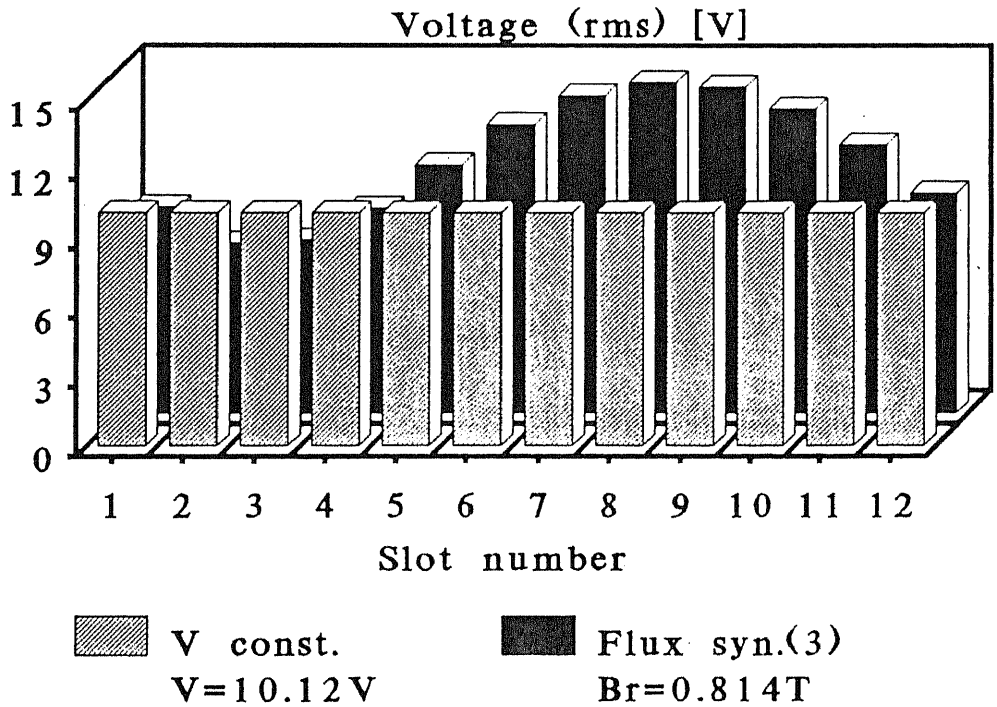

(b) Voltage in each slot.

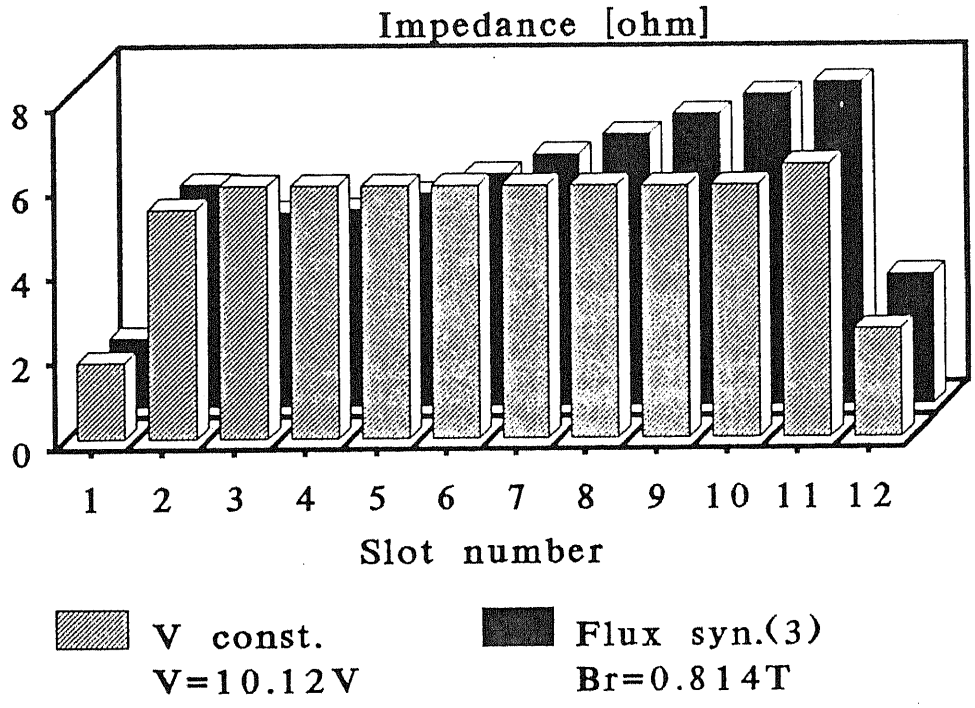

(c) Absolute value of impedance in each slot.

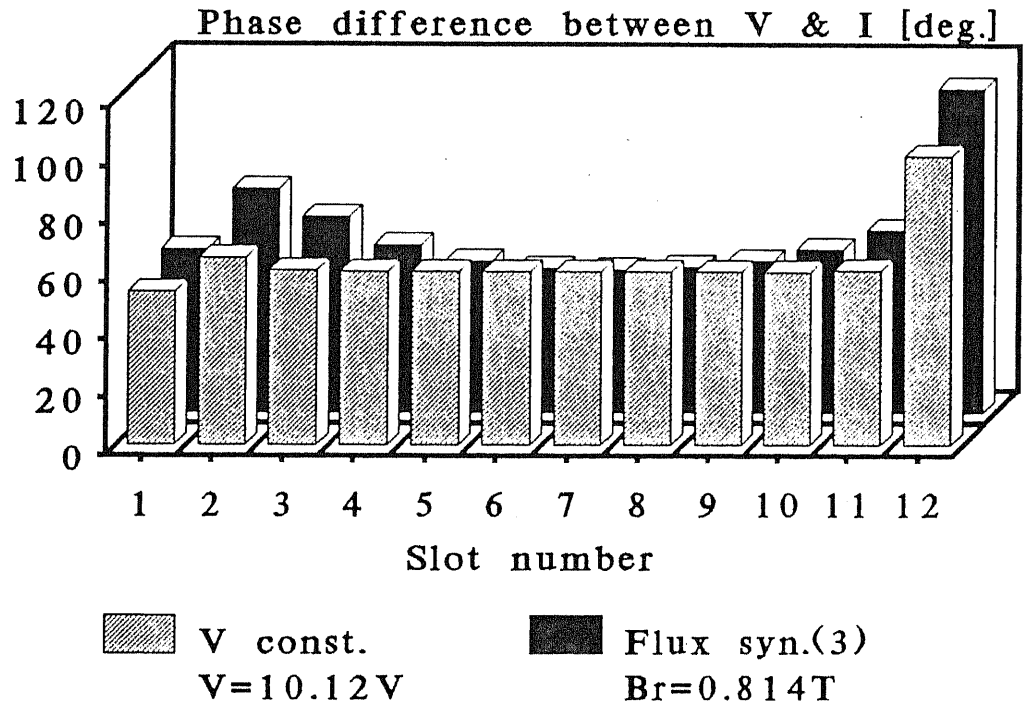

(d) Phase angle of impedance in each slot.

Figure 6.25. Two- pole machine with doubled pole pitch: comparison between the voltage constant- and the flux synthesizing- drives.

6.7. Possibility of the field- coordinates oriented control with the flux syntheses

The argument in the chapter 5 will be verified in this section: from the equations (5.73), the following relation is derived.

[1] From the figure 6.2 (c):
$F_{\max}$ = 50N (without end effect)
$F_{\max}$ = 42N (with end effect)
at $f_{\max}$ = 35Hz.

[2] Hence, the k and T_R are defined with the equations (5.73.a) and (5.73.b) respectively as follows:

$$k_n = \frac{2F_{\max}}{I_S^2} = \frac{2\times 50}{2^2} = 25 \text{ (without end effect)}$$

$$k_e = \frac{2F_{\max}}{I_S^2} = \frac{2\times 42}{2^2} = 21 \text{ (with end effect)}$$

$$T_R = \frac{1}{\omega_{2\,\max}} = \frac{1}{2\times\pi\times 35} = 4.55\times 10^{-3} \text{ [s]}.$$

[3] From the figure 6.6 (a)
B_r = 0.68T, f_1 = 35Hz $\rightarrow$ I_S = 3.1A
hence, when B_r = 0.8T: $I_S = 3.1\times\frac{0.8}{0.68} = 3.64$A
in the case, $I_{Sd} = 3.65\times\cos 45° = 2.58$A

By substituting these k_n, k_e, I_{Sd} and T_R into the equation (5.73.c), we can draw the curves illustrated in the figure 6.26 (a).

On the other hand, the thrust forces with the flux synthesis (3) (B_r = 0.8T *const.*) have been numerically calculated as illustrated in the figure 6.26 (b): the curve of v = 0.0 is almost the same as the curve of "with end effect" in the figure (a), where other curves are shifted below on account of the secondary loss caused by the slot harmonics. It should, however, be emphasized that the curves are straight lines with the same gradient. That is to say, the the drive scheme fulfills one of the fundamental conditions of the possibility to apply the field-coordinates oriented control scheme in low speed operation, where the shift of the curves with speed should be compensated with either a control scheme or a improved motor design. In other words, although the slip frequency characteristics of the thrust force are not one-valued function, the field-coordinates oriented control scheme can be applicated also to an FSLIM in principle with some modification of a controller. The input power and the energy efficiency have been also calculated and illustrated in the figures 6.26 (c) and (d) respectively. Since there is inevitable energy loss for keeping the magnetization, the energy efficiency is not good with a small thrust force *i.e.*, with a low slip frequency.

Normal force can be neglected in the tubular LIM, but it can be a remarkable interference to a suspension system of transport lines composed of ordinary LIMs, as mentioned in the subsection 5.2.2. The normal force depends on operating points as shown in the figure 6.26 (e-1), however, the absolute value of the attractive normal force is anyway large in the test machine, and the perturbation of the force, therefore, is negligible in this case, as we see in the figure 6.26 (e-2).

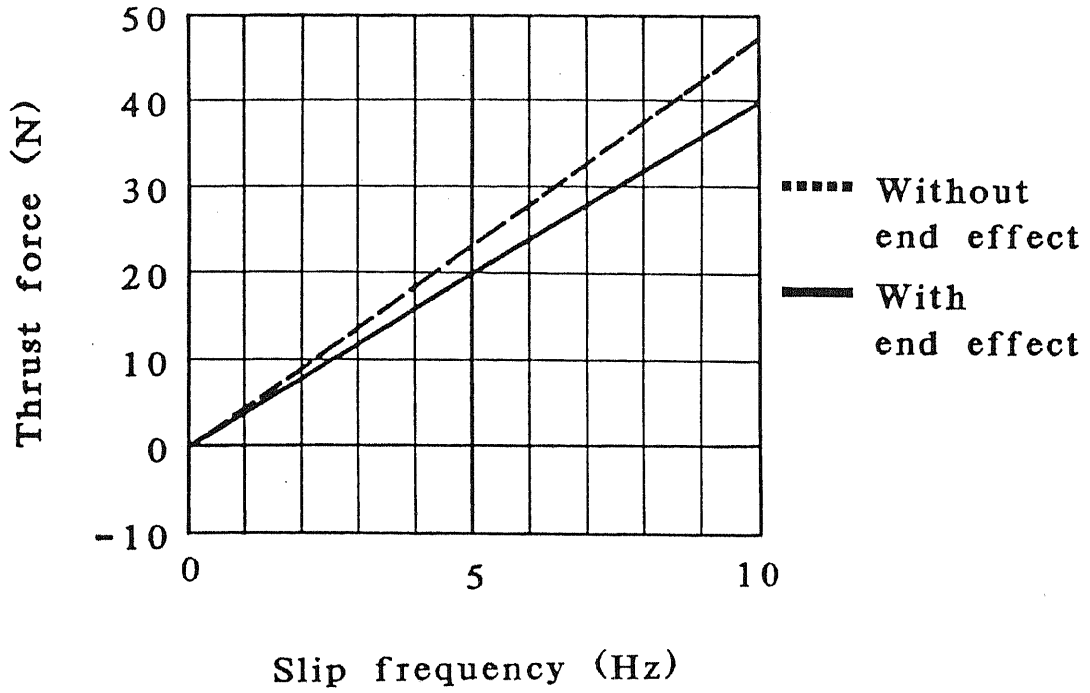

(a) Thrust force calculated from the equation 5.73 (c)

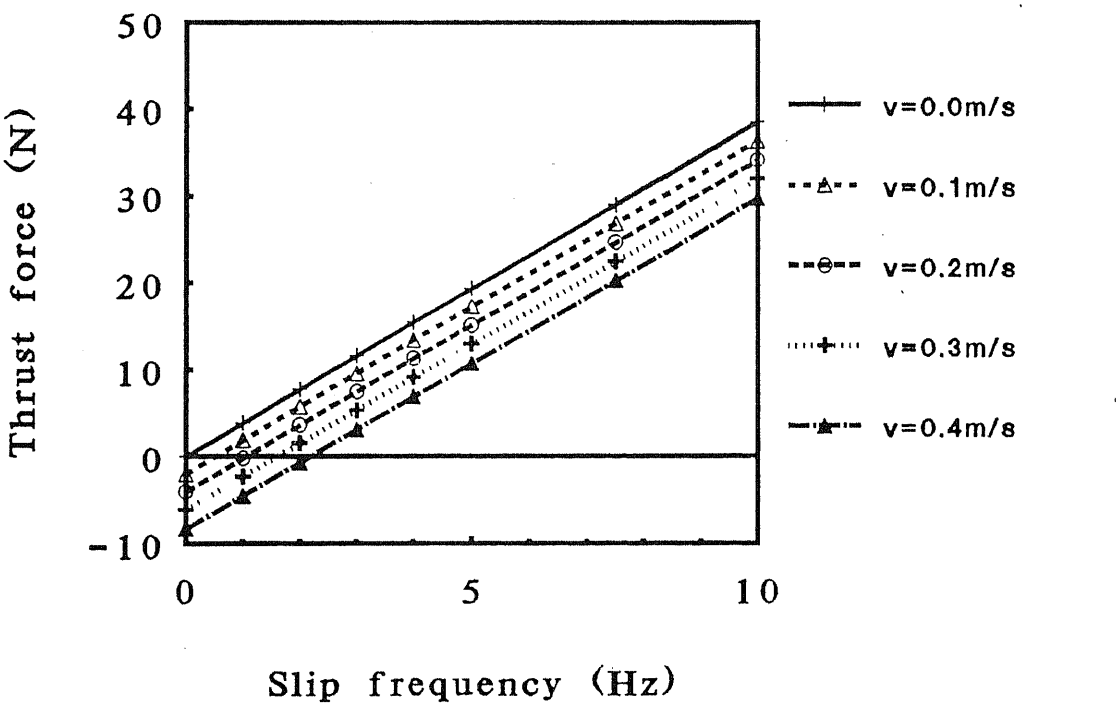

(b) Thrust force calculated directly.

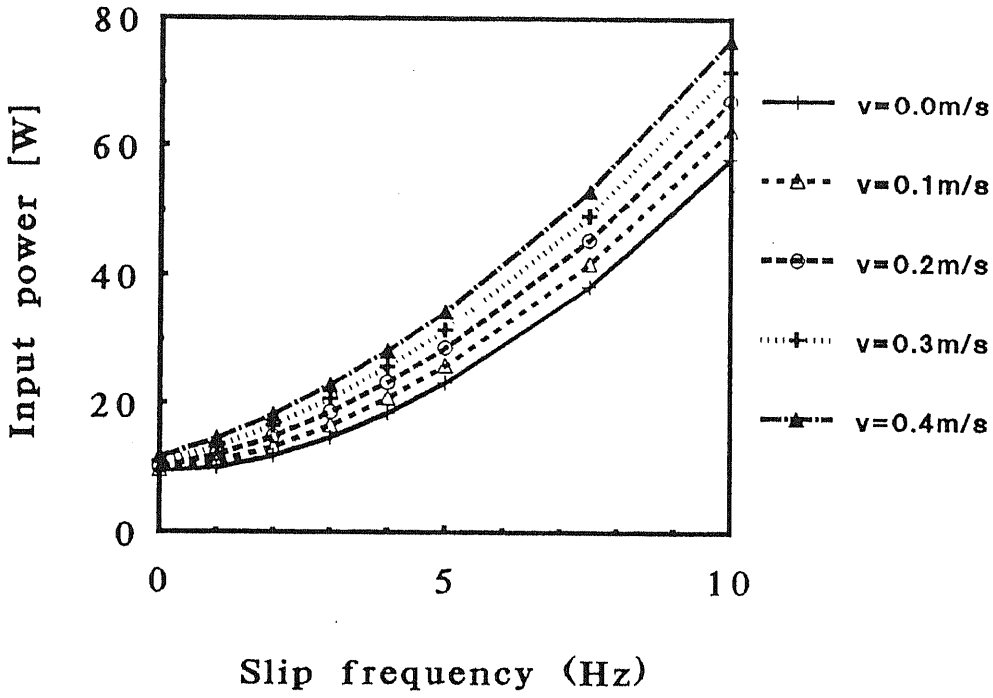

(c) Input power.

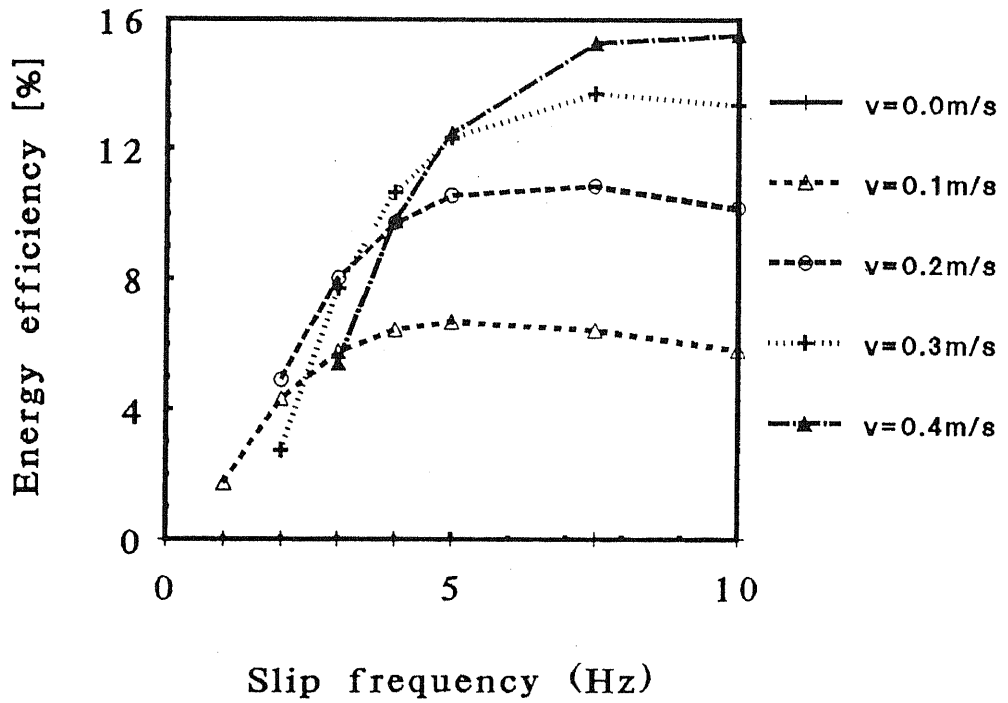

(d) Energy efficiency.

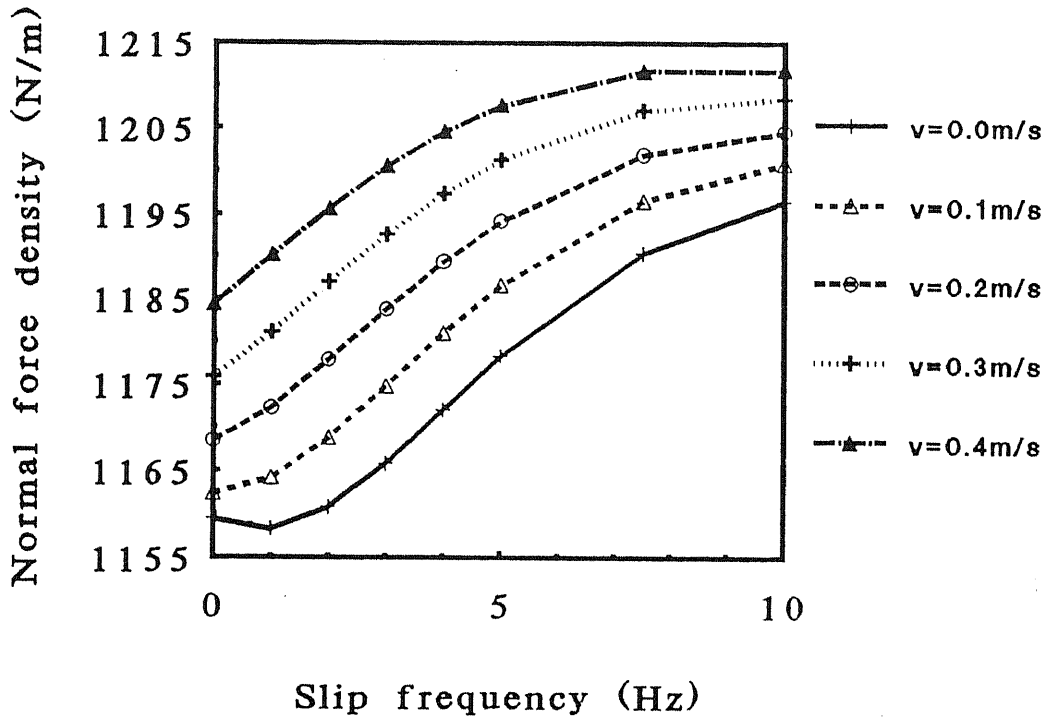

(e-1) Normal force.

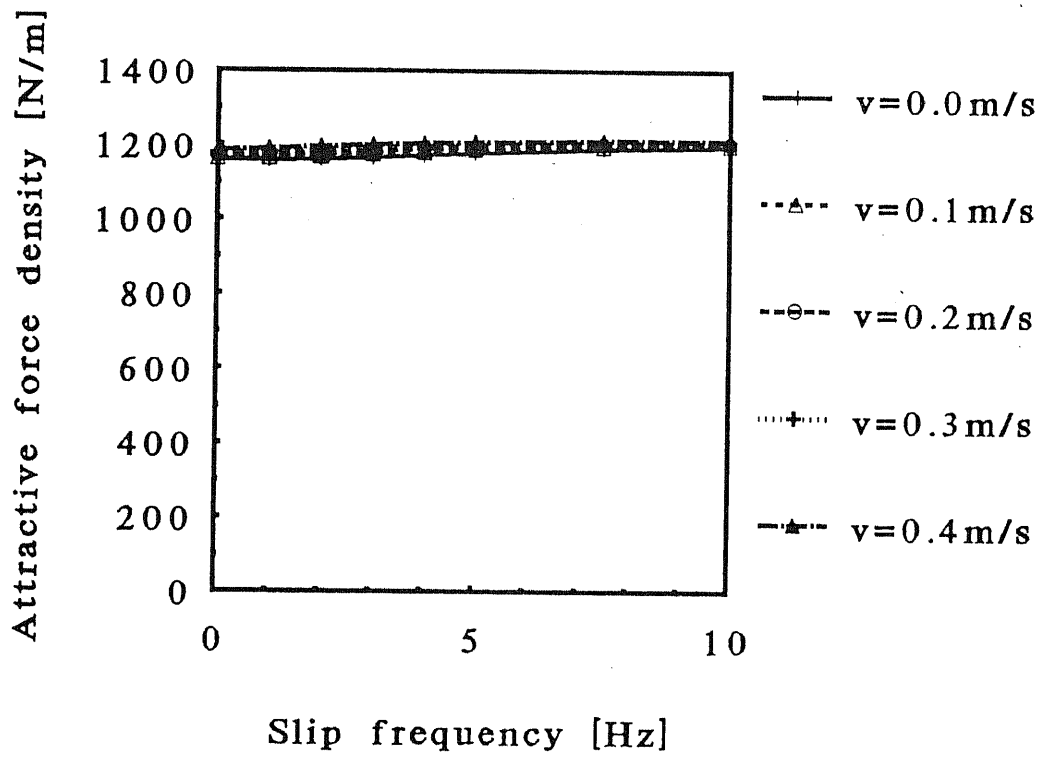

(e-2) Normal force.

Figure 6.26. Basic investigation on the field- coordinates oriented control with the flux synthesis (3) ($B_r = 0.8T$ *const.*).

6.8. Summary of results

- ☐ Slot harmonics as well as the end effect are significant in deterioration of motor efficiency.
- ☐ End effect stays at the both end portions, *i.e.*, impedances of the windings at an inner part of the motor are kept homogeneous with a parallel connection. The structure of the FSLIM illustrated in the figure 4.1 is inherently suitable for suppressing the effect. The unhomogeneity condensed at the both end portions, however, is often more harmful effect than the case of a serial connection.
- ☐ An appropriate flux synthesis relaxes the inhomogeneity: energy efficiency is improved.
- ☐ A fundamental condition of the field-coordinates oriented control scheme, *i.e.*, the linearity of the F_{thrust}—sf curves is fulfilled by applying the flux synthesis, although some trivial modification of converters is necessary due to slot harmonics.

Chapter 7: Conclusions

A novel structure and a control scheme of the flux synthesizing linear induction motor (FSLIM) have been introduced in the research.

An analysis method of eddy current problems, which is especially suitable for LIM calculations, has been mathematically formulated based on the control volume method, where the up-wind scheme is automatically introduced into the field analysis. Mathematical compatibility of the method with the finite element method (FEM) has been theoretically verified. In addition, it has been also described how to formulate voltage equations of an asymmetric linear motor and solve them in the chapter 2.

The theory has been verified by comparing calculations with measurements of a rotary induction motor composed of a continuous aluminum secondary plate. The results have been verified also by comparing them with a classical machine theory and other results calculated with the FEM in the chapter 3.

Examples of basic calculations of an FSLIM have been shown, and it has been concretely described how to decide input-current references corresponding to an intended flux distribution in the chapter 4.

The ideal mathematical model of linear induction motors (LIMs) has been proposed based on the modeling by W. Leonhard for applying the field-coordinates oriented control scheme to a LIM. It is, in particular, important in the chapter 5, how to decide parameters for the control without the equivalent circuit of an induction motor.

Calculated results have been shown and compared with measurements of a tubular test LIM in the chapter 6. With an appropriate flux synthesizing scheme, we can improve electromagnetic characteristics, *e.g.*, energy efficiency. Practical propriety of the theory in the chapter 5 has been verified. As a result, the possibility to applicate the field coordinates oriented control scheme to a LIM has been proved. Furthermore, it should be emphasized that the deterioration of LIM's characteristics with speed is caused not only by the end effect, as it is already well known, but also by slot harmonics: the latter affects in some cases more than the former.

In this dissertation, the possibility of the flux synthesis has been investigated based on a stationary numerical analysis in principle. A future assignment is to verify the concept experimentally with a test machine, in which flux sensors are

implemented to detect the gap flux distribution necessary for the control scheme, and with super multi-phase independent current supply units.

LIST OF PUBLICATIONS

古 関 隆 章
東京大学大学院工学系研究科電気工学専攻（正田研究室）

December 18, 1991

1 内外論文誌

1. T. Koseki, K. Hayafune and E. Masada:
"Lateral Motion of a Short-Stator Type Magnetic Wheel,"
IEEE Transactions on Magnetics, pp. 2350-2352, September 1987

2. 古関隆章・正田英介:
T. Koseki and E. Masada:
車上一次形磁気車輪に用いられる片側式リニア誘導モータの左右方向変位特性
"Kinetic Behavior of Single-Sided Linear Induction Motor in Lateral Direction,"
(Japanese)
電気学会論文誌 D 分冊 108-10
IEEJ Transactions on Industrial Applications, Vol. 108-D, No. 10, pp. 911-918

3. T. Koseki, K. Hayafune, H. Ohsaki and E. Masada:
"Influence of a Lateral Displacement on Stability of Linear Induction Motors,"
to be published in the Journal of Electrical and Electronics Engineering Australia
(E/89404)

2 国内大会・国際会議

2.1 国内大会

1. 古関隆章・藤崎敬介・正田英介:
T. Koseki, K. Fujisaki and E. Masada:
片側式リニア誘導機の左右変位特性
"Lateral Displacement Characteristics of Single-Sided Linear Induction Motor,"

(Japanese)
昭和６１年電気学会全国大会
1986 National Convention of IEEJ, pp. 1068-1069

2. 古関隆章・正田英介:
T. Koseki and E. Masada:
片側式リニア誘導モータの左右方向変位特性と二次導体幅の有限性
"Lateral Displacement Characteristics of Single-Sided Linear Induction Motors Taking the Finite Secondary Plate Width into Consideration," (Japanese)
昭和６２年電気学会全国大会
1987 National Convention of IEEJ, pp. 1034-1035

3. 古関隆章・正田英介:
T. Koseki and E. Masada:
片側式リニア誘導モータを用いた車上一次形磁気車輪の左右方向変位特性
"Lateral Motion of a Short-stator Type Magnetic Wheel with Single-sided Linear Induction Motors," (Japanese)
昭和６２年電気学会産業応用部門全国大会
1987 National Convention of IEEJ - Industry Applications Society, pp. 87-92, August 1987

4. 徐晨・古関隆章・正田英介:
C. Xu, T. Koseki and E. Masada:
都市内中量低速軌道交通システムのための磁気浮上鉄道の一考察
"A Study on a Maglev System for Urban Transit System of Low Speed and Medium Capacity," (Japanese)
昭和６３年電気学会全国大会
1988 National Convention of IEEJ

5. 古関隆章・大平膺一:
T. Koseki, Y. Ohira and E. Masada:
２方向６極リニア誘導モータ特性の基礎的検討
"Fundamental Research of the 6-Pole Biaxial Traveling Magnetic Field Type Linear Induction Motor," (Japanese)
昭和６３年電気学会産業応用部門全国大会
1988 National Convention of IEEJ -Industry Applications Society, pp. 785-786, August 1988

6. 鳥居粛・古関隆章・正田英介:
S. Torii, T. Koseki and E. Masada:
交通システム用リニア同期モータのセクション長短縮に伴う諸特性
"Characteristics of the Short-Section Linear Synchronous Motor," (Japanese)
昭和６３年電気学会産業応用部門全国大会
1988 National Convention of IEEJ -Industry Applications Society, pp. 787-796, August 1988

7. 古関隆章・大平膺一・正田英介:
T. Koseki, Y. Ohira and E. Masada:

XY リニア誘導モータ発生力へのスロットの影響に関する基礎的検討
"Fundamental Investigations on XY-LIM's Forces with Slot-Effects," (Japanese)
平成元年電気学会全国大会
1989 National Convention of IEEJ, No. 678, pp. 6-112/6-113, April 1989

8. 徐晨・古関隆章・正田英介:
C. Xu, T. Koseki and E. Masada:
多目的計画法を用いた都市内用磁気浮上システムについての分析
"Analysis of Maglev Systems for Urban Transit with Multi-Objective Programming, " (Japanese)
平成元年電気学会全国大会
1989 National Convention of IEEJ, No. 1746, pp. 13-175/13-176, April 1989

9. 岡田肇・古関隆章・正田英介:
H. Okada, T. Koseki and E. Masada:
線形多端子網理論を用いたリニア誘導モータの特性検討の一方法
"An Investigation on Linear Induction Motors with the Linear Multi-Terminals Network Theory," (Japanese)
平成 3 年電気学会全国大会
1991 National Convention of IEEJ, pp. 7/135-136

10. 森實俊充・古関隆章・正田英介:
T. Morizane, T. Koseki and E. Masada:
縦型リニア誘導モータの設計方法に対する一考察
"A method of designing linear induction motor for vertical movement," (Japanese)
平成 3 年電気学会産業応用部門全国大会
1991 National Convention of IEEJ -Industrial Application Society, August 1991

11. 古関隆章・正田英介:
T. Koseki and E. Masada:
コントロール・ボリューム法を用いたリニア誘導モータの解析
"Analysis of Linear Induction Motors with Control Volume Method," (Japanese)
平成 3 年電気学会産業応用部門全国大会
1991 National Convention of IEEJ -Industrial Application Society, August 1991

2.2 国際会議

1. E. Masada, T. Koseki and M. Kawashima:
"Lateral Behaviour of a Magnetic Wheel and Its Coordination with the Maglev Control System,"
International Conference of Maglev and Linear Drives 1987, Las Vegas, May 1987

2. T. Koseki, K. Hayafune and E. Masada:
"Kinetic Stabilization of Linear Induction Motor Drives,"
Proceedings of the Electric and Energy Conference 1987, Adelaide, pp. 199-204, October 1987

3. T. Koseki, and E. Masada:
"Lateral Motion of a Short-Stator Type Magnetic Wheel with Electromagnetic Suspension System,"
International Conference on Maglev and Linear Drives 1988, pp. 101-110, Hamburg, June 1988

4. T. Koseki and E. Masada:
"Lateral Stabilization of Linear Induction Motor Drives,"
International Conference on Electrical Machines, Pisa, September 1988

5. T. Koseki, H. Ohsaki and E. Masada:
"A Novel Control Scheme of a Linear Induction Motor,"
International Conference on Maglev and Linear Drives 1989, pp.345-350, Yokohama, July 1989

6. H. Ohsaki, T. Koseki, T. Morizane and E. Masada:
"A novel Linear Induction Motor with an Arbitrary Magnetic Flux in the Air Gap,"
International Power Electronics Conference, pp. 913-918, Tokyo, April 1990

7. T. Koseki, H. Ohsaki, T. Morizane and E. Masada:
"A New Control Scheme of a Linear Induction Motor to Reduce the End Effect,"
International Conference on Electrical Machines, pp. 568-573, Boston, August 1990

8. T. Koseki, T. Morizane, T. Ohsaki and E. Masada:
"Novel Linear Induction Drives: Control Scheme and Converters" European Power Electronics Conference, pp. 1;481-1;486

3 研究会

1. 古関隆章・正田英介:
T. Koseki and E. Masada:
片側式リニア誘導モータの左右方向変位特性
"The Characteristics of the Single-sided Linear Induction Motors with Lateral Displacement," (Japanese)
昭和６１年電気学会マグネティックス研究会
IEEJ Papers of Technical Meeting on Magnetics 1986, MAG-86-128, pp. 101-110

2. 古関隆章・権丙一・正田英介:
T. Koseki, B. Kwon and E. Masada:
吸引浮上形磁気車輪の左右変位特性と制御
"The Lateral Motion of an Electromagnetic Suspension Type Magnetic Wheel and its Control Scheme," (Japanese)
昭和６２年電気学会マグネティックス研究会
IEEJ Papers of Technical Meeting on Magnetics 1987, MAG-87-152, pp. 1-8

3. 古関隆章・中島達人・正田英介
T. Koseki, T. Nakajima and E. Masada:
リニア誘導モータ駆動システムの瞬時値制御
"Theoretical Basis for the Instantaneous Value Control of Linear Induction Motor Drives," (Japanese)
昭和６３年電気学会リニアドライブ研究会
IEEJ Technical Meeting on Linear Drives, LD-88-27, October 1988

4. 古関隆章・大平膺一・正田英介:
T. Koseki, Y. Ohira and E. Masada:
XY リニア誘導モータ発生力の基礎的検討
"Fundamental Investigations of XY-LIM's Forces," (Japanese)
昭和６３年電気学会リニアドライブ・マグネティックス合同研究会
IEEJ Technical Meeting on Linear Drives and Magnetics, LD-88-44/ MAG-88-191, November 1988

5. 森實俊充・古関隆章・正田英介:
T. Morizane, T. Koseki and E. Masada:
縦型円筒型リニア誘導モータの解析手法と推力概算式について
"Analysis and an Approximate Equation of a Tubular Linear Induction Motor for Vertical Movement," (Japanese)
平成３年電気学会リニアドライブ若手研究者シンポジウム
IEEJ Technical Symposium on Linear Drives for Young Researchers 1991, July 1991

6. 森實俊充・古関隆章・正田英介:
T. Morizane, T. Koseki and E. Masada:
縦型リニア誘導モータの解析手法と設計検討への応用
平成３年リニアドライブ研究会
IEEJ Technical Meeting on Linear Drives, LD-91-84, November 1991

4 その他

1. 古関隆章:
T. Koseki:
第 10 回磁気浮上鉄道国際会議報告
"Report of the International Conference on Maglev'88," (Japanese)
IEEJ Transactions on Industrial Applications, Vol. 108-D No.8, pp. 784, August 1988

2. 正田英介・田村穣・古関隆章:
国際交通博（IVA'８８）レポート
鉄道ピクトリアル８８年９月特大号 pp. 124-125, 鉄道図書刊行会

3. 海老原大樹・古関隆章
第４回ヨーロッパ・パワーエレクトロニクス国際会議の話題

OHM 91/11 pp. 106-107, November 1991

Appendix I: Analysis of rotary electric machines with the C.V.- formulation on the two- dimensional polar coordinates

A.1.1. Basic equations

When one substitutes the following conditions:

$$A_r = A_\theta = 0, \quad J_{0r} = J_{0\theta} = 0, \quad \frac{\partial \phi}{\partial z} = 0, \quad v_r = v_z = 0 \tag{A.1}$$

into the equations (2.5.1), the following basic equation on the two- dimensional polar coordinates is derived:

$$\sigma \frac{\partial A}{\partial t} = \frac{1}{r}\frac{\partial}{\partial r}\left[\nu_\theta r \frac{\partial A}{\partial r}\right] + \frac{1}{r}\frac{\partial}{\partial \theta}\left[\frac{\nu_r}{r}\frac{\partial A}{\partial \theta}\right] - \frac{v_\theta \sigma}{r}\frac{\partial A}{\partial \theta} + J_0 \tag{A.2}$$

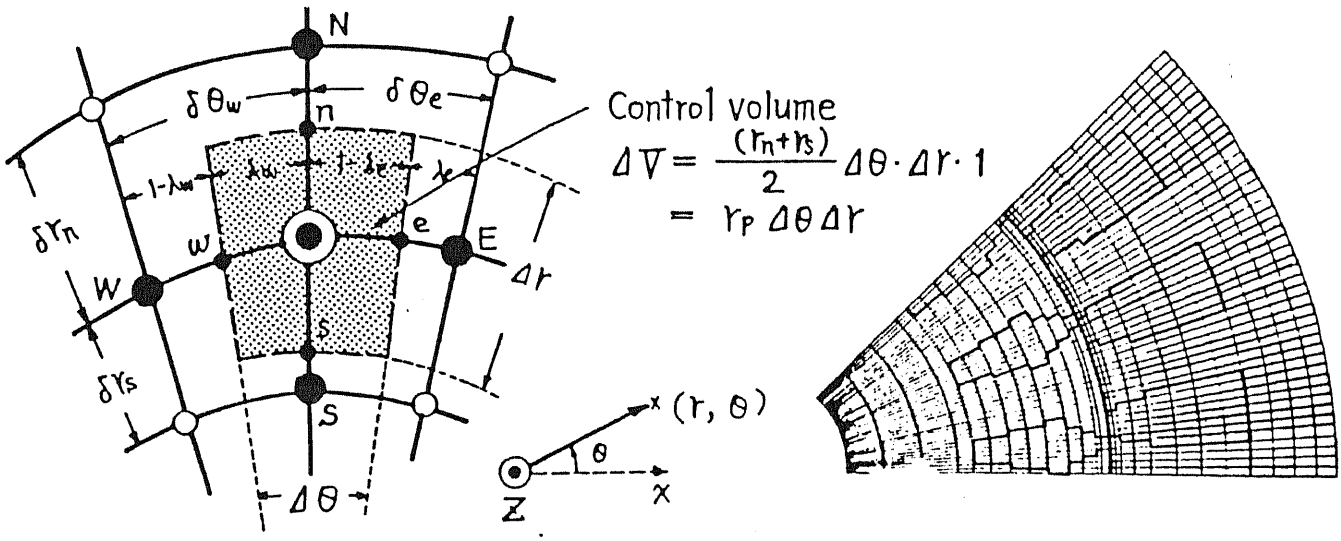

Figure A.1.1. Grids and a control volume on the two- dimensional polar coordinates.

A.1.2. Discrete formulation with a linear interpolating function

Firstly, a formulation with a linear interpolating function is introduced in this subsection. The two- dimensional polar grids and a control volume are illustrated in the figure A.1. The potentials on boundaries of the control volume are assumed as the following forms:

$$A_e = \left[1-\lambda_e\right] A_E + \lambda_e A_P \tag{A.3}$$

$$A_w = \left[1-\lambda_w\right] A_P + \lambda_w A_W \tag{A.4}$$

$$A_n = \left[1-\lambda_n\right] A_P + \lambda_n A_N \tag{A.5}$$

$$A_s = \left[1-\lambda_s\right]A_S + \lambda_s A_P \tag{A.6}$$

The equation (A.2) is multiplied by the step- weighting function, which is unity in the control volume and zero out of it, and integrated as follows:

$$\frac{1}{\Delta t}\int_t^{t+\Delta t}\int_e^w\int_s^n\left[\sigma\frac{\partial A}{\partial t}-\frac{1}{r}\frac{\partial}{\partial r}\left[\nu_\theta r\frac{\partial A}{\partial r}\right]-\frac{1}{r}\frac{\partial}{\partial\theta}\left[\frac{\nu_r}{r}\frac{\partial A}{\partial\theta}\right]+\frac{v_\theta\sigma}{r}\frac{\partial A}{\partial\theta}-J_0\right] r\,dr\,d\theta\,d\tau = 0 \tag{A.7}$$

$$[1st\ term] = \sigma_P\frac{\left[A_P-A_P^0\right]}{\Delta t}\Delta V = \frac{\sigma_P r_P\Delta\theta\Delta r\left[A_P-A_P^0\right]}{\Delta t} \tag{A.8}$$

$$[2nd\ term] = -\left[\nu_\theta r\frac{\partial A}{\partial r}\right]_s^n\Delta\theta = \left[-\nu_{\theta n}r_n\frac{A_N-A_P}{(\delta r)_n}\right]\Delta\theta-\left[-\nu_{\theta s}r_s\frac{A_P-A_S}{(\delta r)_s}\right]\Delta\theta$$

$$= \left\{\frac{\nu_{\theta n}r_n}{(\delta r)_n}\frac{\nu_{\theta s}r_s}{(\delta r)_s}\right\}\Delta\theta A_P-\frac{\nu_{\theta n}r_n}{(\delta r)_n}\Delta\theta A_N-\frac{\nu_{\theta s}r_s}{(\delta r)_s}\Delta\theta A_S \tag{A.9}$$

$$[3rd\ term] = -\left[\frac{\nu_r}{r}\frac{\partial A}{\partial\theta}\right]_e^w\Delta r = \left[-\frac{\nu_{rw}(A_W-A_P)}{r_w(\delta\theta)_w}\right]\Delta r-\left[-\frac{\nu_{re}(A_P-A_E)}{r_e(\delta\theta)_e}\right]\Delta r$$

$$= \left\{\frac{\nu_{re}}{r_e(\delta\theta)_e}+\frac{\nu_{rw}}{r_w(\delta\theta)_w}\right\}\Delta rA_P-\frac{\nu_{re}}{r_e(\delta\theta)_e}\Delta rA_E-\frac{\nu_{rw}}{r_w(\delta\theta)_w}\Delta rA_W \tag{A.10}$$

$$[4th\ term] = \left[v_\theta\sigma A\right]_e^w\Delta r = v_{\theta w}\sigma_w\left\{(1-\lambda_w)A_P+\lambda_w A_w\right\}\Delta r-v_{\theta e}\sigma_e\left\{(1-\lambda_e)A_E+\lambda_e A_P\right\}\Delta r$$

$$= \left\{v_{\theta w}\sigma_w(1-\lambda_w)-v_{\theta e}\sigma_e\lambda_e\right\}\Delta rA_P-\left\{-v_{\theta w}\sigma_w\lambda_w\right\}rA_W-v_{\theta e}\sigma_e\left[1-\lambda_e\right]\Delta rA_E \tag{A.11}$$

$$[5th\ term] = -J_0\Delta V = -J_{0P}r_P\Delta\theta\Delta r \tag{A.12}$$

The results are substituted into the equation (A.7), and the following discrete equation is consequently derived:

$$a_P A_P - a_E A_E - a_W A_W - a_N A_N - a_S A_S = b \tag{A.13}$$

where

$$a_E = \left\{\frac{\nu_{re}}{r_e(\delta\theta)_e} + v_{\theta e}\sigma_e(1-\lambda_e)\right\}\Delta r \tag{A.14}$$

$$a_W = \left\{\frac{\nu_{rw}}{r_w(\delta\theta)_e}-v_{\theta w}\sigma_w\lambda_w\right\}\Delta r \tag{A.15}$$

$$a_N = \frac{\nu_{\theta n}r_n}{(\delta r)_n}\Delta\theta \tag{A.16}$$

$$a_S = \frac{\nu_{\theta s} r_s}{(\delta r)_s} \Delta\theta \tag{A.17}$$

$$a_P^0 = \frac{\sigma_P r_P \Delta\theta \Delta r}{\Delta t} \tag{A.18}$$

$$b = J_{0P} r_P \Delta\theta \Delta r + a_P^0 A_P^0 \tag{A.19}$$

and

$$a_P = a_P^0 + a_E + a_W + a_N + a_S + \left[\sigma_w v_{\theta w} - \sigma_e v_{\theta e}\right] \Delta r \tag{A.20}$$

This discrete equation is proper only in the case of:

$$-1 < \frac{\sigma v r_P (\delta\theta)}{2\,\nu} < 1 \tag{A.21}$$

where $\lambda_e = \lambda_w = \frac{1}{2}$ is assumed for simplicity.

A.1.3. Modified exponential method

The following discrete equation for general transient field is derived by considering the up-wind effect in the same way as the subsection 2.4.4.

$$a_E = \frac{\nu_{re} \Delta r}{\nu_e (\delta\theta)_e} Max\left[0, (1 - 0.1|P_e|)^5\right] + Max\left[\sigma_e v_{\theta e} \Delta r, 0\right] \tag{A.22}$$

$$a_W = \frac{\nu_{rw} \Delta r}{\nu_w (\delta\theta)_w} Max\left[0, (1 - 0.1|P_w|)^5\right] + Max\left[-\sigma_w v_{\theta w} \Delta r, 0\right] \tag{A.23}$$

where the Peclet numbers P_e and P_w are defined as follows:

$$P_e = \frac{\sigma_e v_{\theta e} r_e (\delta\theta)_e}{\nu_{re}} \tag{A.24}$$

$$P_w = \frac{\sigma_w v_{\theta w} r_w (\delta\theta)_w}{\nu_{rw}} \tag{A.25}$$

If $v_\theta \gg 0$, then $a_W = 0$ and $a_E = \sigma_e v_{\theta e} \Delta r$, on the other hand, if $v_\theta \ll 0$, then $a_E = 0$ and $a_W = -\sigma_w v_{\theta w} \Delta r > 0$: the physical validity of the numerical procedure written in the subsection 2.4.1. is always guaranteed.

A.1.4. Stationary analysis

The following discretized equation should be applied for a stationary field analysis using $e^{j\omega t}$.

$$\dot{a}_P \dot{A}_P - a_E \dot{A}_E - a_W \dot{A}_W - a_N \dot{A}_N - a_S \dot{A}_S = \dot{b} \tag{A.26}$$

$$a_E = \frac{\nu_{re}\Delta r}{\nu_e(\delta\theta)_e} Max\Big[0, (1-0.1|P_e|)^5\Big] + Max\Big[\sigma_e v_{\theta e}\Delta r, 0\Big] \tag{A.27}$$

$$a_W = \frac{\nu_{rw}\Delta r}{\nu_w(\delta\theta)_w} Max\Big[0, (1-0.1|P_w|)^5\Big] + Max\Big[-\sigma_w v_{\theta w}\Delta r, 0\Big] \tag{A.28}$$

$$a_N = \frac{\nu_{\theta n} r_n}{(\delta r)_n}\Delta\theta \tag{A.29}$$

$$a_S = \frac{\nu_{\theta s} r_s}{(\delta r)_s}\Delta\theta \tag{A.30}$$

$$\dot{a}_P^0 = j\omega\sigma_P r_P \Delta\theta\Delta r \tag{A.31}$$

$$\dot{b} = \dot{J}_{0P} r_P \Delta\theta\Delta r \tag{A.32}$$

and

$$\dot{a}_P = \dot{a}_P^0 + a_E + a_W + a_N + a_S + \Big(\sigma_w v_{\theta w} - \sigma_e v_{\theta e}\Big)\Delta r \tag{A.33}$$

August, 1991

Appendix II

Report for the International Working Session on Linear Drives (Florence)

A Study on Parameter Identification of Linear Induction Motors

Prof. BOLDEA, Ion (Dr.)

Address: The Polytechnic Institute of Timisoara,
Str. C. Brâncoveanu 54, 1900 Timisoara ROMANIA
Telefax: +40-61-33721

Prof. MASADA, Eisuke (Dr.) & KOSEKI, Takafumi (Mr.)

Department of Electrical Engineering, Faculty of Engineering,
The University of Tokyo
7-3-1, Hongo, Bunkyo-ku, Tokyo 113 JAPAN
Telephone: +81-3-3812-2111 (Ext. 6660 or 6760)
Telefax: +81-3-5684-3972 or +81-3-3818-5706
E-Mail: koseki@audi.masada.t.u-tokyo.ac.jp

In the last meeting in Boston, prof. Boldea proposed a new test method applicable to LIM, in relation with the discussion on the Working paper #2. He promised to present it to the group and asked Prof. Masada to assist him with experimental data obtained with a stand-still testrig in the Univ. of Tokyo on the basis of the new test method.

This is a interim report of this joint work. Part 1. is the proposal of the test scheme by Prof. Boldea. Part 2 is the experimental results of test made on the basis of the proposal and the related consideration of the Univ. of Tokyo group. Assuming the test to apply to practical linear machines, the measuring method is modified from the original in the experimental studies.

In order to make measurements more precise and relate them with the dynamic model, the test scheme should be revised. An intention to present the interim report is to have review and suggestion of the group.

The first proposal by Prof. Ion Boldea

Part I: Linear induction motor parameter identification through non invasive standstill tests

Ion Boldea
(Polytechnic Institute of Timisoara, ROMANIA)

Abstract

Linear induction motors(LIMs) are being applied in various fields from short travel low speed industrial applications to urban or interurban transportation. Consequently considerable efforts have been made to model their behavior. LIM theories to account for longitudinal end-, transverse edge-, skin- and saturation- effects have been developed. Most theories rely on analytical or numerical field distribution analysis for steady state. However, also a few lumped circuit theories have been proposed to deal with steady state and transients. To measure the lumped parameters thus defined, standstill tests or a specially built cage secondary have been proposed. The present paper proposes a double row of fictitious secondary loops (cages) to account for longitudinal, transverse and skin effects. Based on this model, a set of noninvasive standstill tests using search coil flux sensors and hall sensors for secondary fictitious loop current measurement are proposed in order to identify the multiple loop secondary circuits. Tests are then performed or a laboratory model, both at standstill — to identify the parameters — and at speed to prove the model validity for steady state and transients.

1. Introduction

Field theories of LIMs have revealed specific phenomena such as longitudinal end- effect, transverse edge effect, secondary skin effect, open slotting influences and stationary pulsating m.m.f effect in single layer windings, normal and lateral forces etc. However field theories are more suitable for steady state. As linear induction motors are used for direct variable speed linear motion drives, they undergo frequent transients. Circuit theories have been proposed for the scope. Experiments were performed mainly to prove the proposed theories in terms of steady state performance (thrust, normal force, power factor, efficiency, air gap flux density distribution and secondary current longitudinal distribution).

As an exception (Turner, 1981) presents standstill tests on a specially built cage secondary to determine the mutual inductances and cage resistance and leakage inductance for the circuit theory of LIMs. The parameters thus obtained are then successfully applied to describe large transients such reconnection of the supply, loss of a phase and air gap sudden change. However, the necessity to build a special secondary which can hardly be made equivalent with the sheet on iron actual secondary where transverse cage, skin and saturation effects may hardly be neglected, makes the procedure less suitable for parameter estimation. This paper presents a generalized circuit model for LIMs valid both for steady state and transients. A set of noninvasive standstill tests are proposed to measure the defined parameters (inductances and resistances) of the fictitious double cage secondary, equivalent to the actual sheet on iron secondary. The double sided LIM is a particular case of the single sided LIM treated in the paper.

2. The generalized circuit theory (Nondahl, 1979; 1980)

In view of accounting longitudinal, transverse, skin and saturation effects the actual secondary is assimilated to a fictitious double cage with saturable back iron. To assess correctly the primary open slotting effect, the number of secondary fictitious bars should exceed two to three times at least the number of short primary slots. Also to consider the primary winding type influence on longitudinal flux distribution (pulsating m.m.f *etc.*) the model is developed in phase coordinates.

The fictitious double cage secondary concept is introduced to emulate the secondary frequency influence on transverse edge and skin effects (Figure 1.1). With inverters supplying the LIMs, the current harmonics are almost inevitable. Frequency effects in the secondary are argumented by the slow decaying longitudinal end- effect wave whose pole pitch varies with speed. The two fictitious cages are considered coupled only through the main field.

Due to the finite iron length of primary the mutual inductances between each secondary fictitious loop and the primary phases do not vary sinusoidally with position as in rotary induction machines and in general exhibit a continuous component whose amplitude depends on the type of primary winding type (single layer, double layer with half-field end slots), Figure 2a.

There are also self and coupling inductances between neighboring secondary fictitious loops (L_{si}, $L_{si,i-1}$) which depend on position in the sense that they are smaller outside the primary core and higher when below primary open slots (Figure. 2b).

The self inductances of primary phases L_R, L_Y, L_B and their coupling inductances M_{RY}, M_{RB}, M_{YB} are independent of secondary longitudinal position x:

$$\begin{aligned} L_R &= L_{R\sigma} + M_R \\ L_Y &= L_{Y\sigma} + M_Y \\ L_B &= L_{B\sigma} + M_B \end{aligned} \tag{I.1}$$

The primary phase leakage inductances $L_{R\sigma}$, $L_{Y\sigma}$, $L_{B\sigma}$ are not necessarily equal to each other, depending on the type of primary winding applied. The fictitious secondary double cage loops are characterized by constant resistances and leakage R_S, $R_S{}'$, $L_{S\sigma}$, $L_{S\sigma}{}'$. By constant here I mean independent from the longitudinal position. In matrix form the LIM equations are:

$$\begin{bmatrix} V_R \\ V_Y \\ V_B \\ 0 \\ 0 \\ \cdot \\ \cdot \\ 0 \\ 0 \end{bmatrix} = \left[R\right] \begin{bmatrix} i_R \\ i_Y \\ i_B \\ i_{S1} \\ i_{S1}{}' \\ \cdot \\ \cdot \\ i_{Sm} \\ i_{Sm}{}' \end{bmatrix} + \frac{d}{dt} \left[\left[L(x,g,z)\right] \begin{bmatrix} i_R \\ i_Y \\ i_B \\ i_{S1} \\ i_{S1}{}' \\ \cdot \\ \cdot \\ i_{Sm} \\ i_{Sm}{}' \end{bmatrix} \right] \tag{I.2}$$

Equation (I-3) ----- Structure of the inductance matrix

	R	Y	B	S_1	S_1'	S_2	S_2'	S_3	S_3'			S_m	S_m'
R	$L_{R\sigma} + M_R(g,z)$	$M_{RY}(g,z)$	$M_{RB}(g,z)$										
Y	$M_{RY}(g,z)$	$L_{Y\sigma} + M_Y(g,z)$	$M_{YB}(g,z)$										
B	$M_{RB}(g,z)$	$M_{YB}(g,z)$	$L_{B\sigma} + M_B(g,z)$										
S_1	$M_{RS1}(x,g,z)$	$M_{YS1}(x,g,z)$	$M_{BS1}(x,g,z)$	$L_{S\sigma} + M_{S1}(x,g,z)$									
S_1'	- 〃 -	- 〃 -	- 〃 -	$M_{S1}(x,g,z)$	$L_{S\sigma}' + M_{S1}(x,g,z)$			symmetric					
S_2	$M_{RS2}(x,g,z)$	$M_{YS2}(x,g,z)$	$M_{BS2}(x,g,z)$	$M_{S12}(x,g,z)$	$M_{S12}(x,g,z)$	$L_{S\sigma} + M_{S2}(x,g,z)$							
S_2'	- 〃 -	- 〃 -	- 〃 -	- 〃 -	- 〃 -	$M_{S2}(x,g,z)$	$L_{S\sigma}' + M_{S2}(x,g,z)$						
S_3	$M_{RS3}(x,g,z)$	$M_{YS3}(x,g,z)$	$M_{BS3}(x,g,z)$	0	0	$M_{S23}(x,g,z)$	$M_{S23}(x,g,z)$	$L_{S\sigma} + M_{S3}(x,g,z)$					
S_3'	- 〃 -	- 〃 -	- 〃 -	0	0	- 〃 -	- 〃 -	$M_{S3}(x,g,z)$	$L_{S\sigma}' + M_{S3}(x,g,z)$				
				0	0	0	0	$M_{S34}(x,g,z)$	$M_{S34}(x,g,z)$	$L_{S\sigma} + M_{S4}(x,g,z)$			
				0	0	0	0	- 〃 -	- 〃 -	$M_{S4}(x,g,z)$			
S_m	$M_{RSm}(x,g,z)$	$M_{YSm}(x,g,z)$	$M_{BSm}(x,g,z)$	0	0							$L_{S\sigma} + M_{Sm}(x,g,z)$	
S_m'	- 〃 -	- 〃 -	- 〃 -	0	0								$L_{S\sigma}' + M_{Sm}(x,g,z)$

(3)

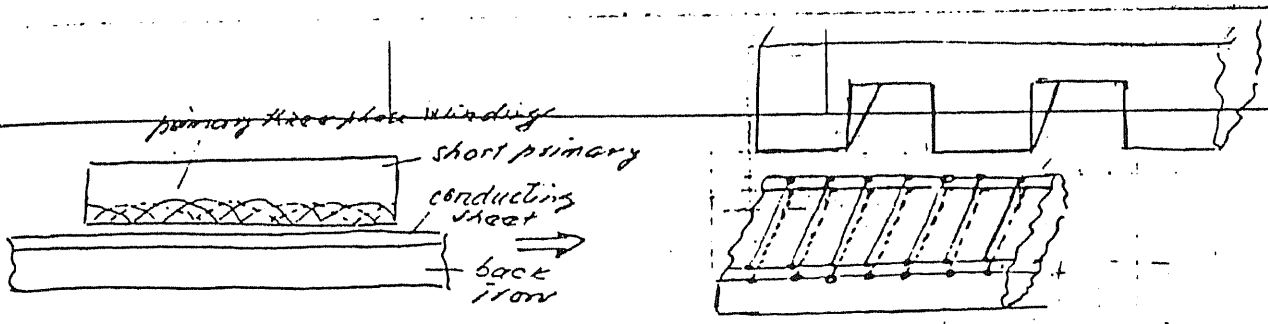

Fig 1.1. Sheet secondary – fictitious double cage

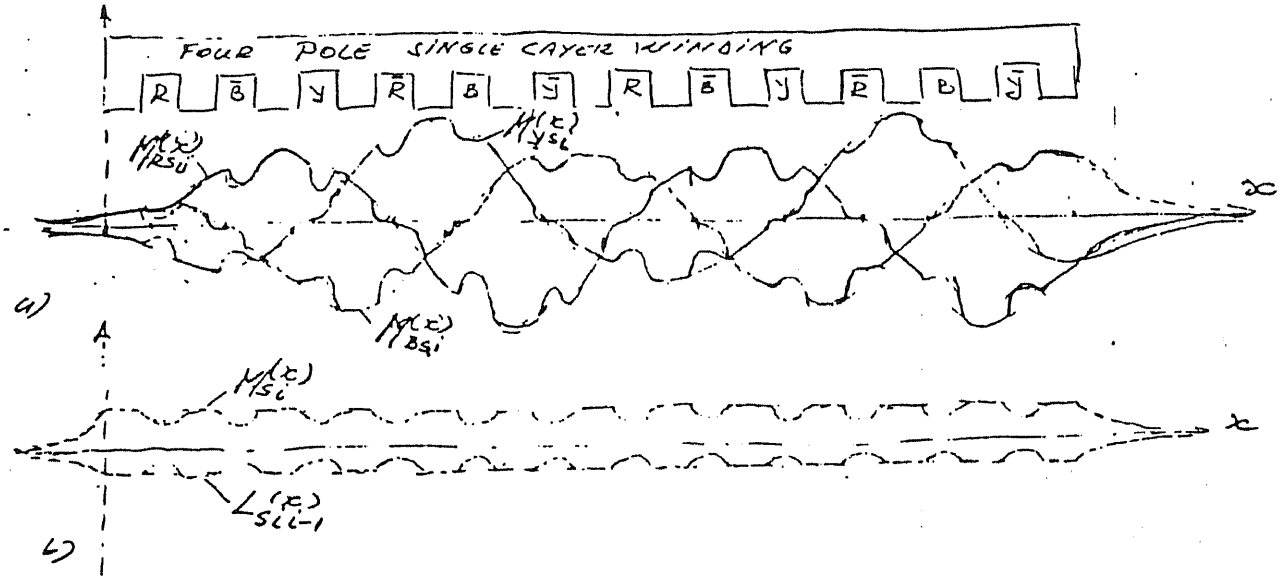

Fig 2. Variation of inductances with position
a) Primary to secondary loop mutual inductances, $L_{Rsi}^{(x)}$, $L_{Bsi}^{(x)}$, $L_{Ysi}^{(x)}$
b) Secondary loop loop fictitious inductance, $L_{si}(x)$, and mutual inductances between neighboring loops, $L_{si,i-1}^{(x)}$

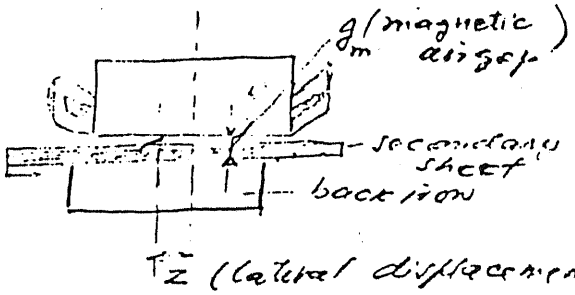

Fig 3. Tip transverse view with lateral displacement

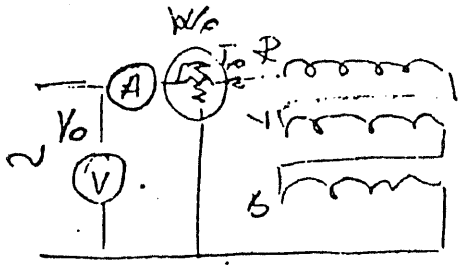

Fig 4. Equivalent primary inductance Lo.

The matrix inductance $\left[L(x,g,z)\right]$ is a square $(2m+3)\times(2m+3)$ dependent on longitudinal position x, magnetic air gap g and lateral displacement z of secondary with respect to primary (Equation (I.3) and Figure 3).

The resistance matrix [R] is:

$$\left[R\right] = diag\left[R_R,\ R_Y,\ R_B,\ R_S,\ \ldots,R_S,\ R_S'\right] \tag{I.4}$$

We should note that x means the position of a point on secondary with respect to primary entry and that the primary equations are written in primary phase coordinates and the secondary equations are written in secondary so, as x advances the first secondary loop moves from the leftest position to the rightest position while a new one takes its place such as all the time there are $2m$ active secondary loops, which extend well beyond primary core length. Only the parameters referring to one secondary loop placed in all the m positions are required. Moreover the dependence of parameters on air gap g and 2, in the absence of saturation need be measured for only one longitudinal position of the secondary loop and different g_s and Z_s.

The equation (I.1) could be rewritten as follows:

$$\left[V\right] = \left[R\right]\left[i\right] + \left[L(x,g,z)\right]\frac{d}{dt}\left[i\right] + \left[\frac{\partial}{\partial x}\left[L(x,g,z)\right]\right]\cdot\frac{dx}{dt}$$
$$+ \left[\frac{\partial}{\partial g}\left[L(x,g,z)\right]\right]\left[i\right]\frac{dg}{dt} + \left[\frac{\partial[J(x,g,z)]}{\partial z}\right]\left[i\right]\frac{dz}{dt} \tag{I.5}$$

So the forces along the three directions, F_x (the thrust force), F_n (the normal force) and F_z (the lateral force) are:

$$F_x = \frac{1}{2}\left[i\right]^T\cdot\frac{\partial}{\partial x}\left[L(x,g,z)\right]\cdot\left[i\right] \tag{I.6}$$

$$F_n = \frac{1}{2}\left[i\right]^T\cdot\frac{\partial}{\partial g}\left[L(x,g,z)\right]\cdot\left[i\right] \tag{I.7}$$

$$F_z = \frac{1}{2}\left[i\right]^T\cdot\frac{\partial}{\partial z}\left[L(x,g,z)\right]\cdot\left[i\right] \tag{I.8}$$

Accounting for saturation is a very difficult task as the level of saturation varies along the machine length x due to longitudinal end- effect. One way to account for it is to calculate the flux level in each of secondary loops:

$$\lambda_{mSi} = M_{RSi}i_R + M_{YSi}i_Y + M_{BSi}i_B + M_{Si}\left(i_{Si} + i_{Si}'\right)$$
$$+ B_{si,i-1}\left(i_{S,i-1} + i_{S,i-1}'\right) + M_{Si,i+1}\left(i_{S,i+1} + i_{S,i+1}'\right) \tag{I.9}$$

initial values of inductances would be assigned first and then, based on λ_{mSi} calculated and assuming that for the secondary frequencies encountered the skin effect in the secondary back iron does not vary, we may calculate the secondary core flux $\lambda_{CSi,i-1}$

$$\lambda_{CSi,i-1} = \lambda_{mSi} - \lambda_{mS,i-1} \tag{I.10}$$

If the inductances in (I.9) are scaled identically according to $\lambda_{cSi,i-1}$ measured and M_R, M_Y, M_B, M_{YB}, M_{YR} and M_{BR} are held dependent on the average core flux λ_C

$$\lambda_C = \frac{1}{m} \sum_{1}^{m} |\lambda_{CSi,i-1}| \tag{I.11}$$

then an iterative procedure may be initiated with renewed inductance until sufficient convergency is reached. It should be emphasized that we need determine through experiments λ_{mSi} with secondary loops different levels of primary currents.

3. Proposed noninvasive standstill measurements

The noninvasive standstill tests are directed toward measuring the resistances and inductances occurring in the equation (I.1). Primary phase resistances R_R, R_Y, R_B may be d.c. measured. Also as a first approximation the primary phase leakage inductances $L_{R\sigma}$, $L_{Y\sigma}$ and $L_{B\sigma}$ may be considered equal to each other and equal to the homo-polar inductance L_0, to be measured in a single phase a.c. standstill test with all phases in series (Figure 1.4):

$$L_0 = L_{R\sigma} = L_{Y\sigma} = L_{B\sigma} = \frac{1}{3\omega_1} \sqrt{\left[\frac{V_0}{i_0}\right]^2 - \left[\frac{W_0}{I_0^2}\right]^2} \tag{I.12}$$

The primary phase and secondary loops self and mutual inductances are to be determined from d.c. primary current decay tests and the secondary loop resistances and leakage inductances from a.c. tests at two different frequences.

Primary phase self and mutual inductances require d.c. decay tests at standstill on each phase while also measuring the induced voltages in the other two phases (Figure 1.5). Integrating the decaying current $i_R(t)$ and, respectively, the induced voltages E_{RY} and E_{RB}, the initial values of flux linkages in the three phases are obtained:

$$L_R i_{R0} = \int R_R i_R(t)\, dt \tag{I.13}$$

$$L_R = M_R + L_{R\sigma}$$

$$M_{RY} i_{R0} = \int E_{RY}(t)\, dt \tag{I.14}$$

$$M_{RB} i_{R0} = \int E_{BR}(t)\, dt \tag{I.15}$$

Thus we obtain $M_R(i_{R0})$, $M_{RY}(i_{R0})$ and $M_{RB}(i_{R0})$.

The same test may be done for different air gaps and lateral displacements to obtain the dependency on g and Z of M_R, M_{RY} and M_{RB}.

The same test could provide valuable additional information if three neighboring search coils as wide as the fictitious secondary loops are placed on the secondary sheet (in the m-positions, successively) together with two Hall devices or equivalent current sensors placed in between to measure the overhang secondary currents (Figure 1.6). The whole set is moved along x into m-positions.

By subtracting the currents of two neighboring overhangs, we obtained the current in the fictitious for placed in between i_{Si}. Recording E_{Si} (in the search coil) and $i_{Si}(t)$ during primary current d.c. decay for m-positions of the set, we may now integrate the recording of E_{Si} to obtain:

$$\frac{1}{n_C} \int E_{Si}(t)\, dt = M_{RSi}(x)\, i_{R0} \tag{I.16}$$

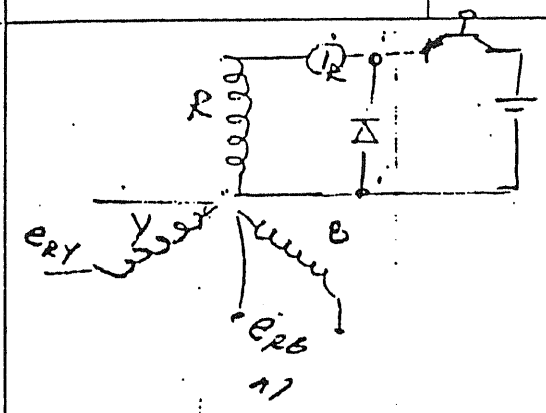

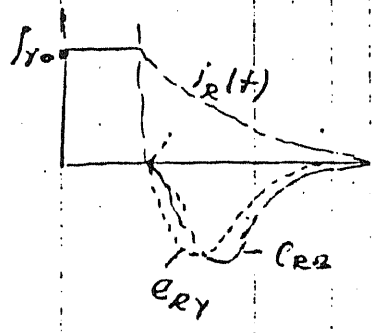

Fig 1.5. D.C. current decay test for Model R
a) Basic connections
b) Time waveforms

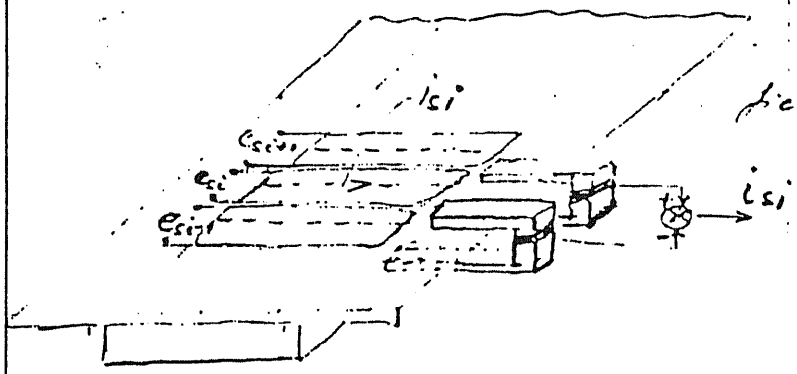

fictitious secondary burden.

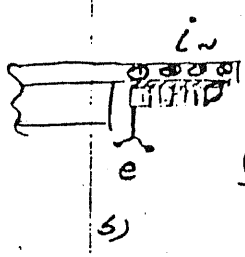

Fig 1.6. Non-invasive test set for secondary fictitious burden identification

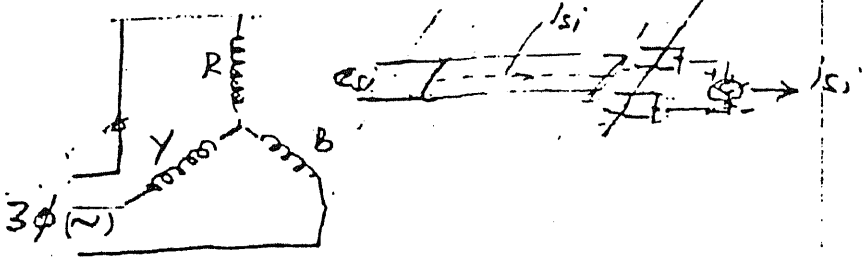

Fig 1.7. A.C. standstill tests

where the n_C is turns of search coil.

The coupling inductance between neighboring secondary fictitious loops may be obtained approximately if a current decay test is per formed solely on the search coil Si recording $i_{Si}(t)$.

$$M_{Si} i_{Si0} = \frac{1}{n_0} \int R_C \, i_{Si}(t) \, dt$$

$$M_{Si,i-1} = \frac{\int E_{Si,i-1} \, dt}{i_{SiC}} \tag{I.17}$$

$$M_{Si,i+1} = \frac{\int E_{Si,i+1} \, dt}{i_{SiC}}$$

The secondary loop self inductance $L_{S\sigma} + M_{Si}$ could also be obtained by recording $I_{Si}(t)$ during primary phase current turn off from a.c. Neglecting the coupling between neighboring secondary loops, the secondary loop current equation during primary current turn off from a.c. is:

$$R_S i_{Si} + \left[L_{S\sigma} + M_{Si} \right] \frac{di_{Si}}{dt} = 0 \tag{I.18}$$

So i_{Si} decreases with the secondary time constant T_S:

$$T_S = \frac{L_{S\sigma} + M_{Si}}{R_S} \tag{I.19}$$

Through curve fitting from $i_{Si}(t)$ decay after primary current turn off T_S may be determined. With R_S known (as will be shown later) M_{Si} will result. This latter test may be considered practical only if the frequency effects in the secondary could be neglected (one secondary cage considered).

The secondary loop resistances and leakage inductances may be obtained through a three phase a.c. standstill short circuit test at two frequencies by considering one fictitious cage for each of the two frequencies (Figure 1.7)

The measurement will be performed only in one position of the experimental set-up. Again, the coupling inductances of neighboring secondary loops are neglected for simplicity. As for LIMs the air gap is large, the main flux may not be neglected during "short circuit" tests and thus we have to measure the induced voltage E_{Si} and the current i_{Si} in the secondary fictitious loop:

$$\frac{1}{n_C} \left[E_{Si} \right]_{RMS} = \left[\sqrt{R_S^2 + \omega_1^2 L_{S\sigma}^2} \right] \cdot \left[i_{Si} \right]_{RMS} \tag{I.20}$$

We may use a common point (connection) when measuring E_{Si} and i_{Si} and thus measure the phase-lag between them ϕ_{Si}:

$$\tan\phi_{Si} = \frac{\omega_1 L_{S\sigma}}{R_S} \tag{I.21}$$

Form equations (I.18) and (I.19) with R_S and $L_{S\sigma}$ are determined with ω_1 known. For $\omega_1{}'$ we obtain $R_S{}'$ and $L_{S\sigma}{}'$. The frequency ω_1 corresponds to about 2-8Hz and $\omega_1{}'$ to above 25Hz. Only for a.c. tests the inductive current sensor (Figure 6b) may be used instead of

Hall sensors.

It should be noted that as the total overhang current is measured, the transverse edge effect in the active zone (below primary core is neglected. For many applications such approximation is practical. The tests may be performed for different air gaps g and lateral displacements z to check it R_S and $L_S\sigma$ vary with g and z as the flux distribution and the transverse edge effect change with g and z large.

Note

I have provided means to measure all parameters from standstill noninvasive tests. In what follows experimental work on a laboratory model is described. Standstill tests we performed to identify the parameters of the generalized circuit theory while running tests and digital simulations with measured parameters were done to prove the validity of the proposed model and parameter identification method. The tests at standstill are considered noninvasive as the search coil — Hall current sensor set-up is placed easily in different positions along the primary in the vicinity of the actual secondary.

References

[I.1] T. H. Nondahl, D. W. Novotny:
"Pole by pole model of a linear induction machine using conformal mapping coefficients" IBID, 1979, pp. 1344-1353

[I.2] T. H. Nondahl, D. W. Novotny: "Three phase pole by pole model of a linear induction machine" Proc. of IEE, Vol. 127, PT. B, No. 2, 1980, pp. 68-82

[I.3] T. R. Turner, T. H. Loye:
"The transient performance of linear induction motors" IEEE Trans. Vol. PAS-100, No. 12, 1981, pp. 4958-4964

Part II: Investigations at the University of Tokyo based on the proposal of Prof. Boldea — Revised Impedance Measurements

KOSEKI Takafumi & MASADA Eisuke
(The University of Tokyo, JAPAN)

1. Introduction

Based on Prof. Boldea's idea written in the part I, we made a simplified plan of the impedance measurements taking a theoretical consistency into account.

As you will read later, you must remove the secondary reaction plate at some measurements for theoretical consistency; we have assumed that the purpose of this measurement is to identify the impedances *only of the primary active part,* because such an experiment is basically impossible with a complete LIM with a specified secondary rail, in other words, you need a special secondary structure only for the measurement, whose conductive plate is removable. If you would be interested in the impedance identification of the complete LIM, all the procedures of the plan should be fundamentally reappraised.

For practical reasons, we made the following assumptions and simplifications.

(1) In stead of his original measurement scheme of *"Decay D.C. Method",* we use a transfer-function-measurement mode of an FFT spectrum analyzer and a VVVF signal source.
(2) The fictitious cage is only a single one; the skin effect is neglected.
(3) The search coils were compelled to be much larger than those in his original idea (*c.a.* $8.2cm \times 5.0cm \times 0.5cm$, 10 turns); the measured admittance of the coil itself, *i.e.* the transfer function V to I, is shown in the figure II.1.
(4) We cannot measure a current in the secondary plat directly.

2. Revised plan of the measurement

EXPERIMENT 1

First, the resistances in the primary windings (R_R, R_Y, R_B) are measured by applying DC currents.

EXPERIMENT 2

As shown in the figure II.2, an AC voltage is applied to the primary windings connected seriously; the primary leakage inductance, $L_{R\sigma}$, $L_{Y\sigma}$, $L_{B\sigma}$, are measured. In the ideal case, no secondary current would be induced, but actually, some harmonic current flows in the plate.

EXPERIMENT 3

Self- and mutual- impedances of the primary- and the secondary- loops are measured. Although it should be performed with the *"Decay D.C. method"* (see the figure II.3 (a)) in his original plan, we have proposed to use an FFT spectrum analyzer with a VVVF signal source for measuring a transfer function of a loop.

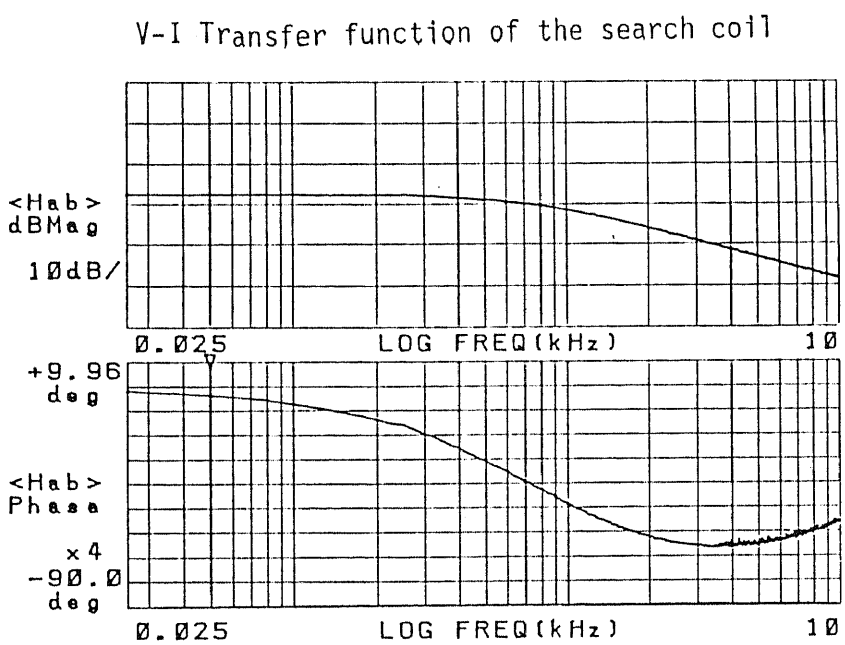

Figure II.1 V-I characteristics of the search coil

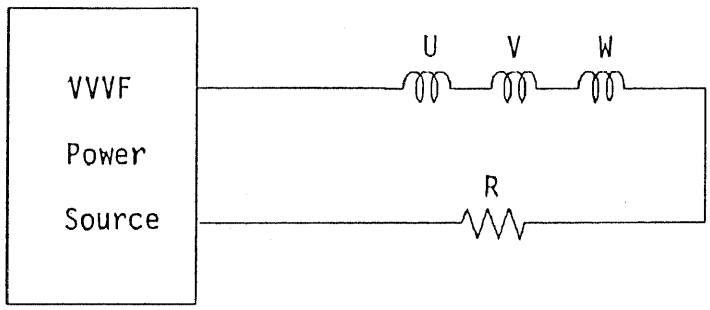

Figure II.2 Measurement circuit of the primary leakage inductances

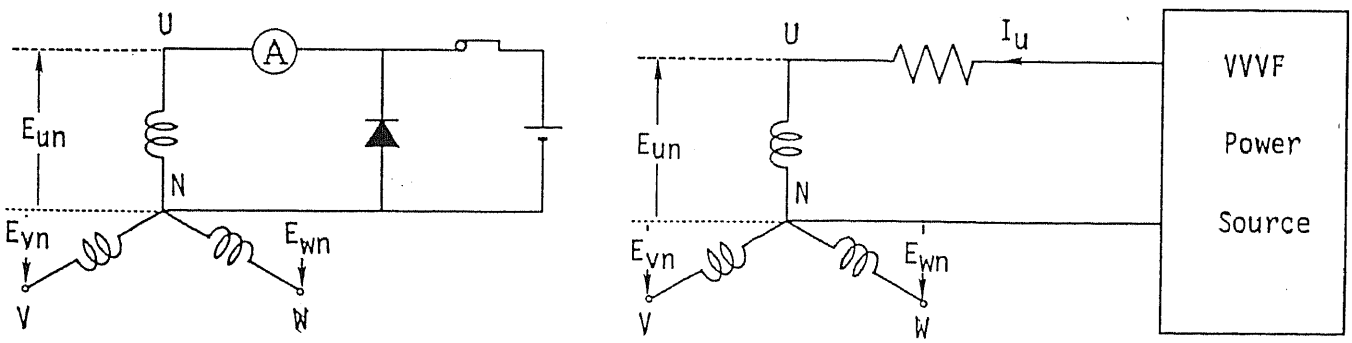

(a) Decay D. C. method (b) Transfer fuction monitoring with FFT analyzer

Figure II.3 Measurement circuits of primary impedances

Experiment 3.1

As shown in the figure II.3 (b), the primary self inductances L_R, L_Y, L_B and the mutual impedances M_{RY}, M_{RB}, M_{YB} are measured. In these measurements, the secondary reaction plate is removed since *no secondary current must be induced.* The results will be compared with the data measured with the circuit shown in the figure II.3 (a) afterwards.

Experiment 3.2

As shown in the figure II.4, a search coil is put on the secondary core *also without the secondary reaction plate.* Mutual inductances between the primary- and the secondary- fictitious loops M_{RSi}, M_{YSi}, M_{BSi} are measured by appling a single phase A.C. signal into the primary winding. You can measure the transfer function from the primary current to the induced voltage E_{Si} in the search coil, which should be equivalent to the secondary fictitious loop, in the same way described in the previous subsection.

Experiment 3.3

You measure the self- and mutual- inductances of the secondary search coils M_{Si}, $M_{Si,Si-1}$, $M_{Si,Si+1}$ by monitoring transfer functions from the current in the central search coil I_{Si} to the induced voltages E_{Si}, E_{Si-1}, E_{Si+1} as shown in the figure II.5. Also in this case, the secondary reaction plate should be removed, since induced secondary currents are substantial disturbances in the inductance identification.

EXPERIMENT 4

You measure a resistance R_S and a leakage inductance $L_{S\sigma}$ of a fictitious loop in the secondary reaction plate (*not a search coil itself*), by monitoring a transfer function from the E_{Si} to the I_{Si} shown in the figure II.6, in the same way as the previous measurements.

Correction of measured data

Since the winding number of the fictitious loop has been assumed to one turn, the data, measured with the search coils with ten turns illustrated in the figure II.6, must be corrected as follows.

The measured inductances have been multiplied by 14.7/8.3 by assuming constant magnetic flux densities in a search coil, and the mutual- inductances between the loops and primary windings are calculated by dividing the measured values by ten. In the same way, the self- and mutual inductances of the secondary loops have been calculated by multiplying the measured data by 14.7/8.3/100. For the experiment 4, we have assumed the equivalent circuit of a transformer with the secondary short circuit illustrated in the figure II.8 between the search coil and the fictitious loop in the secondary conductor, where the primary leakage inductance has been neglected; also the R_S and $L_{S\sigma}$ have been calculated by dividing the measured values by one hundred on account of the one-turn assumed winding number.

Koseki doubts, however, propriety of this procedure. Anyway, it is impossible to measure the secondary current in the plate with a normal rail and current sensors directly, as he proposed in the original report.

3. Prof. Boldea's comments to the revision and discussions

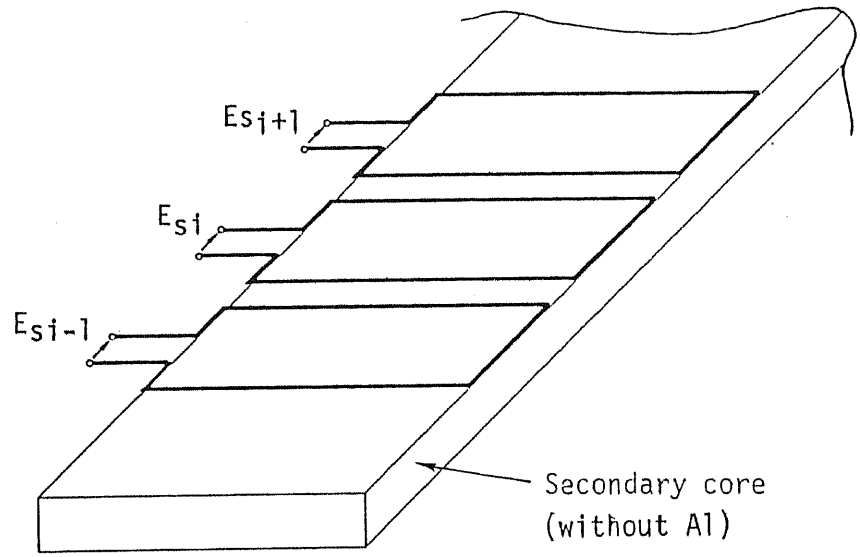

Figure II.4 Measurements of mutual indutances between primary- and secondary circuits

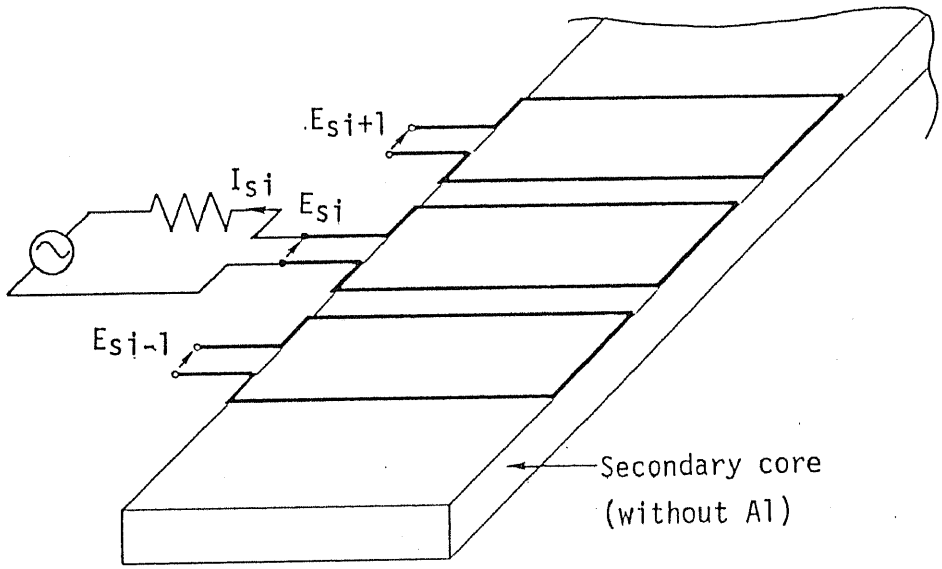

Figure II.5 Measurements of inductances in the secondary rail

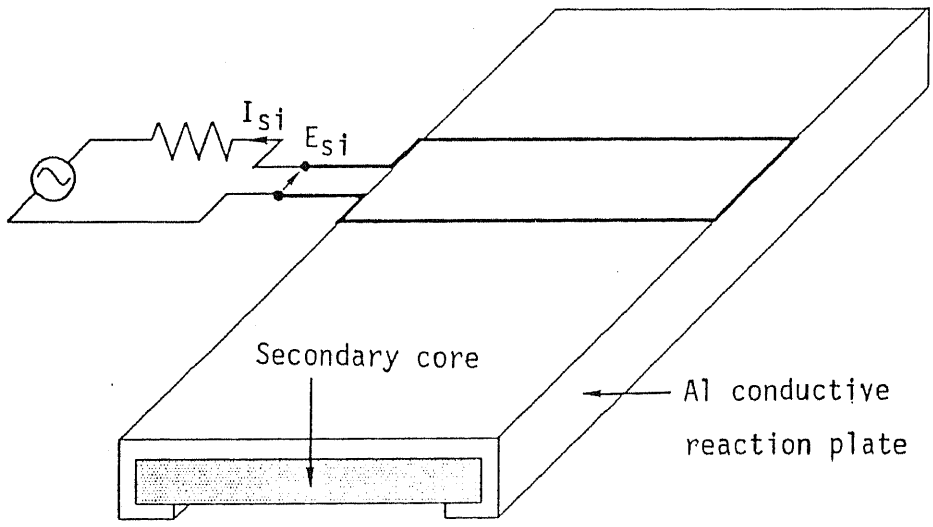

Figure II.6 Measurements of the secondary impedances

3.1. Prof. Boldea's comments

The following comments were sent from Prof. Boldea:

(1) I understand the difficulties in measuring the secondary current through a Hall sensor. So I suggest here to draw two holes at the stack end in the secondary and connect them in counter series to measure the current difference between two neighboring secondary overhang elements. The two coils embrace the secondary overhangs and are placed in the transverse plane at the end of a search coil which covers a secondary circuit element. The measuring (in AC) or the recording of this current (in DC decay test) leads to the required data. The measurements strategy remains the same.

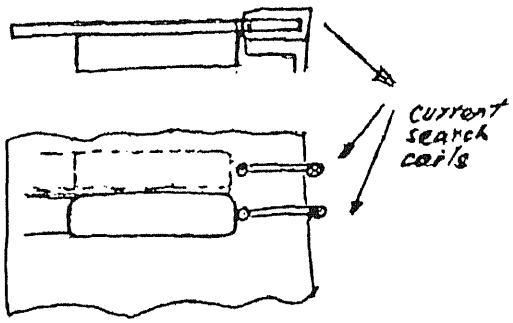

(2) I also fear that the procedure on fig. II.6 to measure secondary impedance though acceptable is too approximative. So I propose to check this aspect by considering that the secondary loop is the secondary of a short circuit transformer whose primary is the search coil characterized by it resistance R_{coil} and proper inductance L_{Si} measured in the absence of secondary. (The figure II.5)

(3) If the secondary back iron is solid the d.c. decay test should be used to determine the magnetizing inductances of primary, and the mutual ones rather than the transfer function with an averaging procedure of an FFT analyzer. With a laminated back iron the latter method may be however safely applied.

3.2. Koseki's opinion

(1) The proposal of Prof. Boldea is right; the secondary current should be directly measured. In our test machine, however, it is impossible to attach the additional current search loops, as is in ordinary LIMs in utility.

(2) His second comment is also right, however, we had no other alternative method for the measurement unfortunately.

(3) A half of his third comment is right, but the other half has no sense. If the eddy current in the cores is not negligible, all the measurement procedure are anyway nonsense. There is no inherent difference between his *"DC decay method"* and our FFT method, since you can observe the electromagnetic phenomena, anyway, only in varying field, *i.e.*, if the eddy current in the core is not negligible, it cannot help having considerable harmful effects also in his *"transient DC-* method". The substantial solution is, hence, only using cores with no conductivity for ideal measurements.

4. Results of the measurements

The three- phase six- terminal impedance matrix in the appendix 1 is written again as follows:

$$\dot{\mathbf{Z}} = \begin{bmatrix} 0.57 + j(1.28) & -0.095 + j(-0.33) & -0.087 + j(-0.30) \\ -0.095 + j(-0.33) & 0.57 + j(1.28) & -0.092 + j(-0.32) \\ -0.089 + j(-0.31) & -0.095 + j(-0.33) & 0.59 + j(1.27) \end{bmatrix} \qquad \text{(A.1.13')}$$

The following impedance matrix $\mathbf{Z}'$ has been calculated by substituting measured results into the equation (A.2.4).

$$\mathbf{Z}' = \begin{bmatrix} 0.88 + j(1.60) & -0.26 + j(-0.54) & -0.31 + j(-0.39) \\ -0.26 + j(-0.53) & 0.81 + j(1.68) & -0.26 + j(-0.54) \\ -0.31 + j(-0.39) & -0.26 + j(-0.54) & 0.95 + j(1.65) \end{bmatrix} \quad \text{(II.1)}$$

This result is different from the equation (A.1.13'). The possible reasons for the difference are as follows:

(1) Only adjacent loops are considered in the modeling of Prof. Boldea; there is no theoretical reason for the assumption.

(2) The measurement with the search coils could be incorrect.

(3) The impedance detection based on the equivalent circuit in the figure II.8 was wrong.

The problems above are discussed in the following subsections.

4.1. Modeling with further loops

Although there is no theoretical reason, Prof. Boldea neglects all the other coils but adjacent ones. The partial block of the impedance matrix L_{22} in the equation (A.2.4) are written approximately as follows:

$$L_{22} = L \begin{bmatrix} 1 & & \\ & \ddots & \\ & & 1 \end{bmatrix} + M_1 \begin{bmatrix} 0 & 1 & & \\ 1 & \ddots & \ddots & \\ & \ddots & \ddots & 1 \\ & & 1 & 0 \end{bmatrix} \quad \text{(II.2)}$$

where the L represents the self inductances of the loops, and the M_j is mutual inductances between the i- and $(i+1)$- loops. In fact, the results in the equation (II.3) has been derived with the $\mathbf{Z}'$ written in the equation (II.2); the results are almost the same as the equation (II.1).

$$\mathbf{Z}' = \begin{bmatrix} 0.90 + j(1.59) & -0.27 + j(-0.54) & -0.32 + j(-0.39) \\ -0.27 + j(-0.52) & 0.84 + j(1.68) & -0.27 + j(-0.54) \\ -0.32 + j(-0.39) & -0.27 + j(-0.54) & 0.97 + j(1.65) \end{bmatrix} \quad \text{(II.3)}$$

If the mutual inductances with the further loops are not negligible, the matrix $\mathbf{Z}'$ are approximately written as follows:

$$L_{22} = L \begin{bmatrix} 1 & & \\ & \ddots & \\ & & 1 \end{bmatrix} + M_1 \begin{bmatrix} 0 & 1 & & \\ 1 & \ddots & \ddots & \\ & \ddots & \ddots & 1 \\ & & 1 & 0 \end{bmatrix}$$
$$+ M_2 \begin{bmatrix} 0 & 0 & 1 & & \\ 0 & \ddots & \ddots & \ddots & \\ 1 & \ddots & \ddots & \ddots & 1 \\ & \ddots & \ddots & \ddots & 0 \\ & & 1 & 0 & 0 \end{bmatrix} + \cdots$$
$$+ M_{3n-1} \begin{bmatrix} 0 & & & 0 & 1 \\ & \ddots & \ddots & \ddots & 0 \\ & \ddots & \ddots & \ddots & \\ 0 & \ddots & \ddots & \ddots & \\ 1 & 0 & & & 0 \end{bmatrix} \quad \text{(II.4)}$$

The resultant $\mathbf{Z}'$ with further loops are as follows:

In the case of considering from M_1 to M_2,

$$\mathbf{Z}' = \begin{bmatrix} 0.87 + j(1.60) & -0.25 + j(-0.54) & -0.30 + j(-0.39) \\ -0.25 + j(-0.53) & 0.81 + j(1.68) & -0.25 + j(-0.54) \\ -0.30 + j(-0.39) & -0.25 + j(-0.54) & 0.94 + j(1.65) \end{bmatrix} \quad \text{(II.5)}$$

In the case of considering from M_1 to M_3,

$$\mathbf{Z}' = \begin{bmatrix} 0.85 + j(1.60) & -0.24 + j(-0.54) & -0.29 + j(-0.39) \\ -0.24 + j(-0.53) & 0.79 + j(1.68) & -0.24 + j(-0.54) \\ -0.29 + j(-0.39) & -0.24 + j(-0.54) & 0.92 + j(1.65) \end{bmatrix} \quad \text{(II.6)}$$

And, in the case of considering from M_1 to M_4,

$$\mathbf{Z}' = \begin{bmatrix} 0.84 + j(1.60) & -0.24 + j(-0.53) & -0.29 + j(-0.39) \\ -0.24 + j(-0.53) & 0.78 + j(1.68) & -0.24 + j(-0.54) \\ -0.29 + j(-0.39) & -0.24 + j(-0.54) & 0.91 + j(1.65) \end{bmatrix} \quad \text{(II.7)}$$

Hence, you should have considered till M_4 at least in this measurement. The number of truncation practically allowable is strongly depends on LIM's dimension and search coils; it is almost impossible to determine the limit generally.

4.2. Search coils

(1) It was checked that the search coils were not short circuit, with a DC-test.

(2) It was also checked that the measurement of the induced voltages was right, by measuring magnetic fluxes in the search coils with flux meter.

No problems were, therefore, found about the search coils themselves.

4.3. Detection of the secondary impedances

In the experiment 4, we could not directly measure the secondary current, and guessed the secondary impedances $L_{S\sigma}$ and R_S based on the equivalent circuit assuming the ideal transformer without primary leakage; the modeling has no theoretical basis, especially, we cannot know actual distributions of the secondary current in the secondary conductive plate. For instance, the equation (II.8) is derived with $R_S = 1.30\times10^{-4}\ \Omega$, and the result (II.9) with $L_{S\sigma} = 6.0\times10^{-5}$ H, where $R_S = 1.37\times10^{-4}\ \Omega$ and $L_{S\sigma} = 5.0\times10^{-5}$ H are assumed in the previous calculations: the resultant small impedance matrix is remarkably sensitive to the secondary impedances.

In the case of the $R_S = 1.30\times10^{-4}\ \Omega$:

$$\mathbf{Z}' = \begin{bmatrix} 0.56 + j(1.44) & -0.12 + j(-0.47) & -0.14 + j(-0.31) \\ -0.12 + j(-0.47) & 0.53 + j(1.55) & -0.12 + j(-0.47) \\ -0.15 + j(-0.31) & -0.12 + j(-0.48) & 0.64 + j(1.51) \end{bmatrix} \quad \text{(II.8)}$$

In the case of the $L_{S\sigma} = 6.0\times10^{-5}$ H:

$$\mathbf{Z}' = \begin{bmatrix} 0.83 + j(1.57) & -0.24 + j(-0.53) & -0.29 + j(-0.38) \\ -0.24 + j(-0.52) & 0.78 + j(1.66) & -0.24 + j(-0.53) \\ -0.29 + j(-0.38) & -0.24 + j(-0.53) & 0.97 + j(1.63) \end{bmatrix} \quad \text{(II.9)}$$

In the case of the $R_S = 1.30\times10^{-4}\ \Omega$ and $L_{S\sigma} = 6.0\times10^{-5}$ H, the following result is obtained, which is in good agreement with the equation (A.1.13').

$$\mathbf{Z}' = \begin{bmatrix} 0.80 + j(1.60) & -0.22 + j(-0.54) & -0.27 + j(-0.39) \\ -0.23 + j(-0.54) & 0.74 + j(1.69) & -0.22 + j(-0.54) \\ -0.27 + j(-0.39) & -0.24 + j(-0.55) & 0.87 + j(1.66) \end{bmatrix} \quad \text{(II.10)}$$

5. Concluding remarks

Consequently, the following two problems should be noted.

(1) Effects of not only adjacent- but also further- loops must be considered.

(2) The secondary impedances should be directly measured.

For measuring directly the secondary impedances, however, you need a secondary rail of special structure written in the comment from Prof. Boldea: the application of his proposal is, hence, compelled to be quite limited.

Your technical advices and comments are cordially welcome.

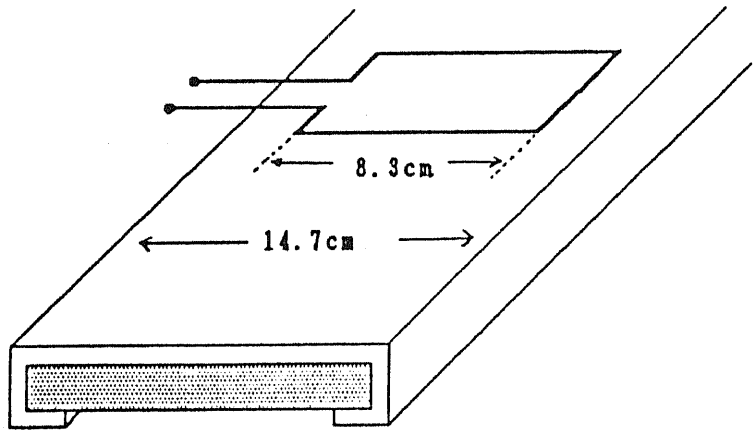

Figure II.7 Dimensions of search coil and secondary rail

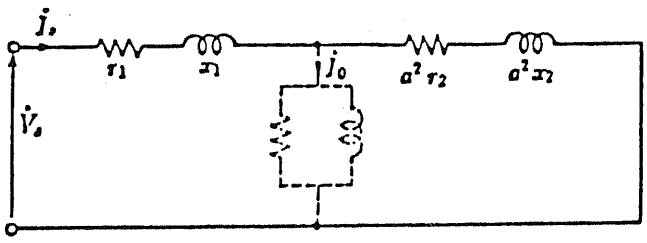

Figure II.8 Equivalent circuit of a transformer with short secondary circuit

Appendix 1: Preliminary experimental results on the LIM

KOSEKI, Takafumi & MASADA, Eisuke
(The University of Tokyo, JAPAN)

1. Introduction

To compare with Boldea's experimental scheme, we carried out preliminary measurements as follows:

(1) measurement and calculation of thrust and normal forces driven by a three phase sinusoidal AC current source,

(2) measurement of terminal impedance with the three- phase AC drive, and

(3) impedance measurement based on the multi-terminal linear network-system theory.

2. Calculated and measured forces

As the first step of the experiments, we measured thrust- and normal- forces with three-phase drives. Measured forces are compared with theoretical analysis in the figure A.1.1.

Fourier series method with the primary equivalent current sheet

3. Terminal impedance with three phases AC drive

With a normal three- phase connection, the terminal voltages and line currents were measured. The results are written in the table A.1.1.

Table A.1.1 Voltage, current and impedance of the U-phase

Frequency [Hz]	30.0	40.0	50.0	60.0	70.0
R [Ω]	0.539	0.617	0.676	0.608	0.601
ω L	1.04	1.33	1.62	2.00	2.24
L [mH]	5.49	5.28	5.14	5.30	5.11

4. Impedance measurement based on the multi-terminals network theory

4.1. Impedance matrix model

4.1.1. Discussion on the LIM as a multi- terminal network — idea from two- dimensional analysis

In order to investigate relations between terminal voltages and line currents of a n-phase motor with asymmetric impedances, discussions based on a 2n-terminal network system is necessary, considering remarkable electromagnetic interferences between each phase.

For instance, a behavior of a three-phase motor on an operating point with the neutral point connection is modeled as a 6-terminal network system shown in the figure A.1.2 (a). Terminal-voltage- and line-current- vectors are defined as follows:

$$\dot{\mathbf{V}} = \left[\dot{V}_1, \dot{V}_2, \ldots, \dot{V}_n\right]^t \tag{A.1.1}$$

$$\dot{\mathbf{I}} = \left[\dot{i}_1, \dot{i}_2, \ldots, \dot{i}_n\right]^t \tag{A.1.2}$$

With the impedance matrix defined in the equation (A.1.3),

$$\dot{\mathbf{Z}} \equiv \begin{bmatrix} Z_{1,1} & \cdots & Z_{1,n} \\ \cdot & \cdots & \cdot \\ \cdot & \cdots & \cdot \\ \cdot & \cdots & \cdot \\ Z_{n,1} & \cdots & Z_{n,n} \end{bmatrix} \tag{A.1.3}$$

the voltage equations are written as follows:

$$\dot{\mathbf{V}} = \dot{\mathbf{Z}} \cdot \dot{\mathbf{I}} \tag{A.1.4}$$

where the motor's characteristics are ideally linear and the velocity of the secondary plate is given.

For a numerical simulation of a voltage source drive using a current source field-analysis program, the field distribution should be calculated with the following input-current vectors.

$$\dot{\mathbf{I}}_1 = \left[1.0e^{j0},\ 0,\ 0,\ \ldots,\ 0\right]^t \tag{A.1.5}$$

$$\dot{\mathbf{I}}_2 = \left[0,\ 1.0e^{j0},\ 0,\ 0,\ \ldots,\ 0\right]^t \tag{A.1.6}$$

$$\cdots \cdots \cdots \cdots \cdots \cdots$$

$$\dot{\mathbf{I}}_n = \left[0,\ 0,\ 0,\ 0,\ \ldots,1.0e^{j0}\right]^t \tag{A.1.7}$$

Using resultant induced terminal voltages, the impedance matrix (A.1.3) can be determined. The admittance matrix is calculated by inversing the impedance matrix. Finally, the line currents corresponding to the given voltages are derived, and the field calculation with a voltage source is carried out again much faster than the first field analysis based on the superposition principle of a linear system.

In the case of impedance measurements, the same procedures should be applied with a single phase drive as shown in the figure A.1.3.

If there is no neutral point connection like the figure A.1.2 (b), *i.e.*, each line current is constrained by the Kirchhoff's first law, the motor should be treated as a four-terminal network — generally, as a 2(n-1)-terminal network — due to a less system freedom.

4.1.2. Physical meaning of the impedance matrix — energy flow at a single phase drive

The energy flow in a motor is written as follows.

$$P_1 = P_{mech} + P_{loss} \tag{A.1.8}$$

Since the voltage between the terminal i and the neutral point is written from the equation (A.1.4) as follows,

$$\dot{V}_i = \sum_{j=1}^{n} \dot{Z}_{ij} \cdot \dot{i}_j \tag{A.1.9}$$

$$\left[i = 1,\ 2,\ \ldots,n\right]$$

the time average power put in the primary windings is written as follows.

$$P_1 = \frac{1}{2} \mathrm{Re} \left[\sum_{i=1}^{n} \dot{V}_i \cdot \dot{I}_i^*\right]$$

$$= \frac{1}{2} \sum_{i=1}^{n} \sum_{j=1}^{n} \mathrm{Re} \left[\dot{Z}_{ij} \cdot \dot{I}_j \cdot \dot{I}_i^*\right] \tag{A.1.10}$$

We define a factor in the impedance matrix as $Z_{ij} \equiv R_{ij} + j\omega L_{ij}$ here.

In a special case where only the single phase AC current I_1 is applied as shown in the figure A.1.2, *i.e.* corresponding to the cases of the equation (A.1.4),

$$\begin{aligned} P_1 &= \frac{1}{2}\,\mathrm{Re}\left[Z_{11}\cdot I_1\cdot I_1^*\right] \\ &= \frac{1}{2}\,|I_1|^2\cdot \mathrm{Re}\left[Z_{11}\right] \\ &= I_{1RMS}^2\cdot R_{11} \end{aligned} \tag{A.1.11}$$

From the equations (A.1.4) and (A.1.11), the following equation is derived.

$$I_{1rms}^2\cdot R_{11} = P_{loss} - F_{brake}\cdot v_2 \tag{A.1.12}$$

It has been shown that the real parts of the factors in the impedance matrix represent the energy flow in a motor. Some of them can be also negative in the generator operation.

4.2. Impedance measurement using an FFT spectrum analyzer

In this section,

(1) all the factors of n^2 in the impedance matrix must be calculated or measured, and

(2) behavior of a LIM always depends on the velocity of the secondary plate and the primary frequency, *i.e.*, it is necessary to calculate or measure the impedance matrix on many operating points.

For the two reasons, the experiments are compelled to be many; a simple experimental scheme is desired.

Frequency dependency of the impedance of the standstill LIM in the Masada Laboratory have been, therefore, directly measured using transfer function mode of a 2 channel FFT spectrum analyzer and VVVF signal source, as shown in the figure A.1.4. An example of the experimental results is shown in the figure A.1.5. The measurements with this "small signal" scheme have been in good agreement with the conventional experimental method. The measured impedance matrix is as follows:

$$\dot{\mathbf{Z}} \equiv \begin{bmatrix} Z_{1,1} & Z_{1,2} & Z_{1,3} \\ Z_{2,1} & Z_{2,2} & Z_{2,3} \\ Z_{3,1} & Z_{3,2} & Z_{3,3} \end{bmatrix} = \begin{bmatrix} 1.405\cdot e^{j65.7deg.} & 0.345\cdot e^{j240.3deg.} & 0.316\cdot e^{j254.4deg.} \\ 0.346\cdot e^{j253.7deg.} & 1.405\cdot e^{j52.2deg.} & 0.336\cdot e^{j254.4deg.} \\ 0.321\cdot e^{j253.7deg.} & 0.345\cdot e^{j240.2deg.} & 1.405\cdot e^{j65.4deg.} \end{bmatrix} \tag{A.1.13}$$

When a symmetric three- phase AC current of 50Hz is applied, the terminal impedance of the U-phase winding Z_U is;

$$\begin{aligned} Z_U &= Z_{1,1} + Z_{1,2}\cdot e^{j\cdot\left[-\frac{2}{3}\pi\right]} + Z_{1,3}\cdot e^{j\cdot\left[-\frac{4}{3}\pi\right]} \\ &= 1.405\cdot e^{j65.7deg.} + 0.345\cdot e^{j120.2deg.} + 0.316\cdot e^{j14.4deg.} \\ &= 0.711 + j\cdot 50.0\times 2\pi\times 5.27\times 10^{-3} \end{aligned} \tag{A.1.14}$$

We define a factor in the impedance matrix as $Z_{ij} \equiv R_{ij} + j\omega L_{ij}$ here.

In a special case where only the single phase AC current I_1 is applied as shown in the figure A.1.2, *i.e.* corresponding to the cases of the equation (A.1.4),

$$\begin{aligned} P_1 &= \frac{1}{2}\,\mathrm{Re}\left[Z_{11}\cdot I_1\cdot I_1^*\right] \\ &= \frac{1}{2}\,|I_1|^2\cdot \mathrm{Re}\left[Z_{11}\right] \\ &= I_{1RMS}^2\cdot R_{11} \end{aligned} \tag{A.1.11}$$

From the equations (A.1.4) and (A.1.11), the following equation is derived.

$$I_{1rms}^2\cdot R_{11} = P_{loss} - F_{brake}\cdot v_2 \tag{A.1.12}$$

It has been shown that the real parts of the factors in the impedance matrix represent the energy flow in a motor. Some of them can be also negative in the generator operation.

4.2. Impedance measurement using an FFT spectrum analyzer

In this section,

(1) all the factors of n^2 in the impedance matrix must be calculated or measured, and

(2) behavior of a LIM always depends on the velocity of the secondary plate and the primary frequency, *i.e.*, it is necessary to calculate or measure the impedance matrix on many operating points.

For the two reasons, the experiments are compelled to be many; a simple experimental scheme is desired.

Frequency dependency of the impedance of the standstill LIM in the Masada Laboratory have been, therefore, directly measured using transfer function mode of a 2 channel FFT spectrum analyzer and VVVF signal source, as shown in the figure A.1.4. An example of the experimental results is shown in the figure A.1.5. The measurements with this "small signal" scheme have been in good agreement with the conventional experimental method. The measured impedance matrix is as follows:

$$\dot{\mathbf{Z}} \equiv \begin{bmatrix} Z_{1,1} & Z_{1,2} & Z_{1,3} \\ Z_{2,1} & Z_{2,2} & Z_{2,3} \\ Z_{3,1} & Z_{3,2} & Z_{3,3} \end{bmatrix} = \begin{bmatrix} 1.405\cdot e^{j65.7deg.} & 0.345\cdot e^{j240.3deg.} & 0.316\cdot e^{j254.4deg.} \\ 0.346\cdot e^{j253.7deg.} & 1.405\cdot e^{j52.2deg.} & 0.336\cdot e^{j254.4deg.} \\ 0.321\cdot e^{j253.7deg.} & 0.345\cdot e^{j240.2deg.} & 1.405\cdot e^{j65.4deg.} \end{bmatrix} \tag{A.1.13}$$

When a symmetric three- phase AC current of 50Hz is applied, the terminal impedance of the U-phase winding Z_U is;

$$\begin{aligned} Z_U &= Z_{1,1} + Z_{1,2}\cdot e^{j\cdot\left[-\frac{2}{3}\pi\right]} + Z_{1,3}\cdot e^{j\cdot\left[-\frac{4}{3}\pi\right]} \\ &= 1.405\cdot e^{j65.7deg.} + 0.345\cdot e^{j120.2deg.} + 0.316\cdot e^{j14.4deg.} \\ &= 0.711 + j\cdot 50.0\times 2\pi\times 5.27\times 10^{-3} \quad \text{(See the table A.1.1.)} \end{aligned} \tag{A.1.14}$$

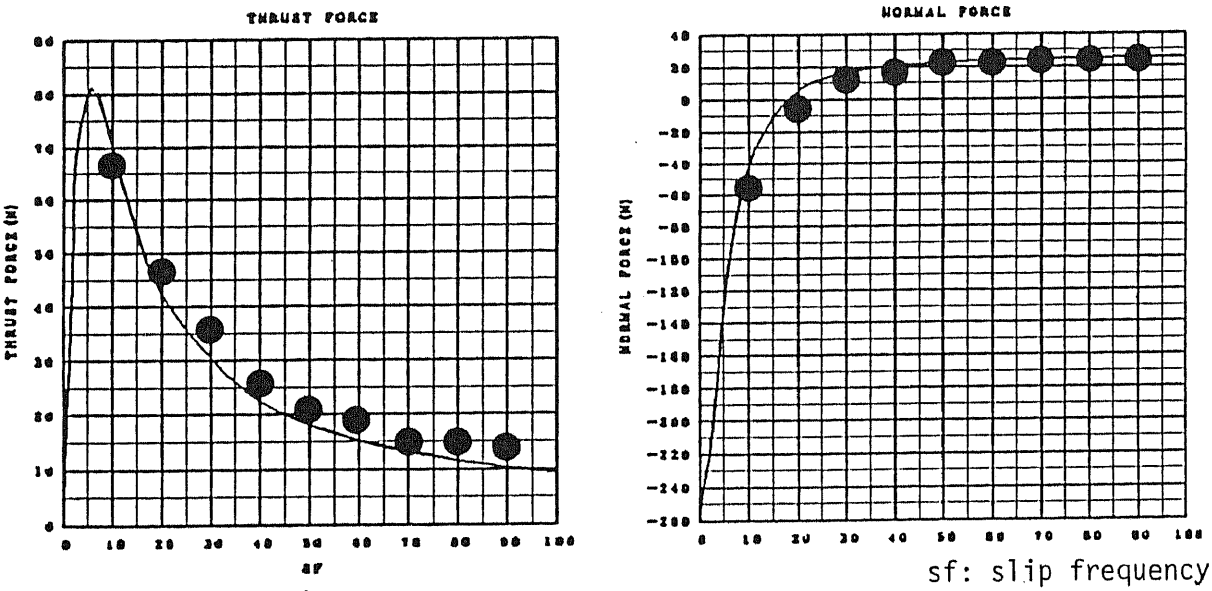

(a) Thrust force

(b) Normal force

Figure A.1.1 Measured forces of the stndstill SLIM

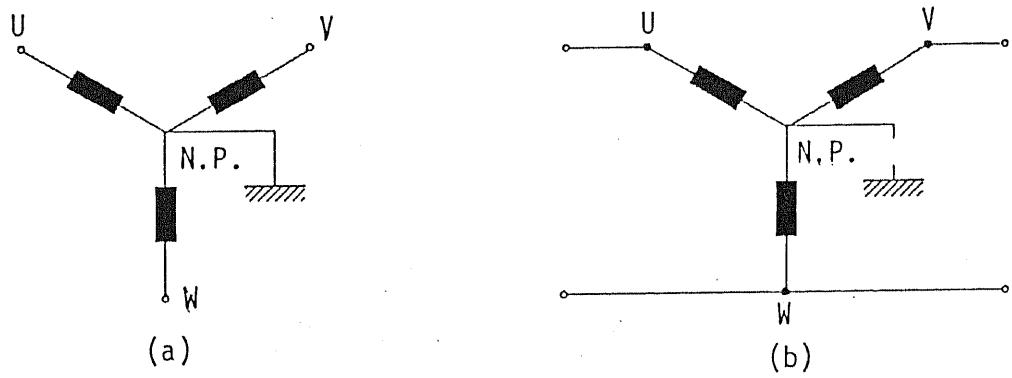

Figure A.1.2 Three phase connection
(a) 6-terminal network with the neutral point connection
(b) 4-terminal network without the neutral point connection

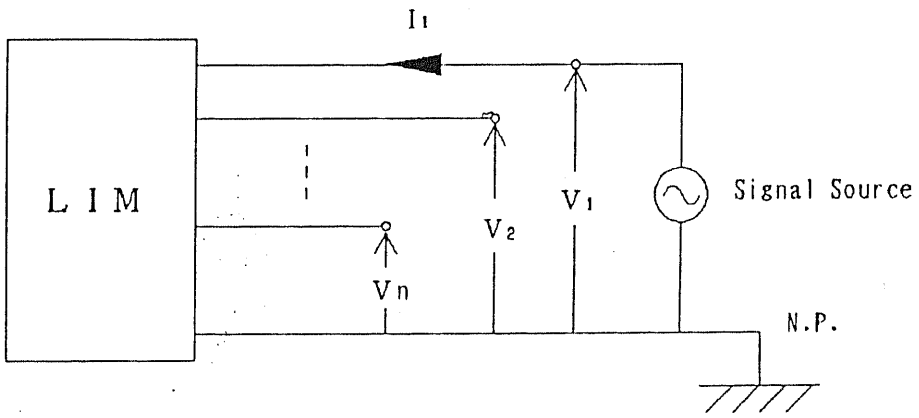

Figure A.1.3 Single phase drive for the impedance measurements

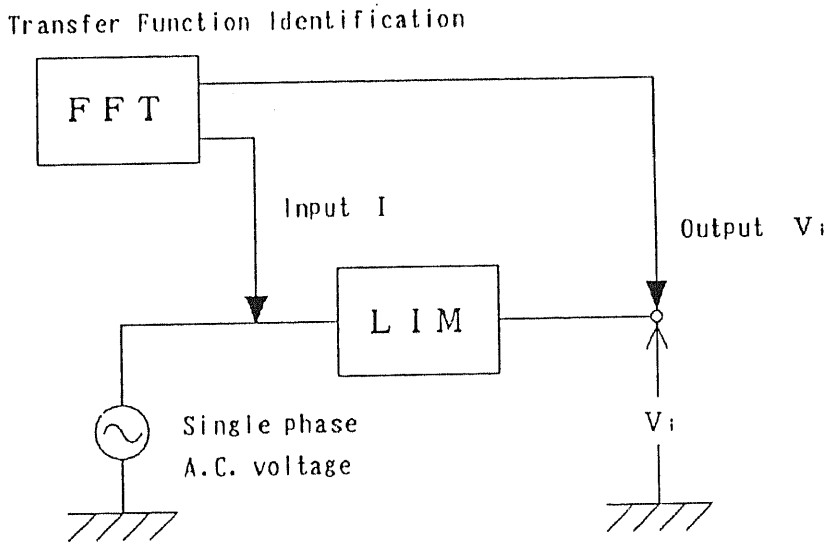

Figure A.1.4 Impedance measurements with FFT and VVVF signal source

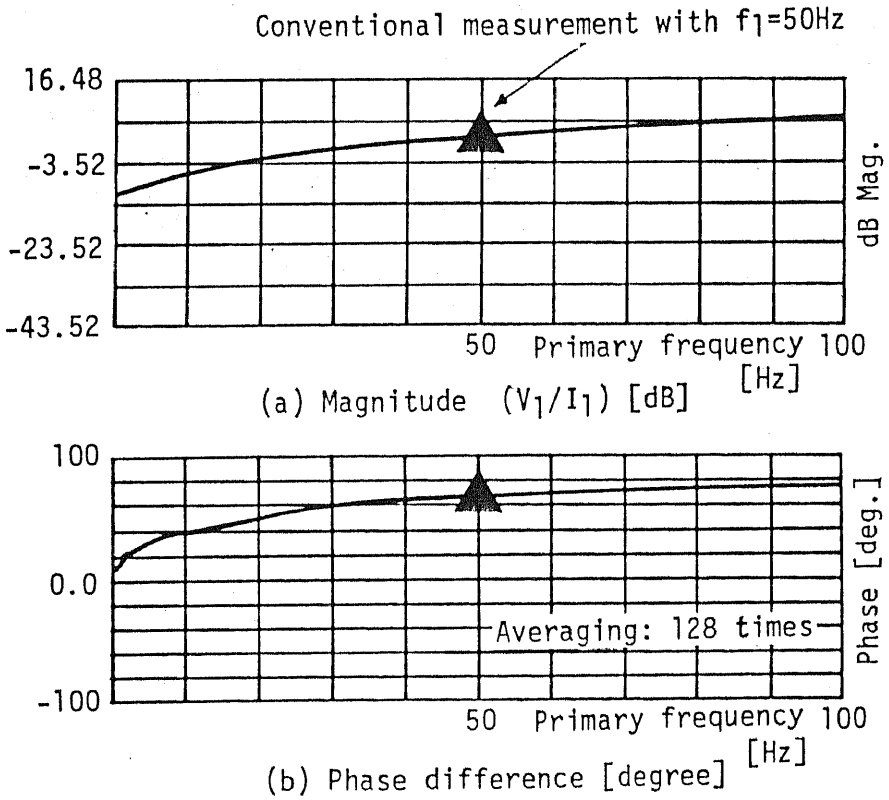

Figure A.1.5 An example of the measured impedances (Transfer function)

Table A.1.2 Dimensions of the standstill single- sided linear induction motor in the Masada Laboratory

[Primary side]	
Primary core width	120mm
Total width with coil ends	300mm
Motor length	1400mm
Pole number	8
Pole pitch	156mm
Primary core height	100mm
[Secondary side]	
Mechanical gap length	10mm
Secondary core width	120mm
Reaction plate thickness	5mm
Secondary core height	30mm

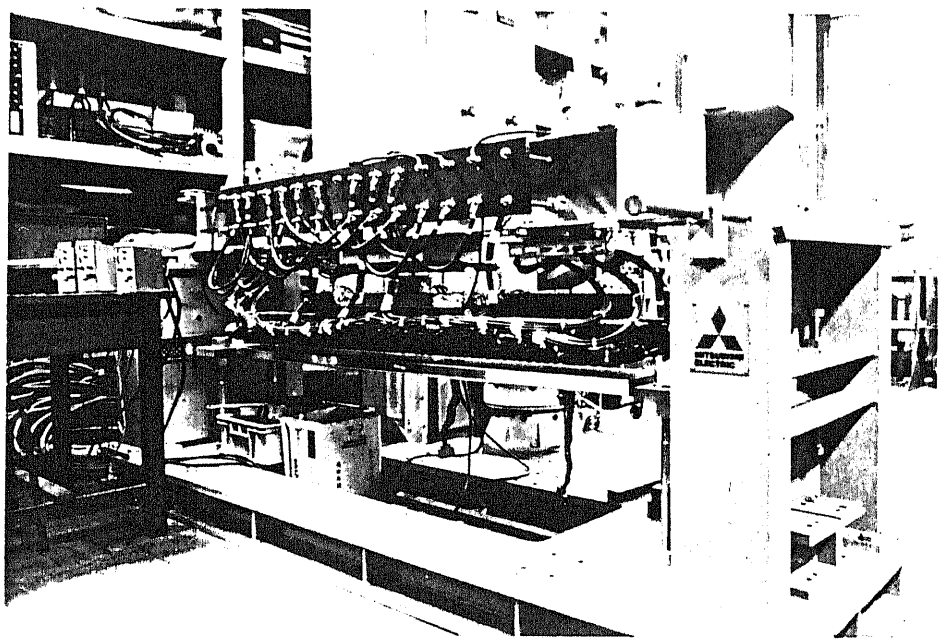

Figure A.1.6 The test machine

Appendix 2: Discussions on the Mathematical Formulations of Prof. I. Boldea

KOSEKI, Takafumi
(The University of Tokyo, JAPAN)

1. Introduction

In this chapter, we discuss following theoretical aspects in Prof. Boldea's plan described in the part I:

(1) relation between his large impedance matrix in the part I and the 3×3 matrix explained in the chapter II.2,

(2) doubt on his formulation of the forces considering the Lagrange's function, and

(3) necessity of the reference-frame transformation for applying your theory to general running cases.

2. Relation between the Boldea's large impedance matrix and the 3×3 matrix

In the part I proposed by Prof. Boldea, the voltage equations are:

$$\begin{bmatrix} V_R \\ V_Y \\ V_B \\ \hline 0 \\ \vdots \\ 0 \end{bmatrix} \begin{matrix} \left.\begin{matrix}\\\\\end{matrix}\right\} \text{Primary} \\ \left.\begin{matrix}\\\\\\\end{matrix}\right\} \text{Secondary} \end{matrix} = \mathrm{diag}\left[r_R, r_Y, r_B, r_1, \cdots, r_n\right] \begin{bmatrix} i_R \\ i_Y \\ i_B \\ \hline i_1 \\ \vdots \\ i_n \end{bmatrix} + \frac{d}{dt} \left[\begin{array}{c|c} \begin{matrix} L_{11} & L_{12} \\ L_{21} & L_{22} \end{matrix} & \begin{matrix} \\ \\ \end{matrix} \\ \hline \begin{matrix} \\ \\ \end{matrix} & \begin{matrix} \\ \\ \end{matrix} \end{array}\right] \begin{bmatrix} i_R \\ i_Y \\ i_B \\ \hline i_1 \\ \vdots \\ i_n \end{bmatrix} \begin{matrix} \left.\begin{matrix}\\\\\end{matrix}\right\} 3 \\ \left.\begin{matrix}\\\\\\\end{matrix}\right\} n \end{matrix} \qquad \text{(A.2.1)}$$

where V_R, V_Y, V_B and $i_1, \ldots, i_n$ are unknown variables.

When you assume steady state operation of a LIM whose structure is homogeneous along the x direction:

$$\begin{bmatrix} \dot{V}_1 \\ \hline 0 \end{bmatrix} = \left[\begin{array}{c|c} R_{11} + j\omega L_{11} & j\omega L_{12} \\ \hline j\omega L_{21} & R_{22} + j\omega L_{22} \end{array}\right] \begin{bmatrix} \dot{I}_1 \\ \hline \dot{I}_2 \end{bmatrix} \equiv \left[\begin{array}{c|c} \overbrace{\dot{Z}_{11}}^{3} & \overbrace{\dot{Z}_{12}}^{n} \\ \hline \dot{Z}_{21} & \dot{Z}_{22} \end{array}\right] \begin{matrix} \left.\begin{matrix}\\\end{matrix}\right\} 3 \\ \left.\begin{matrix}\\\end{matrix}\right\} n \end{matrix} \begin{bmatrix} \dot{I}_1 \\ \hline \dot{I}_2 \end{bmatrix} \qquad \text{(A.2.2)}$$

The 3×3 matrix Z' is defined here,

$$\begin{bmatrix} V_R \\ V_Y \\ V_B \end{bmatrix} = \begin{bmatrix} Z_{11} & Z_{12} & Z_{13} \\ Z_{21} & Z_{22} & Z_{23} \\ Z_{31} & Z_{23} & Z_{33} \end{bmatrix} \begin{bmatrix} I_R \\ I_Y \\ I_B \end{bmatrix} \qquad \text{(A.2.3)}$$

By eliminating the currents vector $\dot{I}_2$ from the equation (A.2.2), the following equation is derived.

$$Z' = Z_{11} - Z_{12} \cdot Z_{22}^{-1} \cdot Z_{21} \qquad \text{(A.2.4)}$$

This relation should be applied to verify his impedance-measurement scheme at the last procedure of our project.

3. Derivation of the thrust force from the voltage equations

If his assumption is physically proper, there is no problem to the equation (I.3). However, some theoretical corrections should be necessary concerning the force calculations from (I.5) to (I.8) as follows. In his formulation, only the reluctance torque can be calculated; there is, however, no reluctance force substantially in LIMs, *i.e.*, you must consider the effect of the induced secondary current.

Although Koseki does not believe that the virtual displacement principle is suitable for LIM calculations, you should start from the following Lagrange's equation (Weh) if you must, nevertheless, calculate forces with the principle.

$$\frac{d}{dt}\left[\frac{\partial \Lambda}{\partial \dot{\xi}_k}\right] - \frac{\partial \Lambda}{\partial \xi_k} + \frac{\partial P_V}{\partial \dot{\xi}_k} = \Gamma_k \tag{A.2.5}$$

where ξ_k means generalized coordinates, and the Lagrangian Λ is defined using the generalized motive energy E^* and the generalized potential energy Θ as follows.

$$\Lambda \equiv E^* - \Theta \tag{A.2.6}$$

P_V is the Reyleigh's loss function and Γ is an generalized input force.

In order to apply the basic equation (A.2.5) to the calculation of a LIM,

$$E^* = T^* + W_m^* \tag{A.2.7}$$

where T^* is the mechanical motive coenergy and W_m^* is the magnetic coenergy. Especially in the case of a linear field,

$$T^* = \sum_{i=1}^{m} \frac{m_i}{2} \cdot \dot{x}_i^2 \tag{A.2.8}$$

where m_i is a mass of a massive point constructing the system and x_i is an x-position of each massive point.

$$W_m^* = \sum_{j=1}^{n} \frac{L_j}{2} \cdot Q_j^2 \tag{A.2.9}$$

where L_j is an inductance and Q_j is an electric charge.

In our problem, the potential energies of springs and of the electric field is zero, hence,

$$\Theta = 0. \tag{A.2.10}$$

Furthermore, the mechanic damping losses (*i.e.*, mechanic damping co-losses P_D^*) is also negligible.

$$\begin{aligned} P_V &= P_D^* + P_v \\ &= \sum_{i=1}^{m} \frac{D_i}{2} \cdot \dot{x}_i^2 + \sum_{j=1}^{n} \frac{r_j}{2} \cdot Q_j^2 \\ &= \sum_{j=1}^{n} \frac{r_j}{2} \cdot Q_j^2 \end{aligned} \tag{A.2.11}$$

According to Prof. Boldea's argument,

$$\Lambda = \sum_{i=1}^{m} \frac{m_i}{2} \cdot \dot{x}_i^2 + \frac{1}{2} \cdot \mathbf{I}^t \cdot L \cdot \mathbf{I} \tag{A.2.12}$$

and

$$P_v = \mathbf{I}^t \cdot R \cdot \mathbf{I}. \tag{A.2.13}$$

Therefore, the thrust force is derived as follows:

$$\frac{d}{dt}\left[\frac{\partial \Lambda}{\partial \dot{x}}\right] - \frac{\partial \Lambda}{\partial x} + \frac{\partial P_v}{\partial \dot{x}} = F_x \tag{A.2.14}$$

hence,

$$F_x = -\frac{\partial}{\partial x}\left[\frac{1}{2}\mathbf{I}^t \cdot L \cdot \mathbf{I}\right] + \frac{d}{dt}\left[\frac{\partial}{\partial \dot{x}}\left[\frac{1}{2}\mathbf{I}^t \cdot L \cdot \mathbf{I}\right]\right] + \frac{\partial}{\partial \dot{x}}\left[\mathbf{I}^t \cdot R \cdot \mathbf{I}\right]. \tag{A.2.15}$$

If the modeling would be ideal, the first term in the right hand side of the equation (A.2.15) should be zero, because it expresses a *reluctance force.* Normal- and side- forces would be formulated in the same way.

Koseki is, however, not sure if such formulations have sense, because it would be almost impossible to derive the forces explicitly in this form. Furthermore, the impedance matrix L must be not the original measured results, but be rewritten with a reference-frame transformation, for considering effects of the motor's velocity.

4. Necessity of reference-frame transformation

The large impedance matrix is measured with *standstill* tests. Since LIM's characteristics depend on the slip, the voltage equations must explicitly contain the effect of the velocity for a general use, especially in order to calculate forces as described in the chapter II.2; a proper reference frame transformation is essential to the parts of the reactance matrix Z_{12} and Z_{21} in the equation (A.2.2), *e.g.,* as written in (Kovács, 1984).

5. Discussions between Prof. Boldea and Koseki

5.1. Prof. Boldea's comment

"The forces expressions are correct in my manuscript (please check the reference (Turner, 1981)). It is the entire force not only the reluctance force (please see the reference (Nondahl, 1980)). The reference system is attached to the primary. The equation of motion should be added for mechanical transients:

$$M \times \frac{dx}{dt} = F_x - F_{load}$$

x- becomes a state variable while for F_n and F_z the small displacement approach may be used. An initial value of x for the front end (first) loop is assigned.

The number of secondary loops may be kept constant with the initial values of secondary current given; for example zero before starting. After 1-2 loops length has passed, the current in the rear loop in neglected and a new loop in the front end is added whose initial current is evidently zero.

It is well understood that the secondary loops extend well beyond the primary length.

For constant speed $x = v \times t$ $v = const.$ and the above motion equation is dropped. With zero initial currents for this case the computation will stop when the primary current will be steady state."

5.2. Koseki's opinion:

Prof. Boldea's formulation are quite similar to Nondahl's: the formulations are theoretically consistent with themselves in the paper (T.H. Nondahl, 1980). The authors do not, however, apply the virtual displacement principle to the thrust calculation, although they use it for calculating normal force; it seems right. On the other hand, Turner calculates the thrust force with the virtual displacement principle in his paper (Turner, 1981), but he uses it in a numerical iterative computing procedure for calculating transient characteristics of a LIM with a cage secondary rail, where the *(small)* impedance matrix is rewritten at each step, *i.e.*, time dependent effects, *e.g.*, slip and speed of the secondary conductive bars, are implicitly included in the numerical process. The two formulations of Nondahl and Turner are, therefore, quite different. Consequently, Koseki's doubt on force calculation of Prof. Boldea still remains.

References

[A.2.1] H. Weh: "Einführung in die elektrische Energieumformung", Vorlesungsmitschrift der TU Braunschweig, FRG, or
e.g. A.2. Sommerfeld: "Theoretische Physik", Bd. 1, Kapitel 6, 4. Auflage, Dieterische Verlagsbuchhandlung, 1949

[A.2.2] P. K. Kovács: "Transient Phenomena in Electrical Machines", Studies in Electrical and Electronic Engineering 9, 1984, Elsevier

[A.2.3] T. H. Nondahl, D. W. Novotny: "Three phase pole by pole model of a linear induction machine" Proc. of IEE, Vol. 127, PT. B, No. 2, 1980, pp. 68-82

[A.2.4] T. R. Turner, T. H. Loye: "The transient performance of linear induction motors" IEEE Trans. Vol. PAS-100, No. 12, 1981, pp. 4958-4964